arXiv:1611.08627v1 [cond-mat.mes-hall] 25 Nov 2016

Review Article

A review of the electronic and optical properties of strained graphene and other similar 2D materials

Gerardo G. Naumis[1], Salvador Barraza-Lopez[2], Maurice Oliva-Leyva[3], and Humberto Terrones[4]

[1] Depto. de Física-Química, Instituto de Física, Universidad Nacional Autónoma de México, Apdo. Postal 20-364, Mexico City 01000, Mexico
[2] Department of Physics, University of Arkansas, Fayetteville, AR 72701, USA
[3] Instituto de Investigaciones en Materiales, Universidad Nacional Autónoma de México, Apdo. Postal 70-360, Mexico City 04510, Mexico.
[4] Department of Physics, Applied Physics, and Astronomy. Rensselaer Polytechnic Institute, Troy, New York, NY 12180, USA

E-mail: naumis@fisica.unam.mx,

Abstract. This review presents the state of the art of strain and ripple-induced effects on electronic and optical properties of graphene. We start by providing the crystallographic description of mechanical deformations, as well as the diffraction pattern for different kinds of representative deformations fields. Then we review the unique elastic properties of graphene and how strain can be produced. Thereafter, we examine various theoretical approaches used to study the electronic properties of strained graphene and discuss the advantages of each. Also we show how such approaches provide a platform for describing exotic properties such as a fractal spectrum related with quasicrystals, a mixed Dirac-Schrödinger behavior, emergent gravity, topological insulator states, among others. Moreover, we review the physical consequences of strain on the optical properties, with particular focus on the Raman spectrum. At the same time, we present recent advances to tune the optical conductivity of graphene by strain engineering, which has opened up new paths in device applications. Finally, we present a brief review of strain effects in multilayered graphene and other promising 2D materials like silicene and other group-IV elements, phosphorene, dichalcogenide- and monochalcogenide-monolayers, with a slight emphasis on the occurrence and effects of novel two-dimensional structural phase transitions occurring at finite temperature.

Keywords: Graphene, mechanical strain, electronic properties, optical properties, two-dimensional materials, dichalcogenide- and monochalcogenide-monolayers,
Submitted to: *Rep. Prog. Phys.*

Contents

1 Introduction 2

2 Description of pristine and deformed Graphene 3
2.1 Unstrained graphene: crystal structure, reciprocal lattice and diffraction 3
2.2 Description of deformed graphene 5

3 Deformations in graphene 8
3.1 Elastic coefficients: Experimental and theoretical characterization 8
3.2 Strain patterns and methods to produce them 10
3.2.1 Graphene on substrates: moiré superlattices 10
3.2.2 Ripples and bending 11

4 Electronic properties 11
4.1 Electronic properties of pristine and disordered graphene 13
4.2 Tight-binding approach to strain 16
4.3 Uniformly strained graphene 16
4.3.1 Simplest form of strain: the isotropic expansion. 20
4.4 Non-uniform uniaxial strain 21
4.5 Ripples and bending 23
4.6 Graphene on substrates: superlattices . 24
4.6.1 Periodic uniaxial strain and ripples: the simplest superlattice. . 24
4.6.2 More general types of superlattices. 25
4.7 Topological phases 29
4.8 Continuum models: effective Dirac equation 30
4.8.1 Uniform strain. 30
4.8.2 Nonuniform strain: Gauge fields and position-dependent Fermi velocity. 31
4.8.3 Time-dependent strain. 33
4.9 Strain from the perspective of discrete differential geometry 34
4.9.1 Underlying assumptions of the continuum, Dirac approach. . . . 35
4.9.2 Derivation of strain-induced gauges. 36
4.9.3 Further discussion of the discrete geometry 38
4.9.4 Open directions within the discrete approach. 40
4.10 Results from density-functional theory . 41

5 Optical properties 43
5.1 Strain engineering of optical absorption 43
5.2 Raman spectrum to determine nanometre-scaled strain variations 43

6 Strain in multi-layered graphene 45

7 Extensions to other 2D systems 48
7.1 Silicene and other group-IV two-dimensional materials 48
7.2 Phosphorene 51
7.3 Transition metal dichalcogenide monolayers 54
7.4 Monochalcogenide monolayers 54

8 Conclusions and outlook 59

1. Introduction

Graphene was the first truly two dimensional (2D) crystal ever discovered [1, 2]. The key ingredient for its discovery was the observation that it becomes visible in an optical microscope if placed on a Si wafer with a carefully chosen thickness [3]. Eventually, this one-atom thick carbon membrane turned out to have the highest known electrical and thermal conductivity [4], as well as the highest stiffness and strength; it supports very high strain prior to mechanical failure [5]. It can be strained well beyond the linear regime, and bent and wrinkled [5].

There has been an ever increasing interest in using strain and the soft-properties of graphene to control the physical properties of this wonderful material [6, 7, 8, 9, 10, 11, 12, 13, 14, 15]. Even a new word has been coined describing this aim: straintronics [16]. In most applications, graphene lays or grows on a substrate. Due to the mismatch between the graphene and substrate lattice parameters, atoms move to reduce its energy producing a certain amount of strain too.

Thus, understanding how strain affects graphene's electronic and optical properties is of paramount importance. However, the interest is not only technological. This system is a playground to produce new physics, from exotic topological quantum phases, to analogies with other fields (from quantum electrodynamics to quantum gravity), and even connects with traditional arts like origami and kirigami. Furthermore, strain in graphene created an appetite for doing similar things with other 2D materials like BN, $NbSe_2$, TaS_2, MoS_2 and many others [7, 9]. The natural next step is the design at will of multi-layered materials and superlattices [7].

Just to cite a few examples of how to exploit these ideas, we mention the experimental observation of Dirac cone replicas on substrates [17, 18] with halved group velocity [19] and sometimes accompanied by a reversal of the Hall effect [18, 20]. Also, we can cite the first atomic observation of the Quantum Hall effect fractal spectrum [21, 20], first predicted in 1976 and known as the Hofstadter butterfly [22]. Other advances are the building of in-plane graphene

heterostructures on hexagonal boron nitride with controlled domain sizes [23] (which is a useful way to build electronic devices [24]). There are interesting proposals for building spin-polarization switches via strain [25], piezoelectricity by Li doping [26], giant pseudomagnetic fields [27] or a giant two-dimensional band-piezoelectric effect by biaxial-strain [28]. Other 2D materials also show potential for piezoelectricity [29, 30, 31, 32] and display interesting connections with glass network formers [33, 34], and glass constraint (rigidity) theory [35].

The amount of bibliography in the field is huge and growing each year. Fortunately, there are other excellent reviews that serve as a guide through this information forest [6, 8, 9, 10, 11, 12, 13, 14, 15]. Each of these reviews has its own focus and thus we recommend the reader to look at such papers for a more complete view of the field. The focus of this one is to provide a basic platform and guide to understand in simple terms representative models and results, with enough physical significance, to get a grasp of the main effects of strain, the emerging consensus on the field, and its new directions.

To give an example, we show that many of the effects of strain are already present in the most simple case, the isotropic expansion. From this realization, one is able to understand well documented more complex situations like the appearance of a mixed Dirac-Schrödinger behavior [16, 36, 37, 38, 39, 40] and pseudomagnetic fields in the Dirac equation [6].

Also, there are several theoretical approaches to treat strain in graphene. Here we will consider the tight-binding approach, the Dirac equation with pseudoelectromagnetic fields, a perspective from discrete differential geometry, and results from density functional calculations (DFT). Each of such approaches leads to comparisons with experimental results and has its own virtues. For example, the pseudomagnetic field approach is excellent to provide a link with quantum electrodynamics but is better suited for studying smooth spatially varying strain. If short-wavelength strain is present, like is the case of graphene grown on a substrate, the tight-binding approach is better suited. The approach based on discrete differential geometry has the advantage of laying out the theory directly onto the atomic lattice. DFT helps to design and improve theories. It also discerns important experimental questions.

With previous considerations in mind, each section of this review was written with the idea of being as independent as possible from the others. At the same time, we have aimed to offer an integrated body of knowledge, with a logical and pedagogical structure.

The layout of this work is as follows. We start by making a review of the deformations in graphene, in particular, we focus our attention in section 2 on how they are described using a mix of crystallography and elastic theory. Section 3 is devoted to study the mechanical properties of graphene and how to produce different kinds of deformations. In section 4 we discuss the electronic properties of strained graphene, providing different theoretical approaches as well as numerical and experimental results. Then in section 5 we review the optical properties, while sections 6 and 7 provide an overview of multilayered graphene and other 2D materials different from graphene. Conclusions and an outlook of the field are presented afterwards.

2. Description of pristine and deformed Graphene

In this section we will discuss some basic properties of the lattice structure of unstrained or strained graphene. The main idea here is to provide a framework to develop the properties of strained graphene later on. The section is divided into two subsections, one deals with unstrained graphene while the other provides the tools for the description of strain.

2.1. Unstrained graphene: crystal structure, reciprocal lattice and diffraction

The starting point for understanding the properties of graphene is to consider the honeycomb lattice structure shown in Figure 1(a). The honeycomb lattice is not a Bravais lattice since there are two kinds of environments for Carbon atoms, denoted as A and B sublattices in Figure 1(a). Notice that atoms in the A sublattice only have first neighbors belonging in the B lattice and viceversa. Such subdivision means that the lattice is bipartite, and many of the electronic and optical properties depend on this general observation [41]. Even non-periodic but bipartite lattices like the quasiperiodic Penrose lattice [42], the random binary alloy in a square lattice [43] or vacancies in graphene [44, 45, 46] share some electronic features with pristine graphene, like zero-energy confined state modes or pseudomobility edges [42].

If we take one of the sublattices, say A, it turns out to be a 2D Bravais triangular lattice with basis vectors:

$$\boldsymbol{a}_1 = \frac{a}{2}(\sqrt{3}, 3), \qquad \boldsymbol{a}_2 = \frac{a}{2}(-\sqrt{3}, 3), \tag{1}$$

where $a = 1.42$Å is the distance between carbon atoms [41] (Figure 1(a)). Notice that the x axis has been chosen in the zigzag direction here. The B sublattice is obtained by a shift of atoms belonging to the A sublattice by $\boldsymbol{\delta}_1$.

However, it is customary to define a triad of vectors:

$$\boldsymbol{\delta}_1 = \frac{a}{2}(\sqrt{3},1), \quad \boldsymbol{\delta}_2 = \frac{a}{2}(-\sqrt{3},1), \quad \boldsymbol{\delta}_3 = a(0,-1), \tag{2}$$

that point out to the first neighbours of A, and which are the first images of $\boldsymbol{\delta}_1$ under the symmetry group of the Bravais lattice, equivalent to the firsts images of $\boldsymbol{\delta}_1$ in a trigonal kaleidoscope. Such images are easy to obtain from the Bravais lattice and $\boldsymbol{\delta}_1$ as follows:

$$\boldsymbol{\delta}_2 = \boldsymbol{\delta}_1 + \boldsymbol{a}_2 - \boldsymbol{a}_1, \quad \boldsymbol{\delta}_3 = \boldsymbol{\delta}_1 - \boldsymbol{a}_1. \tag{3}$$

The corresponding reciprocal lattice, seen in Figure 1(b), has the following basis vectors:

$$\boldsymbol{G}_1 = \frac{2\pi}{3a}(\sqrt{3},1), \qquad \boldsymbol{G}_2 = \frac{2\pi}{3a}(-\sqrt{3},1). \tag{4}$$

As shown in Figure 1(b), the first Brillouin zone (1BZ) is built from the Wigner-Seitz construction, resulting in an hexagon with two inequivalent high-symmetry points [41] $\boldsymbol{K}_\pm = (\pm 4\pi/(3\sqrt{3}a), 0)$. Notice that the form of the 1BZ is a property of the Bravais lattice.

An important feature that has a crucial impact on the optical and electronic properties of graphene is the fact that points $\boldsymbol{K}_+$ and $\boldsymbol{K}_-$ correspond to the intersection of diffraction Bragg lines (instead of Bragg planes, as it is the case for 3D, bulk materials). A Bragg (Voronoi) line bisects a reciprocal lattice vector $\boldsymbol{G}$ at right angles [47] (see Figure 1(b)). In graphene, if $\boldsymbol{k}$ is a wavevector in the reciprocal space, the diffraction lines closer to the Γ point have as equations (known as Laue conditions [47]):

$$2\boldsymbol{k}\cdot\boldsymbol{G}_1 = \pm|\boldsymbol{G}_1|^2, \tag{5}$$

$$2\boldsymbol{k}\cdot\boldsymbol{G}_2 = \pm|\boldsymbol{G}_2|^2, \tag{6}$$

and

$$2\boldsymbol{k}\cdot(\boldsymbol{G}_1+\boldsymbol{G}_2) = \pm|\boldsymbol{G}_1+\boldsymbol{G}_2|^2, \tag{7}$$

where $\boldsymbol{K}_+$ and $\boldsymbol{K}_-$ are the intersections of Equations (5), (6) and (7).

Diffraction impacts the electronic properties through the generation of stationary waves and Van Hove singularities in the density of electronic states [47] (both related through an integral over isoenergetic level curves). Thus, it is worthwhile to calculate the diffraction properties of the lattice. The diffraction pattern is given by the norm of the Fourier transform of the lattice positions multiplied by the atomic form factor [47]. In crystallography, this norm is known as the structure factor.

To obtain the diffraction pattern, we assume that the mass or electronic density results in an scattering potential $V(\boldsymbol{r})$ which can be described as delta functions centered at the graphene lattice with a weight V_0:

$$V(\boldsymbol{r}) = V_0 \sum_l \delta(\boldsymbol{r}-\boldsymbol{r}_l), \tag{8}$$

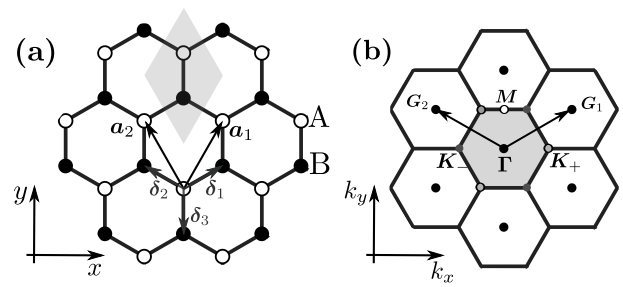

Figure 1. (a) Graphene lattice showing the unit cell (shaded), the lattice vectors $\mathbf{a}_1$ and $\mathbf{a}_2$, and first-neighbor vectors $\boldsymbol{\delta}_1$, $\boldsymbol{\delta}_2$ and $\boldsymbol{\delta}_3$. The bipartite sublattices A and B are also shown, as well as the definition of the reference system used in this work. (b) First Billouin zone (shaded) of unstrained graphene showing the high symmetry points. The Fermi level and the Dirac points coincide with the inequivalent high symmetry points $\boldsymbol{K}_+$ and $\boldsymbol{K}_-$. This is no longer true for strained graphene.

where $\boldsymbol{r}_l$ are the positions of the atoms in graphene. The Fourier transform of this potential, denoted by $\widetilde{V}(\boldsymbol{k})$, is obtained by integrating over the entire area S:

$$\widetilde{V}(\boldsymbol{k}) = \int_S V(\boldsymbol{r}) e^{i\boldsymbol{k}\boldsymbol{r}} dS. \tag{9}$$

For the case of graphene, and for further reference, we will label this transform as $\widetilde{V}_{gp}(\boldsymbol{k})$. It can be written as:

$$\widetilde{V}_{gp}(\boldsymbol{k}) = V_0[1+e^{i\boldsymbol{k}\boldsymbol{\delta}_1}]\sum_{\boldsymbol{G}} \delta(\boldsymbol{k}-\boldsymbol{G}), \tag{10}$$

with $\boldsymbol{G} = l\boldsymbol{G}_1 + h\boldsymbol{G}_2$ and l, h integers. The norm of this transform is:

$$|\widetilde{V}_{gp}(\boldsymbol{k})|^2 = 4V_0^2 cos^2(\boldsymbol{k}\cdot\boldsymbol{\delta}_1/2)\sum_{\boldsymbol{G}} \delta(\boldsymbol{k}-\boldsymbol{G}). \tag{11}$$

The first term in brackets in previous Equation is the structure factor (that we denote $F(l,h)$) while the second is the reciprocal lattice, i.e., where diffraction spots are localized (see Figure 2). For graphene, the diffraction spots form a triangular lattice, and therein, the amplitudes are determined by the structure factor:

$$F_{gp}(l,h) = 4V_0^2 cos^2([l\boldsymbol{\delta}_1\cdot\boldsymbol{G}_1 + h\boldsymbol{\delta}_1\cdot\boldsymbol{G}_2]/2), \tag{12}$$

or

$$F_{gp}(l,h) = 4V_0^2 cos^2\left(\frac{\pi}{3}(2l-h)\right). \tag{13}$$

Previous Equation predicts two intensities, $4V_0^2$ or V_0^2 for the diffraction peaks. Notice however that a real diffraction pattern is taken in 3D, and thus the diffraction spots are replaced by rods. Once this fact is taken into account, Equation 13 is in good agreement with electron diffraction results [48]. However, the experimental shape and widths of the peaks show deviations from the standard diffraction behavior presented here since graphene is not flat. This means that there is a superposition of diffraction rods with slightly different orientations [48]. In bilayer

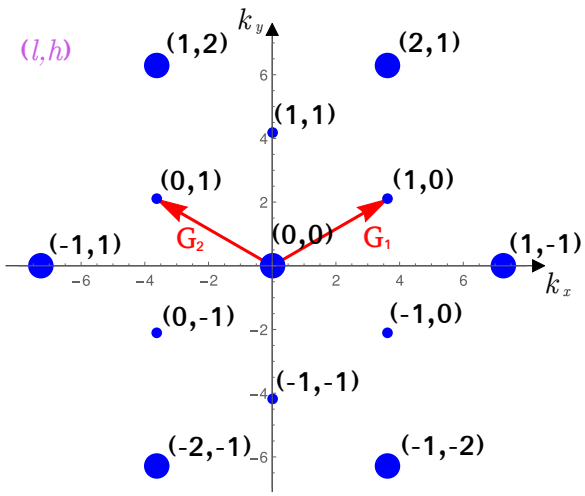

Figure 2. Theoretical computation of graphene's diffraction pattern. The position of each diffraction spot was computed from Equation (11) while the intensity is obtained from Equation (13) for the Miller indexes l and m that label each spot.

graphene, the rods present variations as the crystal is tilted, thus providing a good technique to distinguish between monolayer and multilayered graphene [48].

2.2. Description of deformed graphene

When mechanical deformations are applied to graphene, the atoms are in general displaced (see Figure 3). Within Cauchy-Born assumption, the new positions are usually described by a displacement field $\boldsymbol{u}(\boldsymbol{r})$ where $\boldsymbol{r}$ represents a material point of unstrained graphene [13]. After being deformed, the new position of the atom is:

$$\boldsymbol{r}' = \boldsymbol{r} + \boldsymbol{u}(\boldsymbol{r}). \tag{14}$$

Two kinds of problems arise in elasticity [49, 50]. One is to find $\boldsymbol{u}(\boldsymbol{r})$ given some prescribed forces, usually at the boundaries. The other is to find the forces once $\boldsymbol{u}(\boldsymbol{r})$ is given. The forces produce stress, and are related to $\boldsymbol{u}(\boldsymbol{r})$ by means of the-so called elasticity (or constitutive) equations. For small strain fields, the equations are a generalization of Hooke's law [49, 51].

A further complication is the need to distinguish fields $\boldsymbol{u}(\boldsymbol{r})$ that imply deformations to those which are rigid-body movements corresponding to rotations or translations. This is done by a symmetric strain tensor, that measures deformations and has the following components [51]:

$$\bar{\epsilon}(\boldsymbol{r})_{ij} = (\partial_j u_i(\boldsymbol{r}) + \partial_i u_j(\boldsymbol{r}))/2, \tag{15}$$

and by the antisymmetric strain tensor, that measures rigid-body displacements [51]:

$$\bar{\omega}(\boldsymbol{r})_{ij} = (\partial_j u_i(\boldsymbol{r}) - \partial_i u_j(\boldsymbol{r}))/2. \tag{16}$$

Stresses acting on the system are described by a tensor [49] $\bar{\boldsymbol{s}}(\boldsymbol{r})$. The components of this tensor

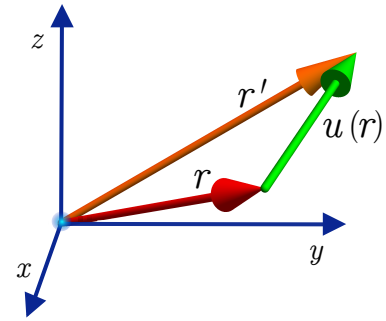

Figure 3. Displacement field. An atomic site at position $\boldsymbol{r}$ is displaced to $\boldsymbol{r}'$ by a position-dependent displacement field $\boldsymbol{u}(\boldsymbol{r})$.

$\bar{s}(\boldsymbol{r})_{ij} = F_i/A_j$ are the forces in the direction i applied over a surface normal to the direction j. In linear elasticity, strain and stress are related via the constitutive equation [51]:

$$\bar{s}(\boldsymbol{r})_{ij} = \bar{C}_{ijls}\bar{\epsilon}(\boldsymbol{r})_{ls}, \tag{17}$$

where $\bar{C}_{ijls}$ is a rank 4 tensor which contains the elastic constants of the material (that is sometimes written as a rank-2 tensor when employing Voigt notation). In Section 3, a full discussion is provided concerning the elastic properties of graphene and how to produce different kinds of deformations.

An important feature to keep in mind is that first-neighbour vectors $\boldsymbol{\delta}_n$ become space-dependent. Within Cauchy-Born approximation, they are given by [52]:

$$\boldsymbol{\delta}'_n(\boldsymbol{r}) \approx \boldsymbol{\delta}_n + (\boldsymbol{\delta}_n \cdot \nabla)\boldsymbol{u}(\boldsymbol{r}) = (\bar{\boldsymbol{I}} + \nabla\boldsymbol{u}(\boldsymbol{r})) \cdot \boldsymbol{\delta}_n, \tag{18}$$

where $\bar{\boldsymbol{I}}$ is the 2×2 identity matrix, and $\nabla\boldsymbol{u}(\boldsymbol{r})$ is the Jacobian of the displacement field, known as the displacement gradient tensor, whose components $i, j = x, y$ given by:

$$[\nabla\boldsymbol{u}(\boldsymbol{r})]_{ij} = \bar{\epsilon}(\boldsymbol{r})_{ij} + \bar{\omega}(\boldsymbol{r})_{ij}. \tag{19}$$

If the deformation does not involve rotations, i.e., $\bar{\boldsymbol{\omega}}(\boldsymbol{r}) = 0$, from Equation (18) and Equation (19) the nearest-neighbor vectors become [52]:

$$\boldsymbol{\delta}'_n = (\bar{\boldsymbol{I}} + \bar{\boldsymbol{\epsilon}}(\boldsymbol{r})) \cdot \boldsymbol{\delta}_n \quad (n = 1, 2, 3). \tag{20}$$

In the rest of this section, we will discuss some particular cases of strain, to illustrate their consequences on the lattice and on diffraction. This material will be useful when discussing electronic and optical properties.

One of the most illustrative cases of strain is the uniform case, for which the positions of carbon atoms at $\boldsymbol{r}$ are transformed by:

$$\boldsymbol{u}(\boldsymbol{r}) = \bar{\boldsymbol{\epsilon}} \cdot \boldsymbol{r}, \tag{21}$$

where $\bar{\boldsymbol{\epsilon}}$ is a uniform strain tensor, *i.e.*, the components of $\bar{\boldsymbol{\epsilon}}$ do not change with the position. The tensor is thus:

$$\bar{\boldsymbol{\epsilon}} = \begin{pmatrix} \epsilon_Z & \gamma_S \\ \gamma_S & \epsilon_A \end{pmatrix}, \tag{22}$$

where ϵ_A and ϵ_Z denote, respectively, the uniaxial strain applied along the armchair and zigzag directions, and γ_S is the shear strain.

Using this field, the new positions of the atoms are given by:

$$\boldsymbol{r}' = (\bar{\boldsymbol{I}} + \bar{\boldsymbol{\epsilon}}) \cdot \boldsymbol{r}, \tag{23}$$

where $\bar{\boldsymbol{I}}$ is the 2×2 identity matrix. According to Figure 4, the new lattice unit vectors under this transformation are:

$$\boldsymbol{a}'_i = (\bar{\boldsymbol{I}} + \bar{\boldsymbol{\epsilon}}) \cdot \boldsymbol{a}_i \quad (i = 1, 2), \tag{24}$$

and using Equation (25), the set of transformed space-independent first-neighbour vectors turn into:

$$\boldsymbol{\delta}'_n = (\bar{\boldsymbol{I}} + \bar{\boldsymbol{\epsilon}}) \cdot \boldsymbol{\delta}_n \quad (n = 1, 2, 3). \tag{25}$$

We dropped the functional dependence of $\boldsymbol{\delta}'_n$ on $\boldsymbol{r}$ in Equation (25). The reason is that for uniform strain, all deformed first-neighbour vectors are deformed the same. From this, it is evident that strain not only changes the Bravais lattice through $\boldsymbol{a}'_i$, but the graphene space group as well, due to the new decoration vectors $\boldsymbol{\delta}'_n$.

It is important to emphasize that Equation (25) is a consequence of assuming that Cauchy-Born rule applies on graphene, which will be the case for uniform biaxial strain. However, for crystals characterized by a lattice with a basis, the strained nearest-neighbor vectors are transformed following a sublattice-dependent rule due to the additional degrees of freedom introduced by the basis atoms. According to Midtvedt et al. [53], Equation (25) should be generalized into $\boldsymbol{\delta}'_n = (\bar{\boldsymbol{I}} + \bar{\boldsymbol{\epsilon}}) \cdot \boldsymbol{\delta}_n + \boldsymbol{\Delta}$, where the vector $\boldsymbol{\Delta}$ is sublattice-dependent.

The reciprocal space lattice is deformed by strain. Using the deformed cell unit vectors given by Equation (24), the corresponding new reciprocal-lattice vectors are given by:

$$\boldsymbol{G}'_i = (\bar{\boldsymbol{I}} + \bar{\boldsymbol{\epsilon}})^{-1} \cdot \boldsymbol{G}_i \quad (i = 1, 2). \tag{26}$$

Figure 5 shows reciprocal lattice vectors for some representative cases of uniform strain.

Following Equations (5, 6, 7), the new high symmetry points in the corners of the first BZ of the strained reciprocal lattice are also obtained by the Wigner-Seitz construction of the primitive cell (Figure 13(b)), resulting in the following positions [54]:

$$\boldsymbol{K}'_+ = \bar{\boldsymbol{M}}_1{}^{-1} \cdot \boldsymbol{C}_+ \qquad \boldsymbol{K}'_- = \bar{\boldsymbol{M}}_2{}^{-1} \cdot \boldsymbol{C}_-, \tag{27}$$

with:

$$\bar{\boldsymbol{M}}_i = \begin{pmatrix} (G'_i)_x & (G'_i)_y \\ (G'_1)_x + (G'_2)_x & (G'_2)_y + (G'_2)_y \end{pmatrix}, \tag{28}$$

and

$$\boldsymbol{C}_\pm = \frac{1}{2} \begin{pmatrix} \pm|\boldsymbol{G}'_i|^2 \\ \mp|\boldsymbol{G}'_1 + \boldsymbol{G}'_2|^2 \end{pmatrix}. \tag{29}$$

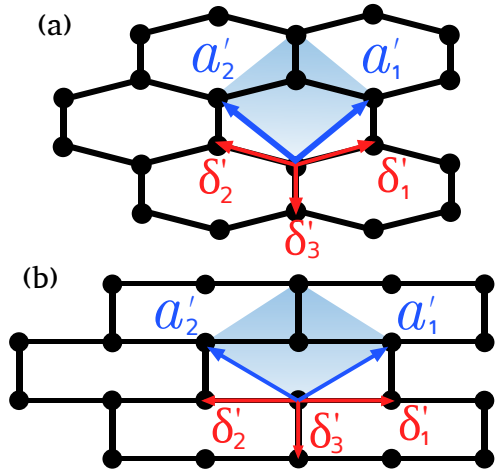

Figure 4. Two examples of deformed lattices in which the deformed unit vectors $\boldsymbol{a}'_1$, $\boldsymbol{a}'_2$ and the first-neighbour vectors $\boldsymbol{\delta}'_1, \boldsymbol{\delta}'_2, \boldsymbol{\delta}'_3$ are indicated. The corresponding unit cell is indicated by the shadowed area. In panel (a), the graphene lattice is slightly distorted, while panel (b) shows the limiting case of a brick-wall lattice. Networks (a) and (b) share the same topology.

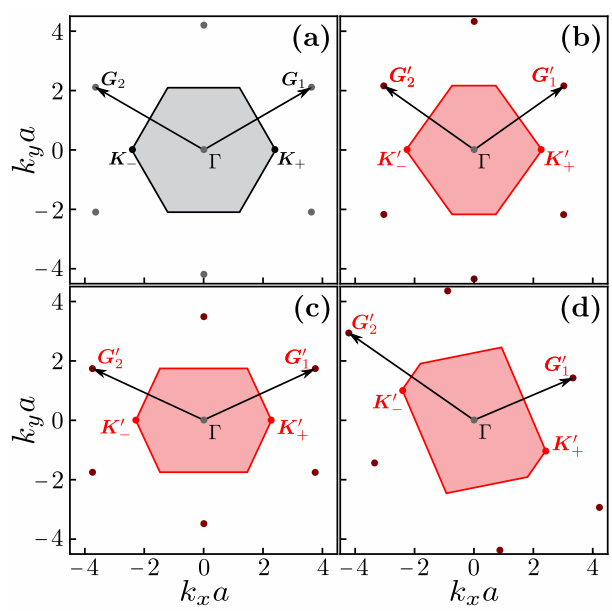

Figure 5. First-Brillouin zone and reciprocal lattice vectors for some representative cases of uniform strain: (a) unstrained graphene, (b) uniaxial strain along the zigzag-direction (zigzag strain) with $\{\bar{\epsilon}_{xx} = 0.2,\ \bar{\epsilon}_{yy} = -\nu\bar{\epsilon}_{xx},\ \bar{\epsilon}_{xy} = 0\}$; (c) uniaxial armchair strain with $\{\bar{\epsilon}_{yy} = 0.2,\ \bar{\epsilon}_{xx} = -\nu\bar{\epsilon}_{yy},\ \bar{\epsilon}_{xy} = 0\}$, and (c) shear strain with $\{\bar{\epsilon}_{xx} = \bar{\epsilon}_{yy} = 0,\ \bar{\epsilon}_{xy} = 0.2\}$.

Here, $(G'_i)_x$ and $(G'_i)_y$ are the x and y components of the deformed reciprocal vectors $\boldsymbol{G}'_i$ for $i = 1, 2$.

Figure 5 presents different cases of strain, showing the first BZ (white lines) and the corresponding high-symmetry points. To first order in strain tensor, it can be demonstrated that high symmetry point positions are given by [16]:

$$\boldsymbol{K}'_+ = \pm\frac{4\pi}{3\sqrt{3}a}(1 - \bar{\epsilon}_{xx}/2 - \bar{\epsilon}_{yy}/2, -2\bar{\epsilon}_{xy}). \tag{30}$$

Finally, the diffraction pattern of the uniform deformed lattice is given by a simple scaling of Equation (10):

$$|\widetilde{V}_{gpu}(\boldsymbol{k})|^2 = 4V_0^2 cos^2\left(\frac{\boldsymbol{k}\cdot\boldsymbol{\delta}'_1}{2}\right)\sum_{\boldsymbol{G}'}\delta(\boldsymbol{k} - \boldsymbol{G}'), \tag{31}$$

where $\boldsymbol{G}'$ is a reciprocal lattice vector modified by strain. This results on the presence of diffraction peaks at:

$$\boldsymbol{G}' = l\boldsymbol{G}'_1 + h\boldsymbol{G}'_2, \tag{32}$$

with the same amplitudes as in graphene since $\boldsymbol{G}'_i\cdot\boldsymbol{\delta}'_1 = \boldsymbol{G}_i\cdot\boldsymbol{\delta}_1$, as it could be expected.

Another important case that will be discussed next is that of a periodic strain field that arises when graphene lays over a substrate, like Ir, Fe or hBN. In this case, the resulting structure is modulated and it forms a superlattice that is usually described as a modulated crystal. However, if the periodicity of the substrate cannot be conmmensurate with that of graphene, the resulting structure resembles that of quasicrystals (which are crystals with classical forbidden symmetries, and described using more reciprocal basis vectors than the dimensionality of the physical space [55]). Such features are easily described as follows.

The periodic nature of the strain field allows to express it using a Fourier series:

$$\boldsymbol{u}(\boldsymbol{r}) = \sum_{\Delta\mathbf{g}}\widetilde{\boldsymbol{u}}(\Delta\boldsymbol{g})e^{i\Delta\mathbf{g}\cdot\mathbf{r}}, \tag{33}$$

where $\Delta\boldsymbol{g}$ are the reciprocal lattice vectors of the supercell, and $\widetilde{\boldsymbol{u}}(\Delta\boldsymbol{g})$ is the contribution of each harmonic. Choosing the right set of $\Delta\boldsymbol{g}$ vectors from experimental data can be a quite complex task, due to the presence of beatings in the superlattice unit cell [56]. From a theoretical point of view, periodicity hold if two vectors $\boldsymbol{T}_1$ and $\boldsymbol{T}_2$ exist such that:

$$\boldsymbol{u}(\boldsymbol{r}) = \boldsymbol{u}(\boldsymbol{r} + \boldsymbol{T}_1) = \boldsymbol{u}(\boldsymbol{r} + \boldsymbol{T}_2). \tag{34}$$

then the vectors $\Delta\boldsymbol{g}$ are found by finding integer linear combinations of the two vectors that satisfy $\Delta\boldsymbol{g_j}\cdot\boldsymbol{T}_i = 2\pi\delta_{i,j}$.

The resulting modulated crystal is said to be conmmensurate when the vectors $\boldsymbol{T}_1$ and $\boldsymbol{T}_2$ fall into the graphene lattice:

$$\begin{aligned}\boldsymbol{T}_1 &= n_1\boldsymbol{a}_1 + n_2\boldsymbol{a}_2\\ \boldsymbol{T}_2 &= m_1\boldsymbol{a}_1 + m_2\boldsymbol{a}_2\end{aligned} \tag{35}$$

for some integers n_1, n_2, m_1 and m_2. Commensurability (35) implies that a supercell can be defined, which comprises the smallest integer numbers of unit cells of both graphene and the support [56]. The system behaves as a quasicrystal when no integer solutions for Equation (35) exist, since in that case it has at least two incommensurate lengths [55].

The reciprocal lattice and the diffraction pattern can be found as follows. Starting with the expression for the charge or mass distribution with a periodic deformation:

$$\widetilde{V}(\boldsymbol{r}) = V_0\sum_l\delta(\boldsymbol{r} - \boldsymbol{r}_l - \boldsymbol{u}(\boldsymbol{r}_l)), \tag{36}$$

the Fourier transform is:

$$\widetilde{V}(\boldsymbol{r}) = V_0\sum_{\boldsymbol{r_l}}e^{i\mathbf{k}\cdot(\mathbf{r_l}+\boldsymbol{u}(\boldsymbol{r_l}))}. \tag{37}$$

Now, we use the periodicity of the strain field by expanding one of the exponentials in a Fourier series:

$$e^{i\mathbf{k}\cdot\boldsymbol{u}(\boldsymbol{r_l})} = \sum_{\Delta\mathbf{g}}\widetilde{U}_{\boldsymbol{k}}(\Delta\boldsymbol{g})e^{-i\Delta\mathbf{g}\cdot\mathbf{r_l}}, \tag{38}$$

where $\Delta\boldsymbol{g}$ are the wavevectors determined from the periodicity of $\boldsymbol{u}(\boldsymbol{r}_l)$, while $\widetilde{U}(\boldsymbol{g})$ are the coefficients of the expansion, found from projecting $e^{i\mathbf{k}\cdot\boldsymbol{u}(\boldsymbol{r_l})}$ into the kernel of the transformation:

$$\widetilde{U}_{\boldsymbol{k}}(\Delta\boldsymbol{g}) = \sum_{\boldsymbol{r_l}}e^{i\mathbf{k}\cdot\boldsymbol{u}(\boldsymbol{r_l})}e^{i\Delta\mathbf{g}\cdot\mathbf{r_l}}. \tag{39}$$

Using Equation (38), the Fourier transform is written as:

$$\widetilde{V}(\boldsymbol{k}) = V_0\sum_{\Delta\boldsymbol{g},\boldsymbol{r_l}}\widetilde{U}_{\boldsymbol{k}}(\Delta\boldsymbol{g})e^{i(\mathbf{k}-\boldsymbol{\Delta}\mathbf{g})\cdot\mathbf{r_l}}. \tag{40}$$

One can also use Equation (10) to rewrite previous Equation as:

$$\widetilde{V}(\boldsymbol{k}) = \sum_{\Delta\boldsymbol{g}}\widetilde{U}_{\boldsymbol{k}}(\Delta\boldsymbol{g})\widetilde{V}_{gp}(\boldsymbol{k} - \Delta\boldsymbol{g}), \tag{41}$$

which is a convolution of two functions, the Fourier transform of the graphene structure and the modulation Fourier transform, a result well known for modulated crystals or quasicrystals [55, 57, 58, 59]. In fact, the structure can also be dealt with by using projections of a higher dimensional lattice [55, 60, 61] within the cut and projection method [55, 62].

Using Equations (11) and (41), the diffraction pattern turns out to be:

$$\begin{aligned}|\widetilde{V}(\boldsymbol{k})|^2 = 4V_0^2\cos^2\left(\frac{\boldsymbol{k}\cdot\delta_1}{2}\right)\\ \times\sum_{\boldsymbol{G},\Delta\boldsymbol{g}}|\widetilde{U}_{\boldsymbol{k}}(\Delta\boldsymbol{g})|^2\delta\left(\boldsymbol{k} - [\boldsymbol{G} + \Delta\boldsymbol{g}]\right),\end{aligned} \tag{42}$$

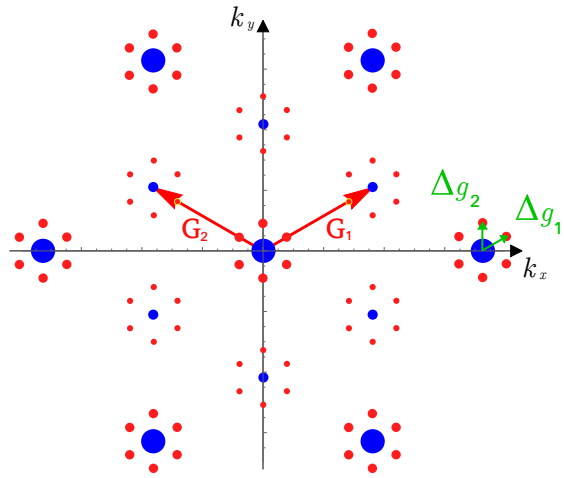

Figure 6. Scheme of the diffraction pattern for periodic strained graphene as obtained from Equation (42). On each graphene's diffraction spot (indicated in blue), phason satellites indicated in red appear due to the periodic modulation. The original reciprocal lattice vectors of graphene, and the new set of reciprocal superlattice vectors are indicated in capital (red) and lowercase (green) letters. This interference effect is akin to the beats appearing in acoustics when two waves of nearly similar frequencies are superposed.

i.e., is made from the diffraction pattern of graphene (for $\Delta\boldsymbol{g} = 0$) plus extra spots at positions $\boldsymbol{G} + \Delta\boldsymbol{g}$. Figure 6 presents such a diffraction pattern, as obtained from Equation (42). Its generic features coincide with X-ray or LEEDS diffraction experiments made with graphene over different sustrates [63, 64]. Since the period of the superlattice is much bigger that the graphene's lattice parameter, $|\Delta\boldsymbol{g}| << |\boldsymbol{G}|$ the new diffraction spots appear as satellites of the original graphene lattice (see Figure 6). The relative peak size is obtained by squaring the amplitudes given in Equations (13) and (42):

$$|\widetilde{V}(\boldsymbol{G}+\boldsymbol{\Delta g})|^2 = 4V_0^2|\widetilde{U}_{\boldsymbol{G}+\Delta\boldsymbol{g}}(\Delta\boldsymbol{g})|^2 \times \cos^2\left(\frac{\pi}{3}(2l-h) + \frac{(l+h)}{2}\boldsymbol{\delta}_1\cdot\Delta\boldsymbol{g}\right). \quad (43)$$

If the modulation and the graphene periods are commensurate in the sense of Equation (35), the satellites will eventually coincide with points of the reciprocal lattice of graphene. When this condition does not hold, the diffraction pattern is densely filled with spots in a self-similar way [55]. Satellites are associated with new degrees of freedom known as phasons [65, 55, 58, 59]. These phasons are Goldstone modes associated with the extra broken-symmetries provided by the modulation, that have a very different dynamics when contrasted with more usual Goldstone modes like phonons [65, 61].

Finally, let us briefly discuss random strain fields. In this case, $\boldsymbol{u}(\boldsymbol{r})$ is a random quantity with a given distribution, for example, a Gaussian. The description is similar to a crystalline lattice with noise due to thermal fluctuations. For example, the diffraction pattern has peaks at the same position as in unstrained graphene, but with a certain width resulting from the convolution of the dispersion distribution. The width is determined by the mean square value of $\boldsymbol{u}(\boldsymbol{r})$, as it happens with the Debye-Waller factor [47].

3. Deformations in graphene

Here, the mechanical properties of graphene are briefly reviewed. For a more exhaustive presentation on this topic, we address the reader to other recent review articles [11, 66, 67, 68]. Once a description of graphene's elastic properties is made, we turn our attention onto how to produce deformations in graphene.

3.1. Elastic coefficients: Experimental and theoretical characterization

Graphene is the thinnest elastic membrane in nature, with an exceptional stress-strain behaviour. It is the material with the highest stiffness and strength ever measured [5, 69]. At the same time, it can be easily bent to get complex folded structures [70, 71] and can withstand elastic deformations up to 25 % [5], much more than in any other crystal. Owing to these outstanding mechanical properties, graphene is an ideal candidate for applications in nanomechanical systems [72, 73, 74] and flexible electronic devices [75, 76].

Many of the mechanical properties of graphene can be understood by continuum mechanics models [77, 78, 79, 80, 81]. Within the theory of linear elasticity for two-dimensional (2D) membranes [82, 83], the elastic energy density $\mathcal{U}$ (energy per unit area) of a strained graphene membrane is given by:

$$2\mathcal{U} = \frac{\mathcal{E}}{1+\nu}\,\mathrm{Tr}(\bar{\boldsymbol{\epsilon}}^2) + \frac{\mathcal{E}\nu}{1-\nu^2}(\mathrm{Tr}\,\bar{\boldsymbol{\epsilon}})^2, \quad (44)$$

where $\bar{\boldsymbol{\epsilon}}$ is the rank-two strain tensor, $\mathcal{E}$ is the Young's modulus and ν is the Poisson's ratio. In general, the strain tensor $\bar{\boldsymbol{\epsilon}}(\boldsymbol{r})$ depends on position. From equation (44), the stress-strain constitutive relation (Hooke's law) for in-plane deformations is obtained by $\bar{\boldsymbol{s}} = \partial\mathcal{U}/\partial\bar{\boldsymbol{\epsilon}}$, where $\bar{\boldsymbol{s}}$ is the stress tensor.

From an experimental point of view, the characterization of the elastic coefficients ($\mathcal{E}$,ν) has been challenging owing to difficulties related to imposing a measurable uniform stress and to problems related with the handling of a membrane of monoatomic thickness. In a pioneer work, Lee et al. [5] reported the value of Young's modulus of graphene by performing nanoindentation measurements. Graphene was suspended

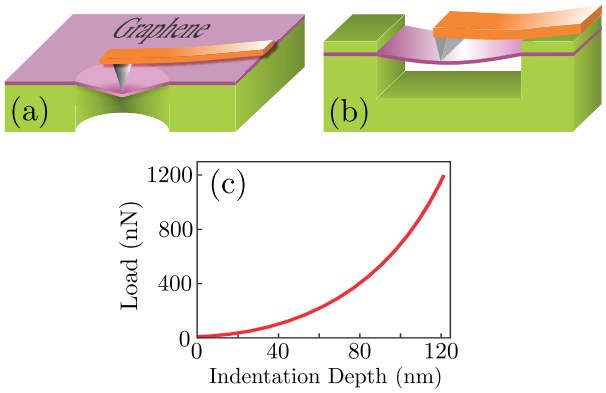

Figure 7. Schematics of an AFM nanoindentation experiments of suspended graphene membranes: (a) indentation circle and (b) indentation ribbon. (c) Typical force-displacement curve of an indented graphene membrane.

over a substrate with circular cavities and indented by the tip of an atomic force microscope (Figure 7). The experimental force-displacement relation was approximated by the Schwering-type equation [84, 85]

$$F = \pi s_0 \delta + \frac{\mathcal{E}}{r^2}\delta^3, \tag{45}$$

where F is the applied force, δ is the indentation at the central point, r is the radius of the drum and s_0 is the pre-tension accumulated in the membrane during the preparation procedure. Typically, the pre-tension values are small: $0.07 - 1\,\mathrm{N/m}$. Using a least-square fitting of equation (45) to the force-displacement curves, Young's modulus was determined to be $\mathcal{E} = 340 \pm 50\,\mathrm{N/m}$ [5]. If the thickness of graphene is assumed to be $d = 0.335\,\mathrm{nm}$, the derived $\mathcal{E}$ corresponds to an ultrahigh 3D Young's modulus of $\mathcal{E}^{3D} = \mathcal{E}/d = 1.0 \pm 0.1\,\mathrm{TPa}$, very close to the in-plane Young's modulus of bulk graphite ($1.02 \pm 0.03\,\mathrm{TPa}$). They also estimated the breaking strength of graphene as $42 \pm 4\,\mathrm{N/m}$ and discovered that the elastic response is highly nonlinear for strains above 10 %.

Subsequently, these experiments were interpreted by Cadelano et al [86] within a generalized nonlinear stress-strain relation for graphene, by incorporating to equation (44) cubic terms in strains. In addition to the Young's modulus and the Possion's ratio, this approach introduced three nonlinear independent elastic coefficients (C_{11}, C_{12}, C_{22} in Voigt's notation), which were estimated from tight-binding atomistic simulations. These three additional high-order moduli uncover the anisotropic character of graphene when nonlinear features are taken into account and, moreover, play a crucial role in determining its failure properties.

Other nanoindentation works [87, 88, 89] have found values of the Young's modulus very close to that reported in [5]. In particular, Huang et al [87] performed nanoindentation experiments on graphene ribbons, which were indented with a wedge-shaped tip. On the basis of the device geometry, the force-displacement relation $F(\delta)$ was approximated according to a suspended bridge model developed to describe the deflection of suspended metallic films, as follows [90]:

$$F = \frac{8ws_0}{l}\delta + \frac{8w\mathcal{E}}{l^3}\delta^3, \tag{46}$$

where w and l are the width and the length of the graphene ribbon. In this case, the extrapolated Young's modulus from the fit of the experimental data, based on equation (46), was $\mathcal{E} = 335 \pm 20\,\mathrm{N/m}$. Even though atomic force microscope nanoindentation is the most employed method to characterize the elastic properties of graphene, other different techniques have been employed, yielding similar results [69, 91, 92].

In contrast, the Poisson's ratio of graphene ν has not been obtained by means of the experiments described above. The typically quoted value is $\nu = 0.16$, which corresponds to the Poisson's ratio for graphite in the basal plane. However, a wide distribution of theoretical values exists in the literature, ranging from 0.1 to 0.4. Atomistic Monte Carlo simulations show Poisson's ratio to be small (≈ 0.1) in a broad temperature interval, being $\nu = 0.12$ at $T = 300\,\mathrm{K}$ [93]. At higher temperature ($T \geq 1700\,\mathrm{K}$), ν can be negative, so that graphene becomes an auxetic material. On the other hand, an ab initio calculation reveals an isotropic in-plane elastic response of graphene at small strains with a Poisson's ratio of 0.186, which, at large strains, becomes anisotropic and strongly dependent on strain [94]. Additionally, molecular dynamic simulations show a Poisson's ratio of 0.21 for graphene, and the ratio significantly depends on the size and chirality in the case of graphene nanoribbons, with a larger value in the armchair direction than in the zigzag direction. On the experimental side, the Poisson's ratio of graphene has not been reported from a direct measurement. On this point, it is worth mentioning that Politano et al [92] recently estimated a Poisson's ratio of 0.19 for graphene grown on various metal substrates.

The bending rigidity κ is another important elastic parameter of graphene that is used, for example, to predict the performance of nanoelectromechanical devices. Within the theory of elasticity for thin plates, the bending rigidity is determined to be $\kappa = \mathcal{E}_{3D} d^3/12(1-\nu^2)$. Evaluating this expression with the parameters of graphene ($\mathcal{E}_{3D} \approx 1\,\mathrm{TPa}$, $d \approx 0.34\,\mathrm{nm}$, $\nu \approx 0.16$) yields $\kappa \approx 20\,\mathrm{eV}$, which is an order of magnitude larger than the estimated value for graphene. The often quoted experimental value for graphene is $\kappa \approx 1.2\,\mathrm{eV}$, which was extracted from graphite's phonon spectrum. Ab initio calculations

predict $\kappa \approx 1.46\,\mathrm{eV}$, and an analytical estimation based on empirical potentials gives $\kappa \approx 1.4\,\mathrm{eV}$. By using a bond orbital model, Zhang et al [95] demonstrated that the breakdown of the plate phenomenology for a graphene monolayer is due to the decoupling of bending and tensional deformations. At the same time, they reported a precise expression for the bending rigidity κ of n-layered graphene, for $(n > 2)$, which probe the plate treatment can be applied to multilayer graphene in experiments involving out-of-plane deformations without layer-sliding.

3.2. Strain patterns and methods to produce them

Strains arise naturally or are produced in a controlled way in graphene. For example, the bonds between Carbon atoms are almost incompressible. Then, less than 0.1 percent of compressive strain creates out-of-plane corrugations, resulting in the formation of ripples and wrinkles [14]. Strain can be produced using different techniques, like bending or elongating the graphene/substrate system or by exploiting the lattice mismatch and/or the thermal expansion mismatch between graphene and its supporting substrate. Several reviews are available where these topics are covered [9, 14, 96]. Here we only review two topics that are recent and important for other sections.

3.2.1. Graphene on substrates: moiré superlattices

When on a substrate, graphene experiences strain due to surface corrugations or to the lattice mismatch to the substrate. Experimentally, this is achieved by growing graphene on top of substrate with different lattice parameter [56], or by rotation of the graphene sheet over a substrate [20]. Using these techniques, uniaxial periodic strain can be produced [97] as well as interference patterns known as moirè patterns [56]. The structural mismatch between graphene and its support results in a superlattice over a distance know as moirè periodicity, which usually ranges from 1 to 20 nm [97, 56]. A new length scale is thus introduced by the superlattice.

Let us explain briefly why this happens. In Figure 8 (a), we present a superposition of two lattices with a small lattice mismatch. This leads to an interference pattern, analogous to the beating phenomena observed when two sounds of slightly different frequencies are superposed. Such beating is observed in Figure 8 (a) as a striped diagonal pattern with a larger periodicity. This resulting superlattice is an example of a Moiré pattern. As shown in Figure 8(b), the wavevector associated with this lattice, denoted by $\boldsymbol{k}_m$, is given by $\boldsymbol{k}_m = \boldsymbol{k}_2 - \boldsymbol{k}_1$, where $\boldsymbol{k}_1$ and $\boldsymbol{k}_2$ are the wavevectors corresponding to each of the superposing lattices [63]. These wavevectors are perpendicular to the stripes seen in Figure 8 (a) and the magnitudes are proportional to

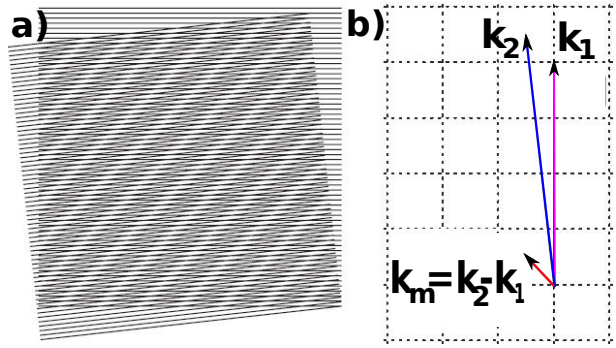

Figure 8. (a) Two superposed patterns with a small lattice parameter difference lead to a moiré superlattice, seen here as a striped diagonal pattern with a larger periodicity than the original lattices. (b) Wave vectors associated with the superposed lattices of (a). The wavevector of the resulting moiré is given by the difference between the original wavevectors. Adapted from Ref. [63] with permission.

the inverse of the lattice parameter. In graphene over sustrates, the description of the moiré pattern can be quite complex, since there are many practical issues to take into account [56].

Consider for example the case of graphene on top of $\mathrm{Ir}(1,1,1)$ [98], as it has been experimentally done via the pyrolytic cleavage of ethylene [63]. Figure 9 presents the resulting superstructure, which has been examined with scanning tunneling microscopy (STM) and low energy electron diffraction (LEEDS) [63]. There is slight lattice mismatch between the graphene and $\mathrm{Ir}(1,1,1)$ lattices, resulting in a (9.32×9.32) moiré with a repeat distance [63] of 2.53 nm. A further refinement indicates that this was an excellent approximation since the actual structure comprises three beatings [56]. Figure 9 b) shows the unitary cell indicated over the superlattice. As explained in subection 2.2, the diffraction pattern of a superlattice is given by a decoration of graphene's diffraction pattern with phason satellites. Figure 9 c) presents such a diffraction pattern of graphene on top of $\mathrm{Ir}(1,1,1)$, obtained from the LEEDS experiment. The satellites due to the periodic modulation are clearly seen and provide invaluable information about the superlattice periods, since they are spaced according to the wavevectors $\boldsymbol{k}_m$, which have a much more smaller norm than the substrate and graphene reciprocal lattices. A similar situation arises when graphene is rotated over the substrate, providing a way to tailor the periodicity of the superlattice [20].

Moiré superlattices provide a powerful strategy to engineer electronic and optical properties. Although most of the ideas behind the moiré construction are clear, the exact crystallographic structure on which their electronic structure depends remains debated [56]. In spite of this, for some weak interaction cases

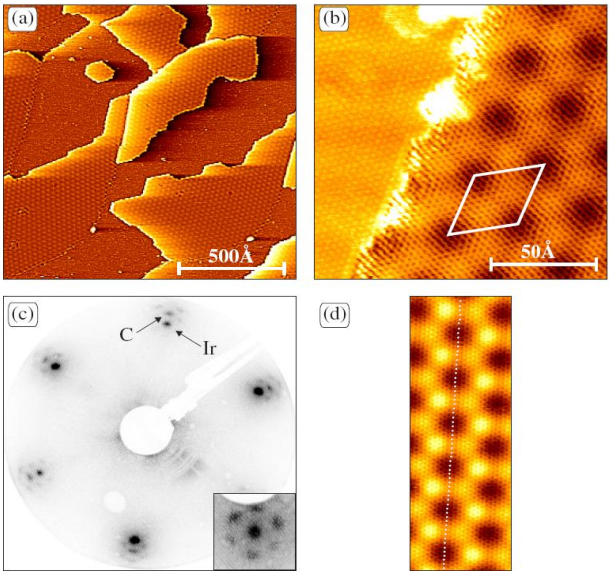

Figure 9. (a) Graphene on Ir(1, 1, 1) as seen on an electronic microscope. (b) A moiré pattern with a periodicity of 25.3 Å can be seen on a graphene flake attached to a Ir step: the unit cell of the superlattice is represented by a rhombus. (c) Low energy electron diffraction pattern (LEED) showing two main spots corresponding to graphene and Ir(1, 1, 1) as indicated. Smaller satellites reflect the moiré periodicity. These spots arise from reciprocal lattice vectors of the supercell, which depend upon the difference between the graphene and Ir(1, 1, 1) reciprocal lattice vectors. (d) A strip of the superstructure, where a Carbon row is shown in white. Reproduced from Ref. [63] with permission.

between graphene and the substrate the details are basically understood [56, 63, 99].

As graphene is twisted, strained and sheared with respect to its substrate, it suffers four geometrical transformations: an isotropic rescaling, a directional rescaling in two directions, and a rotation. In mechanical terms, the isotropic rescaling produces biaxial strain, while the directional rescaling leads to uniaxial strain in two directions[56]. For Ir(1, 1, 1), the biaxial compression is estimated as $\epsilon \approx -0.29\,\%$ and the uniaxial compression in $\epsilon \approx -0.41\,\%$ [56].

3.2.2. Ripples and bending Ripples and bending of the graphene membrane are vertical displacements of the atoms from a plane. The are usually described by the height $z(\boldsymbol{r})$ from the unrippled case as a function of the atom position. Although ripples and bending are usually treated as different from strain, in reality both are coupled. Graphene is a soft-material in the sense that it wrinkles, it can be folded, and it is even possible to do origami with it [100, 101, 102, 103, 104]. In fact, it is difficult to grow perfectly flat graphene [48, 105, 106, 107]. Graphene exhibits a high asymmetry in tensile versus compressive strain, i.e., while the Carbon-Carbon bond length can be increased up to 25 %, it is almost incompressible, and compressive stress rather induces out-of-plane deformations. For example, it has been observed that growing graphene on an anisotropic substrate produces one-dimensional periodic ripples [97]. Molecular dynamics simulations (MD) are helpful to clarify how ripples and strain are interlaced in suspended graphene sheets [108, 109, 110].

Two types of ripples form to relax external strain in suspended graphene. The first is a wavefront ripple orthogonal to the strain front, if external strain is applied along a single direction. The second is a sinusoidal shape, which emerges if the external strain is applied simultaneously along two orthogonal directions [110].

The typical height of the ripples is between 5 Å and 10 Å [108, 109, 110, 111], with a wave-length of around 10 nm. However, the dynamics of relaxation is more complex than expected. A recent experiment with a scanning tunneling microscopy measured the vertical motion of graphene [111]. The set-up of the experiment as well as the reported measurements of height $z(\boldsymbol{r})$, the tunnel current and the mean quadratic displacement of the membrane are shown in Figure 10. The dynamics exhibits rare long-scale excursions reflected in the anomalous mean-squared displacements and Cauchy-Lorentz power law jump distributions [111]. This random quivering of graphene membranes has been proposed to generate electricity for nanomachines.

4. Electronic properties

Much of the information concerning the electronic quality of a material is given by its charge carrier mobility μ. This information is complemented in graphene by the charge concentration n, since charge carriers can be tuned continuously between electrons and holes by using an external electrical field [3].

For typical carrier concentrations of $n \approx 10^{11}\,\mathrm{cm}^{-2}$, a μ exceeding $1.0 \times 10^5\,\mathrm{cm}^2\mathrm{V}^{-1}\mathrm{s}^{-1}$ (at room temperature) and $1.0\times10^6\,\mathrm{cm}^2\mathrm{V}^{-1}\mathrm{s}^{-1}$ (at liquid-helium temperatures) has been observed for suspended graphene [112, 113]. These suspended devices are extremely fragile and difficult to anneal [114]. Flexural modes, which are out-of-plane membrane vibrations, produce most of the electronic scattering once extrinsic defects are removed [113]. In suspended graphene, a significant amount of strain is needed to suppress flexural mode scattering [113]. A very good compromise between n, μ and the ease of building the experimental set-up is achieved by using an hexagonal boron-nitride substrate [114] (hBN), in which $n \approx 10^{11}\,\mathrm{cm}^{-2}$ with a reported μ of $1.0 \times 10^5\,\mathrm{cm}^2\mathrm{V}^{-1}\mathrm{s}^{-1}$. As a comparison, some undoped (intrinsic) semiconductors like $InSb$ exhibit a μ as high as $7.7 \times 10^4\,\mathrm{cm}^2\mathrm{V}^{-1}\mathrm{s}^{-1}$ at room-temperature [3].

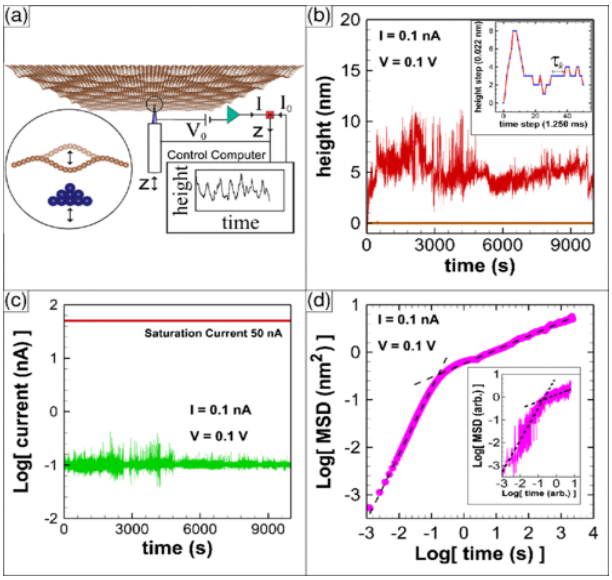

Figure 10. Measurement of free-standing graphene membrane height dynamics. (a) Experimental setup using a scanning tunnel microscope with an inset showing a zoom of the microscope tip and the graphene membrane vibrations (b) Time trace of membrane height (above) and from a rigid sample (below). The inset shows a zoom of the same trace height. (c) Tunneling current as a function of time. (d) Mean-squared displacement of membrane height as a function of time. Dashed lines are fits with the result of a simulation using exponential wait times and Cauchy jump lengths. Reproduced from Ref. [111] with permission. Copyrighted by the American Physical Society.

Typical doped semiconductors like n-Ge can reach $5.0\times 10^3\,\mathrm{cm^2V^{-1}s^{-1}}$. When high quality graphene obtained by mechanical cleavage on top of an oxidized Si wafer is used, this extreme electronic quality translates into a mean free path $l = (h/e)\mu(n/\pi)^{1/2}$ of order 100 nm for $n \approx 10^{12}\,\mathrm{cm}^{-2}$, where h is Planck's constant and e the electron charge [114]. The same extreme electronic quality is behind the observation of a ballistic behavior and a quantum Hall effect at room temperature [3].

Notice that the earlier different values of μ were attributed to different sample qualities, substrates and experimental setups [113]. In other words, imperfections due to wrinkles, edges, flexural scattering and strain affect the electronic properties. Therefore, it is important to keep in mind that even suspended graphene has a certain amount of strain and thus this is a fundamental feature to be taken into account. In spite of this, it is now accepted that most of the electronic and optical properties of pristine graphene are well described by a one band tight-binding Hamiltonian defined in a honeycomb lattice [41, 115]. For low-energy excitations, this approach leads to an effective Dirac Hamiltonian in reciprocal space. DFT calculations are always a good alternative, although a well-tuned tight-binding can cover the entire Brillouin zone [116, 117].

There are several paths to calculate and understand the effects of strain on the electronic properties. Most of them are based in methods used for studying pristine graphene [115, 116]. One approach is to use Density Functional theory (DFT). The second common approach is the use of a modified tight-binding Hamiltonian (TBH), solved by using numerical diagonalization or analytical calculations. The third path is to approximate the TBH near the Dirac points. This leads to an effective Dirac equation where pseudomagnetic fields appear. The last approach is used whenever the strain field varies smoothly in space. Here we will review all approaches starting with the TBH method. In particular, we will present some analytical solvable strain fields that provide useful tools to understand the main consequences of strain. Eventually, a comparison can be made between the different methods for such solvable cases. Under this perspective, one of the most important and instructive cases is the uniform strain. It served to quantify gaps as a function of strain [16] and to clarify some early issues in the derivation of the effective Dirac Hamiltonian for strain [118].

As it will become clear in forthcoming subsections, strain has important consequences that we resume below. The effects for slowly-spatially varying strain [119, 120] are:

- A shift of the Dirac point. The shift is given by a pseudomagnetic vector potential.
- A change in the metric of the lattice, i.e., the structure of reciprocal space is modified.
- The energy scale is changed due to the modification of bond lengths.
- The Fermi velocity becomes anisotropic.
- A pseudoelectric field appears.

For fast-spatially varying strain the Dirac approximation is strongly modified leading to:

- Shift, merging and reproduction of Dirac points.
- The creation of energy gaps.
- The reciprocal lattice can even loose its meaning. In some cases it can be replaced by a superlattice, like the moiré superlattice. A procedure akin to the magnetic lattice concept can be introduced.
- Electronic spatial localization can be greatly affected.

In both slow and fast spatially varying strain, the Dirac points will not coincide with the high symmetry points of the distorted reciprocal lattice [118] (whenever is it possible to define it).

The previous list does not include the effects of uncorrelated, local random strain, which are better described and understood by local impurity fields that

will be discussed later. In other words, strain effects do not only depend in the spatial variation of the Fermi velocity. Strain can be local or have a long-range nature, as well as being random or correlated. For example, local strain can be produced by the tip of a scanning microscope [121, 111], while long-range correlated strain occurs over periodic substrates. Since, strain breaks the symmetry of the honeycomb lattice it is possible in some cases to classify the specific broken symmetries [122] and include to terms in the Hamiltonians with the specific symmetry consideration [13]. In order to avoid overlap with other reviews, here we do not follow this path. Instead, we look for models that represent interesting cases of strains and ripples. These simple models cover many interesting measurable effects, like a gap phase diagram [123, 16], a fractal spectrum [124, 40, 125], anisotropic Fermi velocity [126, 118, 120], mixed Dirac-Schrödinger behavior [16, 36, 37, 38, 39, 40], pseudomagnetic and pseudoelectric fields [6, 127, 120], Landau levels [128, 129], non-trivial topological modes and optical dicroism [130, 131].

Before entering the discussion of the strained case, in the next subsection we review how to understand the electronic properties of unstrained graphene and some of the general effects of disorder. In the remaining subsections, we will discuss the different approaches to treat strained graphene.

4.1. Electronic properties of pristine and disordered graphene

To study the electronic properties of graphene, one of the most fruitful approaches is the tight-binding approximation based on π-electrons [15]. Within this method, the contributions from the three valence electrons in the σ Carbon orbitals are neglected. This leads to the following Hamiltonian matrix model in which only $\pi-$orbitals are considered [41]:

$$\boldsymbol{H}_0 = -t_0 \sum_{\boldsymbol{r}} \sum_{n=1}^{3} a^\dagger_{\boldsymbol{r}} b_{\boldsymbol{r}+\boldsymbol{\delta}_n} + H.c., \tag{47}$$

where $\boldsymbol{r}$ runs over all A sites of the trigonal Bravais lattice, and the hopping integral (also known as the transfer integral) $t_0 \approx 2.7eV$ is obtained by fitting to experimental or numerical data [41]. $a^\dagger_{\boldsymbol{r}}$ and $b_{\boldsymbol{r}+\boldsymbol{\delta}_n}$ are creation and annihilation electron operators on the A sublattice (at position $\boldsymbol{r}$) and B sublattice (at position $\boldsymbol{r}+\boldsymbol{\delta}_n$). This model describes two electrons in a honeycomb lattice, and only first-neighbours are considered.

The bipartite nature of the lattice has many important consequences for the electronic properties, and as explained before, other bipartite lattices with quasiperiodic order [42] or disorder [43, 44, 45, 46] share some features with graphene, like a symmetric spectrum, zero-energy confined state modes or pseudomobility edges [42, 43].

Second nearest-neighbours can be included by using a second transfer integral $t_0^{sn} \approx 0.68eV$ which adds extra terms to Equation (47). It is possible to reproduce the energy dispersion in the whole Brillouin zone using a TB Hamiltonian up to third neighbours [132, 133]. Such corrections play an important role for disordered [45, 46, 134] and strained graphene [54], and for excitations that are no longer considered low-energy in pristine graphene.

Returning to the first-neighbour model with a single $\pi-$orbital per site, Equation (47), one can reduce the Hamiltonian to a 2×2 matrix (because the lattice only contains two-non equivalent sites) by a Fourier transform:

$$a^\dagger_{\boldsymbol{r}} = \frac{1}{\sqrt{N}} \sum_{\boldsymbol{k}} e^{i\boldsymbol{k}\boldsymbol{r}} a^\dagger_{\boldsymbol{k}}, \tag{48}$$

where we introduced a wave-vector $\boldsymbol{k}$. Using a similar transformation for $b_{\boldsymbol{r}+\boldsymbol{\delta}_n}$ leads to the Hamiltonian:

$$\boldsymbol{H}_0 = -t_0 \sum_{\boldsymbol{k}} \sum_{n=1}^{3} e^{-i\boldsymbol{k}\cdot\boldsymbol{\delta}_n} a^\dagger_{\boldsymbol{k}} b_{\boldsymbol{k}} + H.c. \tag{49}$$

The corresponding Schrödinger equation is an effective 2×2 Hamiltonian matrix $H(\boldsymbol{k})$, acting on a wavevector with components $(a_{\boldsymbol{k}}, b_{\boldsymbol{k}})$ and eigenvalues $E(\boldsymbol{k})$:

$$\begin{pmatrix} 0 & H_{AB}(\boldsymbol{k}) \\ H^*_{AB}(\boldsymbol{k}) & 0 \end{pmatrix} \begin{pmatrix} a_{\boldsymbol{k}} \\ b_{\boldsymbol{k}} \end{pmatrix} = E(\boldsymbol{k}) \begin{pmatrix} a_{\boldsymbol{k}} \\ b_{\boldsymbol{k}} \end{pmatrix}, \tag{50}$$

where:

$$H_{AB}(\boldsymbol{k}) = -t_0 f(\boldsymbol{k}), \tag{51}$$

and $f(\boldsymbol{k})$ is the following complex function:

$$H_{AB}(\boldsymbol{k}) = \sum_{n=1}^{3} e^{-i\boldsymbol{k}\cdot\boldsymbol{\delta}_n}. \tag{52}$$

We obtain the well known graphene energy dispersion from this linear system:

$$E(\boldsymbol{k}) = \pm t_0 |\sum_{n=1}^{3} e^{-i\boldsymbol{k}\cdot\boldsymbol{\delta}_n}|. \tag{53}$$

We present the resulting surface $E(\boldsymbol{k})$ obtained from Equation (53) in Figure 11, as well as a transversal cut using a path in reciprocal space. A comparison with a full DFT calculation is also shown in the Figure. The agreement is excellent near the Fermi energy, as it has been confirmed in numerous experiments [15]. Without charge pumping by external fields, the orbitals are half-filled and thus the Fermi energy (E_F) falls at $E = 0$. Equation (53) leads to an effective Dirac equation (see subsection 4.8) and a conical dispersion near $E = 0$, called the Dirac cone. The condition $E = 0$ leads to a pair of special $\boldsymbol{k}$ points labeled by $\boldsymbol{K}_D$ for which $E(\boldsymbol{K}_D) = 0$.

$\boldsymbol{K}_D$ happens to coincide with $\boldsymbol{K}_\pm$ for pristine graphene. Although there is some confusion in the literature about this point [118, 120], this is no longer the case for strained graphene [135, 118, 15]. The existence of two inequivalent Dirac points with the same energy leads to the concept of a valley [41]. That is important for several properties. In particular, effects arising from structural disorder depend upon their feasibility of producing intra- or inter-valley scattering [136].

It is important to remark that Equation (53) can be written without reference to the vectors $\boldsymbol{\delta}_n$. Using Equation (3), Equation (53) transforms into:

$$E(\boldsymbol{k}) = \pm t_0 |\sum (1 + e^{i\boldsymbol{k}\cdot\boldsymbol{a}_1} + e^{i\boldsymbol{k}\cdot(\boldsymbol{a}_1-\boldsymbol{a}_2)})|. \tag{54}$$

In other words, as long as the transfer integral is the same for all bonds, the energy dispersion depends only on the structure of the Bravais lattice. Furthermore, the condition $E(\boldsymbol{K}_D) = 0$ indicates the existence of a peculiar phase-difference at the Dirac point. This is because:

$$E(\boldsymbol{K}_D) = \pm t_0 \sum_{j=1}^{3} Z_j = 0, \tag{55}$$

where $Z_j = 2\pi j/3$ for $j = 0, 1, 2$ are the three complex roots of the equation $Z^3 = 1$. Previous Equation can only be satisfied when there is a phase difference of $2\pi/3$ in the wavefunction for one of the sublattices. Since each bipartite sublattice is made from triangles, this implies that states near the tip of the Dirac cone have a certain amount of frustration, in the sense that phases can not be π between consecutive sites.

Equation (53) yields the Dirac cone: for crystal momentum $\mathbf{q}$ near the Dirac point such that $\boldsymbol{k} = \boldsymbol{K}_D + \boldsymbol{q}$ (Figure 11) we have:

$$E(\boldsymbol{k}) = E(\boldsymbol{q}) = \pm\hbar v_F |\boldsymbol{q}|, \tag{56}$$

where v_F is the Fermi velocity:

$$v_F = \frac{3t_0 a}{2\hbar}. \tag{57}$$

This leads to a linear density of states (DOS):

$$\rho_0(E) = \frac{2|E|}{\pi\hbar^2 v_F^2}, \tag{58}$$

and to the following carrier density:

$$n_0(E) = sgn(E)\frac{2|E|^2}{\pi\hbar^2 v_F^2}. \tag{59}$$

In fact, Dirac cones are topologically protected and thus robust to second nearest neighbour interaction [137]. For small graphene sheets, the linear behavior of the dispersion can change due to edge-related effects. For example, a gap can be opened in graphene nanoribbons depending on the edge type as well as on the number of hexagons along the nanoribbon width

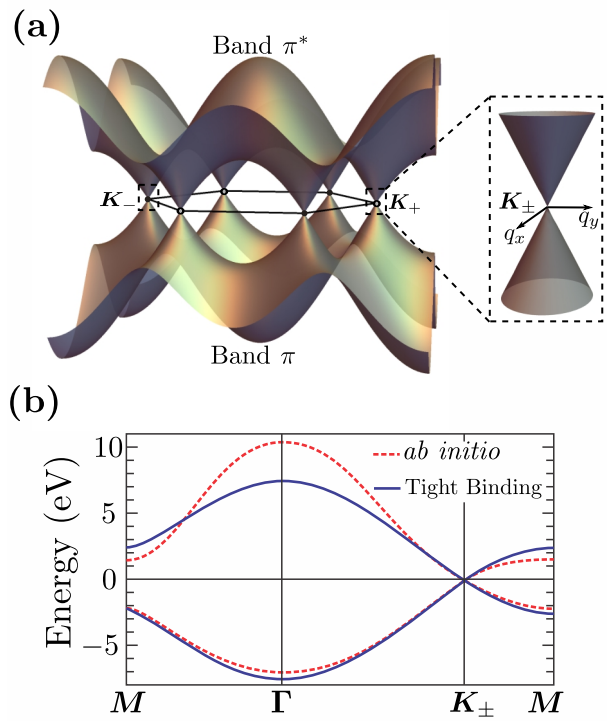

Figure 11. A comparison between a tight-binding and a full DFT theory calculation for pristine graphene. (a) Energy dispersion obtained from Equation (53). A zoom-in at the Fermi energy showing a cone is displayed as well. The vertices of the cones touch at the Dirac point at $\boldsymbol{K}_\pm$. (b) Band structure along a high-symmetry path in the Brillouin zone. The dotted line is obtained from Equation (53) and the other is from DFT a calculation that includes σ and π orbitals.

[116], making this effect a useful property to design electronic devices [24].

We now show that in fact, the Dirac cone and the nearby Van Hove singularity are consequences of this frustration. Less known, although important for the introduction of disorder and spin, is the physical reason behind the cone appearance. It is related with a wavefunction frustration in the underlying triangular lattice [44, 134]. Consider the squared Hamiltonian of Equation (49). Using Equation (50) we obtain that such squared H^2 is diagonal:

$$\begin{pmatrix} H^2_{AB}(\boldsymbol{k}) & 0 \\ 0 & H^2_{AB}(\boldsymbol{k}) \end{pmatrix} \begin{pmatrix} a_{\boldsymbol{k}} \\ b_{\boldsymbol{k}} \end{pmatrix} = E^2(\boldsymbol{k}) \begin{pmatrix} a_{\boldsymbol{k}} \\ b_{\boldsymbol{k}} \end{pmatrix}, \tag{60}$$

implying that the components of the wavefunction on the A and B sublattices are decoupled. Thus H^2 describes a triangular lattice, i.e., the squaring of H renormalizes one of the bipartite sublattices [44, 134] with an spectrum folded around $E = 0$, as indicated in Figure 12.

States near $E = 0$ need to be close to an antibonding nature in a triangular lattice. This produces frustration since wavefunctions can not have a phase difference of π between all neighboring sites

in a triangular lattice. In the absence of disorder, and as explained in Equation (55), some states lower their energy by having phase differences close to $2\pi/3$ as $E \to 0$. Frustration implies that many states are pushed away to higher energies, thus producing a Van Hove singularity at energy $E^2 = t_0^2$. This leads to a simple picture of graphene's spectrum from the underlying triangular sublattice.

We now summarize this picture:

- Band edges in graphene are obtained from the maximum of $E^2(\boldsymbol{k})$, associated with the diffraction spots at Γ points, i.e., for $\boldsymbol{k} = l\boldsymbol{G}_1 + h\boldsymbol{G}_2$ with l and h integers. Here $\nabla_{\boldsymbol{k}} E^2(\boldsymbol{k}) = 0$.
- The Dirac points in graphene correspond to the minimums of the function $E^2(\boldsymbol{k})$. Here also $\nabla_{\boldsymbol{k}} E^2(\boldsymbol{k}) = 0$ (in graphene, the operator $\nabla_{\boldsymbol{k}} E$ is not defined at the Dirac cone tip). Dirac points coincide with the high-symmetry points $K_\pm$, a result expected from the diffraction properties because two Bragg lines intersect therein. Diffraction leads to stationary waves, i.e., to a vanishing group velocity in the triangular lattice.
- Since $E^2(\boldsymbol{k})$ is a periodic bounded function,there must be a third singularity [138], which in this case corresponds to the Van Hove singularity at $E^2(\boldsymbol{k}) = t_0^2$. The singularity is a saddle point of $E^2(\boldsymbol{k})$.

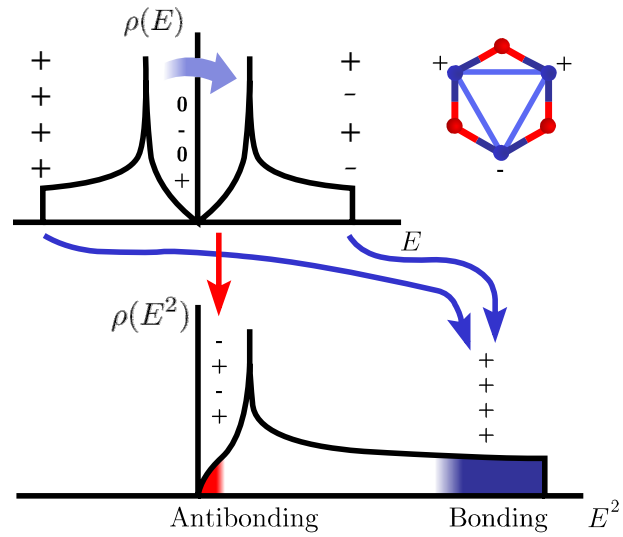

Figure 12. Sketch of the Hamiltonian eigenvalue renormalization from a graphene hexagonal lattice into a triangular one by applying the transformation H^2: the graphene's density of states $\rho(E)$ is transformed into $\rho(E^2)$, resulting in a folding around $E = 0$ that is indicated by arrows. Band edges, central states, and phase differences among sites are represented by $\pm$ signs. Central states at $E = 0$ have a zero amplitude in one sublattice [46]. When one of the sublattices is renormalized, states near $E = 0$ result in edge band states with an antibonding nature in a triangular lattice [44, 134], as indicated in the triangle that appears inside the hexagon. Due to frustration, states are pushed to higher energies leading to Van Hove degeneracies seen as a peaks in the DOS.

When very strong impurities or vacancies are added, the wavefunction tends to be localized in regions of lower frustration which have a decreasing exponential probability with size, leading to a kind of Lifshitz tail [44, 139]. As a result, a pseudomobility edge appears [44, 139], as confirmed in ARPES experiments of graphene doped with H impurities [140]. The corresponding wavefunctions have an interesting multifractal behavior [134]. In a similar way, resonant states appear near the Fermi energy when uncorrelated impurities are added [139, 141, 142]. Its correct location in energy requires the introduction of the second neighbor interaction [141].

It is important to remark that zero energy modes appear due to disorder or to the presence of boundary modes (associated with topological properties). These modes decouple from the renormalization and are related with highly degenerate modes with the property that the sum of wavefunction amplitudes must add to zero for the neighbors of any site in the lattice [43, 46].

In other bipartite lattices such as random binary alloys, these modes are strictly localized and confined [143, 43]. In quasiperiodic lattices, zero energy modes form beautiful fractal nodal lines carrying up to 10% of the spectral weight [144]. For doped graphene, the number of states was obtained by using a sum over moments and disordered configurations [46]. Such modes are especially important for magnetic properties.

The effects of disorder can be classified by the kind of symmetry they break [122]. Different types of randomness realize all possible ten symmetry classes of Dirac Hamiltonians [145], while symmetry considerations lead to different kinds of extra terms [13] to the unperturbed Hamiltonian, Equation (47). As a rule of thumb, the range of the potential determines if intra- or inter-valley scattering is allowed [136, 146, 139]. Inter-valley scattering, associated with long range potentials, allows access to the chirality degree of freedom allowing localization [136, 139], which is otherwise evaded for short-range potentials. Here, chirality is given as the phase of the wave-function projections onto the A and B sublattices [44]. More often is interpreted in terms of the Dirac equation as the projection of a sublattice pseudospin in the momentum direction [133].

The main reason for antilocalization is the absence of backscattering, i.e., to reverse the trajectory of an electron, one must change its momentum from $\boldsymbol{p}$ to $-\boldsymbol{p}$, implying a change of valley. But $\boldsymbol{p}$ is coupled with chirality, which is not changed by short-range

potentials [133]. However, backscattering, as is the case of group-I impurities [140] or vacancies [44], also depends upon the energetic range of the disorder [133]. Further details are given in the excellent books by Foa-Torres, Roche and Charlier [133] or Katnelson [147].

4.2. Tight-binding approach to strain

As indicated in section 2.2, in strained graphene the positions of atoms change from $\boldsymbol{r}$ to $\boldsymbol{r}' = \boldsymbol{r} + \boldsymbol{u}(\boldsymbol{r})$. As a result, distances between atoms change, modifying the hopping parameter along the way. The TB Hamiltonian for strained graphene is obtained by replacing the original lattice positions and hopping parameter in Equation (49), with those resulting from the structural distortion [41]:

$$\boldsymbol{H} = -\sum_{\boldsymbol{r}',n} t_{\boldsymbol{r}',\boldsymbol{\delta}'_n(\boldsymbol{r})} a^\dagger_{\boldsymbol{r}'} b_{\boldsymbol{r}'+\boldsymbol{\delta}'_n(\boldsymbol{r})} + H.c., \tag{61}$$

where $\boldsymbol{r}'$ runs over all sites of the deformed honeycomb lattice and the hopping integral $t_{\boldsymbol{r}',\boldsymbol{\delta}'_n(\boldsymbol{r})}$ varies due to the modification of Carbon-Carbon distances. The operators $a^\dagger_{\boldsymbol{r}'}$ and $b_{\boldsymbol{r}'+\boldsymbol{\delta}'_n(\boldsymbol{r})}$ correspond to creating and annihilating electrons on the A sublattice (at position $\boldsymbol{r}'$) and B sublattice (at position $\boldsymbol{r}' + \boldsymbol{\delta}'_n(\boldsymbol{r})$).

An important feature of Equation (61) is the modification of the first-neighbour vectors $\boldsymbol{\delta}_n$ onto a space-dependent set of first-neighbour vectors $\boldsymbol{\delta}'_n(\boldsymbol{r})$. Its value depends upon $\nabla\boldsymbol{u}(\boldsymbol{r})$ as indicated in Equation (18). This observation is fundamental to obtain the right strained TB Hamiltonian. The lack of this lattice correction in earlier versions of the TB Hamiltonian produced some controversies concerning the contribution of this term to local pseudomagnetic fields in the Dirac approach. Eventually, it has been found that lattice corrections do not contribute to the pseudomagnetic field [52, 108, 109, 148], although they are important for the TB in circumstances where the mean-field Dirac approach is not valid (see subsections 4.8 and 4.9).

In fact, the lack of lattice corrections imply displacements that keep constant distances between neighbours. Under this approximation, the elastic energy is not changed. Such kind of deformation is known as a floppy-mode [149, 150] and it provides a link to the study of electronic properties and network topological constraints [35] known in glasses as the Phillips-Thorpe rigidity theory [151, 149, 150].

To complete the model, modifications of the TB parameters are needed. Usually, this is given by an estimation of overlap changes for π-orbitals as a function of the Carbon-Carbon distance [152, 153, 154]:

$$t_{\boldsymbol{r}',\boldsymbol{\delta}'_n(\boldsymbol{r})} = t_0 \exp[-\beta(|\boldsymbol{\delta}'_n(\boldsymbol{r})|/a - 1)], \tag{62}$$

where β is the electron Grüneisen parameter [147]:

$$\beta = -\frac{\partial \ln t}{\partial \ln a}, \tag{63}$$

estimated for graphene to lie in the interval $\beta \approx 2-3$. This parameter is usually found by analyzing the G-mode Raman scattering peak of strained graphene [155, 156], or by using ab initio calculations [157]. The Grüneisen parameter is a measure of the phonon mode softening rate or hardening. It is a fundamental quantity to understand strain effects as well as thermomechanical properties.

Once the Hamiltonian is written, it can be diagonalized either by numerical calculations or (in some cases) analytically. In the following section we provide some important examples of these procedures. These examples are the following:

(i) Uniform strain field. Here the strain field is independent of the position (but it can depend on sublattice).

(ii) Isotropic expansion. This is a particular case of the uniform strain field.

(iii) Uniaxial non-uniform strain field. There is a direction in which strain is either zero or constant, while its magnitude is arbitrary in the perpendicular direction.

(iv) Arbitrary periodic strain fields. They are usually due to substrates or ripples.

Finally, a note of warning is necessary when using Equation (61). This Hamiltonian does not take into account that hopping terms to second and third neighbours can be incremented with respect to the first-neighbour hopping for strong strain, a feature that has not been completely investigated in the TB approach.

4.3. Uniformly strained graphene

In this case, the strain displacement field and the strain tensor $\bar{\boldsymbol{\epsilon}}$ are space-independent, as explained in Section 2.2. A uniformly strained lattice preserves periodicity, and thus a reciprocal space can be used to solve the tight-binding equations.

It was demonstrated in section 2.2 that the deformed cell unit vectors are given by Equation (24), leading to the new set of first-neighbour vectors $\boldsymbol{\delta_n}'$ indicated in Figure 13(a), and corresponding new reciprocal-lattice vectors are given by Equation 26, which are compared with the unstrained ones in Figure 13(b).

The uniformly-strained lattice is still periodic, so we use a Fourier representation using k-space wavevectors for the operators $a^\dagger_{\boldsymbol{r}'}$ and $b_{\boldsymbol{r}'+\boldsymbol{\delta}'_n}$. Using the Hamiltonian (61), the Hamiltonian for the strained lattice is [118]:

$$\boldsymbol{H} = -\sum_{\boldsymbol{k}} \sum_{n=1}^{3} t_n e^{-i\boldsymbol{k}\cdot(\bar{\boldsymbol{I}}+\bar{\boldsymbol{\epsilon}})\cdot\boldsymbol{\delta}_n} a^\dagger_{\boldsymbol{k}} b_{\boldsymbol{k}} + H.c., \tag{64}$$

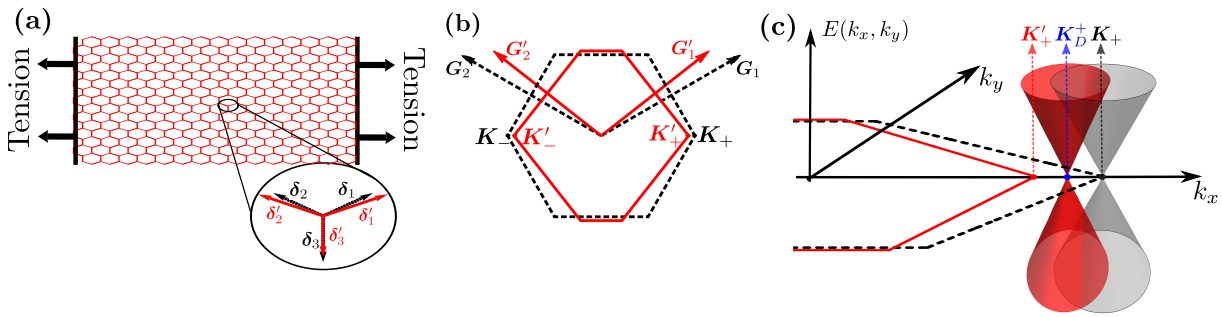

Figure 13. (a) Uniformly-strained graphene lattice showing the strained vectors $\boldsymbol{\delta}'_i$ –that point to the neighbors of $A-$sites– and their unstrained counterparts $\boldsymbol{\delta}_i$. (b) Corresponding strained reciprocal lattice, showing the strained and unstrained reciprocal vectors $\boldsymbol{G}'$ and $\boldsymbol{G}$, as well as the strained and unstrained high-symmetry points $\boldsymbol{K}'_\pm$ and $\boldsymbol{K}_\pm$. (c) Energy dispersion, showing how the distortion of the reciprocal lattice transforms the original Dirac cone into a distorted one with a directional dependent Fermi velocity. The cone vertex is also translated to a new point $\boldsymbol{K}_D$ which does not coincide with $\boldsymbol{K}'_\pm$. The vector displacement from the original position is directly given by the pseudomagnetic vector potential. Adapted from Ref. [120] with permission.

where t_n $(n = 1, 2, 3)$ is the hopping integral between each of the three nearest neighbors of a site:

$$t_n = t_0 \exp[-\beta(|(\bar{\boldsymbol{I}} + \bar{\boldsymbol{\epsilon}})\boldsymbol{\delta}_n|/a - 1)]. \tag{65}$$

Equation (64) can be written as a 2×2 matrix, whose eigenvalues provide the energy-momentum dispersion for graphene under uniform strain:

$$E(\boldsymbol{k}) = \pm|\sum_{n=1}^{3} t_n e^{-i\boldsymbol{k}\cdot(\bar{\boldsymbol{I}}+\bar{\boldsymbol{\epsilon}})\cdot\boldsymbol{\delta}_n}|, \tag{66}$$

and which can be simplified to give:

$$E(\boldsymbol{k}) = \pm\sqrt{\gamma + g(\boldsymbol{k})}, \tag{67}$$

where:

$$g(\boldsymbol{k}) = \sum_{n=1}^{3}\sum_{s>n}^{3} 2t_n t_s \cos\left[\boldsymbol{k}\cdot(\bar{\boldsymbol{I}} + \bar{\boldsymbol{\epsilon}})\cdot(\boldsymbol{\delta}_n - \boldsymbol{\delta}_s)\right], \tag{68}$$

and:

$$\gamma = {t_1}^2 + {t_2}^2 + {t_3}^2. \tag{69}$$

This expression is also valid for any anisotropic honeycomb lattice [158].

Typical contour plots resulting from the energy dispersion given by Equation (67) are shown in Figure 14(a) for unstrained graphene, and in Figures 14(b), 14(c) and 14(d) for other representative strains. The high symmetry points of the strained reciprocal lattice and the first Brillouin zone obtained from Equation (27) are shown as white lines in Figure 14 as well. The Dirac points $\boldsymbol{K_D}$ in reciprocal space are given by $E(\boldsymbol{K_D}) = E_F = 0$ and shown by red dots in Figure 14: the Dirac points do not coincide with the high symmetry points $\boldsymbol{K}'_-$ and $\boldsymbol{K}'_+$ of the strained reciprocal lattice. One can prove that in general, the condition $E(\boldsymbol{K_D}) = 0$ is different from the position of the high-symmetry points of the reciprocal space given by Equation (27). Only for pure graphene the Dirac points coincide with the high symmetry points $\boldsymbol{K}'_-$ and $\boldsymbol{K}'_+$.

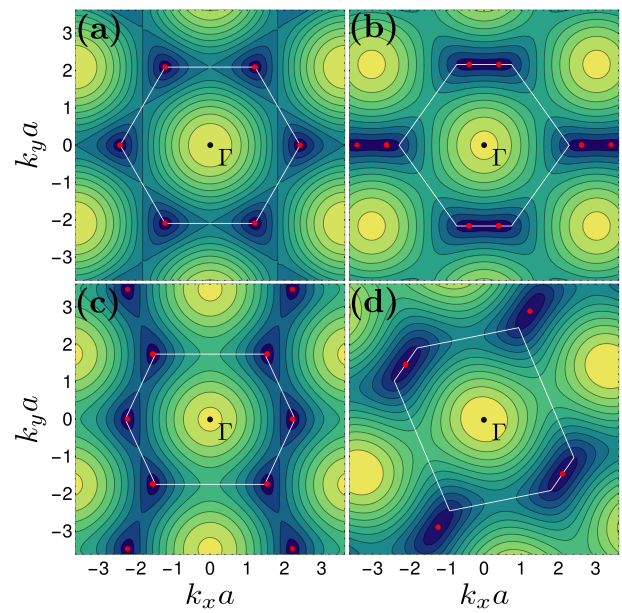

Figure 14. Contour plots of the energy dispersion obtained from Equation (67). The first Brillouin zone is indicated by white lines. The Dirac points, where the Fermi energy lies in, are indicated by red dots. (a) corresponds to unstrained graphene, (b) to uniaxial zigzag strain with $\{\epsilon_{xx} = 0.2,\ \epsilon_{yy} = -\nu\epsilon_{xx},\ \epsilon_{xy} = 0\}$, (c) to uniaxial armchair strain with $\{\epsilon_{yy} = 0.2,\ \epsilon_{xx} = -\nu\epsilon_{yy},\ \epsilon_{xy} = 0\}$, and (d) to shear strain with $\{\epsilon_{xx} = \epsilon_{yy} = 0,\ \epsilon_{xy} = 0.2\}$. Notice how two Dirac cones merge into one in this latter case as the reciprocal lattice turns into a square. For all strains (even case (c)), the Dirac points $\boldsymbol{K}_D$ do not have the same position as $\boldsymbol{K}'_+$ and $\boldsymbol{K}'_-$, which are the vertices of the polygons.

Thus, Dirac point positions are shifted by strain and their actual location needs to be found explicitly from the dispersion relation. This crucial point has not been taken into account in several papers available on the literature, although it has been observed in DFT calculations [159, 160], in relativistic field theory approaches [119, 161] and in tight-binding calculations

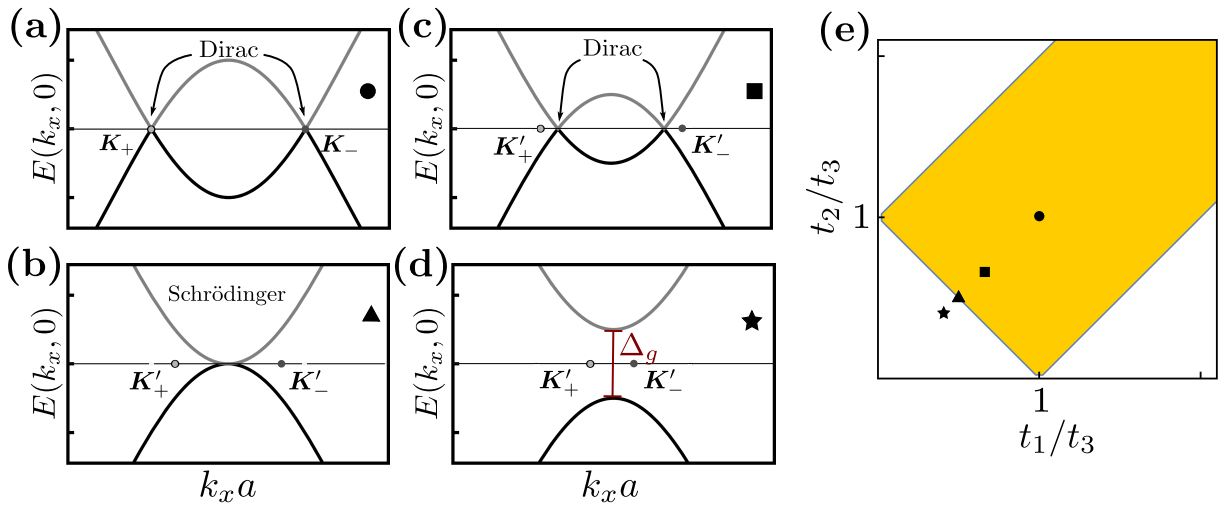

Figure 15. Energy dispersion $E_\pm(k_x, k_y)$ for $k_y = 0$ and (a) $t_2/t_3 = 1$, (b) $t_2/t_3 = 1.5$, (c) $t_2/t_3 = 2$, and (d) $t_2/t_3 = 2.5$. The colored area in panel (e) is the region of a gapless electronic spectra. The four symbols marked in (e) signal the coordinates in parameter space corresponding to conditions (a), (b), (c) and (d).

[118, 120] (see Ref. [162] too). This aspect is analyzed with more detail in the corresponding effective Dirac Hamiltonian; subsection 4.8.

Up to first order in the displacement field, the new Dirac point location is given by [120]:

$$\boldsymbol{K}_D^{\pm} \approx (\boldsymbol{I} - \bar{\boldsymbol{\epsilon}}) \cdot \boldsymbol{K}_\pm + \zeta \boldsymbol{A}, \tag{70}$$

where $\zeta = \pm 1$ is the index for each Dirac valley and the components of $\boldsymbol{A}$ are:

$$A_x = \frac{\beta}{2a}(\bar{\epsilon}_{xx} - \bar{\epsilon}_{yy}), \qquad A_y = -\frac{\beta}{2a}(2\bar{\epsilon}_{xy}). \tag{71}$$

$\boldsymbol{A}$ turns out to be a vector potential whose rotational induces a pseudomagnetic field (subsection 4.8).

The relationship between high-symmetry points and Dirac points is also shown in Figure 13(c), which depicts the deformation of the Dirac cone [118]. As shown in subsection 4.8, this produces an angle-dependent Fermi velocity as the energy dispersion becomes elliptical.

This deformation has two contributions [118], one is the change of reciprocal space and the other is due to energetic overlap changes. Both effects are easy to separate if we set the Grüneisen parameter to $\beta = 0$. This last case corresponds to a lattice with the same transfer integrals and connectivity as in pristine graphene. However, the direct lattices are different, so the reciprocal lattices must also be different.

As an example of this phenomenon, one can strain the honeycomb lattice and turn it into a brick wall lattice. Since the lattice connectivity is the same and $\beta = 0$, both Hamiltonian matrices are the same. It follows that the energy eigenvalues are the same for the brick wall and honeycomb. However, the reciprocal lattice of the brick wall is different from the honeycomb one. Thus, if we plot the energy as a function of the momentum we will get a deformed cone. In the hypothetic situation that $\beta = 0$, we already have that $K_D \neq \boldsymbol{K}'_+$.

A puzzling point is yet to be addressed in the literature. According to the previous developments, energetic effects –which depend on the parameter β– and geometric effects –which depend on the position of $\boldsymbol{K}_\pm$– predict a separation of K_D from $\boldsymbol{K}_\pm$. However, geometrical effects are captured in diffraction and, as explained in Section 2, diffraction leads to singularities in the DOS. Therefore, it is difficult to imagine a situation in which nothing happens to the electron dispersion at the intersection of Bragg lines at $\boldsymbol{K}_\pm$, while a singularity is displaced to $\boldsymbol{K}_\pm$.

This suggest that there is a missing interplay between energetic and geometric effects, and several paths are available to solve this dilemma. One such path requires to assume an electronic stabilization of the structure, like in the Humme-Rothery phases or in the Peierls instability. Another path invokes the breakdown of Cauchy-Born on lattices with a basis, to modify the parameter β [53]. In any case, the shift of Dirac points has dramatic consequences displayed in Figures 14 and 15.

In Figure 15, energy-momentum dispersions $E(\boldsymbol{k}_x, \boldsymbol{k}_y)$ of special significance are shown for $k_y = 0$, by setting $t_1/t_2 = t_0$ and using four values of t_2/t_3.

First, the undistorted lattice are displayed in Figure 15(a) when $t_2/t_3 = 1$. The Dirac points separate from the high symmetry points when $t_2/t_3 = 2$ in Figure 15(c). As the deformation increases up to 20%, the Dirac points merge, as seen in Figure 14 and 15(b). For this magnitude of critical stress, the dispersion relation is linear along the $y-$direction (relativistic Dirac behavior) and quadratic along the

$x-$direction [16, 36, 37, 38, 39, 40] (non-relativistic Schrödinger behavior). As seen in 15(d), a gap Δ_g appears when the hopping anisotropy increases.

In general, the spectrum remains gapless as long as the Hasegawa triangular inequalities are satisfied [123]:

$$\left|\frac{|t_1|}{|t_3|}-1\right| \leq \frac{|t_2|}{|t_3|} \leq \left|\frac{|t_1|}{|t_3|}+1\right|, \tag{72}$$

which correspond to the colored area in Figure 15(e). Each of the four representative key points in the evolution of $E(\boldsymbol{k}_x, \boldsymbol{k}_y)$ seen in Figures 15(a), 15(b), 15(c), and 15(d) are represented in Figure 15(e), which shows that a gap opens past a critical strain when $t_2/t_3 \geq 2$.

The Hasegawa inequalities have important predictive power. For example, one sees in Figure 15(e) that the point $(\frac{t_1}{t_3}, \frac{t_2}{t_3}) = (1,1)$ –corresponding to the dispersion seen in Figure 15(a)– is surrounded by an appreciable shaded area. This means that the gap needs a certain threshold strain to open, depending upon the direction of the applied deformation.

To understand previous point, we observe that deformations in the armchair direction keep the ratio between t_1 and t_2 fixed while t_3 changes. Thus, armchair strain changes hoppings along the diagonal line $t_1/t_3 = t_2/t_3$ in Figure 15(e), and one learns that tensile strain along the armchair direction (armchair strain) will never lead to a gap opening from this figure.

For strain in the zig-zag direction, the argument is reverted, and the system moves in the direction $t_1/t_3 = -t_2/t_3$. In this direction, the shaded ribbon-like area has its narrowest width and a gap opens.

Pereira and Castro-Neto used the Hasegawa inequalities to show that a uniform uniaxial strain in the zigzag direction opens a gap once the elongation reaches 23%. In contrast, a uniform uniaxial strain in the armchair direction is not able to open a gap [15, 16].

Figure 16 presents polar plots of isostrain curves for different angles of the applied strain indicated by arrows [16]. The corresponding values of t_1/t_3 and t_2/t_3 are also indicated and compared with the Hasewaga region. The red isostrain curve indicates the minimal strain (23%) needed to open an electronic band gap.

This Physics is re-emphasized in Figure 17(a), which presents a plot of the energy dispersion for $k_y = 0$ and different values of k_x using a zigzag strain, leading to a parabolic band dispersion once the gap opens. Figure 17(b) presents the evolution of the energy bandgap for strain applied along the zigzag direction. The gap opens linearly once the critical strain of 23% is attained.

The gap opening has been confirmed by ab initio simulations [163]. Ni et. al. confirmed the possibility of a gap opening [164], although the first reported minimal tensile strain for a gap opening

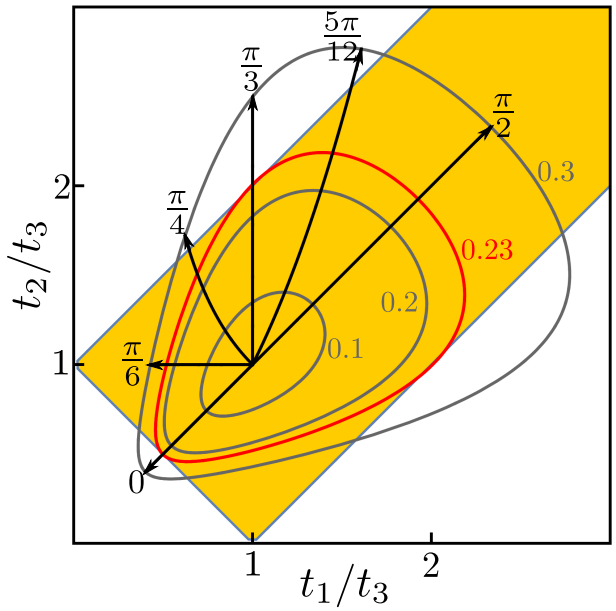

Figure 16. Isostrain curves ($\epsilon = 0.1, 0.2, 0.23, 0.3$) for the direction of the applied strain indicated by arrows. The angles are measured from the zig-zag direction. The corresponding values of t_1/t_3 and t_2/t_3 are also indicated and compared with the Hasewaga region. The critical (red) isostrain curve indicates the minimal strain (23%) necessary to open a gap. No gap is open for tensile strain applied along the armchair direction. Inspired in a plot presented in Reference [16]

was about 0.8%. Later on, the same group revised to 26% their estimate of the minimal tensile strain for gap opening [165], in good agreement with the tight-binding calculation. The problem in the first estimation by Ni et al. [165] was, precisely, the overlooking of the displacement of Dirac points from the high-symmetry points.

It is worthwhile to see see Figure 18 to understand in basic terms why zigzag and armchair strain have such a different effect upon gap opening. Apply a huge tensile strain in the zigzag direction and note that, while t_3 keeps its value due to the invariance $\boldsymbol{\delta}_3' = \boldsymbol{\delta}_3$, both t_1 and t_2 go to zero. As seen in Figure 18 b), the system is nearly dimerized in this limit, keeping only bonds in the y direction. In that case, there are only two eigenvalues of the Hamiltonian $E = \pm t_0$, each with degeneracy $N/2$ with N the number of sites. The location of these states is precisely the same of the Van Hove singularity seen on the DOS for pure graphene (Figure 12). A gap opens, given the finite spacing among these Van Hove singularities.

But as illustrated in Figure 18(c), the situation is different for armchair strain. Here, bonds along the zigzag direction are almost preserved while the interaction between zigzag chains goes to zero with increasing strain, becoming isolated chains at the limit [166]. The DOS of these linear conducting chains

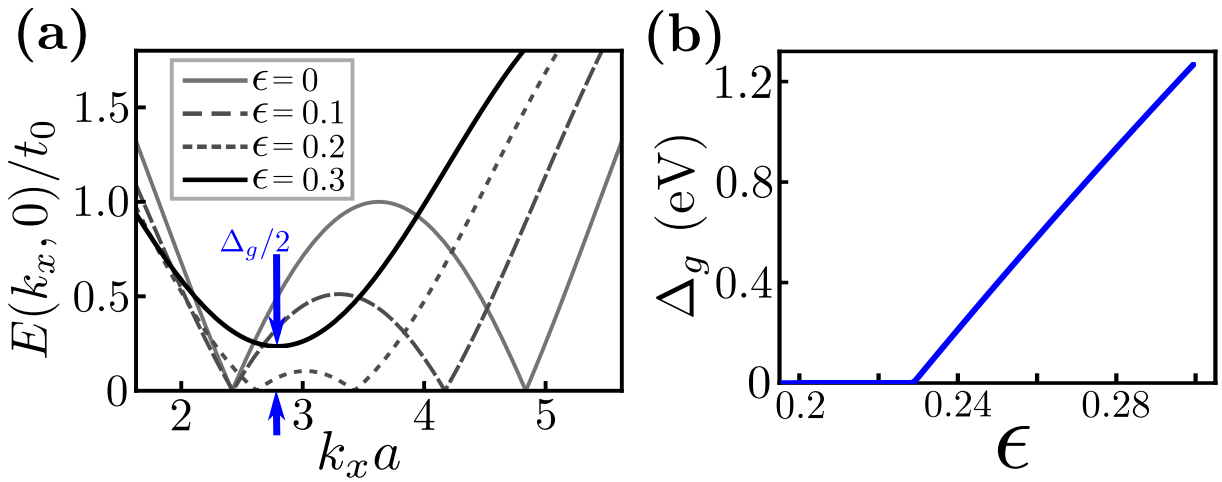

Figure 17. (a) Energy dispersion for $k_y = 0$ and different values of k_x using a zigzag strain. Observe the gap opening indicated by an arrow, as well as the parabolic band shape. (b) Gap size as a function of strain in the zigzag direction. The gap opens linearly once the critical strain of 23% is attained. Inspired on a plot presented in Reference [16]

appears in Figure 18(c), and a semiconducting gap never opens. This limit brings the system close to a quasi-1D system known as a Luttinger liquid [167]. Several systems share this behavior as for example chalcogenide compounds, stripe phases of the copper oxide high-T_c superconductors, carbon nanotubes, two-dimensional gases in large magnetic fields, etc., in which several exotic properties appear [167].

We next analize how the mean electron velocity evolves with strain. It is given by the group velocity of the wave packet:

$$\boldsymbol{v}(\boldsymbol{k}) = \nabla_{\boldsymbol{k}} E(\boldsymbol{k}), \tag{73}$$

where $\nabla_{\boldsymbol{k}}$ is the gradient operator in $\boldsymbol{k}$-space.

For electrons in graphene under uniform strain, we introduce Equation (67) into Equation (73) to obtain,

$$\boldsymbol{v}(\boldsymbol{k}) = \pm \frac{1}{2E(\boldsymbol{k})} \nabla_{\boldsymbol{k}} g(\boldsymbol{k}). \tag{74}$$

The components x and y of $\boldsymbol{v}(\boldsymbol{k})$ are given by [54]:

$$v_l(\boldsymbol{k}) = \pm \sum_{n=1}^{3} \sum_{s>n}^{3} [(1+\epsilon_{ll})(\delta_n^l - \delta_s^l) + \epsilon_{lm}(\delta_n^m - \delta_s^m)] \times t_n t_s \frac{\sin[\boldsymbol{k} \cdot (\bar{\boldsymbol{I}} + \bar{\boldsymbol{\epsilon}}) \cdot (\boldsymbol{\delta}_n - \boldsymbol{\delta}_s)]}{\sqrt{\gamma + g(\boldsymbol{k})}}, \tag{75}$$

where $l, m = \{x, y\}$ and $l \neq m$. Here δ_s^l denotes the l component of the vector $\boldsymbol{\delta_s}$.

It is possible to calculate the electronic and optical conductivity using these expressions. Some groups have studied the electronic conductivity using uniform uniaxial strain for graphene nanoribbons coupled to metallic leads in heterojunctions using the TB method and the Landauer formalism [168]. It becomes easier to apply the effective Dirac equation formalism in some cases (see section 5).

4.3.1. Simplest form of strain: the isotropic expansion. The value of an isotropic expansion resides in being a limiting case that can be solved in a straightforward manner to check the consistency of any strain theory. Such test leads to the discovery of problems in some formulations [118, 119, 120], as it will later be discussed within the effective Dirac Hamiltonian approach in section 4.8.

For isotropic strain, the lattice parameter a is just rescaled to a':

$$a \to a' = (1+\epsilon)a \tag{76}$$

given that the strain tensor is diagonal and $\bar{\boldsymbol{\epsilon}} = \epsilon \bar{\boldsymbol{I}}$. The transformation depends upon the single parameter $\epsilon = (a' - a)/a$. As a result of this rescaled lattice parameter, all hopping parameters from Equation (65) scale to the same value t_0':

$$t_0 \to t_0' = t_1 = t_2 = t_3 \approx (1 - \beta\epsilon) t_0, \tag{77}$$

which rescales the energy units, but leaves the symmetries of the Hamiltonian unchainged.

The reciprocal lattice is preserved for an isotropic expansion, but their basis vectors change to $\boldsymbol{G}_i' = \boldsymbol{G}_i/(1+\epsilon)$: the expansion in real space leads to a contraction of the reciprocal lattice.

The Fermi velocity is rescaled in the following way:

$$v_F' = 3t_0' a'/2\hbar \approx (1 - \beta\epsilon + \epsilon) v_F, \tag{78}$$

while eigenvalues are related with the original ones (E_0) by:

$$E = \frac{t_0'}{t_0} E_0 \approx (1 - \beta\epsilon) E_0, \tag{79}$$

and the dispersion relation has a rescaling of the energy and of reciprocal space as follows:

$$E(\boldsymbol{k}) = \pm(1 - \beta\epsilon) t_0 \sqrt{3 + g(\boldsymbol{k})}, \tag{80}$$

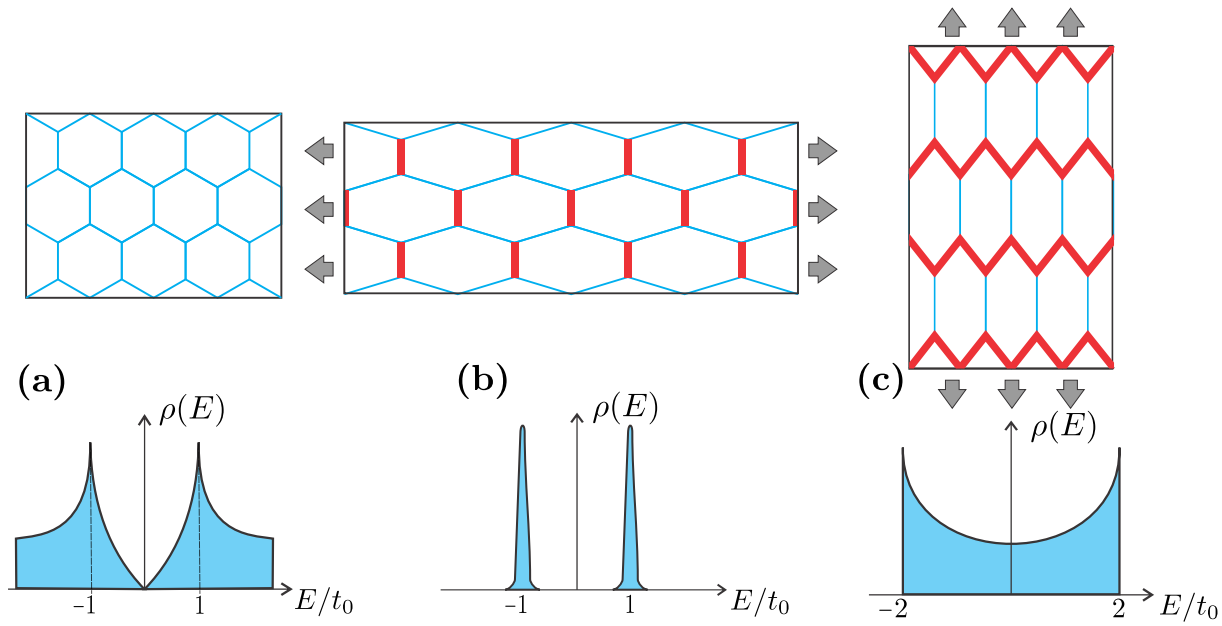

Figure 18. A comparison of uniform strain in two limits. Panel (a) represents unstrained graphene. Panel (b) represents a large strain applied along the zig-zag direction, while in (c) the strain is in the armchair direction. For all cases, the corresponding DOS is indicated below. In (b), the lattice turns into weak perturbed dimers that are indicated in red. The DOS corresponds to a perturbed system of dimers, and the model becomes a degenerate two-level Hamiltonian with energy levels at $E = \pm t_0$, i.e., the states collapses to the Van-Hove singularity observed in unstrained graphene at the same energies. A gap is clearly opened in this case. In (c), the strain preserves chains of bonds indicated in red, and the interaction between chains goes to zero. As a result, the spectrum is made from weakly perturbed degenerate linear chains, with a DOS determined from a linear chain. No gap can be generated in this extreme limiting case. These linear chains resemble a quasi-1D system known as a Luttinger liquid [167].

with:

$$g(\boldsymbol{k}) = 4\cos\left(\frac{3}{2}k_x a'\right)\cos\left(\frac{\sqrt{3}}{2}k_y a'\right) + 2\cos\left(\sqrt{3}k_y a'\right). \quad (81)$$

Given that the form of the energy dispersion is preserved, the DOS can be calculated from Equation (58) by replacing v_F with v'_F:

$$\rho(E) \approx [1 + 2\epsilon(\beta - 1)]\rho_0(E), \quad (82)$$

where $\rho_0(E)$ is the DOS from unstrained graphene. We obtain the carrier concentration using Equation (59) in terms of the unstrained carrier concentration $n_0(E)$ to be:

$$n(E) \approx [1 + 2\epsilon(\beta - 1)]n_0(E). \quad (83)$$

We can conclude from previous paragraphs that isotropic strain rescales the DOS, and that $n(E)$ scales linearly on ϵ multiplied by the positive factor $2(\beta - 1)$. This explains in a simple fashion several important features of strain in graphene without a strong spatial gradient, as such strain can be locally replaced by an average strain, Equations (82) and (83). The important point is that group velocities, currents and conductivities are scaled following a similar procedure. The phenomena described in this subsection leads to effects such as strain-charge coupling, enhanced or decreased chemical reactivity, modulation of optical properties, etc.

4.4. Non-uniform uniaxial strain

The first objective of this section is to introduce the effects due to non-uniform strain as viewed from a tight-binding perspective. Although in principle one can use numerical diagonalization to solve the Hamiltonian given by Equation (49), it is instructive to enhance our understanding by seeking analytical solutions. This allows to map the system to well-known one-dimensional equations which can be solved easily and enhance our physical insight. Furthermore, this type of strain can be produced experimentally [97], and it can also be considered an approximation for the case of graphene on a crystalline substrate with a relative rotational fault. The approach lends itself to an interesting comparison with the effective Dirac equation, and points the way towards using the supercell formalism for other types of strain. As sketched out in Figure 19, one can take advantage of uniaxial strain by noting that its Hamiltonian maps into one-dimensional effective chains [40, 116, 124, 125].

Consider a nanoribbon in which a general uniaxial strain field $\boldsymbol{u}(\boldsymbol{r}) = (0, u_y(y))$ is applied. The symmetry along the unstrained direction– chosen as

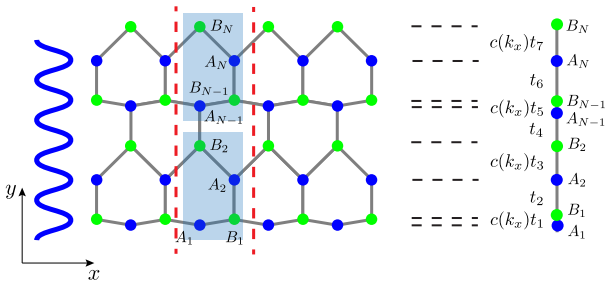

Figure 19. Mapping of a Hamiltonian with uniaxial strain applied along the armchair direction into a modulated chain described by the Hamiltonian in Equation (84). Strain is applied along the armchair, y-direction, as represented by the wavy line to the left. The vertical dotted line represents the unit cell boundary along the x direction. Inequivalent positions of Carbon atom inside the unit cell are indicated by A_j and B_j, where A and B denotes the corresponding bipartite lattice and j labels the position along the $y-$direction. The resulting map is a chain joined by effective bonds. An effective dimerization occurs when $c(k_x) = 0$. (The five-period wavy pattern to the left and the modulated chain do not possess an identical period in the figure, as only two periods of the modulated chain are shown.)

the x direction– is not broken, so that the following solution to the Schrödinger equation can be proposed: $\Psi(\boldsymbol{r}') = exp(ik_x x)\psi(y)$. The resulting Hamiltonian thus depends upon k_x and is labeled $H(k_x)$. As seen in Figure 19, the non-strained case can be thought in terms of a cell with orthogonal lattice vectors and four sites [116].

Focusing our attention to the right of Figure 19, one notes that all sites within the periodic supercell become inequivalent in the y direction. One can label them as A_j and B_j where j is an index for the position in the path, and A or B labels the original bipartite lattice in the absence of strain.

For a system *periodically strained along the armchair direction*, the resulting Hamiltonian describes a one-dimensional modulated chain [124]:

$$H(k_x) = \sum_{j=1}^{N-1} \left[t_{j+1} a_{j+1}^{\dagger} b_j + c(k_x) t_j a_j^{\dagger} b_j \right] + h.c. \qquad (84)$$

where a_j, $a_j^{\dagger}$ and a_j, $b_j^{\dagger}$ are the annihilation and creation operators in the A and B sublattices ,respectively, and N is the number of sites in the A sublattice along the periodic path. The effective bonds for odd j are defined through:

$$t_j = t_0 exp\left[-\beta(u(y_{B_j}) - u(y_{A_j}))\right], \qquad (85)$$

and for even j as:

$$t_j = t_0 exp\left[-\beta(u(y_{A_{j+1}}) - u(y_{B_j})/2)\right]. \qquad (86)$$

The factor $c(k_x)$ contains the phase in the $x-$direction:

$$c(k_x) = 2\cos(\sqrt{3}k_x a/2). \qquad (87)$$

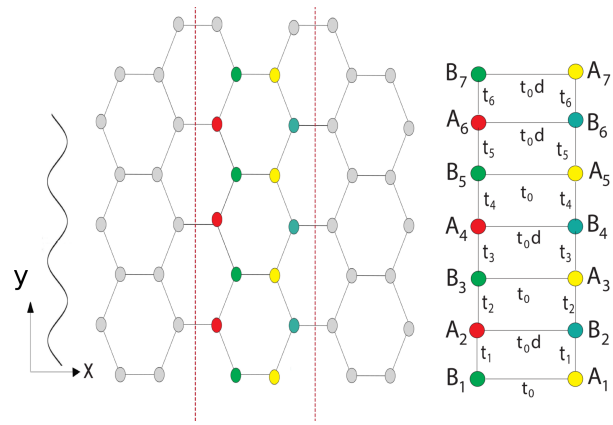

Figure 20. Mapping of the TB Hamiltonian for uniaxial strain applied along the zigzag direction, into a ladder described by the Hamiltonian in Equation (88). The strain is applied in the y-direction as represented by the wavy-line to the left. The vertical dotted line represents the cell boundary along the x direction, while the horizontal dotted lines are projections of atomic positions in the y direction. The inequivalent positions of Carbon atoms are indicated by colors; they map onto the two parallel chains (an effective ladder) shown to the right. Each atom is labeled A_j or B_j according to their bipartite lattice, and j is the position in the ladder.

An interesting situation arises for $k_x = 2/\sqrt{3}a$, where $c(k_x) = 0$ and the chain decouples into dimers [124]. For unstrained graphene, the dimers produce a massive degeneracy leading to Van Hove singularities at $E = \pm 3t$. They are saddle points of the energy dispersion. For strained graphene, the degeneracy can be completely or partially removed [124]. This has interesting consequences for electronic localization as well as for the topological properties of edge modes, as we will discuss for the case of periodic strain.

The process becomes slightly different when dealing with *periodic strain applied along the zigzag direction* [40]. As sketched out in Figure 20, the resulting map describes two modulated chains coupled by bonds of strength t_0 and $t_0 d(k_x)$, where t_j are the values of the transfer integrals along the chains in the y direction. The sites are best labeled A_j or B_j, where j is the position along the chains.

The resulting Hamiltonian is [40]:

$$H(k_x) = \sum_{j=1}^{N} t_0 \left[d(k_x) a_{2j}^{\dagger} b_{2j} + a_{2j+1}^{\dagger} b_{2j+1} \right] + \sum_j t_j a_j^{\dagger} b_{j+1} + h.c. \qquad (88)$$

The values of t_j are:

$$t_j = t_0 \exp\left[-\beta\left(l_j - 1\right)\right]. \qquad (89)$$

l_j are bond lengths:

$$l_j = \left(\left(\delta_{s+2}^{x}\right)^2 + \left[\delta_{s+2}^{y} + u_y\left(y_{B_{j+1}}\right) - u_y\left(y_{A_j}\right)\right]^2 \right)^{1/2}, \qquad (90)$$

where $s = 0, -1$. δ^x_{s+2} and δ^y_{s+2} denote the x and y components of each of the vectors $\boldsymbol{\delta}_1$ and $\boldsymbol{\delta}_2$. For armchair nanoribbons, the phase $d(k_x)$ is given by:

$$d(k_x) = e^{ik_x a}. \tag{91}$$

Using these effective mappings, the spectrum can be found from several methods. Since an effective potential appears, one can expect different effects depending on the form of the potential. For example, if the effective potential is periodic, as it is the case for graphene on a substrate, a result akin to the Harper equation is found. This equation arises in the problem of a constant magnetic field on a lattice. However, the effective equation for periodic strained graphene is not equal to the Harper equation. This result and others concerning the spectrum and localization are analyzed in subsection 4.6.

4.5. Ripples and bending

As explained in detail in Section 2.2, when strain is applied, ripples can appear or disappear depending on the applied stress. From a theoretical point of view, a suitable procedure is to relax strain via molecula dynamics (MD) simulations to obtain ripples. Following this procedure, Monteverde et. al. found that two kinds of ripples appear [110]. As seen in Figure 21(c), the first kind is a wave front ripple orthogonal to the strain front if external strain is applied along a single direction. The second is a sinusoidal shape which emerges if the external strain is applied simultaneously along two orthogonal directions [110].

Adapting the techniques discussed in previous sections, TB calculations can be done with ripples once strain is relaxed. For example, we present in Figure 21(a) the spectrum resulting form a TB calculation using compressive strain in the zigzag direction and tensile along the armchair direction, with periodic ripples obtained via strain-relaxation using MD [110]. A gap of 0.11 eV opens around one of the Dirac valleys, while the gap is twice as large in the other valley: the Dirac points are no longer equivalent because, as discussed in previous sections, the symmetry of the lattice has changed due to strain. The phonon spectrum of Figure 21(b) further reveals the inequivalence between the K and K' points.

The most important ingredient to perform a TB calculation for ripples is that the π-orbitals change their overlapping since the local normal to the graphene plane ($\boldsymbol{N_r}$) is now a function of position (see Figure 22). Let $\theta_{\boldsymbol{r}'}$ denote the angle which determines the relative orientation of a carbon atom in the new strained position $\boldsymbol{r}'$. This angle depends on the local curvature of the layer. The effect of the relative

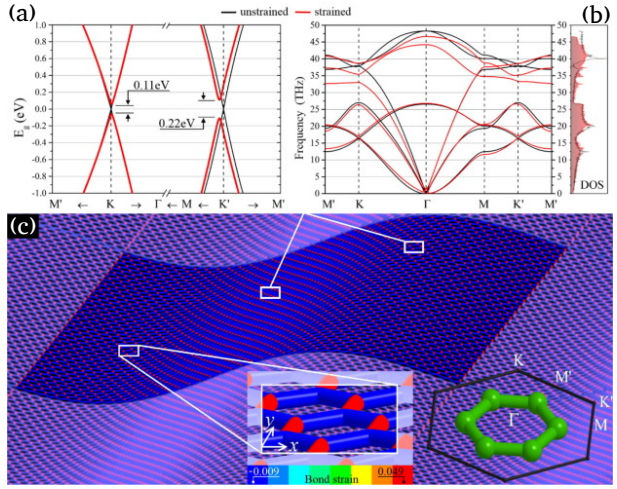

Figure 21. (a) TB calculation of the spectrum for unstrained (black curves) and strained graphene (red curves). The strain is 3.5% compressive in the zigzag direction, and 3.5% tensile along the armchair direction. Notice how the Dirac valleys become inequivalent, with different gap widths. (b) A calculation of the phonon spectra with the same stress, showing important changes. (c) Pattern of the resulting ripples. Red bonds are extended while blue are compressed following the color code that appears at the bottom. High-symmetry points of the Brillouin zone are indicated in the right corner of the panel. Reproduced from Ref. [110] under the terms of the Creative Commons Attribution License.

change of orientation for $\pi-$orbitals and the interatomic distances changes has been described in classic works in the field [153, 41, 128]. The transfer integral becomes in this case [153, 41]:

$$t_{\boldsymbol{r}',\boldsymbol{r}'+\boldsymbol{\delta}'_n(\boldsymbol{r})} = t_0 \left[1 + \alpha \left(1 - \boldsymbol{N}_{\boldsymbol{r}'} \cdot \boldsymbol{N}_{\boldsymbol{r}'+\boldsymbol{\delta}'_n(\boldsymbol{r})}\right)\right] \times \exp\left[-\beta(l_{\boldsymbol{r}',\boldsymbol{r}'+\boldsymbol{\delta}'_n(\boldsymbol{r})}/a - 1)\right], \tag{92}$$

where $\boldsymbol{N}_{\boldsymbol{r}'}$ is the unit vector normal to the surface in the site $\boldsymbol{r}'$ (see Figure 22):

$$\boldsymbol{N}_{\boldsymbol{r}'} = \frac{\hat{\boldsymbol{z}} - \nabla z}{\sqrt{1 + (\nabla z)^2}}, \tag{93}$$

here, $\nabla = (\partial_x, \partial_y)$ is the 2D gradient operator, and $\hat{\boldsymbol{z}}$ is the unit vector in the perpendicular direction to the plane. $l_{\boldsymbol{r}',\boldsymbol{r}'+\boldsymbol{\delta}'_n(\boldsymbol{r})}$ is the interatomic distance between two neighboring sites after a ripple or bent is applied. Here, $\alpha \approx 0.4$ is a constant which couples the hopping term to a relative change of orientation between neighboring π-orbitals. This is the simplest approach, as other orbitals can be hybridized for sharp ripples, thus resulting in a more complex Hamiltonian [169, 170].

To understand general features it is useful to study uniaxial ripples [110]. To give an example, consider zigzag terminated graphene where ripples are independent of the $x-$coordinate. In such scenario, the Hamiltonian given by Equation (84) can be used with t_j replaced by:

$$t_j = t_0 \left[1 + \alpha \left(1 - \boldsymbol{N}_{j+1} \cdot \boldsymbol{N}_j\right)\right] \exp\left[-\beta(l_j - 1)\right], \tag{94}$$

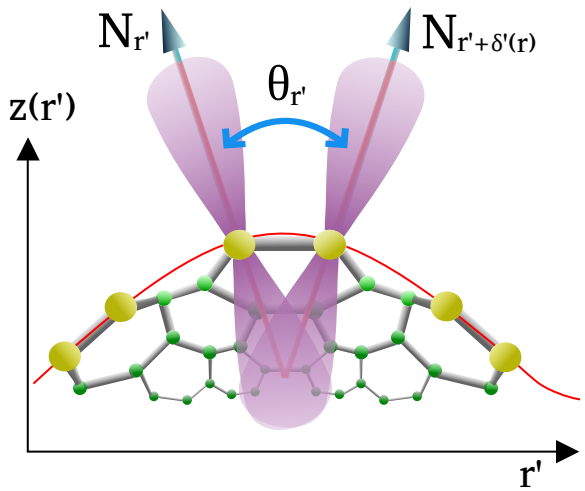

Figure 22. Overlap of $\pi-$orbitals in rippled graphene. The red curve indicates a cut thorough the graphene membrane. Local normal vectors to the surface and the corresponding angle between normals are indicated for a pair of first-neighbour atoms.

where $\boldsymbol{N}_j = \boldsymbol{N}(y_j)$ is defined in Equation (93), and:

$$l_j = \sqrt{1 + \left[z\left(y_{j+1}\right) - z\left(y_j\right)\right]^2}. \tag{95}$$

Here

$$y_j = \frac{1}{4}\left\{3j + \frac{1}{2}\left[1 - (-1)^j\right]\right\}, \tag{96}$$

is the position of carbon atoms in unrippled graphene and $j = 1, 2, ..., N$ labels the sites, as displayed in Figure 19. Similar expressions are available for armchair-terminated graphene [125]. For small amplitude and long wavelength ripples, the model resembles graphene under planar strain. Due to the breakdown of sublattice symmetry, gaps open for wavelengths of the order of the lattice parameter [125]. Strained folded graphene nanoribbons have been recently proposed to assist and enhance electronic transport [171].

4.6. Graphene on substrates: superlattices

As it was explained in Section 2.2, an interesting development in the field is the possibility of producing strain via a substrate which leads to the creation of superlattices. Bloch's theorem can thus be applied using the Fourier components of the resulting potential, as it was done for the diffraction pattern in section 2.2. However, quasi-periodic behavior is to be expected when the lattice parameters are incommensurate.

The nature of the electronic properties depends upon the interaction strenght between graphene and the substrate. In cases when the interaction is weak, mainly of a van der Waals type, the surfaces do not modify the graphene properties substantially. This is the case for hexagonal boron nitride [172, 173, 174], or the carbon face of SiC [175]. These systems share similarities with electrons in lattices with magnetic fields. Thus small gaps appear, as well as Dirac cone replicas and different kinds of localization. Such systems are very interesting for the study of exotic topological quantum phases.

Other surfaces, like metals as Fe, Pt and Re, can form partially covalent bonds with graphene leading to a strong interaction. As a consequence, graphene is rippled with amplitudes between 0.03 Å and 1.6 Å. Many of these properties are easy to understand from the perspective of a periodic uniaxial strain, in which defining one new lattice parameter is required. We review this important case in the following subsection.

4.6.1. Periodic uniaxial strain and ripples: the simplest superlattice. As it was mentioned in the introduction to subsection 3.6, some surfaces lead to strain while others, in which strong forces are present, lead to ripples. Let us review the consequences of both for the simplest cases, periodic uniaxial strain and a periodic uniaxial ripple. For strain, we particularize the results of section 4.4, while the effective Hamiltonian developed in section 4.5 can be used for ripples.

Consider armchair terminated nanoribbons with an oscillating uniaxial strain of the type:

$$u(y) = \frac{\lambda}{\sqrt{3}\beta}\cos\left[\frac{4\pi\sigma}{\sqrt{3}}\left(y - \sqrt{3}/4\right)\right], \tag{97}$$

where λ is a parameter that controls the amplitude of the strain and σ is the spatial frequency, proportional to the inverse of the strain wavelength (the constants for this strain field have been chosen in such a way that the final Schrödinger equation looks simple). Using a linear approximation for $t_{\boldsymbol{r}',n}$, Equation (89) becomes:

$$t_j = t_0\left[1 + \lambda\sin\left(\pi\sigma\right)\sin\left(2\pi\sigma j\right)\right]. \tag{98}$$

Previous values of t_j are identical with those appearing in the Harper chain, which is the one-dimensional effective equation resulting from the problem of an electron in a constant magnetic field [22]. For the Harper equation, σ is the ratio between the magnetic flux and the flux quantum. The energy spectrum for that problem is the Hofstadter butterfly, which turns out to be a complex fractal [22] with interesting topological quantum phases [138].

Although the uniaxial strain hopping parameter given by Equation (88) follows the same sequence as the one seen in the Harper equation, the Hamiltonian differs from the Harper case by the coupling between left and right chains displayed in Figure 20. In other words, the graphene system is actually made from two coupled Harper chains. As in the Harper equation, the most important observation is that for irrational σ,

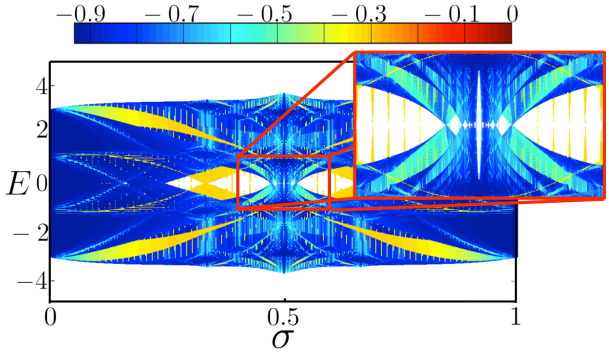

Figure 23. Spectrum for uniaxial periodically strained armchair-terminated graphene. Colours represent the different localization degrees of electron wavefunctions defined in terms of $\alpha(E)$, Equation (99). Blue-colored points are extended states while red-colored points indicate states that tend to be localized. The spectrum contains features akin to the Hoftsadter butterfly fractal. The inset shows a zoom-in around $\sigma = 1/2$. Notice the gap opening for $\sigma = 1/2$, when the strain wavelength is of the order of the lattice parameter. Such gap opens due to the bipartite symmetry breaking. In contrast, the long wavelength limit, i.e., $\sigma \to 0$ and $\sigma \to 1$, the spectrum is gapless with extended states. DOS cuts along constant σ lines are presented in Figure 24. Reproduced from Ref. [40] with permission. Copyrighted by the American Physical Society.

i.e., whenever $\sigma \neq P/Q$ where P and Q are integers, the resulting Hamiltonian is no longer periodic, being instead quasiperiodic. Quasiperiodic Hamiltonians appear when there are two incommensurate parameters [55], in this case the wavelength of the strain and the lattice parameter.

Such Hamiltonians lead to wavefunction localization, fractal properties, etc. [62]. Furthermore, perturbation theory can not be used to solve them due to the small divisor problem [62]. In spite of this, for rational σ (such that $\sigma = P/Q$ with P and Q integers), the system is periodic with period Q for Q even (or $2Q$ for Q odd). The Bloch theorem can thus be applied, resulting in a reduced Hamiltonian matrix of size $Q \times Q$ for Q even (otherwise $2Q \times 2Q$).

The relation among applied strain and system size can be understood from the perspective of superlattices. For commensurate σ, the strain modulation generates a new lattice involving Q sites in the strained direction, creating in turn a reciprocal lattice vector $\Delta \boldsymbol{g}$ that defines a new Brillouin zone. The effective potential can thus be written as a Fourier series, from where the spectrum is found using the Bloch theorem, as it was explained in section 2.2. Although for irrational σ this procedure is no longer valid, it is still possible to study a sequence of rational approximants [62].

The energy spectrum depends upon the numeric properties of σ, as it happens with Harper Equation. As an example, we plot in Figure (23) the spectrum as a function of σ for a typical λ for zigzag nanoribbon under periodical uniaxial strain. The spectrum has a complex nature, with gaps at the Fermi level for some values of σ. The localization of states is also very complex. To show this, colours in Figure (23) represent the localization of eigenfunctions, evaluated through the parameter $\alpha(E)$ that is defined as:

$$\alpha(E) = \frac{\ln \sum_{j=1}^{N} |\psi_j(E)|^4}{\ln N}, \tag{99}$$

where $\psi_j(E)$ is the wavefunction at site j having an energy E.

Blue-colored states in Figure (23) represent extended states. States are extended at $\sigma \to 0$ and $\sigma \to 1$. In this limit, the strain wavelength is much bigger than graphene's lattice parameter. As $\sigma \to 1/2$, the situation is more complicated, since states are extended for some rational values of σ, but they can be surrounded by localized states, seen in red in the figure.

There are interesting localization properties for σ irrational [22, 55, 176]. A powerful way to study these properties in our effective 1D system is the trace map defined as a product of transfer matrices [177]. As seen in Figure 24 the bands present several interesting features as a function of k_x. Within the same figure, several peaks are observed in the DOS, especially for irrational values of σ. These peaks have a counterpart in carbon nanotubes [178], and many of these results are also obtained for periodic ripples in graphene nanoribbons [125].

A fundamental observation from Figures (23) and (24) is that no gap opens for long-wavelength strain. When the strain modulation has a wavelength comparable to the lattice parameters, an asymmetry between A and B sites arises and a gap opens. In this case a tagged field, or in approximate way a reduction from the group C_{6v} to the C_{3v} takes place. As it will be discussed later, the breaking of the sublattice symmetry creates an effective mass as well [109, 125, 170, 179].

4.6.2. More general types of superlattices. The features discussed for periodic uniaxial strain are observed in more general cases. An isotropic expansion basically produces a renormalization of the Fermi velocity, while biaxial strain has several consequences in the band structure, including narrow gap openings that can be obfuscated due to the metallic nature of the substrate.

Superlattices induce a superperiod, and one can use such periodicity to solve a tight-binding equation in the first Brillouin zone of the reciprocal space superlattice, as it was done before for uniaxial periodic strain. In the general case, the TB parameters will depend on strain and ripples produced by the

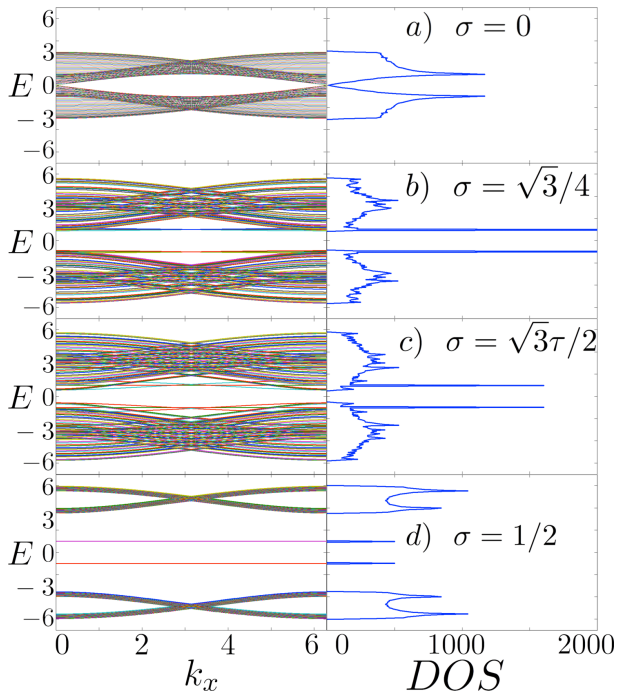

Figure 24. Energy bands as a function of k_x for strained armchair terminated graphene with values of σ as indicated. The resulting DOS appearing at the left shows Van Hove singularities and band gaps.

substrate, and on the particular interaction with the substrate [180].

Details about interactions and effective Hamiltonians are still work in progress. For example, there are several theoretical models to understand graphene on hBN [19, 180]. The electronic dispersion depends strongly on the chosen parameters and on whether the perturbation is inversion-symmetric or inversion-asymmetric. Also, electronic many-body exchange interactions seem to play a role [180]. Thus, the opening of a gap in graphene/h-BN is a highly debated issue, since some studies affirm the existence of a gap opening [180] while others rule it out [19, 20]. Recently, careful ARPES measurements have shown gaps of $100meV$ and $160meV$ depend on the valley degree of freedom, indicating the existence of a strong inversion-symmetry-breaking potential [181]. Local defects in the substrate can induce exotic phases too, like a broken chiral symmetry due to Kekulé ordering [182].

In spite of this, three general features could be argue to occur for graphene on a substrate: the creaion of new Dirac cones around the original ones (known as second or third generation Dirac cones), the opening of minigaps, and Landau levels. The generation of second and third generation Dirac cones is not surprising if we recall the results deduced in subsection 2.2 for diffraction on modulated structures. Therein, phason satellites spots were found around pristine graphene diffraction spots. Each of these satellites produces new Bragg lines resulting in a singularity on the electronic dispersion. Following such ideas, the aim of this section is to provide a basic framework to understand the mechanisms behind gap opening and Dirac cone replicas, and to review some relevant experimental results.

To do so, we feel that a lot can be learned from the generic properties of periodic modulations assuming that the interaction between the substrate and graphene is weak. This is the case for graphene over h-BN, in which van der Waals forces are present. Strain and ripples modify the creation/annihilation operators and the TB parameters of the Hamiltonian defined in Equation (61). In addition, the substrate lattice produces local shifts of the energy (i.e., it creates a space-dependent on-site potential) that must be included into Equation (61) and leads to a more general Hamiltonian denoted by $\boldsymbol{H}_{Sl}$:

$$\boldsymbol{H}_{Sl} = \boldsymbol{H} + \sum_{\boldsymbol{r}'\in A} V_A(\boldsymbol{r}')a^\dagger_{\boldsymbol{r}'}a_{\boldsymbol{r}'} + \sum_{\boldsymbol{r}'\in B} V_B(\boldsymbol{r}')b^\dagger_{\boldsymbol{r}'}b_{\boldsymbol{r}'}, \tag{100}$$

where $V_A(\boldsymbol{r}')$ and $V_B(\boldsymbol{r}')$ are the local on-site potential energy at A and B sublattices created by the substrate. For hBN, the B and N sites have different interactions with graphenes so that $V_A(\boldsymbol{r}')$ and $V_B(\boldsymbol{r}')$ are different, even under the assumption that hBN matches the graphene lattice exactly. In that approximation $V_A(\boldsymbol{r}')$ and $V_B(\boldsymbol{r}')$ are space independent, and the Hamiltonian is reduced to:

$$\boldsymbol{H}_{Sl} = \boldsymbol{H}_0 + \sum_{\boldsymbol{r}\in A} V_A a^\dagger_{\boldsymbol{r}}a_{\boldsymbol{r}} + \sum_{\boldsymbol{r}\in B} V_B b^\dagger_{\boldsymbol{r}}b_{\boldsymbol{r}}. \tag{101}$$

Previous expression is a tagged field akin to the one obtained under uniaxial strain for small strain wavelength ($\sigma \to 1/2$). This way, Equation (50) for pristine graphene is converted into:

$$\begin{pmatrix} V_A & H_{AB}(\boldsymbol{k}) \\ H^*_{AB}(\boldsymbol{k}) & V_B \end{pmatrix} \begin{pmatrix} a_{\boldsymbol{k}} \\ b_{\boldsymbol{k}} \end{pmatrix} = E(\boldsymbol{k}) \begin{pmatrix} a_{\boldsymbol{k}} \\ b_{\boldsymbol{k}} \end{pmatrix}, \tag{102}$$

The new eigenvalues are,

$$E(\boldsymbol{k}) = \bar{V} \pm \sqrt{\bar{V}^2 + E_0^2(\boldsymbol{k}) - V_A V_B} \tag{103}$$

where the average potential is defined as $\bar{V} = (V_A + V_B)/2$ and $E_0^2(\boldsymbol{k})$ is the energy dispersion for pristine graphene. Since $E_0^2(\boldsymbol{K}_\pm) = 0$, a gap opens having the following magnitude:

$$\Delta = |V_A - V_B|. \tag{104}$$

The diagonal terms in Equation (102) can be expressed as an average potential plus a mass term in the effective Dirac Hamiltonian, as can be readily seen by expanding $E_0^2(\boldsymbol{k})$ around $\boldsymbol{K}_\pm$. This explains in a rough way why short wavelength strain fields open small gaps.

In a more general case, $V_A(\boldsymbol{r}')$ and $V_B(\boldsymbol{r}')$ have a period determined by the superlattice. Then, it is possible to follow the procedure explained in subsection 2.2 for the diffraction pattern of modulated structures, i.e., one makes use of a Fourier expansion of the potentials, operators and tight-binding parameter in supercell Hamiltonian (101). The Fourier components can be treated using second-order perturbation theory [19, 180]. However, as explained before, there is no consensus about which terms to include. Therefore, we will only discuss the basic mechanisms behind the formation of Dirac cones replicas from a TB approach here.

All operators are Fourier-decomposed first. For example, the two sets of annihilation and creation operators are written using two wavevectors $\boldsymbol{k_1}$ and $\boldsymbol{k_1}+\boldsymbol{k}$:

$$a^{\dagger}_{\boldsymbol{r}'} = \frac{1}{\sqrt{N}}\sum_{\boldsymbol{k_1}} e^{i[(\boldsymbol{k_1}+\boldsymbol{k})\cdot(\boldsymbol{r}+\boldsymbol{u}(\boldsymbol{r}))]} a^{\dagger}_{\boldsymbol{k}+\boldsymbol{q}}, \tag{105}$$

and:

$$b_{\boldsymbol{r}'+\boldsymbol{\delta}'_n(\boldsymbol{r})} \approx \frac{1}{\sqrt{N}}\sum_{\boldsymbol{k}} e^{-i\boldsymbol{k}\cdot(\boldsymbol{r}+\boldsymbol{u}(\boldsymbol{r}))} e^{-i\boldsymbol{k}\cdot\boldsymbol{\delta}'_n(\boldsymbol{r})} b_{\boldsymbol{k}}. \tag{106}$$

The periodicity of $\boldsymbol{u}(\boldsymbol{r})$ is accounted for by introducing a Fourier expansion in the reciprocal space superlattice vectors $\Delta\boldsymbol{g}$:

$$e^{-i\boldsymbol{k_1}\cdot\boldsymbol{u}(\boldsymbol{r})} = \sum_{\Delta\boldsymbol{g}} e^{i\Delta\boldsymbol{g}\cdot\boldsymbol{r}} \tilde{V}_{\boldsymbol{k}_1}(\Delta\boldsymbol{g}), \tag{107}$$

where $\tilde{V}_{\boldsymbol{k}_1}(\Delta\boldsymbol{g})$ are the expansion coefficients. In Equation (106), the strained first-neighbour vectors (lattice corrections) $\boldsymbol{\delta}'_n(\boldsymbol{r})$ are given by Equation (18), i.e., they transform via the tensor operation $(\bar{\boldsymbol{I}} + \nabla\boldsymbol{u}(\boldsymbol{r}))$. To gain a better understanding, assume that $\boldsymbol{u}(\boldsymbol{r})$ has a longwave-length character. Then one can neglect the gradient of the field, resulting in the approximation $\boldsymbol{\delta}'_n(\boldsymbol{r}) = \boldsymbol{\delta}_n$. This is precisely the same result as the one observed for uniform strain, and it coincides with computations done before the inclusion of lattice corrections [52]. It follows that locally, this strain is nearly similar to a uniform strain, as expected for a gentle strain gradient. Under this assumption, bond length variations are negligible and $t_{\boldsymbol{r}',\boldsymbol{r}'+\boldsymbol{\delta}'_n(\boldsymbol{r})} \approx t_0$. Also, we assumed that short-wavelength strain is negligible for simplicity ($V_A(\boldsymbol{r}') = V_B(\boldsymbol{r}') = 0$).

By using all these assumptions in the Hamiltonian given by Equation (61), one obtains:

$$\boldsymbol{H}_{Sl}(\boldsymbol{k}) = \sum_{\Delta\boldsymbol{g},\boldsymbol{k}} \tilde{V}_{-\Delta\boldsymbol{g}}(\Delta\boldsymbol{g}) E_0(\boldsymbol{k}) a^{\dagger}_{\boldsymbol{k}-\Delta\boldsymbol{g}} b_{\boldsymbol{k}}. \tag{108}$$

Now we observe that for the first-generation high-symmetry points, obtained from setting $\boldsymbol{k} = \boldsymbol{K}_{\pm}$, we have $\boldsymbol{H}_{Sl}(\boldsymbol{k}) = 0$ since $E_0(\boldsymbol{K}_{\pm}) = 0$. This indicates that $\boldsymbol{K}_{\pm}$ are still tips of Dirac cones, and correspond to the first-generation Dirac cones. Let us consider momentums close to phason satellites of $\boldsymbol{K}_{\pm}$, i.e., we consider $\boldsymbol{k} = \boldsymbol{K}_{\pm} + \Delta\boldsymbol{g}_1 + \boldsymbol{q}$, where $\boldsymbol{q}$ is a small wavevector. Equation (108) reads as follows in that case:

$$\boldsymbol{H}_{Sl}(\boldsymbol{k}) = \sum_{\Delta\boldsymbol{g},\boldsymbol{k}} \tilde{V}_{-\Delta\boldsymbol{g}}(\Delta\boldsymbol{g}) E(\boldsymbol{K}_{\pm} + \Delta\boldsymbol{g}_1 + \boldsymbol{q}) \tag{109}$$

$$\times a^{\dagger}_{\boldsymbol{K}_{\pm}+\Delta\boldsymbol{g}_1+\boldsymbol{q}-\Delta\boldsymbol{g}} b_{\boldsymbol{K}_{\pm}+\Delta\boldsymbol{g}_1+\boldsymbol{q}}. \tag{110}$$

By setting $\boldsymbol{q} = -\Delta\boldsymbol{g}_1$, we observe that $E(\boldsymbol{K}_{\pm} + \Delta\boldsymbol{g}_1 + \boldsymbol{q}) = 0$ again, leading to a Dirac point at momentum corresponding to the satellite at position $\boldsymbol{K}_{\pm} + \Delta\boldsymbol{g}_1$. Higher-order satellites will produce the same effect, leading to higher-order Dirac replicas.

In fact, the transfer integrals in the TB Hamiltonian are not severely affected in the absence of strong strain gradients. As a result, the Hamiltonian matrix for finite systems has the same eigenvalues as in graphene, but the metric of reciprocal space is changed by a folding of the original energy dispersion into the second Brillouin zone (SBZ). This mechanism is a generic effect of small periodic modulations in the limits of the Brillouin zone [47]. Extra Fourier components enter the convolution when the derivative $\nabla\boldsymbol{u}(\boldsymbol{r})$ is not neglected.

Dirac cone replicas appear as a result of graphene's phason satellites in the diffraction spots. If one considers the squared Hamiltonian that was introduced in subsection 4.1, the electronic dispersion has a minimum at intersections of Bragg lines at the boundaries of a SBZ. As a result, each new phason satellite produces a new minima in $\nabla_{\boldsymbol{k}} E^2((k))$ due to a vanishing group velocity. This minima has a parabolic dependence in the squared triangular lattice since it corresponds to the lower band edge (see subsection 4.1). The minima becomes a Dirac cone when the square root is taken to recover graphene. In other words, the extra diffraction spots produce singularities in the electron dispersion that enter as standing waves in the supercell structure. The effect of a non-trivial atomic basis in monoatomic unit cells is well known for hexagonal-close packed (hcp) structures, where one talks about Jones zones due to the vanishing of the structure factor associated with the hexagonal top and bottom faces of the unitary cell prism [47].

The Dirac cone replicas have been observed in many experiments. For example, for graphene on hBN [183] the layers can be highly strained [173, 174, 184]. Several methods have been proposed to understand the electronic properties of graphene on hBN by including strain in a TB approximation [19, 180] or as pseudomagnetic fields in the Dirac equation [185].

Figure 25 presents a recent ARPES measurement of the graphene/hBN electron dispersion [181]. The ARPES technique allows to extract the electron energy $(E - E_F)$ as a function of the component of electron momentum in the plane of the sample, denoted by $k_{||}$.

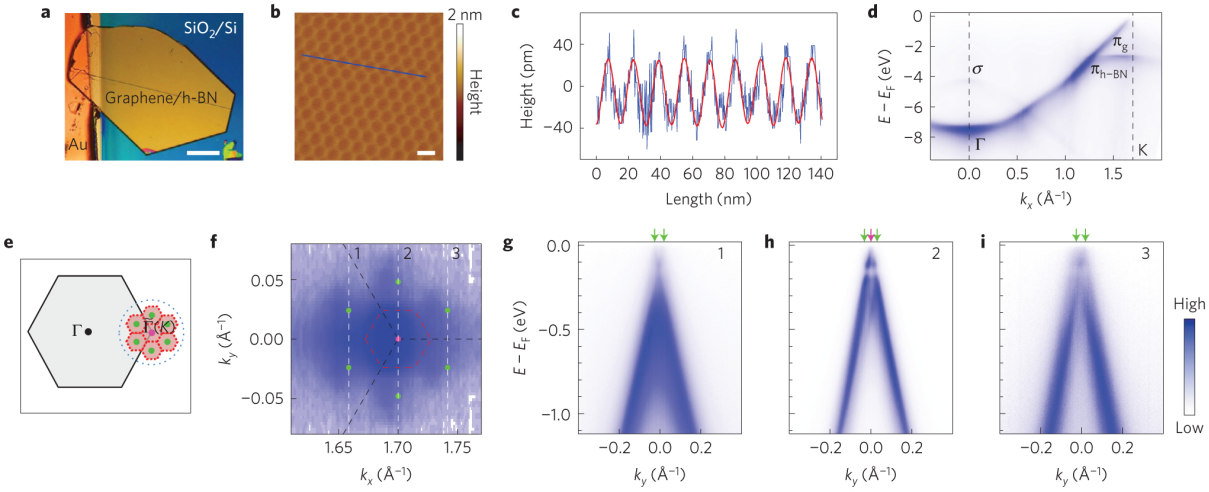

Figure 25. Dirac cone replicas and band gap opening as seen in an ARPES spectrum of graphene on hBN. (a) Optical image of the sample. The white bar scale is 100μm. (b) Atomic force microscope image of the moiré pattern. The white scale bar is 20 nm. (c) Height-profile along the blue line shown in (b). The data is shown in blue, while the red curve is obtained by using a high-pass filter. (d) Dispersion along a $\Gamma - K$ path in the Brillouin zone, showing the σ and π bands of graphene and hBN. (e) Schematics of the Brillouin zone of graphene (gray hexagon) and the phason satellites indicated in green, corresponding to the second-Brillouin zone (SBZ) centers. The SBZs areas are shadowed with pink and indicated with pink-dotted lines. The Γ and $\bar{\Gamma}(K)$ points of graphene are also indicated. (f) Constant energy map at E_F. The green dots indicates the tips of the Dirac cones replicas observed at the six nearest SBZ centers. The red dot is the original Dirac cone. The Brillouin zone of graphene is indicated by broken black lines, while the Brillouin zone of the superlattice is indicated with red broken lines. (g), (h) and (i) are the dispersions obtained along the cuts 1, 2 and 3 that are indicated in panel (f) by white broken lines. The tips of the original Dirac cones are indicated with pink arrows, while the Dirac cone replicas are indicated with green arrows. Reprinted by permission from Macmillan Publishers Ltd: Nature Phys. [181], copyright (2016).

Second-generation Dirac cones (SDCs) are clearly seen in Figure 25(f), 25(g), 25(h) and 25(i). The experiment is quite challenging as the separation of the original Dirac cone and the cloned Dirac cones is extremely small, of the order of the reciprocal superlattice vector $\Delta \boldsymbol{g} \approx 0.05 A^{-1}$. This requires samples of extremely high quality directly grown by remote plasma-enhanced chemical vapor deposition [181].

The ARPES study reveals unambiguously SDCs at the corners of the superlattice Brillouin zone, ocurring only at one of the two valleys [181]. Gaps of approximately 100 meV and approximately 160 meV are observed at the SDCs and the original graphene Dirac cone [181], and seem to imply an important role for a strong inversion-symmetry-breaking perturbation potential in the physics behind graphene/hBN.

Another important feature of graphene on hBN is the observation of Landau levels and a fractal spectrum in ultraclean graphene on hBN subjected to electrostatic and magnetic fields [20]. The measured spectrum was a repeating butterfly-shaped motif, known as Hofstadter's butterfly [22]. This spectrum has also been found in bilayer graphene [186], as it will be discussed in detail in Section 6. The main reason for the fractal spectrum is the non-commensurability of graphene-sustrate lattices, as in the case of an uniaxial strained lattice. Interestingly, there are second- and third-generation Dirac points, leading to pronounced peaks in resistivity [20]. Small lattice incommensurability prevents the opening of gaps seen in perfectly lattice-matched graphene on hBN, and leads to a renormalized Dirac dispersion with a trigonal warping [19, 173].

Graphene over Ir (111) represents another example of the effects produced by interaction with a substrate. Figure 26 shows the ARPES spectra at different azimuthal angles around the $\Gamma - K - M$ direction [17]. For comparison, Figure 26(a) shows the spectrum of Ir$(1,1,1)$ without graphene, while Figures 26(b), 26(c) and 26(d) display the spectrum with graphene included, along three different azimuthal angles. The main effects observed are minigaps indicated by arrows, and replica bands, including with a Dirac cone replica [17]. The measured gap width is between 0.1 and 0.2 eV. The Dirac cone of graphene is not hybridized with Ir, indicating a weak interaction with the substrate [17].

These minibands and gaps can be reproduced a tight-binding calculation that include up to three nearest neighbours, as shown with dotted lines in Figure 26 [17]. However, there is an important issue here. In principle, the reciprocal vector of the moiré supercell implies a long-wave superperiodic potential,

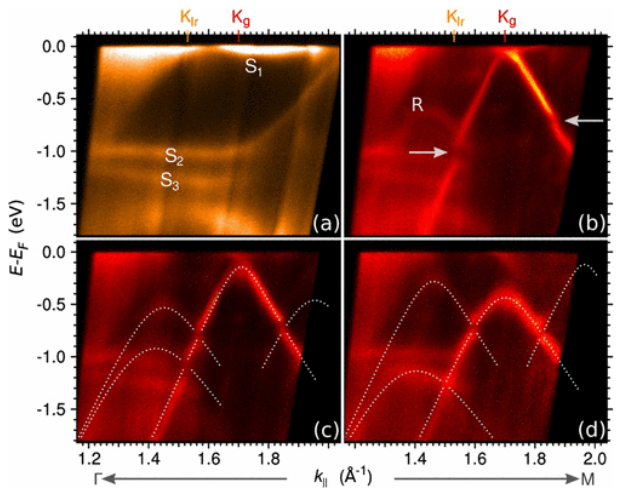

Figure 26. ARPES spectrum of graphene on Ir(1, 1, 1). The K points of iridium (K_{Ir}) and graphene (K_g) are indicated for reference. (a) Clean Ir(1, 1, 1) on an azimuthal angle of $0.5° \pm 0.1°$. Three surface states are indicated by S_1, S_2, S_3. (b) ARPES for Ir(1, 1, 1) covered by graphene using the same angle. The horizontal arrows denote minigaps in the primary Dirac cone. A replica band is indicated by the letter R. (c) and (d): The same spectra as in (b) but for azimuthal angles of $1.4° \pm 0.1°$ and $3.0° \pm 0.1°$, respectively. Dotted lines are results from tight-binding calculations on a superlattice. Reproduced from Ref. [17] with permission. Copyrighted by the American Physical Society.

since the moiré reciprocal lattice vector $\Delta \boldsymbol{g}_m = \boldsymbol{G}_{gr} - \boldsymbol{G}_{Ir}$ is smaller than $\boldsymbol{G}_{gr}$ or $\boldsymbol{G}_{Ir}$, which are the original reciprocal vectors of graphene and Ir(1, 1, 1) respectively. As stated in previous sections, and as seen in Figure 23, a long-wave superperiodic potential is not able to open a gap. This requires to break the symmetry of the bipartite lattices within each unitary cell of graphene [179], as discussed for the case of uniaxial strain before. In terms of the low-energy Dirac approximation, it requires an effective mass. This is indeed the case for graphene on Ir(1, 1, 1), since atoms in the two bipartite lattices are locally (and globally) inequivalent [56]. From the above considerations, the strain field must have contribution from short and long wave-length periodic strain.

A band gap of 0.26 eV has been experimentally determined for graphene on SiC [187], and also attributed to the bipartite lattice symmetry breaking [188]. This band gap, nevertheless, has also been assigned to many body interactions [189]. A wider band gap of 0.51 eV, has been observed for graphene on MgO (1, 1, 1) and attributed to the bipartite lattice symmetry breaking [190, 191]. Another interesting feature of strained generated superlattices is the possibility of angle-dependent bandgap engineering [192], as well as spin-dependent transport and polarization [193].

4.7. Topological phases

An emerging field is that of topological modes due to strain [13]. These are quantized edge modes that are robust against disorder because they are topologically protected [194]. Topological effects on carrier transport were first studied in magnetic fields applied on semiconductors within the context of the quantum Hall effect (QHE) [22]. Eventually, it was recognized that topological modes were quantum phases with the peculiarity of not breaking any symmetry, unlike the common cases seen in all previously known phase transitions [194]. Since the systems do not break any symmetry, they are described using topological invariants instead of order parameters. For unstrained graphene, most of the QHE topological aspects are now well understood [137]. Since strain can be treated as a pseudomagnetic field, it is natural to expect topologically protected properties in deformed graphene.

One of the first tasks to observe the topological QHE modes on graphene was to design a strain field leading to a constant pseudomagnetic field [128]. Such proposal was recently refined to program extreme pseudomagnetic fields by uniaxial stretch of nanoribbons designed with varying width [195] and also on "artificial graphene" lattices [196, 197] (see more on this in section 4.9). It is possible to generate Landau states using this profile, which is one of the QHE hallmarks. In fact, the first experimental observation of the QHE fractal spectrum and topological modes has been obtained using bilayered graphene over a hBN sustrate, as explained in Section 6. Also, the experimental tuning of Dirac states by strain in the topological insulator Bi_2Se_3 is expected to have an important impact in the field [198]. Several proposals concerning this idea were published before such achievement. As an example, a strain based graphene electronic device was proposed to observe a zero-field topological quantum phase transition between the time-reversal-symmetry-broken quantum spin Hall (QSH) and quantum anomalous Hall states. The main feature of such device is the absence of an actual magnetic field [199].

We use the case of uniaxial strain in nanoribbons to show how topological properties arise. Consider the Hamiltonian for uniaxial strain along the zigzag direction given by Equation (84), with hopping parameters calculated via Equations (85) and (86). Furthermore, consider a strain field $\boldsymbol{u}(y) = cos(2\pi\sigma y)$. For a wavelength such that $\sigma = 1/(2a)$, t_j takes only two values. By performing a Fourier transform of Equation (84) to k-space using:

$$a_j = \frac{1}{\sqrt{N/2}} \sum_{k_y} e^{-ik_y(j)3/2} a_{k_y}, \tag{111}$$

and:

$$b_j = \frac{1}{\sqrt{N/2}} \sum_{k_y} e^{-ik_y(j)3/2} b_{k_y}, \quad (112)$$

the resulting Hamiltonian becomes:

$$H(\boldsymbol{k}) = h_x(\boldsymbol{k})\sigma_x + h_y(\boldsymbol{k})\sigma_y, \quad (113)$$

where σ_x and σ_x are the x and y Pauli matrices,

$$h_x(\boldsymbol{k}) = 2(1-\lambda)\cos(\sqrt{3}k_x/2) + (1+\lambda/2)\cos(3k_y/2), \quad (114)$$

and

$$h_y(\boldsymbol{k}) = (1+\lambda/2)\sin(3k_y/2). \quad (115)$$

$H(\boldsymbol{k})$ (Equation (113)) is the Su-Schrieffer-Heeger model for polyethylene [200], in which non-trivial topological phases appear once a gap is opened [200, 201], here obtained by choosing an amplitude $\lambda > 1/2$. For the gapless system ($\lambda < 1/2$) there are topological modes still, corresponding to flat bands that join Dirac points, that are known as Fermi arcs [40, 202] that appear in Weyl semimetals [203, 204]. For such topological states, the invariants used for the gapped spectra are ill-defined, and one needs to use a new invariant [203, 204]. This simple example shows how topological properties appear due to strain. As Landau levels are known to appear in monolayer and bilayer graphene due to the substrate interaction [20], the topology associated with constant magnetic fields is expected [167, 204], including the fractal Chern-beating phenomena [176] and topological collisions at Van-Hove singularities [138]. Finally, time-dependent strain is able to generate interesting topological properties as well [205, 206, 207, 208].

4.8. Continuum models: effective Dirac equation

As seen in Section 4.1, π-electrons in pristine graphene have a linear dispersion relation in the low-energy regime ($|E| \lesssim 1$eV) near the corners of the 1BZ [209]. This dispersion can be described in terms of a 2×2 Hamiltonian, obtained by expanding the tight-binding Hamiltonian in momentum space around to $\boldsymbol{K}_+$ and $\boldsymbol{K}_-$ points (see Equations (5-7) and Figure 1) by means of the replacement $\boldsymbol{k} = \boldsymbol{K}_+ + \boldsymbol{q}$ and a subsequent expansion up to first order in $\boldsymbol{q}$ [210, 211]:

$$H_{ps} = \hbar v_F \begin{pmatrix} 0 & q_x - iq_y \\ q_x - iq_y & 0 \end{pmatrix} = \hbar v_F \boldsymbol{\sigma} \cdot \boldsymbol{q}, \quad (116)$$

where $\boldsymbol{\sigma} = (\sigma_x, \sigma_y)$ is a vector whose components are Pauli matrices. Analogous expansion around $\boldsymbol{K}_-$ gives $H = \hbar v_F \boldsymbol{\sigma}^* \cdot \boldsymbol{q}$, with $\boldsymbol{\sigma}^* = (-\sigma_x, \sigma_y)$. Making the replacement $\boldsymbol{q} \to -i\hbar\nabla$ in correspondence to the $\boldsymbol{k} \cdot \boldsymbol{p}$ or effective mass approximation, the Hamiltonian in Equation (116) is a two-dimensional equivalent of the Dirac Hamiltonian for massless fermions [212]. However, in contrast to the relativistic problem, the role of the velocity of light c is played by the Fermi velocity $v_F \approx c/300$. Also, the two-component description given by Pauli matrices operates on the sublattice degree of freedom instead of the real spin, hence the term *pseudospin* that is highlighted as H_{ps}. *Pseudospin up* is another way to call sublattice A and *pseudospin down* labels sublattice B.

The behaviour of the low-energy charge carries in graphene, as massless relativistic fermions, yields in a number of unprecedented phenomena in condensed matter physics, such as an anomalous quantum Hall effect, Klein tunneling, Zitterbewegung, "minimum" conductivity of $\sim 4e^2/h$ even when the carrier concentration tends to zero, universal transmittance expressed in terms of the fine-structure constant, among others [213, 214].

4.8.1. Uniform strain. The procedure to obtain the effective Dirac Hamiltonian for graphene under a uniform strain is essentially the same as that used for pristine, undeformed graphene. One starts with a TB Hamiltonian in momentum space for strained graphene:

$$H = -\sum_{n=1}^{3} t_n \begin{pmatrix} 0 & e^{-i\boldsymbol{k}\cdot(\bar{\boldsymbol{I}}+\bar{\boldsymbol{\epsilon}})\cdot\boldsymbol{\delta}_n} \\ e^{i\boldsymbol{k}\cdot(\bar{\boldsymbol{I}}+\bar{\boldsymbol{\epsilon}})\cdot\boldsymbol{\delta}_n} & 0 \end{pmatrix}, \quad (117)$$

and considers momenta close to the Dirac points to capture appropriately the strain-induced anisotropy [118, 127, 120]. Here, one needs to find the new Dirac point positions explicitly from the dispersion relation (66). As mentioned earlier in section 4.3, to first order in strain tensor, the Dirac points $\boldsymbol{K}_D^{\pm}$ are given by equations (70) and (71). Then, consistently expanding (117) around the Dirac points by means of $\boldsymbol{k} = \boldsymbol{K}_D^{\pm} + \boldsymbol{q}$, one finds that [118, 127, 120]:

$$H_{ps} = \hbar v_F \boldsymbol{\sigma} \cdot (\bar{\boldsymbol{I}} + \bar{\boldsymbol{\epsilon}} - \beta\bar{\boldsymbol{\epsilon}}) \cdot \boldsymbol{q}, \quad (118)$$

is the effective Dirac Hamiltonian for uniformly strained graphene. It can be immediately verified that, for $\bar{\boldsymbol{\epsilon}} = 0$, the Hamiltonian (118) reduces to the Hamiltonian (116) of unstrained graphene. At the same time, The Hamiltonian in Equation (118) can be seen as a particular case of the generalized effective Dirac Hamiltonian reported in [158] for a honeycomb lattice with weak anisotropy in the hopping parameters.

Some remarks about the effective Hamiltonian (118) follow. First, it is independent of the choice of reference system. Second, it has two contributions due to strain: a β-independent term, $\hbar v_F \boldsymbol{\sigma} \cdot \bar{\boldsymbol{\epsilon}} \cdot \boldsymbol{q}$, which is purely geometric; and a β-dependent term $-\hbar v_F \beta \boldsymbol{\sigma} \cdot \bar{\boldsymbol{\epsilon}} \cdot \boldsymbol{q}$arising from strain-induced changes in the hopping parameters. For graphene, both contributions have the same order of magnitude. Third, from

equation (118) one can identify a Fermi velocity tensor given by [118, 120]:

$$\bar{\boldsymbol{v}} = v_F(\bar{\boldsymbol{I}} + \bar{\boldsymbol{\epsilon}} - \beta\bar{\boldsymbol{\epsilon}}), \tag{119}$$

whose tensorial character is due to the elliptic shape of the isoenergetic contours around $\boldsymbol{K}_D$. The principal axes of $\bar{\boldsymbol{v}}$ are collinear with the principal axes of $\bar{\boldsymbol{\epsilon}}$. For a uniaxial strain, for example, the eigenvalues of $\bar{\boldsymbol{v}}$ are [16]:

$$v_{\parallel} = v_F(1 - \tilde{\beta}\epsilon), \quad v_{\perp} = v_F(1 + \tilde{\beta}\nu\epsilon), \tag{120}$$

where $\tilde{\beta} = \beta - 1$, ν is the Poisson's ratio, ϵ is the strain and $v_{\parallel}(v_{\perp})$ is the Fermi velocity parallel (perpendicular) to the direction of the applied strain. In [215], an accurate and alternative approach is carried out to estimate $v_{\parallel}$ and $v_{\perp}$ from a fitting of the π-bands obtained with a DFT calculation for graphene under uniaxial strains along the zigzag and armchair directions.

Consider an isotropic expansion, $\bar{\boldsymbol{\epsilon}} = \epsilon\bar{\boldsymbol{I}}$, as a consistency test. It was demonstrated in section (4.3.1) that the Fermi velocity of graphene is given by $v_F(1 + \epsilon - \beta\epsilon)$ to first order in ϵ (see equation (78)). Therefore, any expression reported as Fermi velocity tensor for strained graphene [148, 170, 126, 216, 217] to be evaluated for $\bar{\boldsymbol{\epsilon}} = \epsilon\bar{\boldsymbol{I}}$ must reproduce $v_F(1 + \epsilon - \beta\epsilon)$. When this simple test is not fulfilled, the most probably cause will be an expansion around points of the reciprocal space which are not the true Dirac points [120, 127].

One can use the Hamiltonian (118) to evaluate other quantities up to the first order in strain tensor. For example, the local density of states (LDOS) is given by [148, 218, 219]:

$$\rho(E) \approx \rho_0(E)\Big(1 - \tilde{\beta}\mathrm{Tr}\bar{\boldsymbol{\epsilon}}\Big), \tag{121}$$

where $\rho_0(E)$ is the local density of states for unstrained graphene given by Equation (58). Since $\tilde{\beta} > 0$, the strain effect in the LDOS depends on the sign of $\mathrm{Tr}\,\bar{\boldsymbol{\epsilon}}$ which can be written as $\mathrm{Tr}\,\bar{\boldsymbol{\epsilon}} = A/A_0 - 1$, being A (A_0) the area of the strained (unstrained) graphene sample. Thus, for an expanded sample ($A/A_0 > 1$) the effect is a local decrease of the LDOS, whereas for a compressed sample ($A/A_0 < 1$) the effect is a local increase. The LDOS does not change for a shear strain ($A/A_0 = \mathrm{Tr}\,\bar{\boldsymbol{\epsilon}} = 0$). These results permit understanding scanning tunnelling spectroscopy measurements, which are sensitive to the LDOS [220].

Anisotropic Dirac quasiparticles described by the effective Hamiltonian $H = \hbar(v_x\sigma_x q_x + v_y\sigma_y q_y)$ have Landau levels given by $E_n = \sqrt{v_x v_y/v_F^2}E_n^{(0)}$ [162], where $E_n^{(0)} = \mathrm{sgn}(n)\sqrt{2e\hbar Bn}$ are the conventional relativistic Landau levels [221]. This result can be extrapolated to strained graphene, described by Hamiltonian (118) if one diagonalizes the Fermi velocity tensor (119) and multiplies its eigenvalues. After some algebraic manipulations up to first order in strain tensor, it can be shown that the Landau levels of uniformly strained graphene are given by:

$$E_n = E_n^{(0)}\left(1 - \frac{\tilde{\beta}}{2}\mathrm{Tr}\bar{\boldsymbol{\epsilon}}\right). \tag{122}$$

Last expression explains corrections of the Landau levels in the presence of a position-dependent Fermi velocity which is interpreted as emergent gravity within an approach based on general relativity [222].

4.8.2. Nonuniform strain: Gauge fields and position-dependent Fermi velocity. If the spatial variation of the strain is small on the lattice scale, one expands the Hamiltonian obtained for uniform strain, Equation (118), around the true Dirac point in the momentum space, and goes to real space by the replacement [127, 120]:

$$\bar{v}_{ij}q_k \to \bar{v}_{ij}(\boldsymbol{r})\left(-i\frac{\partial}{\partial r_k} - K_k^D(\boldsymbol{r})\right) - \frac{i}{2}\frac{\partial\bar{v}_{ij}(\boldsymbol{r})}{\partial r_k}, \tag{123}$$

where the last term assures hermiticity of the ensuing Hamiltonian [148, 126]. This transformation makes space-dependent $\bar{\boldsymbol{\epsilon}} = \bar{\boldsymbol{\epsilon}}(\boldsymbol{r})$ [223, 224]. Thus, the Dirac points and the Fermi velocity (both functions of $\bar{\boldsymbol{\epsilon}}$ for uniform strain) now become functions of position $\boldsymbol{r}$, as denoted by $\boldsymbol{K}_D^{\pm}(\boldsymbol{r})$ and $\bar{\boldsymbol{v}}(\boldsymbol{r})$, respectively. As a consequence, $\boldsymbol{K}_D^{\pm}(\boldsymbol{r})$ can be interpreted as a pseudovector potential (gauge field), which yields an alternative physical picture for the strain-induced pseudomagnetic field [225]. The rotational of the gauge field $\boldsymbol{K}_D(\boldsymbol{r})$ gives [120]:

$$\begin{aligned}\boldsymbol{B}_s &= \nabla\times\boldsymbol{K}_D^{\pm}(\boldsymbol{r}),\\ &= \nabla\times(\bar{\boldsymbol{\epsilon}}(\boldsymbol{r}) - \bar{\boldsymbol{\omega}}(\boldsymbol{r}))\cdot\boldsymbol{K}^{\pm} \pm \nabla\times\boldsymbol{A}(\boldsymbol{r}),\\ &= \pm(\partial_x A_y - \partial_y A_x),\\ &= \mp\frac{\beta}{2a}(2\partial_x\bar{\epsilon}_{xy}(\boldsymbol{r}) + \partial_y\bar{\epsilon}_{xx}(\boldsymbol{r}) - \partial_y\bar{\epsilon}_{yy}(\boldsymbol{r})).\end{aligned} \tag{124}$$

Inclusion of the local rotation tensor $\bar{\boldsymbol{\omega}}(\boldsymbol{r})$ through equation (18) can be employed to demonstrate the lack of $\boldsymbol{K}^{\pm}$-dependent pseudovector potentials [226, 52] (another way to demonstrate this is presented later on in the context of the discrete approach [108, 109] (seccion 4.9)). Equation (124) is the expression of the strain-induced pseudomagnetic field $\boldsymbol{B}_s$ that appears in early derivations [152, 227] where, unlike the approach presented here, the pseudovector potential comes from an expansion of the strained TB Hamiltonian around the fixed points $\boldsymbol{K}_{\pm}$. The emergence of the pseudomagnetic field due to nonuniform strain has been also considered from a symmetry analysis [170, 228] or from a quantum field theory in curved spaces [229, 230]. In section

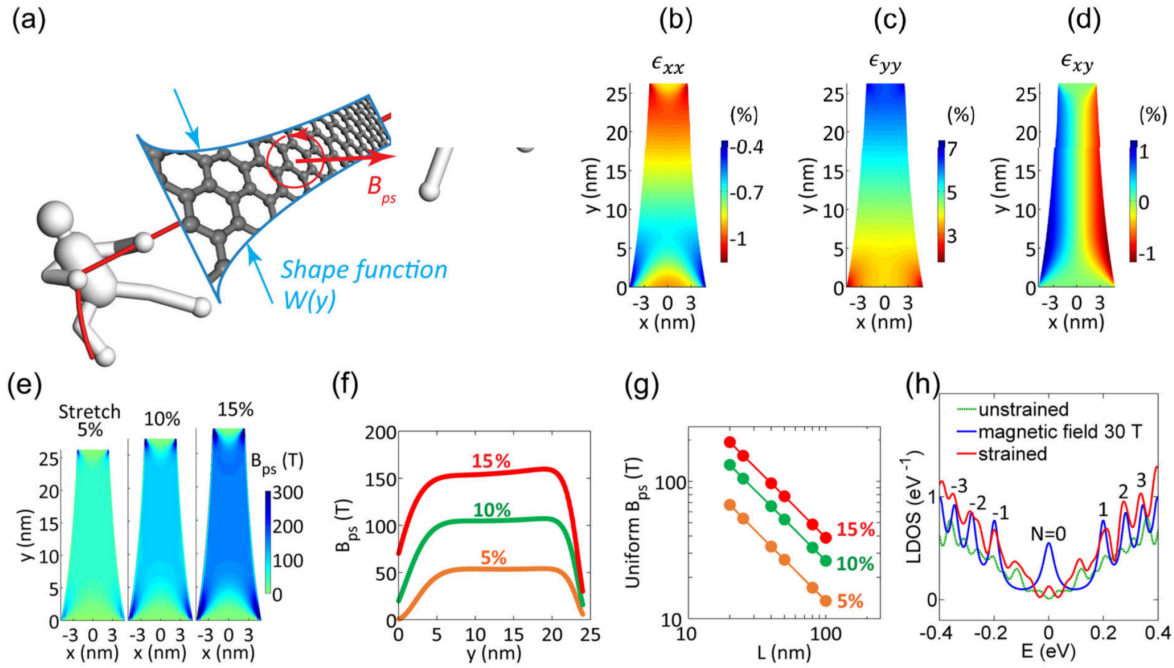

Figure 27. (a) Schematics of a graphene strip of varying width under a uniaxial pulling, leading to a uniform pseudomagnetic field $\boldsymbol{B}_{ps}$. (b)-(d) Contour plots of the resulting strain components, ϵ_{xx}, ϵ_{yy}, and ϵ_{xy} under a 5 % uniaxial stretch. (e) Resulting pseudomagnetic fields in the graphene nanoribbon shown in (a) under a uniaxial stretch of 5 %, 10 %, and 15 %, respectively. (f) Intensity of the pseudomagnetic field as the function of position along the centerline of the graphene ribbon for various applied stretches. (g) Intensity of the pseudomagnetic field is shown to be linearly proportional to the applied uniaxial stretch and inversely proportional to the length of the graphene ribbon L. (h) Local density of states of unstrained graphene and graphene with a constant strain gradient determined by density functional theory calculations. Reproduced from Ref. [195] with permission. Copyrighted by the American Physical Society.

4.9, we will present another derivation of the strain-induced pseudogauge fields from considerations based on discrete differential geometry.

According to the replacement (123) into Hamiltonian (118), the effective Dirac Hamiltonian for graphene under a nonuniform strain can be written as [127, 120]:

$$H_{ps} = -i\hbar\boldsymbol{\sigma}\cdot\bar{\boldsymbol{v}}(\boldsymbol{r})\cdot\nabla - \hbar v_F\boldsymbol{\sigma}\cdot\boldsymbol{A}(\boldsymbol{r}) - \hbar v_F\boldsymbol{\sigma}\cdot\boldsymbol{\Gamma}(\boldsymbol{r}), \quad (125)$$

where the position-dependent Fermi velocity tensor $\bar{\boldsymbol{v}}(\boldsymbol{r})$ is given by:

$$\bar{\boldsymbol{v}}(\boldsymbol{r}) = v_F\big(\bar{\boldsymbol{I}} + \bar{\boldsymbol{\epsilon}}(\boldsymbol{r}) - \beta\bar{\boldsymbol{\epsilon}}(\boldsymbol{r})\big), \quad (126)$$

and the components of the corresponding complex vector field $\boldsymbol{\Gamma}(\boldsymbol{r})$ are:

$$\Gamma_i = \frac{i}{2v_F}\partial_j\bar{v}_{ij}(\boldsymbol{r}) = \frac{i(1-\beta)}{2}\partial_j\bar{\epsilon}_{ij}(\boldsymbol{r}), \quad (127)$$

with an implicit sum over repeated indices. Keep in mind that the complex gauge field $\boldsymbol{\Gamma}$ is due to a position-dependent Fermi velocity, and its presence guarantees the hermiticity of the Hamiltonian (125). Unlike $\boldsymbol{A}$, $\boldsymbol{\Gamma}$ is a purely imaginary, so that, $\boldsymbol{\Gamma}$ cannot be interpreted as a gauge field. Therefore, it does not give rise to pseudomagnetism in the density of states [148]. At present, experimental signatures of such complex gauge field $\boldsymbol{\Gamma}$ remain as open questions; see section 4.9 for a discussion of Hermicity within the context of space-dependent pseudospin Hamiltonians.

Besides graphene, the procedure described in previous paragraph has been recently employed to obtain the effective low-energy Hamiltonian of 3D Dirac semimetals [161] and certain class of 3D Weyl semimetals [231] under mechanical deformations. In general, this approach corresponds to the scheme of emergence of gauge fields and gravity in the vicinity of the Dirac, Weyl or Majorana points in the energy spectrum [232, 233, 234].

Nowadays, the transport signatures of the pseudomagnetic fields remain the most investigated strain-induced effects [235, 236, 237, 238, 239, 240, 241, 242]. The nature of these fictitious fields yields the possibility of observing Landau quantization and a pseudo-quantum Hall effects under zero external magnetic fields. Early proposals of such strain distributions [128, 129] are technically challenging because they require complex stress fields applied at the boundaries of graphene sample, but they can be engineered in molecular graphene [196]. Zhu *et al.* recently conceived an alternative method to achieve programmable extreme pseudomagnetic fields with uniform distributions over

large areas [195] by a pulling along one axis (see Figure 27). They revealed the special shape in which a graphene strip must be cut (like a 2D projection of a musical horn) so that, pulling on its ends yields a constant strain gradient and, accordingly, a uniform pseudomagnetic field.

Experimental confirmation of the strain-induced pseudomagnetic field was reported on scanning tunneling microscopy of graphene nanobubbles [27]. The scanning tunneling spectroscopy (STS) spectra measured directly over the nanobubbles (strained graphene regions) showed a series of peaks in the same manner as if graphene was subjected to an external magnetic field [243]. Giant values of the pseudomagnetic fields $\boldsymbol{B}_s$, of 300 Tesla were determined. For comparison and as a matter of context, (pulsed) magnetic fields of up to 100 Tesla can only be obtained in state-of-the-art experimental facilities.

Subsequently, many experimental confirmations of the pseudomagnetic fields in graphene have been carried out under other different strain configurations [244, 245, 246, 247, 248, 249, 250, 251] and in various graphene-like systems such as, molecular graphene [196], photonic crystals [252] and optical lattices [253]. Beyond graphene, strain-induced gauge fields have been also characterized in bilayer graphene [254, 255, 256], borophene [257], topological insulators [258], transition metal dichalcogenides [9, 259, 260] and three-dimensional Dirac and Weyl semimetals [161, 231, 261, 262, 263].

The effects solely due to a position-dependent Fermi velocity tensor on the spinor wavefunction of charge carriers are now discussed. For this purpose, consider that:

$$\bar{\boldsymbol{v}}(x) = v_F \begin{pmatrix} 1+f(x) & 0 \\ 0 & 1 \end{pmatrix}, \quad \boldsymbol{\Gamma} = (if'(x)/2, 0), \tag{128}$$

i.e., the Fermi velocity is varying along the x axis. At the same time, we assume $\nabla \times \boldsymbol{A}(\boldsymbol{r}) = 0$, to disregard the effect of the pseudomagnetic field. As possible scenarios of the considered problem see the references [120, 264, 265].

Then, from Equation (125), we can write the corresponding time-independent Dirac equation for the spinor wavefunction Ψ as

$$\begin{aligned} &\big(-i(1+f(x))\partial_x - \partial_y - if'(x)/2\big)\psi_2 = \varepsilon\psi_1, \\ &\big(-i(1+f(x))\partial_x + \partial_y - if'(x)/2\big)\psi_1 = \varepsilon\psi_2, \end{aligned} \tag{129}$$

where $\varepsilon \equiv E/(\hbar v_F)$ and E is the energy. Following the calculation presented in Ref. [120], this system has as solution to the spinor wavefunction

$$\Psi(\boldsymbol{r}) = A \exp\Big[ik_y y + \int^x \frac{ik_x - f'(\tilde{x})/2}{1+f(\tilde{x})} d\tilde{x}\Big] \begin{pmatrix} 1 \\ se^{i\theta} \end{pmatrix}, \tag{130}$$

where $e^{i\theta} = (k_x + ik_y)/|\varepsilon|$, $\varepsilon = \pm(k_x^2 + k_y^2)^{1/2}$, A is a normalization constant and $s = \pm 1$ denotes the conduction band and valence bands, respectively.

Some important remarks follows from the solution (130). Firstly,

$$|\Psi|^2 \sim (1+f(x))^{-1} \tag{131}$$

therefore, a position-dependent Fermi velocity induces an inhomogeneity in the carrier probability density, which was early analysed by using a quantum field theory approach in curved spaces [266]. However, a position-dependent Fermi velocity does not lead to the emergence of band-gap structure in the energy spectrum. Besides, given the arbitrariness of the function $f(x)$, Equation (130) allows to consider scenarios more complex that those described by Kronig-Penney-like models for the variation of the Fermi velocity along a direction [267, 268, 269, 270].

4.8.3. Time-dependent strain. As discussed above, a nonuniform deformation of the graphene lattice can be interpreted as a pseudomagnetic field given by equation (124). Within the same theoretical framework and by analogy with the normal electromagnetic field, one can recognized that a time-dependent deformation gives rise also to a pseudoelectric field expressed by $\boldsymbol{E}_s = -\partial_t \boldsymbol{A}$ [271, 272], which can accelerate the electrons and induce current. However, since $\boldsymbol{E}_s$ couples with opposite signs in the two valleys, does not cause a net electric current. Some works have been devoted to reveal observable consequences due to this pseudoelectric field but, the predicted effects, e.g., topological electric current [273, 274] or modification of the Raman spectrum [275], are not experimentally confirmed yet.

An interesting analogy with a real electromagnetic problem is given by considering a time-dependent deformation field of the graphene lattice $\boldsymbol{u}(\boldsymbol{r}, t)$ of the form [276],

$$\boldsymbol{u} = (0, u_0 \cos(Gy - \omega t)), \tag{132}$$

with $u_0 \ll a \ll 2\pi/G$, i.e. the atomic displacement u_0 is much less than the unstrained carbon-carbon distance a, while the wavelength $2\pi/G$ is much greater than a. As illustrated in Figure 28 (a), this deformation wave propagates along the y direction, which is rotated an arbitrary angle θ respect to the crystalline coordinate system $x_0 y_0$. For the latter, the x_0-axis points along the zigzag direction of graphene lattice. Therefore, for $\theta = 0$ the mechanical wave moves along the armchair direction of graphene lattice, whereas for $\theta = \pi/2$, it moves along the zigzag direction.

It is very important to keep in mind that the general expression of the pseudovector potential $\boldsymbol{A}$, respect to the rotated frame xy, is given by [277],

$$\begin{aligned} A_x &= \frac{\beta}{2a}\Big((\bar{\epsilon}_{xx} - \bar{\epsilon}_{yy})\cos 3\theta - 2\bar{\epsilon}_{xy}\sin 3\theta\Big), \\ A_y &= \frac{\beta}{2a}\Big(-2\bar{\epsilon}_{xy}\cos 3\theta - (\bar{\epsilon}_{xx} - \bar{\epsilon}_{yy})\sin 3\theta\Big), \end{aligned} \tag{133}$$

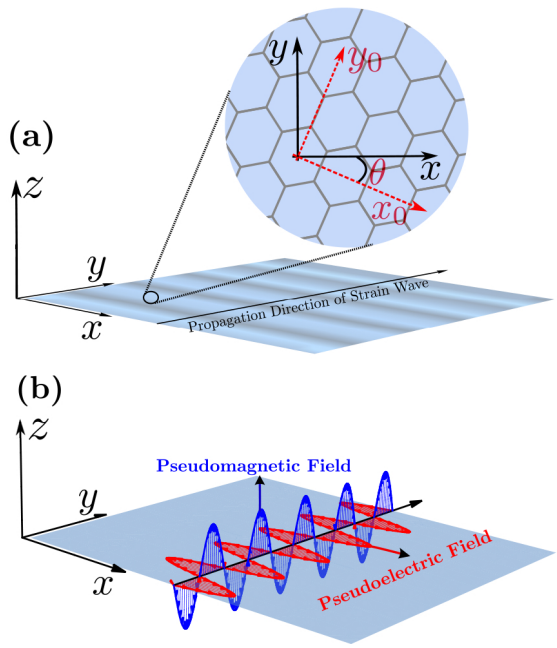

Figure 28. (a) Schematic representation of a deformation wave propagates in graphene. The dark regions on the sample represent zones of higher density of carbon atoms. The inset plays the relation between the arbitrary coordinate system xy and the crystalline coordinate system x_0y_0. (b) Unstrained graphene under the equivalent pseudoelectromagnetic wave. The pseudoelectric field lie in graphene plane, whereas the pseudomagnetic field is perpendicular to this. Reproduced from Ref. [276] with permission.

whose periodicity of $2\pi/3$ in θ, reflects the trigonal symmetry of the underlying honeycomb lattice. Then, for the case of the deformation field (132), from Equation (133), it is obtained the following effective gauge field,

$$\boldsymbol{A} = \frac{\beta u_0 G}{2a}\sin(Gy - \omega t)(\cos 3\theta, -\sin 3\theta). \tag{134}$$

Hence the deformation wave (132) leads to a pseudoelectromagnetic wave propagating along the y-axis at the velocity $v_s = \omega/G$, which can be assumed equal to the sound velocity in graphene [276]. Note that while the pseudomagnetic field $\boldsymbol{B}_s$ oscillates perpendicularly to the graphene sample (see Figure 28 (b)), the pseudoelectric field $\boldsymbol{E}_s$ oscillates in the sample plane but, in general, it is not perpendicular to the propagation direction of the strain wave. As noted in Ref. [276], when the deformation wave propagates along the zigzag direction, i.e. for $\theta = \pm\pi/2 + 2n\pi/3$), the pseudoelectric field oscillates along the propagation direction of the pseudoelectromagnetic wave. So that, in this case, the pseudoelectromagnetic wave behaves more like a sort of longitudinal mechanical wave. In contrast, when the deformation wave propagates along the armchair direction, i.e. for $\theta = n\pi/3$, the pseudoelectric fields oscillates transversally to the propagation direction

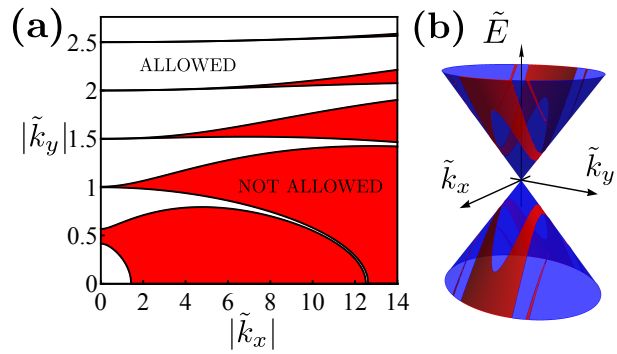

Figure 29. (a) Chart of the allowed bands (white regions) for the quasi momentum $\tilde{\boldsymbol{k}}$ (in units of G), with $A_0 \equiv \beta u_0/(2a) = 0.15$ and the strain wave propagating along the armchair direction. The diagram is symmetrical respect to both axes. (b) Associated Dirac cone, whose red (blue) strips correspond to the forbidden (allowed) values of the quasi-energy $\tilde{E}(\tilde{k}_x, \tilde{k}_y)$ (in units of $\hbar v_F G$) due to the deformation wave. Reproduced from Ref. [276] with permission.

of the pseudoelectromagnetic wave, as the expected behavior of a normal electromagnetic wave. Then including the strain-induced pseudovector potential (134) via minimal coupling, and disregarding the effect of a position-dependent Fermi velocity, the resulting effective Dirac equation reads

$$v_F\boldsymbol{\sigma}\cdot(-i\hbar\nabla - \boldsymbol{A})\boldsymbol{\Psi} = i\hbar\partial_t\boldsymbol{\Psi}. \tag{135}$$

As solutions of this equation, Oliva-Leyva et a. [276] found Volkov-type states [278, 279], which propagates preferably in the propagation direction of deformation. In addition, they reported a band structure of allowed and not allowed values for the quasi-momentum and for the quasi-energy, as illustrated in see Figure (29). The form of the emergent band structure is given by the propagation direction of the strain wave respect to the crystalline directions of graphene lattice. In consequence, a deformation wave might produce a collimation effect over the charge carriers and, accordingly, an alternative mechanism to archive electron beam collimation, beyond other traditional methods [280, 281].

Time driven strain has important topological aspects. In the case of electromagnetic fields, is known that Floquet bands have topological properties [282]. For strain, zero-energy modes appear at the edges of the Floquet zone[205, 206, 207] with a complex topological quantum-phase diagram [208].

4.9. Strain from the perspective of discrete differential geometry

Just as the justification for the models provided thus far is to enhance our understanding of strain-induced effects, the motivation for the discrete approach was to follow a non-traveled route based on the geometry

of meshes with the aim to give an additional angle to this fascinating Physics. The main point of this approach is to consider the graphene membrane as an atomistic mesh, and to employ novel geometrical tools used to deal with discrete meshes [283] to describe the electronic properties of deformed graphene, without recourse to a continuum deformation field that every other author in the field employs. The discrete approach has an unique economy to it, and it will be argued in this section that it also generates unique insights.

The discrete approach takes as input atomic locations on strained structures (such as those created from molecular dynamics), as opposed to the deformation field discussed up to this point [108, 109, 284]. Within the continuum approach, deformation fields are customarily superimposed to the discrete, atomistic lattice as in Figure 30 [285], but the discrete program comes down to re-expressing the theory beyond continuum elasticity and explicitly on the atomic lattice, such that matters of spatial scale can be analyzed.

We divide the discussion on this section into four parts: We first indicate the motivation for the discrete approach. Then, we reproduce the derivation of strain-induced gauges in graphene. A dedicated discussion of the discrete geometry which captures graphene's shape without recourse to continuum approximations is presented next, and the discussion is closed by pointing to open avenues of research within this approach.

4.9.1. Underlying assumptions of the continuum, Dirac approach. The main assumption of all theories aiming to understand the effects of mechanical strain in terms of pseudo-electromagnetic gauges is expressed in Ref. [128], and it goes as follows:

"If a mechanical strain varies smoothly on the scale of interatomic distances, it does not break sublattice symmetry but rather deforms the Brillouin zone in such a way that the Dirac cones located in graphene at points K and K' are shifted in opposite directions" (see Refs. [41, 152] as well). Previous statement says that one can understand the effects of mechanical strain on the electronic structure in terms of a semiclassical approach, provided that strain preserves sublattice symmetry.

In this semiclassical approach, a local and strain-induced pseudo-magnetic field $\mathbf{B}_s(\mathbf{r}) = \nabla \times \boldsymbol{A}_s(\mathbf{r})$ and a deformation potential $V_s(\mathbf{r})$ are added into a pseudospin Hamiltonian $H_{ps}(\mathbf{q})$ (Equation (116)). The semiclassical approximation is justified if the strain is slowly varying, that is, when it extends over many unit cells and preserves sublattice symmetry [6, 152, 128].

The way we understood the problem [108, 109],

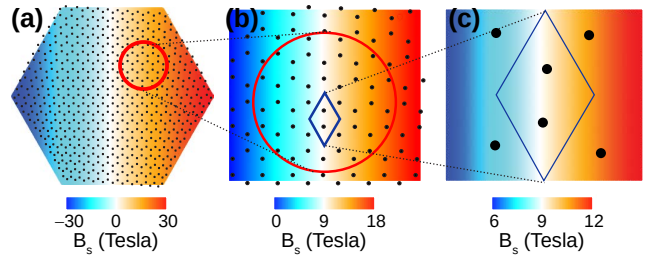

Figure 30. In the approach from continuum elasticity, strain-induced fields are defined regardless of spatial scale. A unit cell "plaquette" is shown in (b) and (c) for comparison. Those "plaquettes" are the underlying geometrical objects in the discrete approach. One defines the pseudospin Hamiltonian H_{ps} at individual plaquettes employing the semiclassical approximation of low-energy expansions of a tight-binding Hamiltonian in reciprocal space that are modulated in space. As a result, strain-induced gauge fields become discrete themselves. Reproduced from Ref. [109] with permission.

sublattice symmetry is directly linked to the Hermicity of the Dirac Hamiltonian, and it means that phase factors for A and B atoms can be considered conjugated at any given unit cell. If atomic positions are explicitly known, one can determine the extent to which phases of atoms A and B cease to be conjugated as the deviation from the origin of a phasor built up by adding $\boldsymbol{\delta}_i$ for atom A and $\boldsymbol{\delta'}_i$ for atom B which, as seen in Figure 31, are not necessarily equivalent:

$$\sum_{i=1}^{3}(\boldsymbol{\delta}_i + \boldsymbol{\delta}'_i) \neq 0. \tag{136}$$

The deviation of this phasor sum from zero is a direct numerical measure of "slow-varying strain" and of "distortions preserving sublattice symmetry."

One has to preserve crystal symmetry for reciprocal space to exist, so when crystal symmetry is strongly perturbed, the reciprocal space representation starts to lack physical meaning, presenting a limitation to the semiclassical theory, including ours. Lack of sublattice symmetry may not allow proper phase conjugation of pseudospin Hamiltonians at unit cells undergoing very large mechanical deformations. Nevertheless, one must realize that this check cannot proceed on a description of the theory within a continuum media, because by construction there is no direct reference to actual atoms on a continuum.

One can disgress further: in mechanics of continuum media, there is always a suitable spatial scale in which a mechanical distortion appears homogeneous enough. Therefore, it is not possible to assess sublattice symmetry on a continuum, and proper phase conjugation of pseudospin Hamiltonians H_{ps} is an implicit assumption of that theory. Indeed, as a matter of definition there is no explicit information of interatomic distances on a continuum media, and continuum elasticity is based on a pillar known as

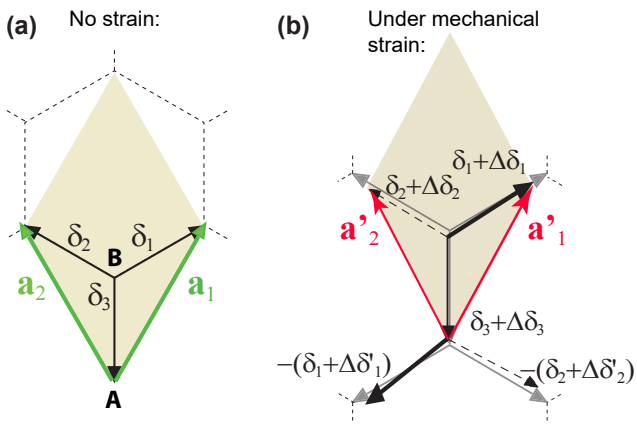

Figure 31. (a) Definitions of geometrical parameters in a unit cell. (b) Sublattice symmetry relates to how pairs of nearest-neighbor vectors (either in thick, or dashed lines) are modified due to strain. Reproduced from Ref. [109] with permission.

Cauchy-Born rule, which essentially means that the deformation field is followed at all spatial scales, even within a single unit cell. In reality, such assumption may break down [286].

4.9.2. Derivation of strain-induced gauges. Consider the unit cell before (Figure 31(a)) and after arbitrary strain has been applied (Figure 31(b)). For easier comparison of our results, the starting structure coincides with Figure 1, and with those shown in Refs. [6] and [128].

When mechanical strain is applied (Figure 31(b)), each local pseudospin Hamiltonian will only have physical meaning at the unit cells where:

$$\Delta\boldsymbol{\delta}'_j \simeq \Delta\boldsymbol{\delta}_j (j = 1, 2). \tag{137}$$

Condition (137) can be re-expressed in terms of changes of angles $\Delta\alpha_j$ or lengths ΔL_j for pairs of nearest-neighbor vectors $\boldsymbol{\delta}_j$ and $\boldsymbol{\delta}'_j$ (solid and dashed lines are drawn in Figure 31(b) for better comparison):

$$(\boldsymbol{\delta}_j+\Delta\boldsymbol{\delta}_j)\cdot(\boldsymbol{\delta}_j+\Delta\boldsymbol{\delta}'_j) = |\boldsymbol{\delta}_j+\Delta\boldsymbol{\delta}_j||\boldsymbol{\delta}_j+\Delta\boldsymbol{\delta}'_j| \cos(\Delta\alpha_j), \tag{138}$$

$$sgn(\Delta\alpha_j) = sgn\left([(\boldsymbol{\delta}_j + \Delta\boldsymbol{\delta}_j) \times (\boldsymbol{\delta}_j + \Delta\boldsymbol{\delta}'_j)] \cdot \hat{k}\right). \tag{139}$$

In previous Equations, $\hat{k}$ is a unit vector along the z-axis, sgn is the sign function ($sgn(a) = +1$ if $a \geq 0$ and $sgn(a) = -1$ if $a < 0$), and:

$$\Delta L_j \equiv |\boldsymbol{\delta}_j + \Delta\boldsymbol{\delta}_j| - |\boldsymbol{\delta}_j + \Delta\boldsymbol{\delta}'_j|. \tag{140}$$

Preservation of sublattice symmetry [128] requires that $\Delta L_j \simeq 0$ and $\Delta\alpha_j \simeq 0$ ($j = 1, 2$). Forcing sublattice symmetry to hold from the start amounts to introducing an artificial mechanical constraint on the atomistic lattice.

The next task consists in determining how reciprocal lattice vectors change to first order in displacements under mechanical load. In order for reciprocal lattice vectors to make sense at each unit cell, Equation (137) must hold ($\Delta\alpha_j$ and ΔL_j are all close to zero). In that case one sets $\Delta\boldsymbol{\delta}'_j \to \Delta\boldsymbol{\delta}_j$ for $j = 1, 2$, and define the change in lattice vectors as follows:

$$\Delta\mathbf{a}_1 \equiv \Delta\boldsymbol{\delta}_1 - \Delta\boldsymbol{\delta}_3, \tag{141}$$

$$\Delta\mathbf{a}_2 \equiv \Delta\boldsymbol{\delta}_2 - \Delta\boldsymbol{\delta}_3, \tag{142}$$

or in terms of (two-dimensional) components:

$$\Delta\mathcal{A} \equiv \begin{pmatrix} \Delta\delta_{1x} - \Delta\delta_{3x} & \Delta\delta_{2x} - \Delta\delta_{3x} \\ \Delta\delta_{1y} - \Delta\delta_{3y} & \Delta\delta_{2y} - \Delta\delta_{3y} \end{pmatrix}. \tag{143}$$

The matrix $\mathcal{A}$ changes to $\mathcal{A}' = \mathcal{A} + \Delta\mathcal{A}$ and $\mathcal{A}'^{-1}$ becomes to first order in displacements:

$$\mathcal{A}'^{-1} = (1+\mathcal{A}\Delta\mathcal{A})^{-1}(\mathcal{A}^{-1}) \simeq \mathcal{A}^{-1} - \mathcal{A}^{-1}\Delta\mathcal{A}\mathcal{A}^{-1}. \tag{144}$$

This way, the reciprocal lattice vectors are renormalized by:

$$\Delta\mathcal{B} = -2\pi \left(\mathcal{A}^{-1}\Delta\mathcal{A}\mathcal{A}^{-1}\right)^T. \tag{145}$$

This additional term was missed in Ref. [226], where the theory was expressed on a continuum (see Refs. [52, 148] too). Equation (145) can be employed to calculate the shifts of the $K-$points due to strain, and $\mathbf{K}$ requires the following additional contribution [109]:

$$\Delta\mathbf{K} = -\frac{4\pi}{3a_0^2}\left(\Delta\delta_{1x} - \Delta\delta_{2x}, \frac{\Delta\delta_{1x} + \Delta\delta_{2x} - 2\Delta\delta_{3x}}{\sqrt{3}}\right), \tag{146}$$

where $\delta_{i,j}$ is the $j-$component of vector $\boldsymbol{\delta}_i$. Given that $\Delta K' = -\Delta\mathbf{K}$ [109], one finds that the K ($\mathbf{K}$) and K' ($-\mathbf{K}$) points shift in opposite directions, as expected [41, 128].

Equation (137) provides a numerical assessment for mechanical strain that varies smoothly on the scale of interatomic distances and does not break the sublattice symmetry [128]. On the other hand, arbitrary strain breaks down to some extent the periodicity of the lattice, and "short-range" strain can be identified to occur at unit cells where $\Delta\alpha_j$ and ΔL_j cease to be zero by significant margins.

This observation provides the rationale to next express strain-created gauge fields without ever leaving the atomic lattice: When $\Delta\boldsymbol{\delta}'_j \simeq \Delta\boldsymbol{\delta}_j$ at each unit cell a mechanical distortion can be considered "long-range," and the first-order theory is valid. The process to lay down the gauge terms to first order is now described. Local gauge fields can be computed as low energy approximations to the following 2×2 pseudospin Hamiltonian:

$$\begin{pmatrix} E_{s,A} & g^* \\ g & E_{s,B} \end{pmatrix}, \tag{147}$$

with $g \equiv -\sum_{j=1}^{3}(t + \delta t_j)e^{i(\boldsymbol{\delta}_j+\Delta\boldsymbol{\delta}_j)\cdot(\mathbf{K}+\Delta\mathbf{K}+\mathbf{q})}$.

Keeping exponents to first order, one has that:

$$(\boldsymbol{\delta}_j + \Delta\boldsymbol{\delta}_j)\cdot(\mathbf{K}+\Delta\mathbf{K}+\mathbf{q}) \simeq \boldsymbol{\delta}_j\cdot\mathbf{K} + \boldsymbol{\delta}_j\cdot\Delta\mathbf{K} + \Delta\boldsymbol{\delta}_j\cdot\mathbf{K} + \boldsymbol{\delta}_j\cdot\mathbf{q}. \quad (148)$$

The exponent is next expressed to first-order:

$$e^{i(\boldsymbol{\delta}_j\cdot\mathbf{K}+\boldsymbol{\delta}_j\cdot\Delta\mathbf{K}+\Delta\boldsymbol{\delta}_j\cdot\mathbf{K}+\boldsymbol{\delta}_j\cdot\mathbf{q})} \simeq ie^{i\boldsymbol{\delta}_j\cdot\mathbf{K}}\boldsymbol{\delta}_j\cdot\mathbf{q} + e^{i\boldsymbol{\delta}_j\cdot\mathbf{K}}[1+i(\boldsymbol{\delta}_j\cdot\Delta\mathbf{K}+\Delta\boldsymbol{\delta}_j\cdot\mathbf{K})], \quad (149)$$

and explicit calculation yields [109]:

$$\sum_{j=1}^{3} e^{i\boldsymbol{\delta}_j\cdot\mathbf{K}}[1+i(\boldsymbol{\delta}_j\cdot\Delta\mathbf{K}+\Delta\boldsymbol{\delta}_j\cdot\mathbf{K})] = 0. \quad (150)$$

The term linear on $\Delta\mathbf{K}$ on Equation (150) cancels out the fictitious $K-$point dependent gauge fields proposed in Ref. [226], which originated from the term linear on $\Delta\boldsymbol{\delta}_j$ in this same equation. Equation (150) is a consistency check for the discrete formulation of the theory made completely in the atomistic lattice.

In the presence of strain, Equation (147) takes the following form in the low-energy regime:

$$H_{ps} = \begin{pmatrix} 0 & t\sum_{j=1}^{3} ie^{-i\mathbf{K}\cdot\boldsymbol{\delta}_j}\boldsymbol{\delta}_j\cdot\mathbf{q} \\ -t\sum_{j=1}^{3} ie^{i\mathbf{K}\cdot\boldsymbol{\delta}_j}\boldsymbol{\delta}_j\cdot\mathbf{q} & 0 \end{pmatrix} + \begin{pmatrix} E_{s,A} & -\sum_{j=1}^{3}\delta t_j e^{-i\mathbf{K}\cdot\boldsymbol{\delta}_j} \\ -\sum_{j=1}^{3}\delta t_j e^{i\mathbf{K}\cdot\boldsymbol{\delta}_j} & E_{s,B} \end{pmatrix}, \quad (151)$$

with the first term on the right-hand side reducing to the standard pseudospin Hamiltonian in the absence of strain. The change of the hopping parameter t is related to the variation of length, as explained in Refs. [6] and [152]:

$$\delta t_j = -\frac{|\beta|t}{a_0^2}\boldsymbol{\delta}_j\cdot\Delta\boldsymbol{\delta}_j. \quad (152)$$

This way, Equation (151) becomes:

$$\mathcal{H}_{ps} = \hbar v_F\boldsymbol{\sigma}\cdot\mathbf{q} + \begin{pmatrix} E_{s,A} & f_1^* \\ f_1 & E_{s,B} \end{pmatrix}, \quad (153)$$

with $f_1^* = \frac{|\beta|t}{2a_0^2}[2\boldsymbol{\delta}_3\cdot\Delta\boldsymbol{\delta}_3 - \boldsymbol{\delta}_1\cdot\Delta\boldsymbol{\delta}_1 - \boldsymbol{\delta}_2\cdot\Delta\boldsymbol{\delta}_2 + \sqrt{3}i(\boldsymbol{\delta}_2\cdot\Delta\boldsymbol{\delta}_2 - \boldsymbol{\delta}_1\cdot\Delta\boldsymbol{\delta}_1)]$, and $\hbar v_F \equiv \frac{\sqrt{3}a_0 t}{2}$. The parameter f_1 can be expressed in terms of a vector potential: A_s $f_1 = -\hbar v_F\frac{eA_s}{\hbar}$. This way:

$$A_s = -\frac{|\beta|\phi_0}{\pi a_0^3}[\frac{2\boldsymbol{\delta}_3\cdot\Delta\boldsymbol{\delta}_3 - \boldsymbol{\delta}_1\cdot\Delta\boldsymbol{\delta}_1 - \boldsymbol{\delta}_2\cdot\Delta\boldsymbol{\delta}_2}{\sqrt{3}} - i(\boldsymbol{\delta}_2\cdot\Delta\boldsymbol{\delta}_2 - \boldsymbol{\delta}_1\cdot\Delta\boldsymbol{\delta}_1)]. \quad (154)$$

In the absence of a full Poisson solver, one may estimate the diagonal entries [152] in Equation (147) as follows [109]:

$$E_{s,A} = -\frac{0.3eV}{0.12}\frac{1}{3}\sum_{j=1}^{3}\frac{|\boldsymbol{\delta}_j - \Delta\boldsymbol{\delta}_j| - a_0/\sqrt{3}}{a_0/\sqrt{3}}, \quad (155)$$

and

$$E_{s,B} = -\frac{0.3eV}{0.12}\frac{1}{3}\sum_{j=1}^{3}\frac{|\boldsymbol{\delta}_j - \Delta\boldsymbol{\delta}'_j| - a_0/\sqrt{3}}{a_0/\sqrt{3}}. \quad (156)$$

These entries represent the scalar deformation potential, which are taken to linear order in the average bond increase [163]. In numerical calculations, the deformation potential given by these entries tends to be asymmetric within the A and B sublattices, which gives rise to a mass term [109, 170].

The derivations are completed with the following, second, consistency check. In the absence of significant curvature, the continuum limit is achieved when $\frac{|\Delta\boldsymbol{\delta}_j|}{a_0} \to 0$ (for $j = 1, 2, 3$). One then has (Cauchy-Born rule): $\boldsymbol{\delta}_j\cdot\Delta\boldsymbol{\delta}_j \to \boldsymbol{\delta}_j\begin{pmatrix} \bar{\epsilon}_{xx} & \bar{\epsilon}_{xy} \\ \bar{\epsilon}_{xy} & \bar{\epsilon}_{yy} \end{pmatrix}\boldsymbol{\delta}_j^T$, where $\bar{\epsilon}_{ij}$ are the entries of the strain tensor.

This way Equation (154) becomes:

$$A_s \to \frac{|\beta|\phi_0}{2\sqrt{3}\pi a_0}(\bar{\epsilon}_{xx} - \bar{\epsilon}_{yy} - 2i\bar{\epsilon}_{xy}), \quad (157)$$

as expected [6, 128].

Besides representing a consistent first-order formalism, the discrete approach may be especially suited for the analysis of "raw" atomistic data –obtained, for example, from molecular dynamics simulations: the relevant equations (154, 155, 156) take as input the changes in atomic positions upon strain directly. An important observation is that the number of pseudospinors one can define in the discrete approach is finite: $N/2$ space-modulated pseudospinor Hamiltonians can be built for a graphene membrane having N atoms. This is a consequence of a formalism that is inherently bound to (and never leaves) the discrete atomistic lattice.

Some examples of the predictions from the discrete approach concerning strain gauges are presented in Figure 32; see Refs. [108, 109, 284] too. The main contribution from Figure 32 is the discrete pseudomagnetic field resolved over individual atoms, and the estimation of the deformation potential E_s.

It becomes convenient to bring to attention a subtle point concerning the nature of the distortions of the graphene lattice. The point is that a rippled graphene membrane may require a certain degree of load in order to iron-out ripples and start accumulating actual tensile strain. This point is emphasized in Figure 33 [109], which has a dependence consistent with experiments of graphene under load. Additional mechanical and energetic issues concerning graphene suspended on small holes have been addressed by Verbiest and coworkers in the recent past too [287]. Now that the consistency (and insight) gained from the discrete approach has been discussed, we wish to present some mathematical constructions that

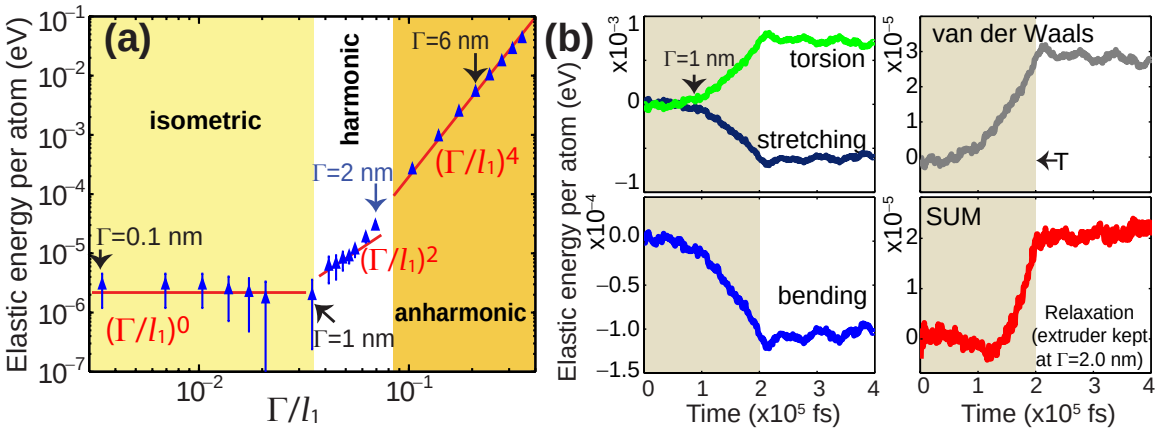

Figure 33. (a) The elastic energy versus indentation displays three distinct regimes: (i) isometric, where the membrane follows an extruder with no change in energy in a deformation that mostly modifies angles among atoms, but not their separation, (ii) a harmonic distortion, and (iii) the non-linear regime with a force (energy) proportional to the third- (fourth-)power of the indentation, c.f., Figure 7 and Equation (45). The isometric regime is customarily neglected in the literature, but it could exist on graphene membranes with plies or other corrugations that are "ironed out" prior to the actual creation of strain. (b) The decomposition of the elastic energy indicates that bending requires an energy that is an order of magnitude smaller than that required to stretch a Carbon-Carbon bond. Reproduced from Ref. [108] with permission. Copyrighted by the American Physical Society.

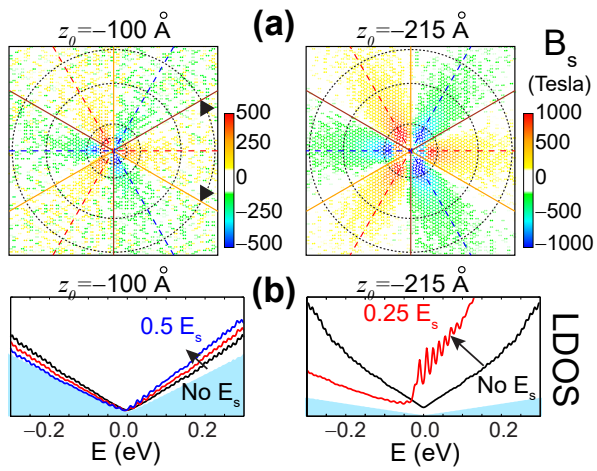

Figure 32. (a) B_s for $z_0 = -100$ and -215 Å loads. (b) LDOS with screened values of the deformation potential E_s at $r = 0$, for $z_0 = -100$ and -215 Å. Reproduced from Ref. [284] with permission. Copyrighted by the American Physical Society.

are common in describing meshes that find a niche application in two-dimensional crystals.

4.9.3. Further discussion of the discrete geometry The local geometry of a two-dimensional (2D) surface is determined by four invariants of its metric (g) and curvature (k), that indicate how much it stretches and curves with respect to a reference non-deformed shape. Suitable choices are the determinant and the trace of g, the Gauss curvature $K \equiv \det(k)/\det(g)$, and the mean curvature $H \equiv Tr(k)/(2Tr(g))$.

In the existing literature, graphene's geometry is commonly studied in terms of a continuous displacement field $\epsilon_\alpha(\xi^1, \xi^2)$. Specifically, on thin-plate continuum elasticity the strain tensor is $\epsilon_{\alpha\beta} = (\partial_\alpha\epsilon_\beta + \partial_\beta\epsilon_\alpha + \partial_\alpha\epsilon_\beta\partial_\beta\epsilon_\alpha + \partial_\alpha z\partial_\beta z)/2$, with z an out-of-plane elongation. There, differential geometry and mechanics couple as:

$$g_{\alpha\beta} = \delta_{\alpha\beta} + 2\epsilon_{\alpha\beta}, \qquad k_{\alpha\beta} = \hat{\mathbf{n}} \cdot \frac{\partial \mathbf{g}_\alpha}{\partial \xi^\beta}, \tag{158}$$

where $\mathbf{g}_\alpha(\xi^1, \xi^2)$ is a tangent vector field, $\delta_{\alpha\beta}$ is the reference (flat) metric and $\hat{\mathbf{n}} = \frac{\mathbf{g}_{\xi^1} \times \mathbf{g}_{\xi^2}}{|\mathbf{g}_{\xi^1} \times \mathbf{g}_{\xi^2}|}$ is the local normal. The point is that, since the graphene lattice is a collection of atoms joined by chemical bonds, is it possible to furnish a geometry for deformed graphene that does not require transforming the atomistic lattice into an artificial continuum.

Using the atomistic lattice in Figure 34(a-b), the discrete metric is defined from the local lattice vectors $\mathbf{a}_\alpha$ [284, 288] $g_{\alpha\beta} = \mathbf{a}_\alpha \cdot \mathbf{a}_\beta$, and the discrete Gauss curvature (K_D) originates from the angle defect $\sum_{i=1}^{6} \theta_i$ [283, 289]:

$$K_D = (2\pi - \sum_{i=1}^{6} \theta_i)/A_p. \tag{159}$$

Here θ_i ($i = 1, ..., 6$) are angles between vertices shown in Figure 34(a). The Voronoi tessellation shown in dark blue in Figure 34(a) with an area A_p generalizes the Wigner-Seitz unit cell on conformal 2D geometries. As a consitency check, it may be noted that the angle defect adds up to 2π on a flat surface, making the Gaussian curvature $K_D = 0$, as expected.

The discrete mean curvature H_D measures relative orientations of edges and normal vectors along a closed

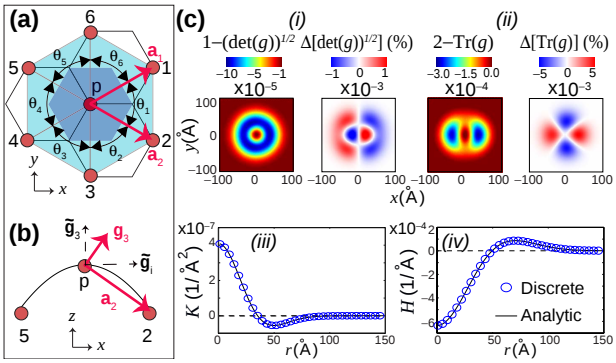

Figure 34. (a) Top view of polyhedra used to determine the four geometrical invariants from the metric and curvature. Circles represent atoms on the A-sublattice. Local lattice vectors are $\mathbf{a}_1$ and $\mathbf{a}_2$; θ_i are internal angles to edges $\mathbf{e}_i$ and $\mathbf{e}_{i+1}$; and the central shaded hexagon is the Voronoi cell. (b) Side view highlights the differences between continuum and discrete vector fields. (c) i: $\sqrt{\det(g)}$, ii: $Tr(g)$, iii: K and iv: H for a smooth gaussian bump where discrete and continuum results coincide. Percent differences $\sqrt{\det(\tilde{g})} - \sqrt{\det(g)}$ and $Tr(\tilde{g}) - Tr(g)$ are also shown. Reproduced from Ref. [284] with permission. Copyrighted by the American Physical Society.

path:

$$H_D = \sum_{i=1}^{6} \mathbf{e}_i \times (\boldsymbol{\nu}_{i,i+1} - \boldsymbol{\nu}_{i-1,i}) \cdot \hat{\mathbf{n}}/4A_p. \tag{160}$$

Here, $\mathbf{v}_i$ is the position of atom i on sublattice A, and $\mathbf{e}_i = \mathbf{v}_i - \mathbf{v}_p$ is the edge between points p and i (note that $\mathbf{a}_{1(2)} = \mathbf{e}_{1(2)}$). $\boldsymbol{\nu}_{i,i+1}$ is the normal to edges $\mathbf{e}_i$ and $\mathbf{e}_{i+1}$ (i is a cyclic index), and $\hat{\mathbf{n}} = \frac{\sum_{i=1}^{6} \boldsymbol{\nu}_{i,i+1} A_i}{\sum_{i=1}^{6} A_i}$ is the area-weighted normal with $A_i = |\mathbf{e}_i \times \mathbf{e}_{i+1}|/2$ [283]. For the purposes of discrete geometry, the metric and curvatures are formally decoupled objects.

As discussed in Ref. [288] and Figure 36, the discrete geometry readily admits generalization to deal with samples that have atomistic defects.

The discrete metric and curvatures furnish geometry consistent with a crystalline structure, and lead to the faithful characterization of graphene's morphology beyond the effective-continuum paradigm, Equation (158). This may be advantageous when the atomic conformation is known, as a fitting of the atomic lattice onto an effective continuum is not needed. The discrete geometry is accurate regardless of elastic regime, hence it can be used to verify whether the conditions for continuum elasticity hold in the problem at hand, and the geometrical distortion shown in Figure 35 leads to the strain-derived gauge fields presented in Figure 32.

Some results on a system where the concepts learned in this section make plenty of sense are next showcased. In molecular graphene [196], CO molecules are employed to establish a triangular, insulating, lattice. Interstitials among CO atoms create

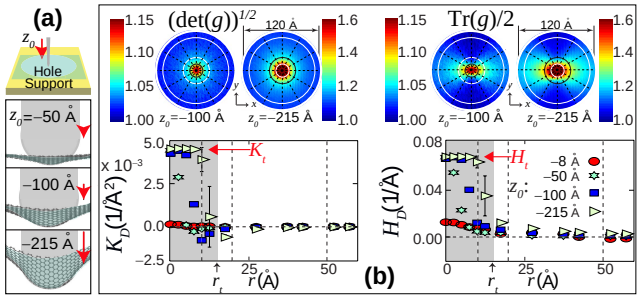

Figure 35. (a) Graphene under load by a semi-spherical tip of radius $r_t = 15$ Å. (b) Geometrical invariants as the indentation proceeds. Under load, the metric increases unbounded, yet curvatures can only saturate to K_t and H_t as graphene conforms to the tip (see flat horizontal lines $K_D = K_t$ and $H_D = H_t$, for $0 \leq r \lesssim r_t$ at $z_0 = -100$ and -215 Å). Reproduced from Ref. [284] with permission. Copyrighted by the American Physical Society.

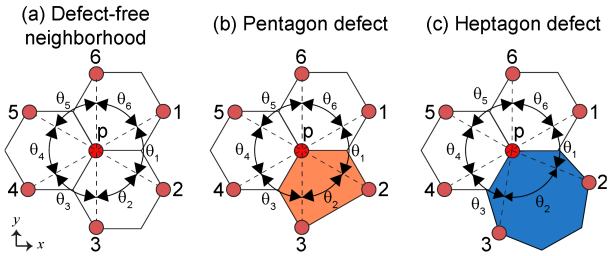

Figure 36. The neighborhood of an atom changes upon appearance of topological defects. (a) Neighborhood with no topological defects. The more common defects are: (b) a pentagon defect, (c) a heptagon defect, or a combination of (b) and (c). Reproduced from Ref. [288] with permission. Copyright 2014 American Chemical Society.

conducting paths whose intersections conform what is known as a dual lattice [283]. Those intersections conform the so-called "artificial graphene" lattice.

One first determines whether it is possible to define the honeycomb, dual lattice (artificial graphene lattice), under arbitrary strain. To be concise, a honeycomb lattice can be locally defined only when the number of "atoms," or intersections, is conserved.

To visualize this idea, Figure 37 shows the evolution of a triangular lattice and its dual, the honeycomb one, under a horizontal shear strain. The direct (triangular) lattice is shown in black circles and thin black lines, while its dual is shown in white or red dots, and edges appear in thicker black lines. Color was employed to distinguish neighboring honeycombs in the dual lattice. The point is that the honeycomb (artificial graphene) lattice in this case is a geometrical construct realized by bisecting lines, and it is therefore not subject to force minimization processes that would take place on actual graphene.

At the undeformed configuration (subplot 37(a))

one notes the existence of two white circles per black circle; these two white circles represent the A and B sublattice sites on the (dual) honeycomb lattice that is seen as (golden) conducting paths in Ref. [196].

As seen in Figure 37(b), when shear is introduced onto the triangular CO lattice, a pair of neighbouring intersections of (bold black) bisectors (artificial atoms) come closer together. As shear reaches the point in which atoms on the (initially triangular) lattice lie along vertical lines (Figure 37(c)), the lattice becomes rectangular, and the two "atoms" on the dual lattice collapse into one. This means that the number of "atoms" may be ill-defined, which essentially means that no pseudospin Hamiltonians (which require two atoms, or sublattices) can be defined at these unit cells.

The observation made in previous paragraph cannot be reached when working with a continuum approximation of the system: in that formalism one would never be able to discuss the collapse of the Honeycomb lattice, providing another example of how the discrete approach may be insightful. A natural question to ask now is whether the considerations in the present paragraph are of any consequence for experiment [196].

And they are. In Figure 39 the experimental STM images of molecular graphene are shown [196]. The (dual) lattice is superimposed in red, and it follows all conducting (golden) paths, exactly.

In Ref. [128], it was shown that a finite displacement field of the form:

$$\Delta \mathbf{r} = q(2xy, (x^2 - y^2)), \tag{161}$$

applied to a honeycomb lattice leads to a constant pseudo-magnetic field. But it is not the honeycomb lattice, but the triangular CO lattice the one that is directly available to experiment [196] and set up following the prescription given by Equation (161). Thos displacements do not lead to a honeycomb lattice consistent with Equation (161):

The direct (CO, triangular) and dual (honeycomb) lattices transform by different amounts. The process leading to the dual lattice is illustrated in Figure 38. There, the "atom" positions obtained by applying the strain field to the honeycomb lattice seen as Figure 39(a) are shown as green open circles. Actual locations obtained when the strain field is applied to the triangular lattice, leading to an excellent match to experiment, are shown by the red motifs.

As indicated in previous paragraphs, it is the (direct) triangular lattice that is directly accessible in the experiment [196], and the hexagonal (dual) lattice reaccommodates in response to the changes to the direct lattice. The artificial graphene lattice shown as golden conducting paths is a Voronoi tessellation of the triangular lattice. Using imaging processing techniques, it is possible to determine the center of the black CO molecules, and to determine the connections that are shown in red in Figure 39. Note that the Voronoi tessellation shown in red follows the conducting paths in the experimental data extraordinarily well.

To further demonstrate that the displacement field in Equation (161) was directly applied to the CO molecules and not to the artificial graphene lattice, one can superimpose the dual hexagonal lattice onto the experimental image when the triangular lattice is displaced following Equation (161) for $q = 0$, $q = 5$, and $q = 10 \times 10^{-4}$ Å^{-1}, which leads to a remarkable agreement.

The red arrows in Figure 39 start at "atomistic" locations predicted when the displacement given by Equation (161) is applied to the dual lattice, and end at the actual "atomistic" locations seen in experiment. Those arrows thus indicate the actual deviation from a strain pattern that should lead to a constant magnetic field. We note that, in experiment, the magnetic field was only ascertained at the origin, which is the only spatial location where the density of states were reported [196].

In addition, and as it was foreseen in Figure 37, the number of "atoms" begins to decrease at the largest amounts of strain. This is emphasized within yellow circles, where two atomic positions collapse into one. Pseudospin Hamiltonians are not properly defined at these locations any more.

At unit cells where such collapse has not taken place, it is possible to assess preservation of sublattice symmetry by adding vectors joining neighboring atoms. This is done in Figure 38, where the vectors joining nearest neighbouring atoms are shown at the unit cell shown in light green. These vectors do not add up to zero, and the amount to which they deviate from one another is directly related to the amount in which sublattice symmetry is not preserved in the system. It is remarkable that no such analisis based on the evident discreteness of the experimental system, and which lends itself to an increased insight, has been provided to date.

4.9.4. Open directions within the discrete approach. The exposition of the discrete approach is closed with a short discussion of an open avenue for further exploration. Given that the model is laid out to describe arbitrary strain, it is desirable to generalize these concepts to include back-scattering. As a starting point, this could be done by enhancing the present description to include cross-terms among inequivalent $K-$points.

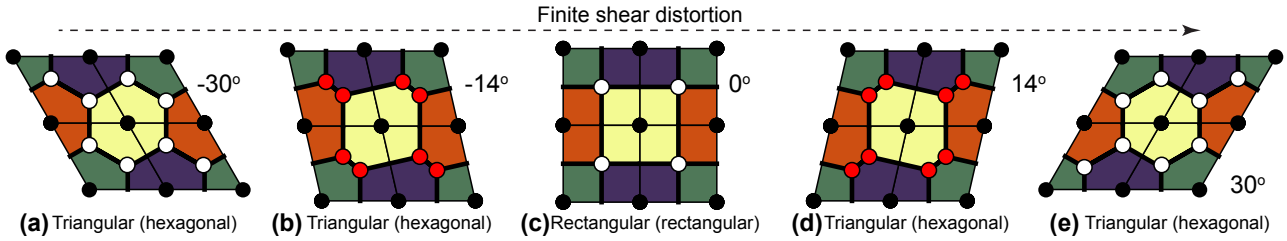

Figure 37. A shear distortion converts a triangular lattice onto a rectangular one, and the dual from hexagonal to rectangular: The number of "atoms" in the dual lattice (white and red circles) is not preserved. There are four atoms in the dual lattice in plot (c), and eight in all the others. This gradual collapse of the atoms on the dual lattice is highlighted by the red circles in (b) and (d). Image courtesy of Bradley Klee.

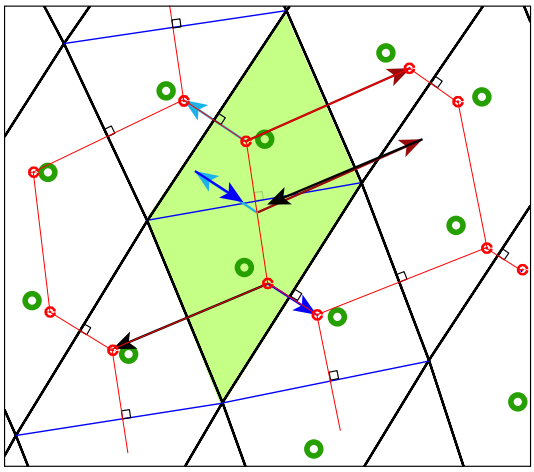

Figure 38. A zoom-in that demonstrates the construction leading to atomistic positions. Intersections of blue and black lines are positions of CO molecules obtained from Ref. [196]. The red lines bisect the triangular lattice, and lead to the Voronoi tessellation resulting in the honeycomb lattice. As described in Figure 31, the amount to which nearest-neigbouring atoms deviate from one another, is related to the extent to which sublattice symmetry is violated at any given unit cell. The discrete approach is thus properly suited to unveil inherent assumptions of the continuum approach to strain in graphene.

4.10. Results from density-functional theory

Ab-initio or first principles methods are becoming more accessible due to the availability of fast computers. One of the most used ab-initio methods is based on the Density Functional Theory (DFT) which can be traced to 1964 with a manuscript by Hohenberg and Kohn in which the ground state of an interacting electron gas is obtained through an electron density universal functional [290]. This work lead to the important theorem which establishes that for any system of interacting particles in an external potential, the external potential is uniquely determined by the ground state density (charge density). This theory was latter generalized by Levy [291]. Therefore, under the DFT approach, the total energy can be expressed as:

$$E(\rho) = K(\rho) + U(\rho) + E_{ex}(\rho), \tag{162}$$

where $K(\rho)$ is the kinetic energy of a system of noninteracting particles of density ρ, $U(\rho)$ is the classical electrostatic energy due to coulombic interactions, and $E_{ex}(\rho)$ is a term that includes the exchange and correlation energies in addition to other many-body contributions. Note that all the terms depend on the charge density.

In order to compute the third term of the above equation, certain approximations are needed, the simplest approximation is the Local Density approximation (LDA) which mainly comes from the exchange-correlation energy of a uniform electron gas [292, 293, 294]. The LDA approach can be improved to include inhomogeneous effects of the electron gas by implementing a gradient expansion of the density, leading to the non local spin density approximation (NLSD) or gradient corrected approximation [294, 295, 296, 297].

In order to be able to apply the DFT approach to the lattice dynamics of a system, density functional perturbation theory (DFPT) has been developed: In this method, the second derivative of the total energy with a given perturbation is computed. Depending on the perturbation, different properties can be obtained, for example, if the perturbation is in the ionic positions, phonon dispersions can be obtained, if the perturbation is in the unit cell vectors, elastic constants can be calculated [298, 299, 300].

Nowadays it is possible to perform DFT calculations on thousands of atoms systems to understand their electronic, mechanical, vibrational and chemical properties and graphene is not the exception. Graphene band structure has been calculated by DFT since the beginning of carbon nanotube research in the 1990's in order to understand not only these amazing 1-D tubular structures [301]. Moreover, other carbon allotropes such as Fullerenes [302] and 3-D systems known as Schwarzites [303, 304] have also been studied with DFT.

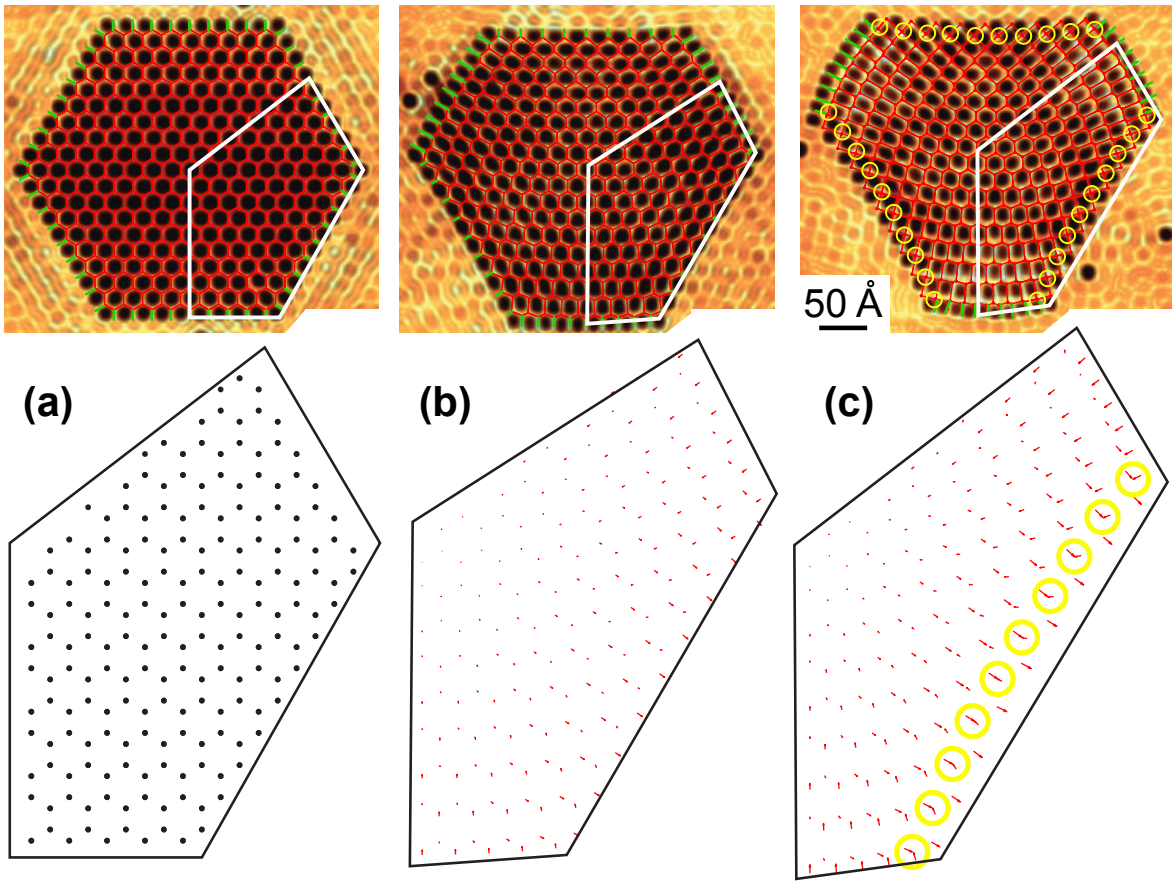

Figure 39. Upper row: Evolution of the honeycomb (dual) lattice ("artificial graphene") as the (direct) triangular lattice is displaced following Equation (161), for (a) $q = 0$, (b) $q = 5$, and (c) $q = 10 \times 10^{-4}$ Å^{-1}. Experimental data is shown for direct comparison [196]. The (dual) hexagonal lattice does not follow the displacement field given in Equation (161) –red arrows are corrections to actual crossings– and as a result, the pseudomagnetic field is not quite constant. Vectors within yellow circles in (c) highlight the collapse of "atoms" positions onto a single point, which means that the number of "atoms" is not preserved any more. None of these conclusions could have been reached within the continuum approach. Experimental data was adapted by permission from Macmillan Publishers Ltd. from Ref. [196], copyright (2016). Voronoi tesselation courtesy of Bradley Klee.

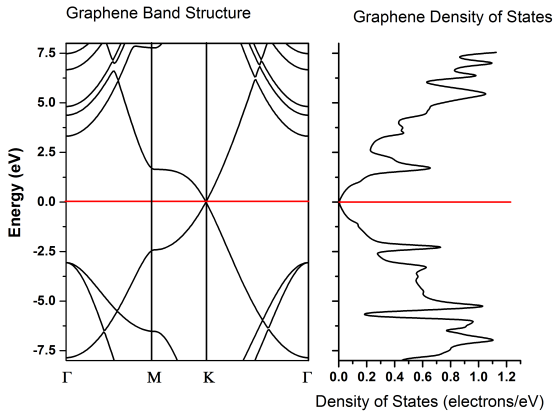

Figure 40. Band Structure and Density of States of Graphene calculated using DFT-LDA.

From the DFT-LDA graphene band structure and density of states (DOS) it is possible to appreciate their main features: the zero band gap at the $\boldsymbol{K}$ points in the Brillouin zone and the linear energy dispersion, closed to the $\boldsymbol{K}$ points (see figure of bands and DOS of DFT-LDA graphene Figure 40).

Also strain effects in graphene can be computed through DFT finding that the band gap is more sensitive to uniaxial strain than to bi-axial strain [305]. Some authors report a band gap opening under uniaxial strain of 12.2 % (parallel to the C-C bonds) up to 0.486 eV, and others with a combination of uniaxial strains report a gap opening of 1 eV [160]. However, the stability of graphene under these extreme strains should be carefully analyzed by DFPT to see if the phonon dispersion does not exhibit negative frequency values. DFT confirms that under uniaxial strain the symmetry of graphene is broken and under bi-axial strain the hexagonal lattice symmetry is

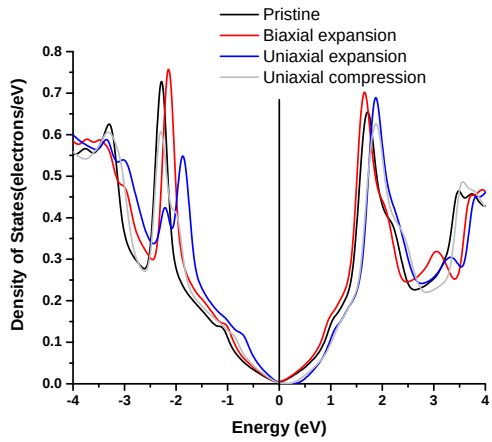

Figure 41. DFT calculation of the graphene density of states under strain. Uniaxial strain was applied in the zigzag direction using a compression of $\bar{s}_{xx} = 5.0\,\text{GPa}$ and a expansion $\bar{s}_{xx} = -5.0\,\text{GPa}$. The biaxial expansion used was $\bar{s}_{xx} = \bar{s}_{yy} = -5.0\,\text{GPa}$.

preserved. Figure 41 shows that when small biaxial strain is applied, the density of states (DOS) changes little around the $\boldsymbol{K}$ points, but when uniaxial strain is applied, noticeable changes in the DOS can be observed, even generating a small band gap. As will be seen in the Raman section of this review, the phonon dispersions are very sensitive to strain.

5. Optical properties

Experiments on the optical response of graphene indicate that its absorbance is uniquely expressed by the fine structure constant α, which has a more or less constant magnitude $\pi\alpha \approx 2.3\%$ over a broad range of frequencies from the far-infrared to the visible spectrum [306, 307]. Thus absorbance leads to a universal optical conductivity for graphene equal to $\sigma_0 = e^2/4\hbar$ for zero chemical potential, which is ultimately a consequence of the behaviour of charge carriers as massless Dirac fermions [166, 308, 309, 310, 311].

5.1. Strain engineering of optical absorption

The strain-induced anisotropy in the electron dynamics results in an anisotropic optical conductivity [130, 312, 313, 218, 158, 314, 315]. Combining the effective Dirac Hamiltonian (118) and the Kubo formula, the general expression for the optical conductivity tensor is [218, 219]:

$$\bar{\boldsymbol{\sigma}}(w) \simeq \sigma_0(w)\big(\bar{\boldsymbol{I}} - 2\tilde{\beta}\bar{\boldsymbol{\epsilon}} + \tilde{\beta}\text{Tr}(\bar{\boldsymbol{\epsilon}})\bar{\boldsymbol{I}}\big), \tag{163}$$

where $\sigma_0(w)$ is the (isotropic) frequency-dependent conductivity in the absence of strain [316].

For example, Equation (163) yields $\sigma_{\parallel,\perp}(w) = \sigma_0(w)(1 \mp \tilde{\beta}\epsilon(1+\nu))$ for uniaxial strain, where $\sigma_\parallel(\sigma_\perp)$ is the optical conductivity parallel (perpendicular) to the direction of the applied strain, ν is the Poisson's ratio and ϵ is the applied strain [130]. Note that the optical conductivity along the direction of the strain decreases while the transverse conductivity increases by the same amount. Thus, an increase of $\sigma_\perp$ helps explain the variation of waveguide transmission of hybrid graphene integrated microfibers elongated along their axial direction [317].

The strain-induced anisotropy of the optical absorption yields two effects: dichroism and modulation of the transmittance as a function of the polarization direction. For normal incidence of linearly polarized light upon strained graphene, the transmittance is given by (Equation (163) [131]):

$$T(\theta_i) \approx 1 - \pi\alpha\big(1 - \tilde{\beta}(\bar{\epsilon}_{xx} - \bar{\epsilon}_{yy})\cos 2\theta_i - 2\tilde{\beta}\bar{\epsilon}_{xy}\sin 2\theta_i\big), \tag{164}$$

whereas the dichroism effect is expressed by:

$$\theta_t - \theta_i \approx \alpha\tilde{\beta}\big(\frac{\bar{\epsilon}_{yy} - \bar{\epsilon}_{xx}}{2}\sin 2\theta_i + \bar{\epsilon}_{xy}\cos 2\theta_i\big), \tag{165}$$

where $\theta_i(\theta_t)$ is the incident (transmitted) polarization angle. Expressions (164) and (165) show π-periodic modulations respect to the incident polarization angle θ_i which are due to the physical equivalence between θ_i and $\theta_i + \pi$ for linearly polarized light at normal incidence.

Equation (164) yields $T(\theta_i) = 1 - \pi\alpha(1 - \tilde{\beta}(1+\nu)\epsilon\cos 2\theta_i)$ for uniaxial strain [130], where ϵ is the magnitude of strain, ν is the Poisson ratio and θ_i is measured with respect to the stretching direction. This periodic modulation of the transmittance as a function of polarization direction has been experimentally confirmed by measuring the modulation in the transmittance of visible light $\triangle T$ through strained graphene, and extracting the magnitude ϵ for uniaxial strain by means of $\epsilon \approx \triangle T/(2\pi\tilde{\beta}(1+\nu))$ by Raman spectroscopy measurements [318].

5.2. Raman spectrum to determine nanometre-scaled strain variations

Raman spectroscopy is an important technique to characterize layered materials because it is not invasive and is very sensitive to defects, number of layers, strain, curvature, doping, etc. In the context of carbon nanostructures, Raman spectroscopy has been used in Fullerenes [319], carbon nanotubes [320], and graphene [321, 322, 323, 324]. Carbon-based materials such as graphite, carbon nanotubes and graphene are characterized by three main Raman features: One signal around $1590\,\text{cm}^{-1}$ called the G band which is a first-order signal due to the in-plane vibrations of

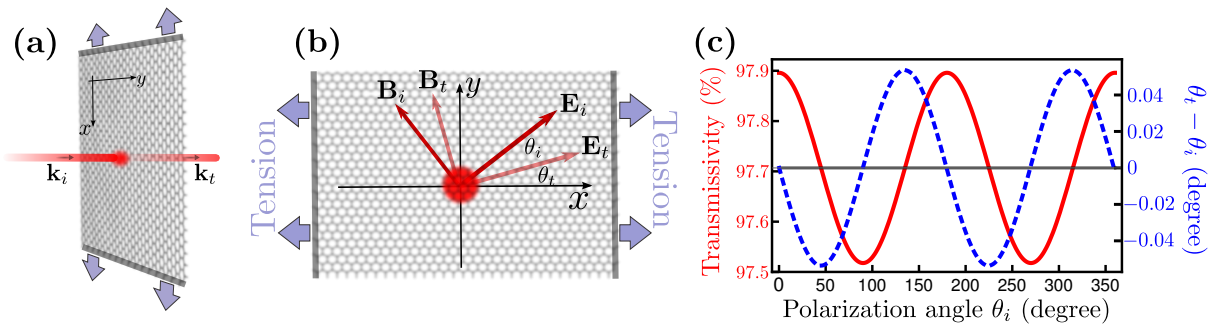

Figure 42. (a) Scattering of normal-incident linearly polarized light over strained graphene. (b) Schematic representation of the dichroism induced by the anisotropic absorption. The electromagnetic fields lie in the graphene plane. (c) Rotation of the transmitted field and transmittance as a function of the incident polarization angle for uniaxial strain with $\epsilon = 0.03$.

the carbon atoms (E_{2g} modes in graphite), another signal at around $1350\,\mathrm{cm}^{-1}$ called the $D-$band that originates from defects in the lattice, and a $2D$ band around $2700\,\mathrm{cm}^{-1}$.

The D and the $2D$ signals involve double (second order) resonance processes [321, 322, 323]: For the D band, intervalley electron scattering takes place involving a defect and a TO phonon around the K point in the first Brillouin zone (1BZ). For the $2D$ band, the double resonance does not involve defects but phonons around the $K-$ point in the 1BZ. One unique characteristic is that the $2D$ band exhibits a much higher intensity than the G band. These features are seen in Figure 43, where the Raman signal of pristine graphene is compared to that of nitrogen-doped graphene. Here, the D' signal –due to intravalley electron scattering by a defect involving a LO phonon– is observed too. On the other hand, the D and D' signals are greatly reduced in pristine graphene due a small amount of defects. Figure 44 shows the DFT phonon dispersion.

Symmetry becomes lowered when graphene is exposed to uniaxial tensile stress, and a shift to lower frequencies accompanied of a splitting of the LO and TO modes at the gamma point in the BZ is produced, giving rise to Raman bands G^+ and G^- [326, 155, 327]. Figure 45 shows a series of Raman spectra of graphene under uniaxial strain [326], and a DFT calculation shows the splitting in the phonon dispersion that is in agreement with experimental results. Also note that there is a shift of the phonons around the K towards lower frequencies under tensile stress,thus agreeing with the observed shifts of the $2D$ band. The Grüneisen parameters –that relate the rate of change of phonon frequencies with respect to strain– can be obtained from the Raman shifts under strain [155, 328].

Symmetry is preserved when uniform biaxial strain is applied, so there is no splitting of the G band (See 46), but only a shift towards lower frequencies in the case of tensile stress, and to higher frequencies

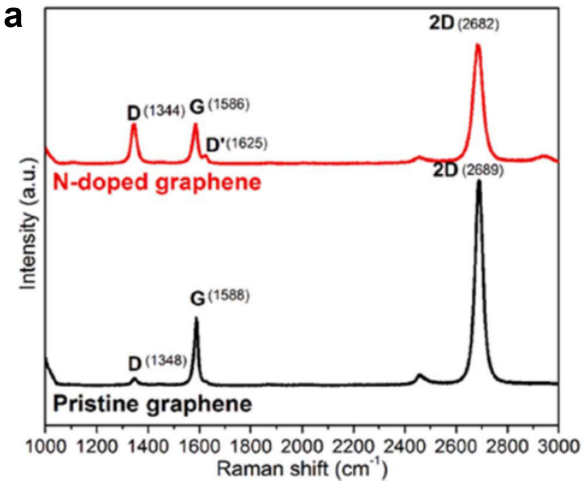

Figure 43. Experimental Raman espectra of nitrogen doped graphene and pristine graphene. Reproduced from Ref. [325] with permission.

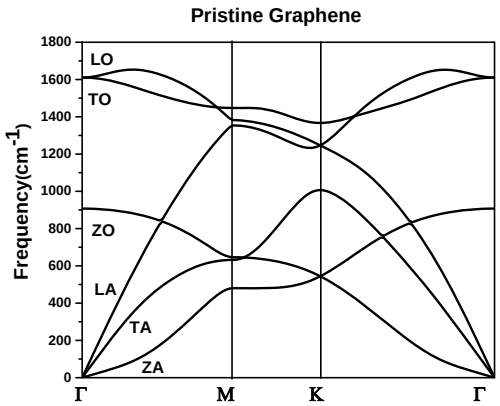

Figure 44. Density functional theory (DFT) calculation of the phonon dispersion of graphene highlighting the transverse, longitudinal and zero acoustic and optical modes.

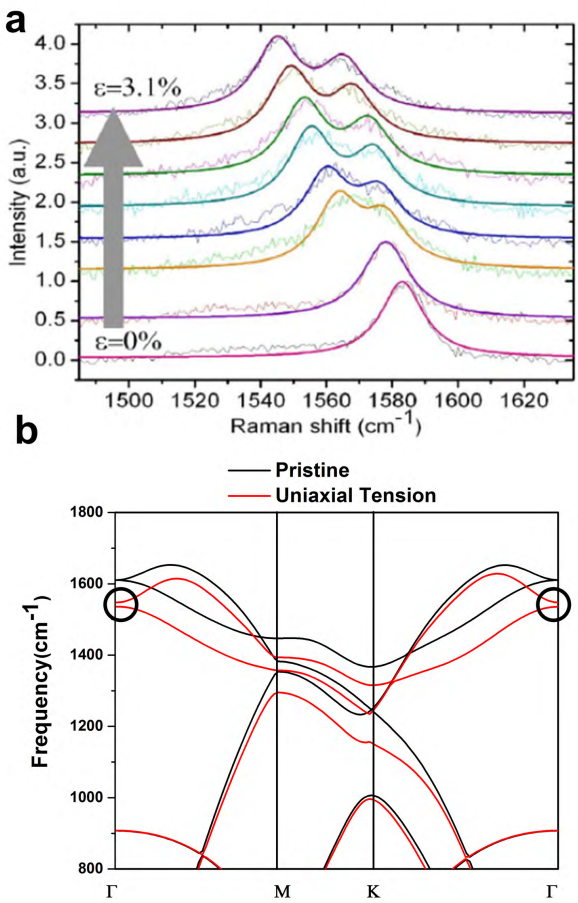

Figure 45. Graphene under uniaxial tensile strain: (a) Experimental Raman espectra of graphene under uniaxial tensile strain showing the splitting of the G band (reproduced from Reference [326]). (b) DFT calculation showing the shift and the splitting of graphene under uniaxial stress along the zigzag direction $\bar{s}_{xx} = -3.5\,\text{GPa}$ compared to pristine graphene (the black circles show the splitting at the Γ point in the 1BZ.

for compressive stress [155]. Raman spectroscopy also plays a crucial role in the characterization of other 2D materials such as transition metal dichalcogenides (TMDS) [329, 330, 331] and phosphorene [332, 333].

6. Strain in multi-layered graphene

Even though multi-layered graphene is not a truly 2D material, it can be studied with the techniques discussed so far for graphene. Layers can be stacked following different sequences that depend on the relative placement of the graphene's bipartite lattices A and B in different layers [334]. Nowadays, it is possible to control the stacking sequences, including the addition of other different layered materials to build nanocomposites [335]. For graphite, the most common stacking is known as Bernal stacking (see Figure 47(b)), where B atoms of layer 2 (B2) sit

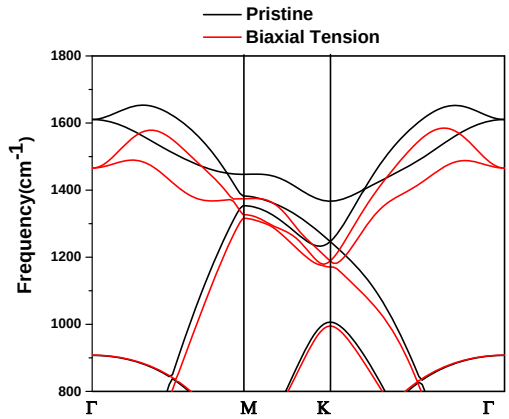

Figure 46. Graphene under biaxial tensile strain: DFT calculation showing the shift and the splitting of graphene under biaxial tensile stress $\bar{s}_{xx} = \bar{s}_{yy} = -3.5\,\text{GPa}$ compared to pristine graphene. Note that there are no splitting at the Γ point in the 1BZ.

directly on top of A atoms of layer 1 (A1), while B1 and A2 atoms are in the center of the hexagons of the opposing layers [336, 337]. In Figure 47(c) the structure of ABA trilayer graphene is presented as well.

The band structure of multilayered graphene can be understood using the Slonczewski-Weiss TB model for graphite [338]. Within this model, there is a hopping parameter t_0 as in monolayer graphene to account for the intra-layer interaction, as indicated in Figure 47(b) by arrows. For bilayer graphene, there are five hopping parameters γ_i with $i = 0, ..., 4$ to account for the different kinds of overlaps of Π-orbitals. Also, there are four on-site energies $\epsilon_{A1}, \epsilon_{B1}, \epsilon_{A2}, \epsilon_{A2}$ on the four atomic sites. As indicated in Figure 47(c), these parameters were determined by infrared spectroscopy [339], resulting in $t_0 = 3.16$ eV, $\gamma_1 = 0.381$ eV, $\gamma_3 = 0.38$ eV, $\gamma_4 = 0.14$ eV, $\epsilon_{B1} = \epsilon_{A2} = 0.022$ eV and $\epsilon_{A1} = \epsilon_{B2} = 0$. In trilayer graphene, two others parameters γ_2 and γ_5 are needed in addition.

The following 4×4 Hamiltonian matrix describes the single-particle electronic dispersion for bilayer graphene:

$$H = \begin{pmatrix} \epsilon_{A1} & -t_0 f(\boldsymbol{k}) & \gamma_4 f(\boldsymbol{k}) & -\gamma_3 f^*(\boldsymbol{k}) \\ -t_0 f^*(\boldsymbol{k}) & \epsilon_{B1} & \gamma_1 & \gamma_4 f(\boldsymbol{k}) \\ \gamma_4 f^*(\boldsymbol{k}) & \gamma_1 & \epsilon_{A2} & -t_0 f(\boldsymbol{k}) \\ -\gamma_3 f(\boldsymbol{k}) & \gamma_4 f^*(\boldsymbol{k}) & -t_0 f^*(\boldsymbol{k}) & \epsilon_{B2} \end{pmatrix} \quad (166)$$

where $f(\boldsymbol{k})$ is given by Equation (52). The four resulting bands are schematically represented in Figure 47(b); they red are parabolic and touch without a gap within this single-particle picture. Nevertheless, a gap does open at low temperatures due to electron-electron interaction [340, 341, 342].

Within a single-particle, low-energy picture, it

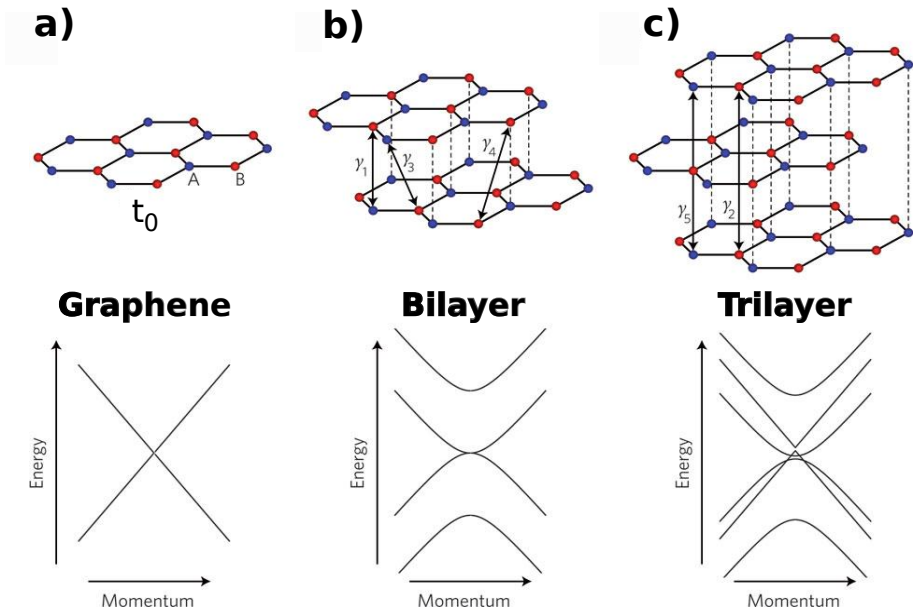

Figure 47. Unstrained lattice structure (upper panels) and a sketch of their corresponding energy dispersion (lower panels) for (a) monlayer graphene, (b) Bernal stacked bilayer graphene and (c) Bernal stacked trilayer graphene. Blue atoms belong to the A bipartite lattice while red atoms belong to the B lattice. The arrows indicate the different kinds of interactions that appear in a TB calculation, parametrized by t_0 for intra-layer interaction, and γ_i with $i = 1, ..., 5$ for inter-layer interactions. The Dirac cone seen in (a) for graphene is replaced by parabolic bands in (b), while trilayer graphene includes both types of bands. Reprinted by permission from Macmillan Publishers Ltd: Nature [337], copyright (2011).

is possible to obtain an effective Hamiltonian [338]. Trilayer graphene can be treated in a similar way, resulting in a mixing of the bilayer and monolayer energy dispersion that is shown in Figure 47(c).

Strain in bilayer graphene can be studied using the methodology presented for graphene with the peculiarity of having extra degrees of freedom in the deformation associated with the presence of two layers [343, 344]; band gaps can be opened by in-plane layer distortions or by pulling the layers apart [344].

Also, triaxial strain effects can be described by an effective pseudo-magnetic field [345]. Using this methodology, it has been found that in-plane strain applied equally to both layers breaks the layer symmetry, i.e., at low energy, just one of the layers feels the pseudo-magnetic field while the zero-energy pseudo-Landau level is missing in the other layer. This effect produces a gap between the lowest non-zero levels [345].

When two graphene layers are rotated relative to each other by an angle θ away from Bernal stacking, a moiré pattern is produced [346]. This stacking misorientation mimics the effect of in-plane pseudomagnetic fields [256].

A very important advance made possible by using rotationally faulted biaxial graphene was the first experimental observation of the Hofstadter butterfly [21]. This fractal spectrum was predicted to occur for electrons in a lattice under a constant magnetic field [22]. Its importance was paramount since it provided a platform to understand the Quantum Hall effect (QHE) in terms of topological phases. Originally, the problem of electrons in a constant field was studied by Landau, giving rise to the well known Landau levels with energy $E = (n + 1/2)\hbar\omega$ and n integer. As noted by Hofstadter, the lattice length adds a new scale in the problem that competes with the magnetic length [22]. As a result, the spectrum is controlled by the ratio between the elementary quantum flux (ϕ_0) and the magnetic flux (ϕ). This results in a one dimensional effective problem, where the potential depends on the ratio ϕ/ϕ_0. The corresponding Equation is known as the Harper equation, and is quite similar to the equation dictating the dynamics of uniaxial strained graphene.

As it was discussed with graphene monolayers in previous sections, the spectrum depends upon the ratio ϕ/ϕ_0 and it leads to a periodic or quasiperiodic behavior depending on whether ϕ/ϕ_0 is rational or irrational. The corresponding spectrum is a complex fractal, known as the Hofstadter butterfly [22] with interesting topological properties [138]. For small ratios of the fluxes, Landau levels are recovered. However, the fractality only appears at bigger ratios. Unfortunately, for atomic systems this requires the use of magnetic fields well beyond the available sources. However, such fractal spectrum was measured recently by using bilayer graphene over a hBN sustrate [21].

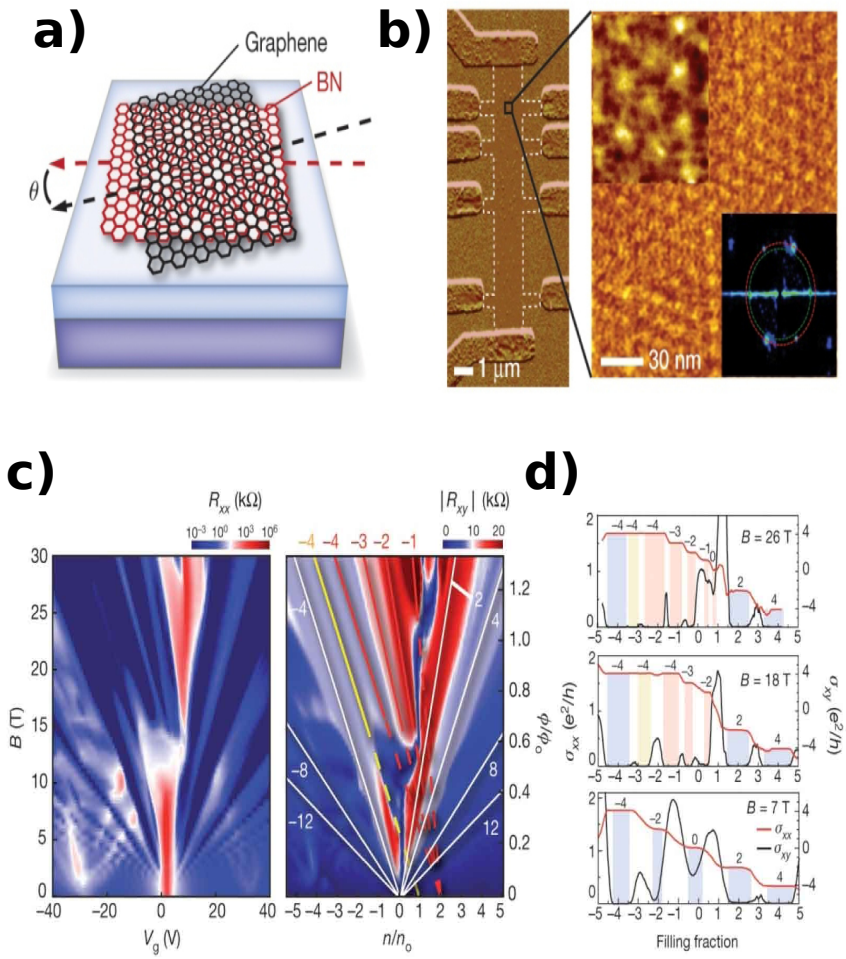

Figure 48. Moiré superlattice and anomalous quantum Hall states. (a) Sketch of bilayer graphene on hBN. The rotation of graphene by the mismatch angle θ determines the wavelength. (b) Left: AFM image of the multiterminal Hall device. Right: a magnified region of the same device. The resulting pattern is a triangular lattice (upper inset shows a further magnified region). A fast Fourier confirms the triangular lattice symmetry. (c) Diagram showing the longitudinal resistance, R_{xx} (left), and Hall resistance, R_{xy} (right) for the device presented in (b). R_{xx} is plotted versus magnetic field on the vertical axis and versus gate voltage $V_{(g)}$. R_{xy} is plotted as a function of the magnetic flux ratio ϕ/ϕ_0 on the vertical axis and the normalized carrier density n/n_0 on the horizontal axis. QHE states corresponding to the conventional BLG spectrum are indicated by white lines. Solid yellow and red lines track the QHE outside the conventional spectrum, with dashed lines indicating the projected n/n_0. The slope of each line is shown on the top axis as well as the intercept. Each pair of parameters are the solution of a Diophantine equation [21], characteristic of topological states in the QHE [138]. (d) Longitudinal and transversal Hall conductivities corresponding to line cuts at constant magnetic field (constant ϕ/ϕ_0). The color bars indicate the features with the same color appearing in (c). For magnetic fields of 12 T and 26 T, additional QHE states appear with non-integer Landau level filling fractions. Reprinted by permission from Macmillan Publishers Ltd: Nature [21], copyright (2013).

As shown in Figure 48 (a), the mismatch angle θ between both lattices determines the moiré pattern (see section 3). In panel (b) of Figure 48, the resulting triangular pattern and the device used to measure the electronic properties are shown. In Figure 48(c), the longitudinal resistance R_{xx} (left), and Hall resistance, R_{xy} (right) measured by Dean et. al. [21] are presented. R_{xx} is plotted as a function of the gate voltage V_g and magnetic field $B(T)$, while R_{xy} as a function of the magnetic flux ratio ϕ/ϕ_0 on the vertical axis and the normalized carrier density n/n_0 on the horizontal axis, where n_0 is the carrier density at zero gate voltage. Both plots reveal fountain-like structures characteristic of the Hofstadter butterfly [138] (associated to these structures there are Van Hove singularities).

Moreover, the slope and intercept with the vertical axis of each observed line in Figure 48(c) are the

solution of the Diophantine equation, characteristic of topological states in the QHE, and in Figure 48(d), the longitudinal and transversal Hall conductivities corresponding to line cuts for three constant magnetic fields (constant ϕ/ϕ_0) are presented.

7. Extensions to other 2D systems

In this subsection, a brief and incomplete guide to other strained 2D materials is presented. Although there are some recent reviews already covering this subject [9, 13, 14], this rough guide highlights differences and similarities with graphene. This allows for a quick identification of the methods and ideas suitable to be applied. This short review covers the following materials: silicene and other group-IV two-dimensional materials, phosphorene, transition metal-dichalcogenides and layered monochalcogenides.

There is a vastly unexplored avenue within two-dimensional atomic materials that relates symmetry operations to structural phase transitions. Before focusing on individual materials, the three requirements to observe such transitions are established:

(i) A necessary (but insufficient) condition is the existence of degeneracies of the structural ground state. An example of these symmetry operations appears in Figure 49(a). They exist when reflections with respect to the two-dimensional plane, or the exchange of x- and y-coordinates on structures that have rectangular unit cells, change the original arrangement of atoms (Figure 65(a)).

(ii) The existence of an energy pathway that joins these degenerate ground states, having a barrier smaller than the melting point (see Figures 49(b) and 65(b)).

(iii) Thermodynamic equilibrium makes all degenerate ground states to be evenly sampled. Therefore, the last condition is that sufficiently large mono-domains (that minimize strain at domain boundaries and hence reduce the structural energy) can be created.

When conditions (i-iii) above are satisfied, there will be structural two-dimensional structural phase transitions on these materials at finite temperature [34], which tune their material properties [347] just as strain does.

7.1. Silicene and other group-IV two-dimensional materials

Silicene [348, 349, 350] is a 2D material that is attracting a lot of interest in part due to its compatibility with the available present technology in electronics (for a review on Silicene see Ref. [351]). If the silicene sheet is flat (called α silicene), all of the

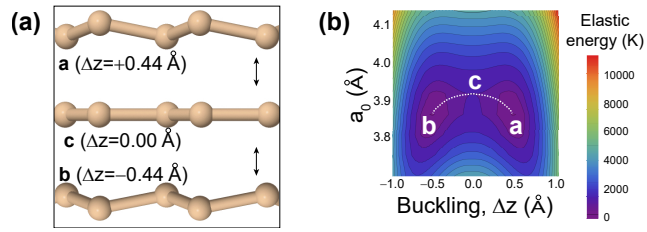

Figure 49. Two-dimensional structural phase transitions occur when (a) symmetry operations change the location of basis atoms, (b) the degenerate structures can be turned onto one another via an energy path that has a maximum energy smaller than the melting point, that in the present case corresponds with a planar structure having an energy of about 450 K and (c) sufficiently large monodomains (which reduce boundary-wall strain) exist. Past that critical temperature, the material acquires the structure displayed as *c*, on average.

methods discussed for studying graphene carry over [351]. Thus strain produces similar effects as those in graphene. However, the silicon sheet is low-buckled (β silicene): its lattice is similar to that of graphene, with the particularity that Si atoms in the two triangular bipartite sublattices are vertically displaced by 0.46 Å. The interatomic distance between atoms is 2.28 Å, which is larger than the C-C distance in graphene [351]. A simple tight-binding method can be derived to calculate its electronic properties.

β silicene also referred to as low-buckled silicene requires taking into account the coupling of π and σ electrons leading to an effective 8×8 matrix Hamiltonian [352] (see [169] as well). In spite of this, most of the research on strain has been made using DFT.

It has been shown in DFT calculations that the Dirac point is preserved for β silicene up to 5 % of strain[352]. This can be explained by the fact that the in-plane symmetry is unchanged. Higher strain induces hole doped Dirac states because of weakened Si-Si bonds [353]. The Grüneisen parameter shows a significant variation, from 1.64% for a strain of 5% to 1.42% for 25% [353].

Due to a larger spin-orbit coupling than that of graphene, low-buckled silicene is a quantum spin Hall insulator [355] with a topological quantum phase transition controlled by an out-of-plane electric field [356, 357]. The field-induced electronic transition can be further tuned by an in-plane hydrostatic biaxial strain ε owing to the curvature-dependent spin-orbit coupling (SOC) [169]. It is a $Z_2 = 1$ topological insulator phase for biaxial strain $|\varepsilon|$ smaller than 0.07, and the band gap can be tuned from 0.7 meV for $\varepsilon = +0.07$ up to a fourfold 3.0 meV for $\varepsilon = -0.07$.

As seen in Figures 50 and 51, first-principles calculations also show that the critical field strength E_c can be tuned by more than 113%, with the absolute values nearly 10 times stronger [354, 358] than the

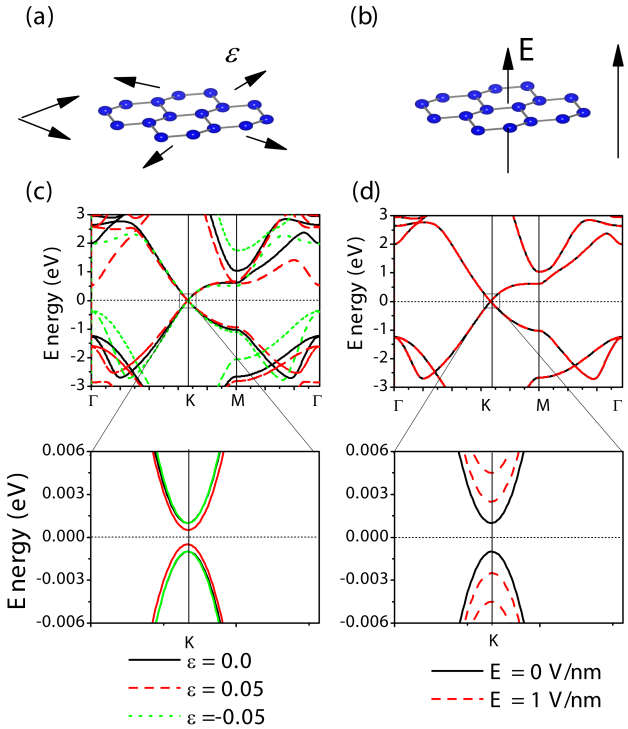

Figure 50. The electronic properties of silicene are independently tuned by (a) in-plane biaxial strain ε, and (b) an out-of-plane E-field E_z. Subplots (c) and (d) are band dispersions under typical values of ε or E_z, respectively. Insets are zoom-ins of the band dispersion near the $K-$point (the Fermi level is set to zero; note the overlapping bands for $\varepsilon = 0.00$ and 0.05 on (c)). Here, we will explore the combined effects of ε and E_z on its electronic structures. Reproduced from Ref. [354] with permission.

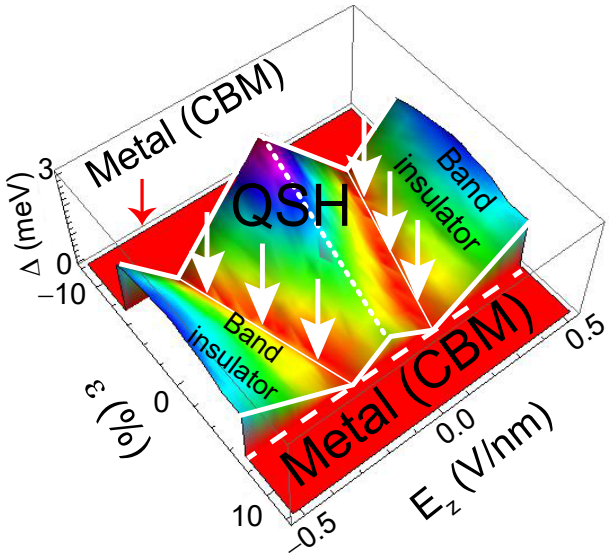

Figure 51. Topological quantum phase diagram of silicene with respect to in-plane biaxial strain ε and out-of-plane $E-$field E_z. The vertical axis is the band gap Δ. The critical E-field E_c, at which there is a phase transition from a topological insulator into a band insulator have been indicated by vertical white arrows. The metallic state has a zero value of Δ that is shown in red, and the area marked by QSH represents the topological spin Hall state phase. Reproduced from Ref. [354] with permission.

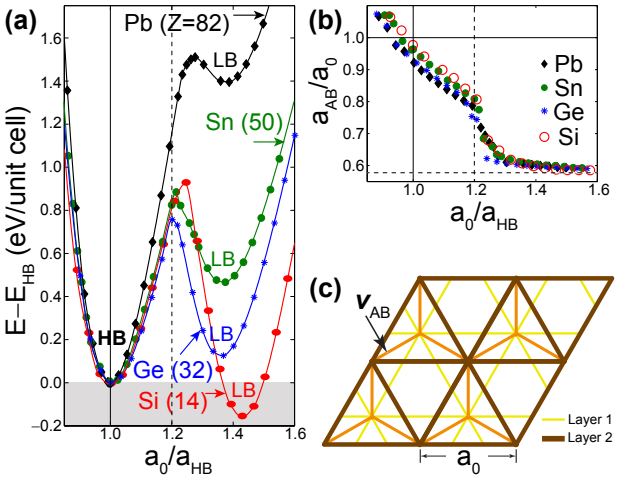

Figure 52. (a) The high-buckled phase becomes more stable with increasing atomic number. (b) Nearest-neighbor distances $a_{AB} \equiv |\mathbf{v}_{AB}|$ approach the lattice constant a_0 ($a_{AB} \simeq a_0$) at the high-buckled energy minimum; the structure transitions to a low-buckled phase at roughly $1.2a_{HB}$. (c) The high-buckled structure is a HCP bilayer. Reproduced from Ref. [360] with permission. Copyrighted by the American Physical Society.

theoretical predictions based on a tight-binding model [356, 357]. Due to the curvature-enhanced SOC, the buckling structure of the honeycomb lattice thus enhances the tunability of both the quantum phase transition and the SOC-induced band gap, which are crucial for the design of field-effect topological field-effect transistors based on two-dimensional materials.

Atomistic defects play an important role in the structural properties of silicene nanoribbons, as the Young modulus exhibits a complex dependence on the combinations of vacancies and on temperature [359].

Additional group-IV two-dimensional materials have been proposed, and experimental efforts to synthesize them are well under way. This subsection is concluded by highlighting relevant energetic considerations that raise the stakes to generate crystalline two-dimensional phases out of group-IV elements.

In Figure 52(a) the total DFT energy as a function of the lattice constant is displayed. Thus, while silicene has a structural minima at the low-buckled, $\beta-$phase, the actual structural minima for two-dimensional materials in group-IV is at the minima labeled HB at the figure, which is a hexagonal-close-packed bilayer with nine-fold coordination shown in Figure 52(a) [360]: the structural minima is not the one proposed in Ref. [361] and latter reproduced in Ref. [362].

A possibility for tuning the band-gap in low-buckled two-dimensional tin is to add fluorine atoms to

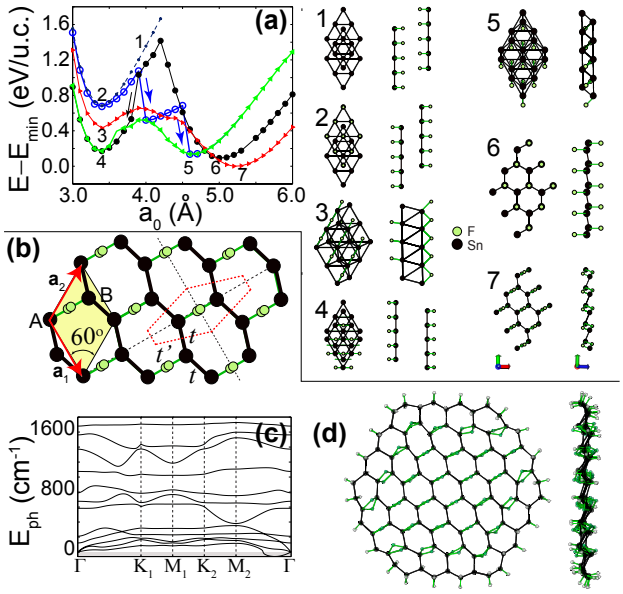

Figure 53. (a) Phases of 2D fluorinated tin; structures shown to the right. (b) Symmetries of the most stable structure (7), depicting triangular (dashed) and Wigner-Seitz (within dotted perimeter) unit cells, the two symmetry axes, and the two Sn sublattices A and B. Structural stability is demonstrated by (c) phonon dispersion curves and (d) the structural stabilization of a finite-size sample. Reproduced from Ref. [360] with permission. Copyrighted by the American Physical Society.

the two-dimensional structure [361], a result confirmed in Ref. [362]. As it turns out, such fluorinated structure labeled 6 in Figure 53(a), is not the structural minima either. As seen in Figure 53(a), the actual minima of fluorinated stanene corresponds to structure 7, which is displayed in a larger scale in Figure 53(b). In the minima of fluorinated stanene, pairs of fluorine atoms tilt to bridge Tin atoms, which breaks the three-fold symmetry of the lattice and has profound consequences on electronic properties.

Indeed, the 1BZ in Figure 54(a) shows a top view of the conduction band and the high-symmetry points in momentum space. As seen in Figure 54(b), the arrangement of parallel 1D Tin wires gives rise to an electronic structure with only two anisotropic Dirac cones, located away from the K-points at positions $\mathbf{V}_1$ and $\mathbf{V}_2 = \pm 0.85\mathbf{K}_1$, respectively. The existence of only two-Dirac cones is a consequence of the reduced structural symmetry, and 54 represents the first two-dimensional material where a chemical route to create a reduced number of valleys is discussed [360].

If one identifies the $x-$axis with the line joining tin atoms across fluorine bridges, then the Fermi velocity is close in magnitude to that of graphene and it is anisotropic: $v_{Fy} = 5.4 \times 10^5$ m/s (Figure 54(c)), and $v_{Fx} = 2.1 \times 10^5$ m/s (Figure 54(d)) and a $2\Delta = 0.02$ eV gap opens due to SOC, five times larger than the intrinsic gap due to spin-orbit coupling (SOC) in graphene [169]. Phase 6 transitions from a topological insulator to a trivial insulator, but the electronic structure of the optimal phase remains robust under larger isotropic strain.

As it was discussed for silicene, the electronic dispersion in Figure 54(b-d) can be understood in terms of a 2×2 $\pi-$electron tight-binding Hamiltonian discussed before [162], in which an effective coupling t' is set among the tin atoms originally linked by fluorine bridges (thin bonds on Figure 53(b)), and t is the coupling among actual Tin atoms (thick bonds on Figure 53(b)). The blue dashed lines in Figure 54(c,d) are fitted with $t = 0.8$ eV and $t' = \frac{v_{Fx}}{v_{Fy}} t$, which reproduce first-principles results [360].

When spin-orbit coupling is taken into account, an oblate low-energy Dirac-Hamiltonian is realized at the vicinity of the $\mathbf{V}_{1,2}$ points. The relevant subspace is four-dimensional at any given valley, and the task is to reproduce the spin texture displayed in Figure 54(e) where spin projects onto the $+x$ or the $-x$ directions while leaving the sublattice (pseudospin) degree of freedom unpolarized. The numerical results on Figure 54(e) are consistent with a coupling $\tau_z \sigma_x s_x$ [360] and the low-energy dynamics is given by:

$$H = -i\hbar \Psi^\dagger (v_{Fx} \tau_z \sigma_x \partial_x + v_{Fy} \sigma_y \partial_y) \Psi + \Psi^\dagger (\Delta \tau_z \sigma_x s_x) \Psi. \quad (167)$$

An unprecedented specific coupling of momentum –including direction– with spin oriented along $\hat{\mathbf{x}}$ and valley degrees of freedom is thus realized by the second term in previous equation. The valley degree of freedom can be addressed by a bias along the $\mathbf{V}_1 - \mathbf{V}_2$ axis that breaks inversion symmetry (this will be the case for monochalcogenide monolayers [363], which also have a low structural symmetry below their transition temperature [347]). Similarly, a magnetic field along the $\hat{\mathbf{x}}$ axis will break time-reversal symmetry, locking the valley and crystal momentum direction at the $\mathbf{V}_1$, $\mathbf{V}_2$ points. The dynamics discussed in Ref. [360] thus invites applications of 2D fluorinated tin for valleytronics.

The discussion on silicene ends by reemphasizing its structural degeneracies, and contrasting them with the lack of similar degeneracies existent in graphene (and in transition metal dichalcogenide monolayers for that matter).

To that end, the energy landscape [364] is displayed for graphene and silicene in Figure 55 as a function of the buckling vertical distance Δz and the lattice parameter a_0. The reader will attest that, while graphene has a single energy minima at $\Delta z = 0$ (i.e., under a planar structure), silicene has two such minima that are mirror images upon a reflection about the two-dimensional plane. The energy barrier separating these two minima is equal to 450 K. The

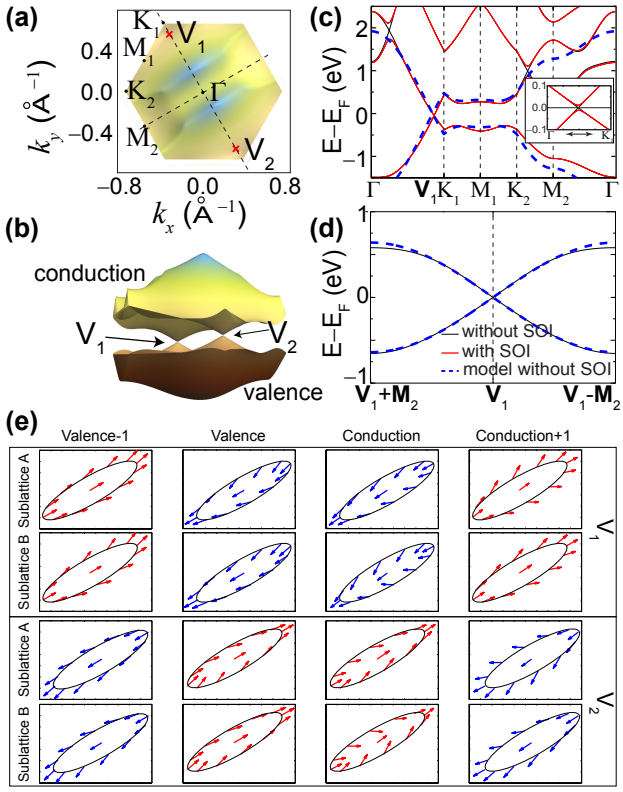

Figure 54. (a) Conduction band on the first Brillouin zone, highlighting high-symmetry points and locations of valleys $\mathbf{V}_1$ and $\mathbf{V}_2$ away from the K- and K'-points. (b) The two valleys on the Brillouin zone arise from the two-fold symmetry of the atomic structure. (c-d) Band structures along high-symmetry lines, including a two-band tight-binding fit. (e) Spin texture resolved over valley ($\boldsymbol{\tau}$), energy, and sublattice ($\boldsymbol{\sigma}$) degrees of freedom. (The spin projection onto the $z-$axis is of the order of 1% at most.) Reproduced from Ref. [360] with permission. Copyrighted by the American Physical Society.

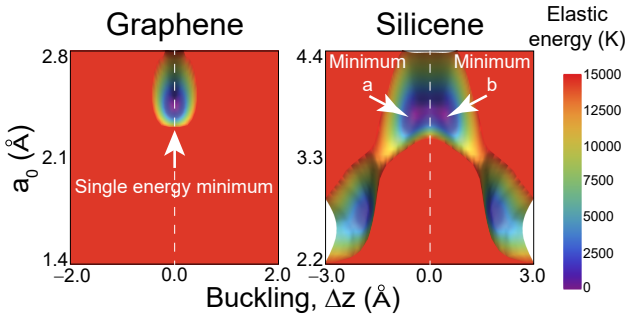

Figure 55. Highlighting the lack of structural degeneracies of graphene, and the two-fold structural degeneracy of $\beta-$silicene. The energy barrier separating these two minima is 450 K.

result conveyed by Figure 55 makes a direct call for studying two-dimensional materials that possess structural degeneracies at finite temperature [34, 347].

7.2. Phosphorene

Phosphorene is a single-layer material obtained by exfoliation of layered black phosphorus (BP). Black phosphorene, Figure 56(a), has a semiconducting gap that is tunable with the number of layers, and by in-plane strain [9, 365, 366, 367, 368]. Phosphorene [369, 370, 371] has many allotropes that are either semiconducting or metallic depending on their two-dimensional atomistic structure [372, 373, 374, 375]. The unit cells of blue phosphorene is displayed on Figure 56(b). As it will be shown when discussing monochalcogenides later on, phosphorene does not satisfy condition (ii) in section 7.1, and it melts before undergoing any two-dimensional phase transition [34].

The outstanding performance of transistors built using phosphorene in 2014 ignited intense research activities [369, 376]. Many groups consider this material as better suited for electronics than graphene due to several factors: the ease of fabrication, a 0.2 eV direct gap, a band topology not altered by thickness with an impressive anisotropy [377, 378]. It possess a reasonable on/off ratio (10^4-10^5) with a good carrier mobility (around 1000 cm2/V.S) suitable for many applications [378]. Concerning the mechanical properties, it has a highly anisotropic Young modulus and Poisson ratio [379]. All these remarkable features are a result of the stacked layered structure and weak van der Waals (vdWs) interlayer interactions. Considering the existence of reviews on this material [378, 379], results from our teams will be mostly highlighted in what follows.

One of the most interesting findings is that the inclusion of many body effects is essential for the correct description of the electronic properties of monolayer BP[368]; for example by changing the gap from 0.90 eV to 2.31 eV. Also, the authors of Ref. [368] found that tensile strain enhances electron transport along the zigzag direction, while biaxial strain is able to tune the optical band gap from 0.38 eV (at 0.8% strain) to 2.07 eV (at 5.5%). Another interesting phenomena resulting from ab initio calculations is the notable increasing of the electron-phonon interaction by biaxial strain [380]. This results in a predicted raising of $10K$ for the superconductor transition temperature at 4% strain.

Using a low-energy TB Hamiltonian that includes the spin-orbit interaction for bulk phosphorene it has been found that a compressive biaxial in-plane strain and a perpendicular tensile strain leads to a topological phase transition [381]. Protected edge states are observed for zigzag nanoribbons when the system is in the topological phase. For a width of 100 nm, the energy gap is at least three orders of magnitude larger than the thermal energy at room temperature [381].

This section ends with an study that links the

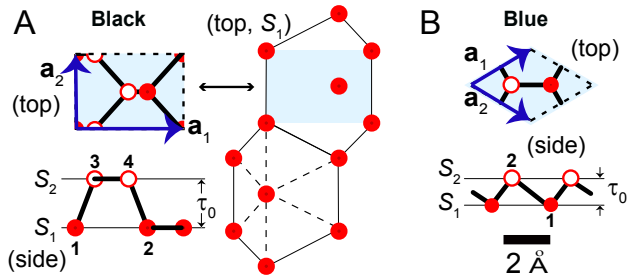

Figure 56. Unit cells for (a) black and (b) blue phosphorene monolayers that are formed by two sublayers (S_1 and S_2) separated by a distance τ_0. Sublayers in black phosphorene are irregular –distances among nearest atoms belonging to the same sublayer are not identical– as emphasized by the dashed lines joining atoms belonging to sublayer S_1 on the rightmost structure in (a). Reproduced from Ref. [382] with permission.

local geometry of phosphorene with the magnitude of its semiconducting band gap.

Theoretical studies of defects on planar phosphorene indicate that dislocation lines do not induce localized electronic states within the electronic bandgap [383]. This somehow unexpected result was employed to build semiconducting phosphorene cones that have a finite curvature [382].

As described in Section 4.9, four invariants from the metric (g) and curvature (k) tensors determine the local geometry of a 2-D manifold, and a planar structure can be described by $Tr(g) = 1$, $Det(g) = 1$ (i.e., no strain), $H = 0$, and $K = 0$ (i.e., no curvature) at both sublayers S_1 and S_2. In addition, their thickness τ is equal to τ_0 before a structural distortion sets in. These five numbers quantify the local reference (flat) geometry.

Structural defects induce curvature and strain [384], and may lead to the chemical degradation of phosphorene. In Figure 57 phosphorene cones were built from finite disk-like planar structures, with edges passivated by hydrogen atoms. The black phosphorene cone seen in Figure 57(a) is created by first removing an angular segment –that subtends a $\phi = 46°$ angle– from a planar structure that has a dislocation line [383], and then joining the two "ridges" that are highlighted by the red segments on the planar structure in Figure 57(a). Atoms are placed in positions dictated by an initial (analytical) conical structure, and were subsequently optimized at the DFT level to relieve structural forces [382]. Blue phosphorene has a (buckled) honeycomb structure reminiscent of graphene, so the conical structure seen to the left of Fig. 57(b) was generated by removing an angular segment subtending a $\phi = 60°$ angle on planar blue phosphorene, and following similar prescriptions afterwards.

The local geometry is displayed to the right on Figures 57(a) and 57(b). The data is arranged into three rows that indicate the geometry of the planar structure at sublayer S_1, and the local geometry of the cones at sublayers S_1 and S_2. An additional plot shows the value of τ/τ_0 that tell us of local vertical compression.

There is strain induced by the dislocation line on the planar black phosphorene structure, as indicated by the color variation on the $Tr(g)$ and $Det(g)$ plots, that implies having atoms at closer/longer distances than in the reference structure, Figure 57(a). A slight curvature on the black phosphorene planar structure, induced by the dislocation line, is also visible on the H plot in Figure 57(a). The planar blue phosphorene sample does not have any dislocation line, and for that reason the metric shows zero strain ($Tr(g) = 1$ and $Det(g) = 1$) and zero curvature ($H = 0$ and $K = 0$) on that reference structure (Figure 57(b)).

The black phosphorene conical structure seen on Figure 57(a) displays a compression near its apex and an asymmetric elongation towards the edges. In addition, there is a radially-asymmetric non-zero curvature; the observed asymmetry reflects the presence of the dislocation/disclination axis, which provides the structure with an enhanced structural rigidity. This rigidity is confirmed by the ratio τ/τ_0 close to unity. The blue phosphorene cone has a more apparent radial symmetry, except for the disclination line that is created by the conical structure, as reflected on the metric invariants and on H. There is compression (elongation) at the apex, and elongation (compression) along the disclination line in sublayer S_1 (S_2). The disclination line has a semi-cylindrical shape and hence a zero radius of curvature along the disclination line, resulting in a zero Gaussian curvature along such line.

Figure 52 indicates that the blue phosphorene cone acquires the largest curvatures of these two cones. This is so because the angular segment removed from the planar blue phosphorene sample has a comparatively larger value of ϕ. One notes the rather smooth curvature at the apex on the blue phosphorene conical structure after the structural optimization.

The change of τ with respect to τ_0 is created by an out-of-plane strain or by shear. The blue phosphorene cone shows out-of-plane compression near the apex. The distance among planes in black phosphorene is closer to its value in an ideal planar structure throughout, showing scatter around the dislocation line.

The main point from Figure 57 is the strain induced by curvature. The strain pattern observed on that Figure is far more complex than those reported before for planar phosphorene [365, 366, 367, 368], and the discrete geometry captures the strain pattern with the precision given by actual atomic positions.

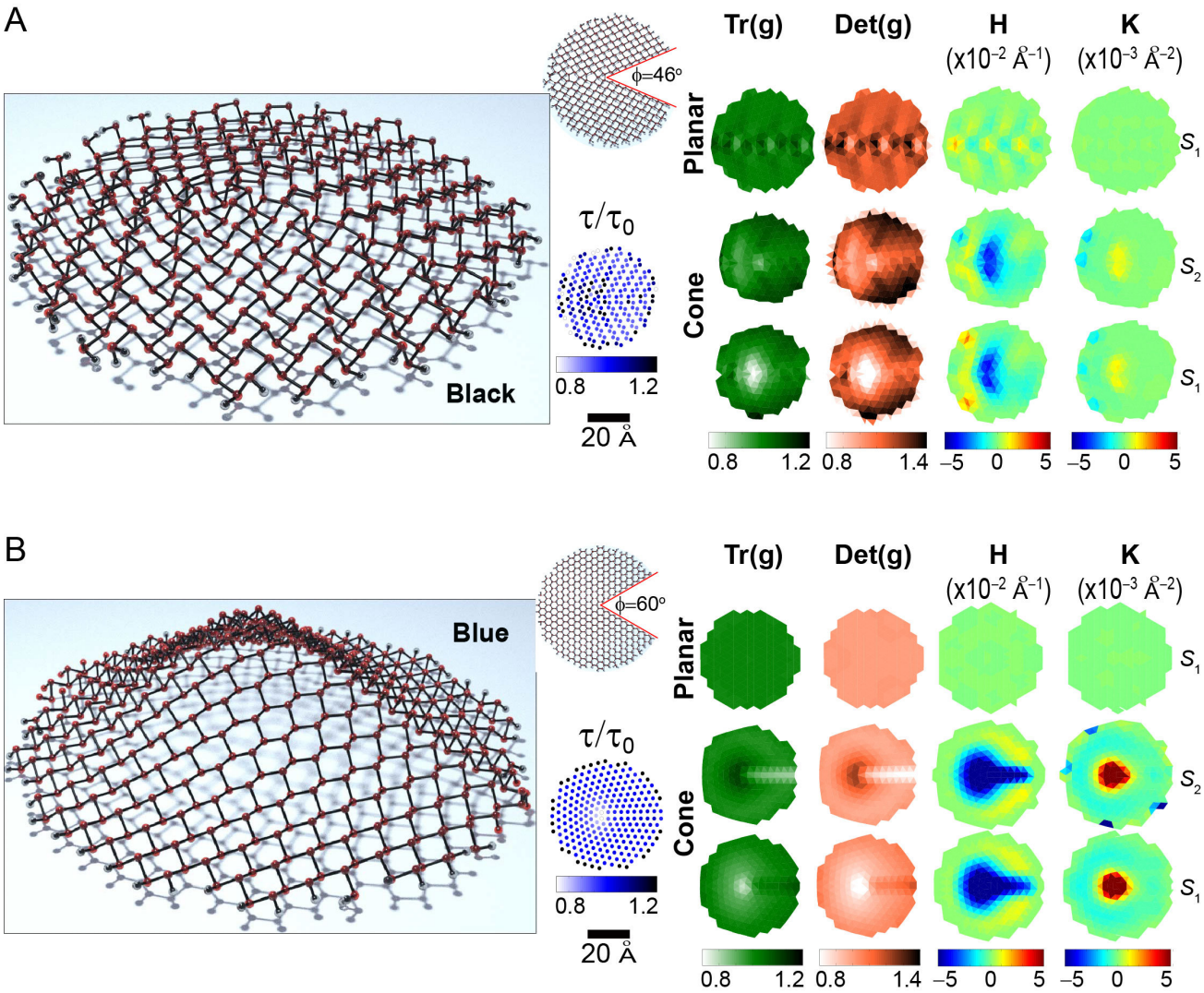

Figure 57. (a) Black and (b) blue phosphorene cones are built by removing the angular segments in white from the planar structures (as illustrated at the upper-right corner of the conical structures), joining the cut structures along the red (disclination) lines, and a subsequent structural optimization. The discrete local geometry of these conical structures at sublayers S_1 and S_2 is given by four local invariants ($Tr(g)$, $Det(g)$, H and K) that are obtained at each atomic position. These invariants are contrasted with the geometry of planar structures ($Tr(g) = 1$, $Det(g) = 1$, $H = 0$, and $K = 0$) that is depicted at the uppermost row for sublayer S_1. The change in relative height τ/τ_0 is shown at each atomic position as well. Features such as: (i) strain induced by the dislocation line in planar black phosphorene; (ii) a sensible compressive strain near the apex; (iii) curvature lacking a radial symmetry; and (iv) the lack of significant changes in τ on conical black phosphorene, are clearly visible. The disclination line on the blue phosphorene cone is reflected on the metric invariants and on H: This disclination has a semi-cylindrical shape, that yields an overall radially-symmetric Gaussian curvature K. In addition, a decrease of τ, and an in-plane compression (elongation) at sublayer S_1 (S_2) near the apex can also be seen on the blue phosphorene cone. Reproduced from Ref. [382] with permission.

Black and blue phosphorene monolayers are both semiconducting 2-D materials with a direct bandgap, and we investigate how this semiconducting gap evolves with their shape. The semiconducting gap E_g = is equal to 1.1 (2.2) eV for the finite-size planar black (blue) phosphorene monolayers on display in Figure 58, before the removal of the angular segments.

Size-effects on the semiconducting gap of planar structures were first determined: The magnitude of the gap E_g increases as the number of atoms decreases on strain-free disk-like planar structures; c.f., Figure 58,. For an infinite number of atoms –i.e., for a fully periodic planar 2-D crystal– the gap converges to the values indicated by the dash and dash-dot lines on Figure 58; namely, 0.8 eV and 2.0 eV for black and blue phosphorene, respectively. These magnitudes were obtained from standard density-functional theory [369, 372]. Although we acknowledge that other methods describe the dielectric properties more accurately on smaller samples [366], our focus is on the trend the

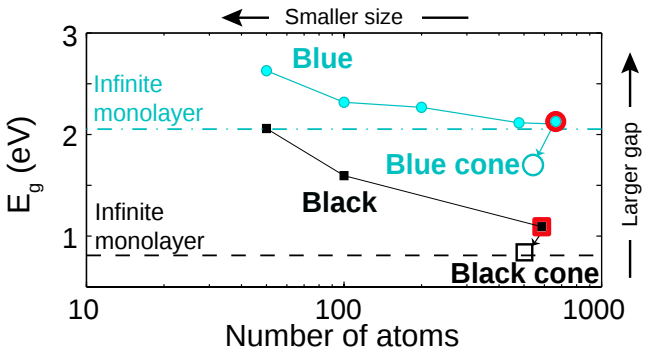

Figure 58. The semiconducting gap of planar black and blue phosphorene monolayer discs increases as the number of atoms decreases. Even though the number of atoms must be reduced to create a conical shape from a planar structure, the gap decreases on conical structures with such decrease of the number of atoms, as indicated by open ticks and the tilted arrows: This reduction of the gap on a conical structure thus has a purely geometrical origin. (Dash and dash-dot lines indicate these gaps when the number of atoms is infinite.) Reproduced from Ref. [382] with permission.

gap follows, and given that the trend is geometrical in nature, it will stand correct despite of the particular method employed in computing the semiconducting gap.

Phosphorene is well-known to oxidize readily [386, 387] and, as shown in Figure 59, structural defects provide the only structural mechanism known to dissociate O_2 dimers [385].

As in graphene, another emerging field is the study of strained multilayered black phosphorus sheets. It has been found that a periodic stress produces a remarkable shift of the optical absorption band-edge, up to 0.7 eV between the regions under tensile and compressive stress [388]. This tunability greatly exceeds the reported value for strained transition metal dichalcogenides. According to theoretical models, the periodic stress modulation can yield to quantum confinement of carriers at low temperatures [388].

7.3. Transition metal dichalcogenide monolayers

The family of two dimensional transition metal-dichalcogenides (TMDCs), with chemical composition MX_2 where M is a transition metal and X a chalcogenide, is one of the most promising for solving fundamental scientific and technological challenges [389]. They have electronic properties ranging from semiconducting to superconducting, with no surface dangling bonds and the added feature of a high thermal stability and an enhanced spin-orbit coupling [390]. Although the first reports on TMDCs are almost 60 years old[389], a surge occurred after the discovery of graphene and the building of a high-quality field-effect transistor [391].

Two particulary promising applications are in photonics and electronics. For photonics applications, TMDCs posses a strong exciton-binding energies in materials like MoS_2, WS_2,$MoSe_2$ and WSe_2, a feature that promises a new age of atomic-scale photonics[392]. For electronics applications, the most attractive feature is the formation of abrupt tunnel junctions. Such effect is due to their two dimensional nature, which results in very small geometric screening lengths.

Transition metal dichalcogenides nanoribbons can have interesting properties due to edges, as for example an enhanced catalytic activity [393], useful for several applications like in dye-sensitized solar cells [394] or as robust electrocatalyst for Hydrogen generation [64]. Three basic mechanisms explain the active properties due to edges: quantum confinement, edge topology, and for very narrow nanoribbons, the electronic interaction between edges [393].

In MX_2 materials, mechanical deformation is an important tool to modify the electronic properties. According to a density-functional-based tight binding method calculation, when isotropic and uniaxial strain is applied to MoS_2, the bandgap is linearly lowered until a semicondutor-metal transition occurs for 11% of strain [395]. The first experiments of MoS_2 strained up to 2% are in general agreement with the tight binding calculation, since the bandgap decreases around 70 meV for each % of strain[396]. This scenario have been confirmed in experiments that demonstrate a continuous and reversible tuning of the optical band gap by as much as 500 meV by applying very large biaxial strains [397].

More recently, strained MoS_2 and WSe_2 field-effect transistors (FETs) have been fabricated on a $500\mu m$ flexible polyimide substrate[398]. In Fig. (60) we present the transfer characteristics of such WSe_2 FET as reported by Shen et. al. [398]. By comparing the transfer characteristics, is clear that strain induces a band gap tunability. According to Shen et. al.[398], Fig. (60) a is clear evidence of a band gap reduction of 100 meV in WSe_2 under 1.35% uniaxial tensile strain, attributed to a decrease in the Schottky barrier (SB) for electrons without any change for hole injection into the valence band.

7.4. Monochalcogenide monolayers

This review is concluded by highlighting structural aspects different from strain that may be of relevance on two-dimensional atomic materials with structural degeneracies. Group-IV monochalcogenides contain one element from column-IV (Si, Ge, Sn, Pb) and a chalcogen heavier than Oxygen (S, Se, Te). To facilitate the discussion, an average atomic number $\bar{Z}$

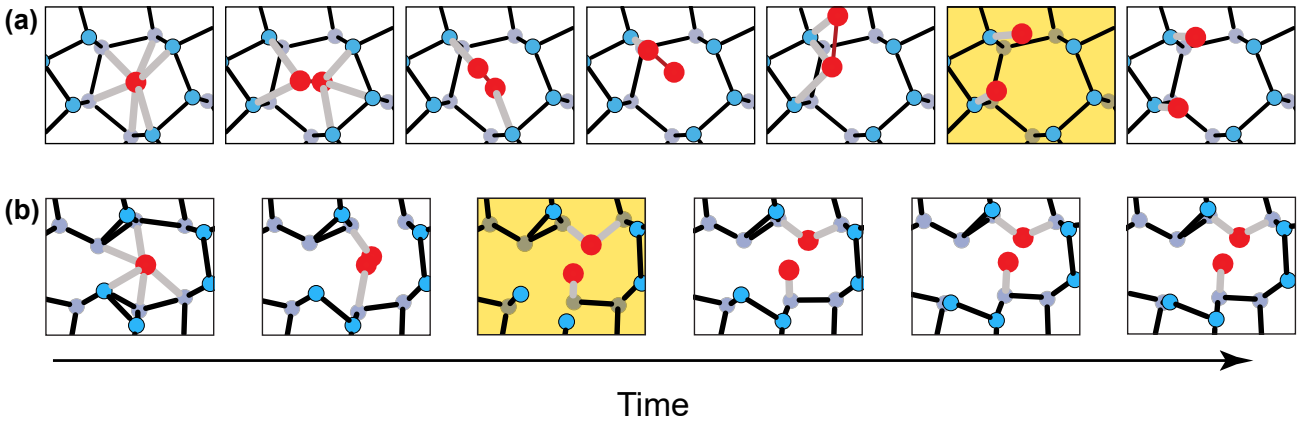

Figure 59. Unveiling the dissociation of O_2 at intrinsic defects. The first frames to the left show the initial vertical placement of O_2 within the intrinsic defects. Oxygen dissociation at these intrinsic defects occurs at the frames highlighted in yellow. Frames at the far right show the optimized structures, at which distances among O atoms are 2.96 and 3.08 Å for at structure (a) and (b), respectively. For reference, the equilibrium distance among O atoms in O_2 is 1.25 Å. Reproduced from Ref. [385] with permission.

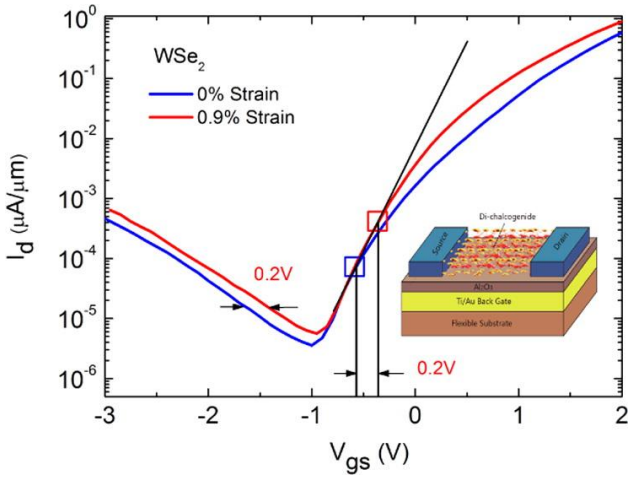

Figure 60. Transfer characteristics of a WSe_2 FET built over a flexible polyimide substrate, as sketched in the figure. V_{gs} is the gate voltage while I_d is the current. The measurement were made at room temperature for 0% (blue curve) and 0.9% (red curve) of tensile strain. A higher flat band voltage of 0.2V is observed under strain as indicated by the arrows. Reprinted with permission from Ref. [398]. Copyright 2016 American Chemical Society.

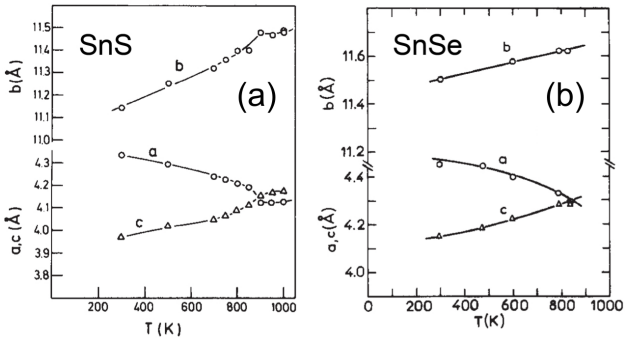

Figure 61. The structural phase transition in bulk, layered SnS and SnSe is signaled by the coalescence of in-plane lattice parameters, labeled a and c on this Figure. Adapted from Ref. [401] with permission.

is defined as follows [34]:

$$\bar{Z} = \frac{1}{4}\sum_{i=1}^{4} Z_i, \tag{168}$$

where the sum is over the four atomic elements on a unit cell, each having atomic number Z_i ($i = 1, 2, 3, 4$). Materials such as SnTe, PbSe, and PbTe, for which $\bar{Z} > 50$ realize a rocksalt bulk structure. They are topological crystalline insulators [399], and will not be discussed here. On the other hand, group-IV monochalcogenides with $\bar{Z} < 50$, such as SnSe ($\bar{Z} = 42$), SnS ($\bar{Z} = 33$), GeSe ($\bar{Z} = 33$) and GeS ($\bar{Z} = 24$), are known to realize a layered, black-phosphorus-like phase [400]. The important point for the ensuing discussion is that these layered monochalcogenides undergo structural phase transitions at finite temperature and prior to melting.

One signature of these structural transitions is provided in Figure 61 [401], where a coalescence of in-plane lattice parameters (labeled a and c, where $a \simeq c$) was shown to occur in bulk layered SnS and SnSe. The structural transition turns a *Pnma* structure onto a *Cmcm* one. As displayed in Figure 62, this structural phase transition was shown to lead to an unexpectedly large thermal figure of merit ZT [402], which may result in novel thermoelectric applications based on bulk SnSe. The nature of the structural transition in the bulk, displayed in Figure 63 was analyzed more recently, and attributed to electronic (orbital) modes [403].

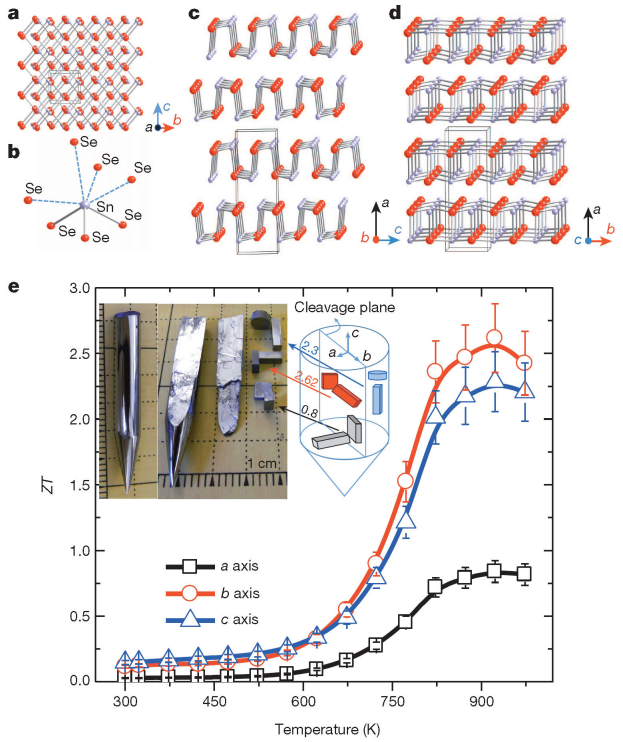

Figure 62. (a) Crystal structure of bulk SnSe along the a axis: grey, Sn atoms; red, Se atoms. (b), Highly distorted $SnSe_7$ coordination polyhedron with three short and four long SnSe bonds. (c) Structure along the b axis. (d) Structure along the c axis. (e). Thermal figure of merit ZT along different axial directions; the ZT measurement uncertainty is about 15% (error bars). Inset images: left, a typical crystal; right, a crystal cleaved along the (l00) plane, and specimens cut along the three axes and corresponding measurement directions. Inset diagram, how crystals were cut for directional measurements. Reproduced with permission from Macmillan Publishers Ltd. from Ref. [402], copyright (2014).

It is time to turn the discussion to monolayers of these materials. At this moment, they are yet to be experimentally exfoliated down to monolayers, so all the discussion that follows is of a theoretical character. Their salient characteristics in structures at zero Kelvin are:

- A rectangular unit cell. As seen in Figure 64, this unit cell with a reduced symmetry leads to a unique placement of valleys in the first Brillouin zone [404, 405, 406, 363]. Valleys in dichalcogenide monolayers are addressable with circularly-polarized light, but the valleys in monochalcogenide monolayers can be addressed with linearly-polarized light [407]. (The extraordinary effect of lower structural symmetry on valley placement was touched upon in Section 7.1 and Figure 54.)
- An inherent piezoelectricity, given their diatomic chemical composition, and the placement of such atoms within the unit cell [29, 30, 408].

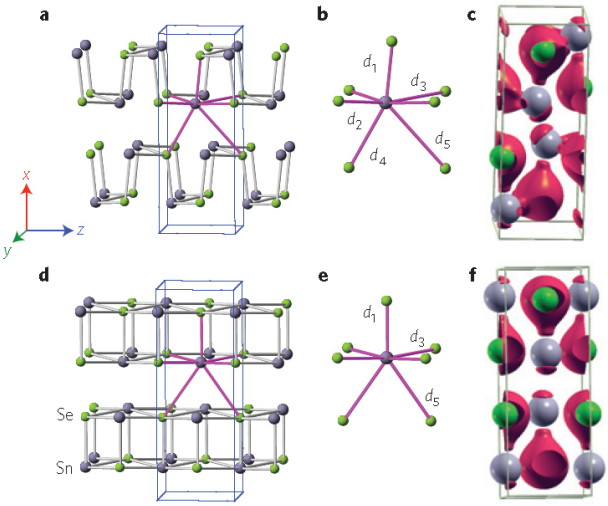

Figure 63. (a,d) Crystal structures of SnSe in the Pnma (a) and Cmcm (d) phase (conventional non-primitive cell for the latter), showing the double bilayer structure and *Pnma* distortion. (b,e) Sn coordination polyhedron corresponding to the structures in (a,d), respectively. (c,f) Valence electron density (isosurface at $0.26e\text{Å}^{-3}$), computed from first principles for the structures in (a,d), respectively. Sn atoms are in grey and Se atoms in green. The Sn $5s_2$ lone pairs are seen as "caps" in the space between bilayers. Reproduced with permission from Macmillan Publishers Ltd. from Ref. [403], copyright (2015).

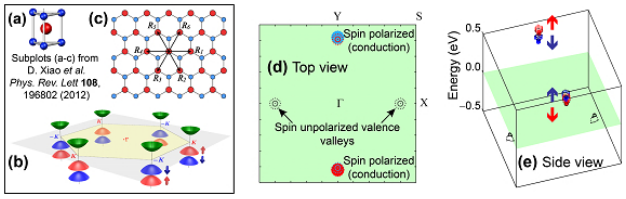

Figure 64. Contrasting the spin polarization, number of valleys, and their placement on the first Brillouin zone for MoS2 and SnSe monolayers: (a-c) The MoS_2 monolayer displays spin splittings at the valence-band valley, and the conduction and valence band valleys lie at the same location in reciprocal space. (d-e) Spin-polarized conduction-band valley and valence band valleys for SnSe: the electron/valley couplings on subplots (d-e) are unique to IV-VI monolayers and can originate a new platform for valleytronics in 2D. Subplots (a-c) are adapted from Ref. [409] with permission. Copyrighted by the American Physical Society.

Just as it is the case for silicene (Figures 49 and 55), 2D materials with rectangular unit cells such as black phosphorene and monochalcogenide monolayers have a natural structural degeneracy with a relatively low energy barrier. In the latter case, and as seen in Figure 65(a), the degeneracy occurs on monochalcogenide monlayers upon exchange of lattice vectors. Additional degeneracies occur upon reflection of the basis vectors, Figure 65(b), yielding a four-fold degenerate structural ground state. Anharmonicity of the phonon dispersion is a consequence of the bistability of the energy profile shown in Figure 65 [410]. The energy landscape originally presented in

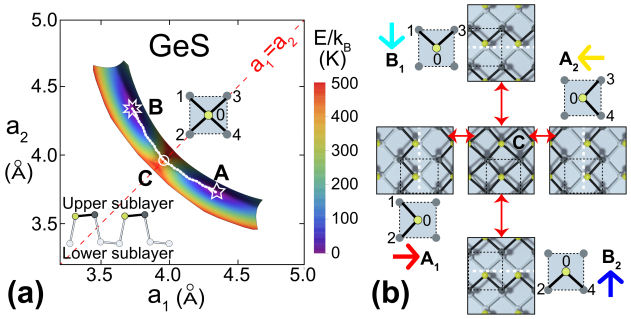

Figure 65. (a) The elastic energy landscape $E(a_1, a_2)$ as a function of lattice parameters a_1 and a_2 is generic to all monolayers with a Pnma structure, and it is exemplified on a GeS monolayer at zero temperature. A dashed white curve joins points A and B at two degenerate minima ($E_A = E_B = 0$). The circle labeled C at (4.0 Å, 4.0 Å) is a saddle point with an atomistic structure in which atom 0 forms bonds to four in-plane neighbors, and the elastic energy barrier is defined by E_C. (b) Atomistic decorations (i.e., the specific pair of atoms bonding atom 0) increase the structural degeneracy at points A and B. The four degenerate ground states are named A_1, A_2, B_1 and B_2, and assigned in-plane arrows that label them uniquely. Reproduced from Ref. [34] with permission. Copyright (2016) American Chemical Society.

Ref. [34] has been subsequently confirmed in Ref. [411]. Similarly, the fourfold degenerate structural ground states have later been reported in Refs. [411] and [412].

Now that the issue of structural degeneracies has been discussed, it is time to show why one should expect phase transitions in these materials. This was done by looking at the evolution of a_1/a_2 and E_C evolve with $\bar{Z}$. A technical note becomes needed here, in the sense that the energy barriers are extremely sensitive to the choice of pseudopotentials employed in calculations, and so it is desirable to employ pseudopotentials that reproduce all-electron results. This was the case for all results in Ref. [34], where all pseudopotentials were thoroughly validated [413]. Given that 1 K $\propto 10^{-4}$ eV, differences of the order of 50 K in estimates of the barrier amount to tiny differences in total energies of the order of 5 meV in calculations carried out by different teams.

Nevertheless, the values of a_1/a_2 and E_C averaged over their magnitude from three different calculations displayed in Figure 66 show an exponential decay with mean atomic number $\bar{Z}$. Light compounds such as black phosphorus monolayer or SiS monolayers ($\bar{Z} = 15$) have the largest values of a_1/a_2 and E_C and do not satisfy condition (ii) expressed in the opening remarks of Section 7, so these materials will directly melt before showing eny sign of a two-dimensional structural phase transition.

On the other hand, ultrathin Pb-based monochalcogenides ($\bar{Z} > 48$) have a rock-salt structure so that $a_1/a_2 = 1$ and $E_C = 0$ [399]. All remaining monochalcogenide monolayers (MMs) have values of

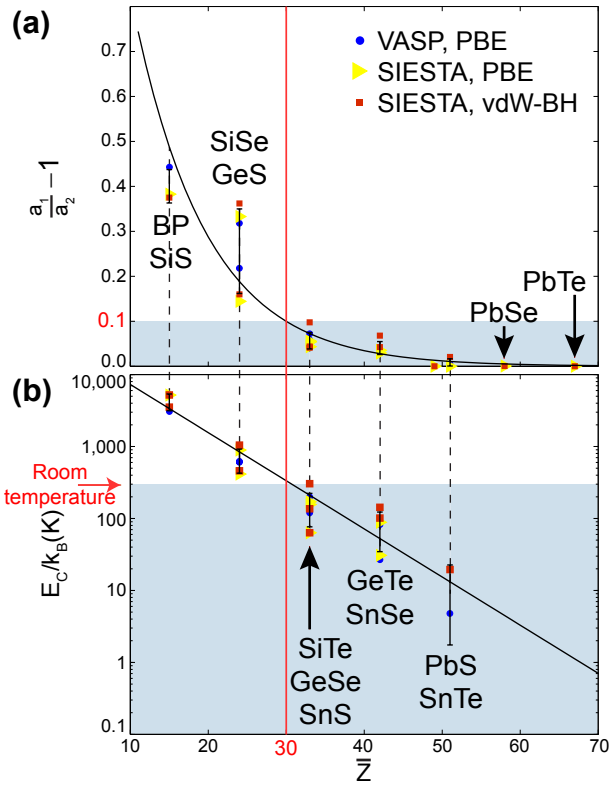

Figure 66. (a) The ratio a_1/a_2 among orthogonal in-plane lattice constants decreases exponentially with the mean atomic number $\bar{Z}$, and (b) E_C decays exponentially with $\bar{Z}$ as well. $E_C/k_B < 300$ K (and $a_1/a_2 \leq 1.1$) for $\mathbf{Z} \geq 30$, prompting the question whether three-fold coordinated GeSe, SnS and SnSe monolayers are disordered near room temperature. Structures with $a_1 \simeq a_2$ display a five-fold-coordinated and non-degenerate ground state with $E_C \simeq 0$. Solid lines are exponential fits. Reproduced from Ref. [34] with permission. Copyright (2016) American Chemical Society.

a_1/a_2 and E_C lying somewhere in between, which implies a vast tunability with atomic number and the possibility displaying a two-dimensional phase transition.

Bond covalency is gradually sacrificed with increasing atomic number to favor a higher atomistic coordination and a weaker (i.e., metallic) bonding. It has been shown that group-IV two-dimensional materials turn from a threefold- to a ninefold-coordinated phase with increasing atomic number [360]. In the case of monochalcogenide monolayers, a threefold-coordinated structure evolves towards a fivefold-coordinated one with increasing $\bar{Z}$ [34].

It is relevant for the present discussion to note that the ratio of in-plane lattice constants of monochalcogenides increases with the number of layers [363]. This raises the transition temperatures in going from monolayers to the bulk, which means that E_c is tunable by the number of layers too.

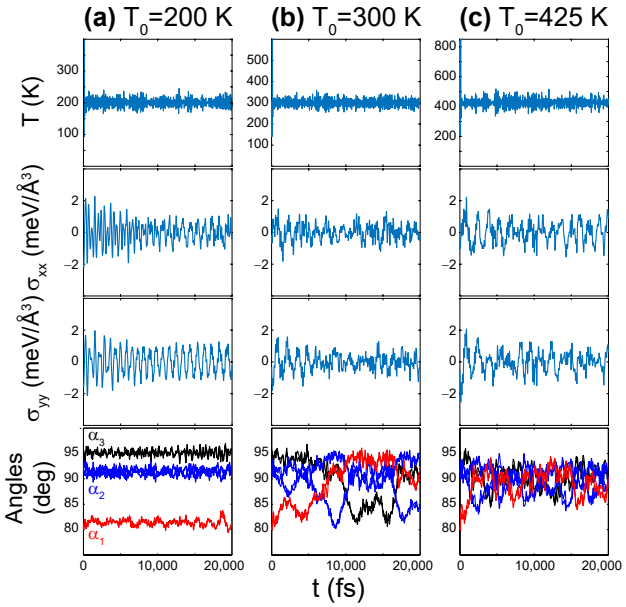

Figure 67. Time-evolution of temperature, in-plane stress, and angle order parameters for a GeSe monolayer. Among other measures [34, 347], the transition is signaled by the coalescence of angles towards 90° (see row at 425 K).

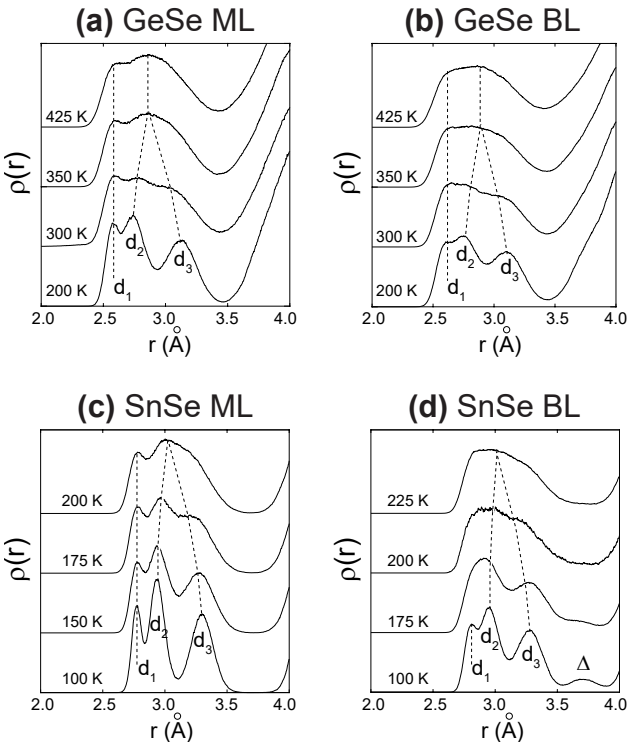

Figure 68. The structural transition in monochalcogenide monolayers (MLs) and bilayers (BLs) is signaled by the coalescence of peaks d_2 and d_3 into a single, broad peak.

So far, the structural degeneracies of monochalcogenide monolayers have been discussed, and an argument for estimating energy barriers among these degenerate states has been given. Such physics is at play in bulk ferroelectrics like $BiFeO_3$, that has a 6-fold structural degeneracy. In $BiFeO_3$, the low-symmetry ferroelectric ground state is created by the lone pair of Bi_3^+ moving off-center from the initially-cubic unit cell. The structural signature of the phase transition is a structure with an average cubic symmetry.

In the case of monochalcogenide monolayers, which are ferroelectrics as well, the lone pair is located at the chalcogen [400, 403], and this two-dimensional structural phase transition has been probed via molecular dynamics (MD) in Figures 67, 68 and 69 [34, 347]. Basically, the instantaneous temperature, pressure against the walls holding the monolayer equilibrate. And angles formed among atoms lying at the same sublayer turn to 90° at the transtion (see Figures 69(b), and 65(a) for definitions of sublayers): what this means is that the structure becomes square on average at the transition. Additional order parameters, such as lattice parameters, and interatomic distances (Figure 68) provide additional signatures for this structural transition [34, 347]. The dynamical range of angles being sampled implies that the transition is not static; it is for this reason that we characterized it of order-disorder type in Ref. [34]: the distribution of lattice parameters seen in Figure 69(c-f) attest to the large range of fluctuations in these structurally-degenerate two-dimensional structures that are already known to give rise to floppy and anharmonic phonon modes [403].

As discussed in Ref. [347], some consequences of the transition are as follows: No in-gap states develop as the structural transition takes place, so that these phase-change materials remain semiconducting below and above T_c. Nevertheless, as the in-plane lattice transforms from a rectangle onto a square at T_c, the electronic, spin, optical, and piezo-electric properties dramatically depart from earlier predictions.

Indeed, the $Y-$ and $X-$points in the Brillouin zone become effectively equivalent at T_c, leading to a symmetric electronic structure. The spin polarization at the conduction valley edge vanishes, and the hole conductivity must display an anomalous thermal increase at T_c. The linear optical absorption band edge must change its polarization as well, making this structural and electronic evolution verifiable optically. A pyroelectric response of about 3×10^{-12} C/Km was also predicted for monolayers of GeSe and SnSe (due to their inherent AB-stacking, a net dipole moment only exists in structures with an odd number of layers), and the quenching of the dipole moment was latter confirmed in Ref. [414]. The results in Ref. [347] thus uncover the fundamental role of temperature as a control knob for the physical properties of few-layer group-IV monochalcogenides, and conclude the review

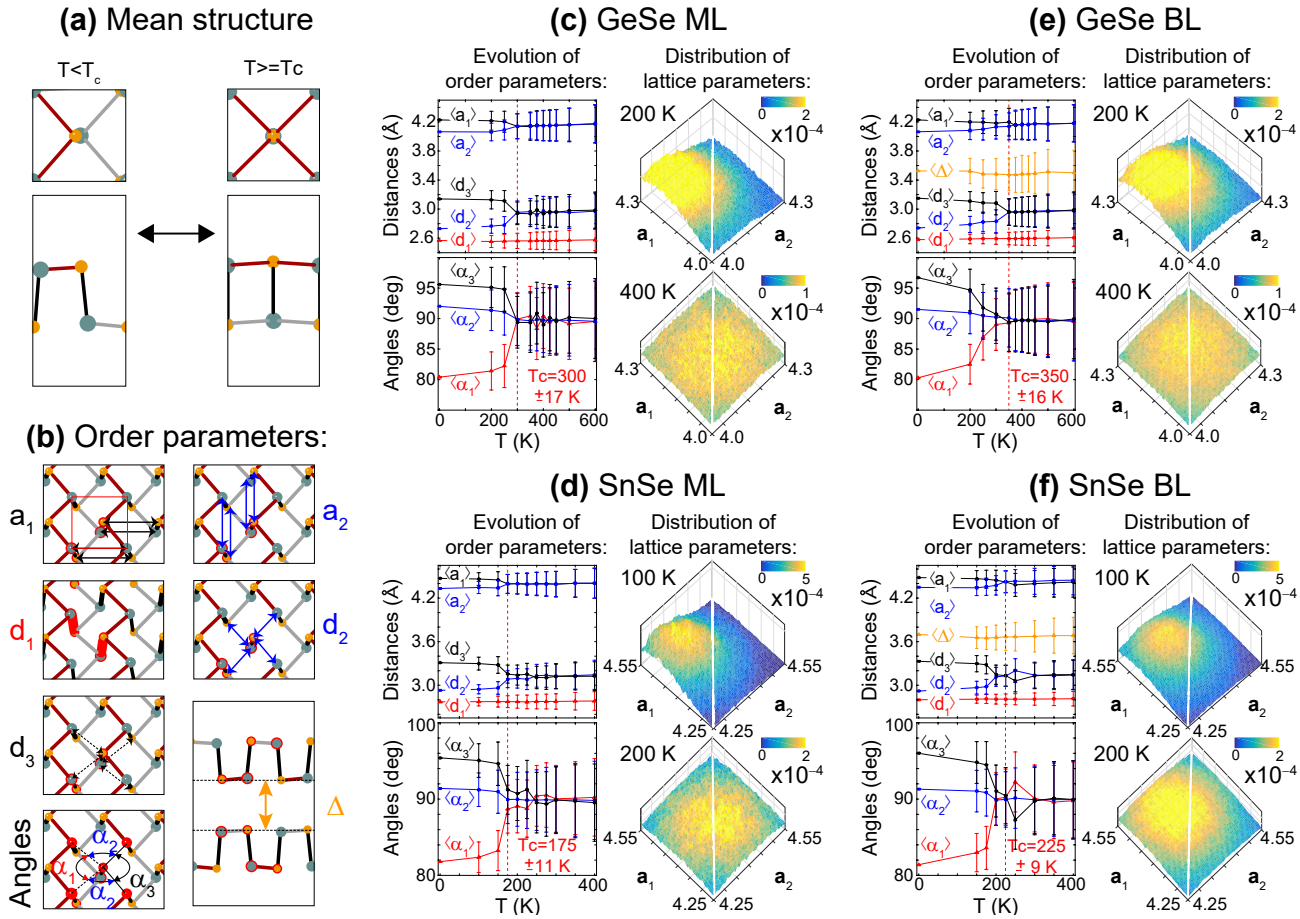

Figure 69. (a) Schematic depiction of the structural transition. (b) Structural order parameters highlighting the transition. (c to f) Left: thermal averages for the order parameters provided in (b) as a function of T for GeSe and SnSe MLs and BLs. T_c is reached when average values agree ($\langle a_1\rangle = \langle a_2\rangle$, $\langle d_2\rangle = \langle d_3\rangle$, and $\langle \alpha_1\rangle = \langle \alpha_3\rangle$). The average distance among layers $\langle\Delta\rangle$ for BLs is shown too. Right: the distribution of lattice parameters a_1 and a_2 dramatically highlights the fluctuations leading to the error bars on the subplots on the left. The line $a_1 = a_2$ is shown in white. Reproduced from Ref. [347] with permission. Copyrighted by the American Physical Society.

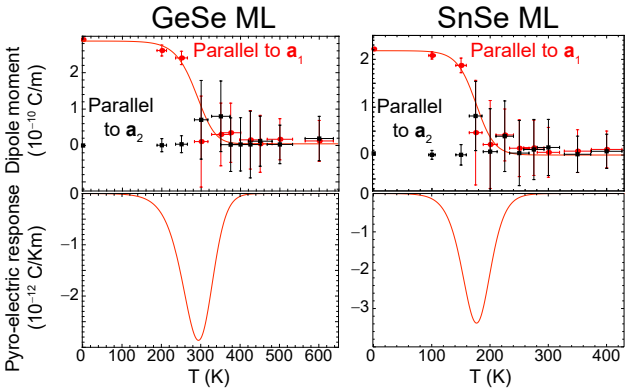

Figure 70. The structural transition in monochalcogenide monolayers (MLs) quenches the intrinsic electric dipole and creates a pyroelectric response. Reproduced from Ref. [347] with permission. Copyrighted by the American Physical Society.

of this novel material family.

8. Conclusions and outlook

Mechanical deformations in graphene and other 2D systems is a very active field of research, and the possibility of tailoring very strong magnetic fields via pseudomagnetic potentials produced by sustrates is opening new research avenues. In more than one sense, strained 2D materials are a playground for realizing interesting physical systems, like Luttinger liquids, topological phases, broken chiral symmetry phases due to Kekulé ordering, two-dimensional structural phase transitions, and so on. Topological phases, spintronics, direct band-gap semiconductors or band gap tunability are among the most important areas of actual research.

Although research in graphene is mature in many senses, there are many open questions, like the kind of perturbations needed to treat graphene over substrates, or even more basic questions like the mismatch between energetic and geometry descriptions observed in uniformly-deformed graphene. Even the

existence of gaps in graphene strained using different ways is a highly debated issue and more work is needed to elucidate this question.

Furthermore, the treatment of pseudomagnetic potentials needs to be formalized using techniques borrowed from the electromagnetic case using concepts like magnetic groups and lattices, and can also employ tools like discrete geometry. Multilayered systems still represent a tantalizing promise to design at will materials by stacking one-atom thickness surfaces.

Deformations and structural phase transitions in other 2D materials like silicene and monochalcogenides monolayers are still in the process of being explored, where there are many new interesting questions that deserve attention.

Acknowledgments

We would like to thank Juan Carlos Obeso, Pedro E. Roman-Taboada, José Eduardo Barrios-Vargas, Raad E. Haleoot, Ryu Nakae and Manuel Mon for support in revising the manuscript, help with the figures and discussion of the subject. We also thank V. Pereira, S. Roche, A. Kitt, A. Pacheco-Sanjuan, M.A.H. Vozmediano, F. de Juan, M.A Zubkov, E. Harriss, P. Kumar, L. Bellaiche, B. Klee, G.E. Volovik and G. Montambaux for enlightening discussions during several phases of our research in this field. This work was partially supported by DGAPA-UNAM project IN102717, by an Early Career Grant from the DOE (SC0016139, SBL) by NSF XSEDE (TG-PHY 090002, SBL) and by the Arkansas High Performance Computing Center which is funded through multiple National Science Foundation grants and the Arkansas Economic Development Commission. M.O.L. acknowledges a postdoctoral fellowship from DGAPA-UNAM. H.T. acknowledges NSF (EFRI 1433311).

References

[1] K. S. Novoselov, A. K. Geim, S. V. Morozov, D. Jiang, Y. Zhang, S. V. Dubonos, I. V. Grigorieva, and A. A. Firsov. Electric field effect in atomically thin carbon films. Science, 306(5696):666–669, 2004.

[2] K. S. Novoselov, D. Jiang, F. Schedin, T. J. Booth, V. V. Khotkevich, S. V. Morozov, and A. K. Geim. Two-dimensional gas of massless dirac fermions in graphene. Proc. Natl. Acad. Sci. USA, 102(30):10451–10453, 2005.

[3] Geim A. K. and Novoselov K. S. The rise of graphene. Nat Mater, 6(3):183–191, mar 2007. 10.1038/nmat1849.

[4] Alexander A. Balandin, Suchismita Ghosh, Wenzhong Bao, Irene Calizo, Desalegne Teweldebrhan, Feng Miao, and Chun Ning Lau. Superior thermal conductivity of single-layer graphene. Nano Lett., 8(3):902–907, 2008.

[5] Changgu Lee, Xiaoding Wei, Jeffrey W. Kysar, and James Hone. Measurement of the Elastic Properties and Intrinsic Strength of Monolayer Graphene. Science, 321(5887):385–388, 2008.

[6] M.A.H. Vozmediano, M.I. Katsnelson, and F. Guinea. Gauge fields in graphene. Physics Reports, 496:109–148, 2010.

[7] Novoselov K. S., Fal[prime]ko V. I., Colombo L., Gellert P. R., Schwab M. G., and Kim K. A roadmap for graphene. Nature, 490(7419):192–200, oct 2012. 10.1038/nature11458.

[8] Mark A. Bissett, Masaharu Tsuji, and Hiroki Ago. Strain engineering the properties of graphene and other two-dimensional crystals. Phys. Chem. Chem. Phys., 16:11124–11138, 2014.

[9] Rafael Roldán, Andrés Castellanos-Gomez, Emmanuele Cappelluti, and Francisco Guinea. Strain engineering in semiconducting two-dimensional crystals. Journal of Physics: Condensed Matter, 27(31):313201, 2015.

[10] Salvador Barraza-Lopez. Discrete differential geometry and the properties of conformal two-dimensional materials. Synthetic Metals, 210, Part A:32–41, 2015. Reviews of Current Advances in Graphene Science and Technology.

[11] Costas Galiotis, Otakar Frank, Emmanuel N. Koukaras, and Dimitris Sfyris. Graphene Mechanics: Current Status and Perspectives. Annual Review of Chemical and Biomolecular Engineering, 6(1):121–140, 2015. PMID: 25898069.

[12] Jin-Wu Jiang, Bing-Shen Wang, Jian-Sheng Wang, and Harold S Park. A review on the flexural mode of graphene: lattice dynamics, thermal conduction, thermal expansion, elasticity and nanomechanical resonance. Journal of Physics: Condensed Matter, 27(8):083001, 2015.

[13] B. Amorim, A. Cortijo, F. de Juan, A.G. Grushin, F. Guinea, A. Gutiérrez-Rubio, H. Ochoa, V. Parente, R. Roldán, P. San-Jose, J. Schiefele, M. Sturla, and M.A.H. Vozmediano. Novel effects of strains in graphene and other two dimensional materials. Physics Reports, 617:1–54, 2016.

[14] Shikai Deng and Vikas Berry. Wrinkled, rippled and crumpled graphene: an overview of formation mechanism, electronic properties, and applications. Materials Today, 19(4):197–212, 2016.

[15] V. Meunier, A. G. Souza Filho, E. B. Barros, and M. S. Dresselhaus. Physical properties of low-dimensional sp^2-based carbon nanostructures. Rev. Mod. Phys., 88:025005, May 2016.

[16] Vitor M. Pereira, A. H. Castro Neto, and N. M. R. Peres. Tight-binding approach to uniaxial strain in graphene. Phys. Rev. B, 80:045401, Jul 2009.

[17] I. Pletikosić, M. Kralj, P. Pervan, R. Brako, J. Coraux, A. T. N'Diaye, C. Busse, and T. Michely. Dirac Cones and Minigaps for Graphene on Ir(111). Phys. Rev. Lett., 102:056808, Feb 2009.

[18] Yankowitz Matthew, Xue Jiamin, Cormode Daniel, Sanchez-Yamagishi Javier D., Watanabe K., Taniguchi T., Jarillo-Herrero Pablo, Jacquod Philippe, and LeRoy Brian J. Emergence of superlattice Dirac points in graphene on hexagonal boron nitride. Nat Phys, 8(5):382–386, may 2012. 10.1038/nphys2272.

[19] Carmine Ortix, Liping Yang, and Jeroen van den Brink. Graphene on incommensurate substrates: Trigonal warping and emerging Dirac cone replicas with halved group velocity. Phys. Rev. B, 86:081405, Aug 2012.

[20] Ponomarenko L. A., Gorbachev R. V., Yu G. L., Elias D. C., Jalil R., Patel A. A., Mishchenko A., Mayorov A. S., Woods C. R., Wallbank J. R., Mucha-Kruczynski M., Piot B. A., Potemski M., Grigorieva I. V., Novoselov K. S., Guinea F., Fal/'ko V. I., and Geim A. K. Cloning of Dirac fermions in graphene superlattices. Nature, 497(7451):594–597, may 2013.

[21] Dean C. R., Wang L., Maher P., Forsythe C., Ghahari

F., Gao Y., Katoch J., Ishigami M., Moon P., Koshino M., Taniguchi T., Watanabe K., Shepard K. L., Hone J., and Kim P. Hofstadter/'s butterfly and the fractal quantum Hall effect in moire superlattices. Nature, 497(7451):598–602, may 2013.

[22] Douglas R. Hofstadter. Energy levels and wave functions of Bloch electrons in rational and irrational magnetic fields. Phys. Rev. B, 14:2239–2249, Sep 1976.

[23] Liu Zheng, Ma Lulu, Shi Gang, Zhou Wu, Gong Yongji, Lei Sidong, Yang Xuebei, Zhang Jiangnan, Yu Jingjiang, Hackenberg Ken P., Babakhani Aydin, Idrobo Juan-Carlos, Vajtai Robert, Lou Jun, and Ajayan Pulickel M. In-plane heterostructures of graphene and hexagonal boron nitride with controlled domain sizes. Nat Nano, 8(2):119–124, feb 2013. 10.1038/nnano.2012.256.

[24] G. G. Naumis, M. Terrones, H. Terrones, and L. M. Gaggero-Sager. Design of graphene electronic devices using nanoribbons of different widths. Applied Physics Letters, 95(18), 2009.

[25] G.S. Diniz, E. Vernek, and F.M. Souza. Graphene-based spin switch device via modulated Rashba Field and Strain. Physica E: Low-dimensional Systems and Nanostructures, pages –, 2016.

[26] Mitchell T. Ong and Evan J. Reed. Engineered Piezoelectricity in Graphene. ACS Nano, 6(2):1387–1394, 2012. PMID: 22196055.

[27] N. Levy, S. A. Burke, K. L. Meaker, M. Panlasigui, A. Zettl, F. Guinea, A. H. Castro Neto, and M. F. Crommie. Strain-Induced Pseudo-Magnetic Fields Greater Than 300 Tesla in Graphene Nanobubbles. SCIENCE, 329(5991):544–547, JUL 30 2010.

[28] Wang Xiaomu, Tian He, Xie Weiguang, Shu Yi, Mi Wen-Tian, Ali Mohammad Mohammad, Xie Qian-Yi, Yang Yi, Xu Jian-Bin, and Ren Tian-Ling. Observation of a giant two-dimensional band-piezoelectric effect on biaxial-strained graphene. NPG Asia Mater, 7:e154, jan 2015.

[29] Lídia C. Gomes, A. Carvalho, and A. H. Castro Neto. Enhanced piezoelectricity and modified dielectric screening of two-dimensional group-iv monochalcogenides. Phys. Rev. B, 92:214103, Dec 2015.

[30] Ruixiang Fei, Wenbin Li, Ju Li, and Li Yang. Giant piezoelectricity of monolayer group iv monochalcogenides: Snse, sns, gese, and ges. Applied Physics Letters, 107(17), 2015.

[31] Michael N. Blonsky, Houlong L. Zhuang, Arunima K. Singh, and Richard G. Hennig. Ab initio prediction of piezoelectricity in two-dimensional materials. ACS Nano, 9(10):9885–9891, 2015. PMID: 26312745.

[32] Matthias Droth, Guido Burkard, and Vitor M. Pereira. Piezoelectricity in planar boron nitride via a geometric phase. Phys. Rev. B, 94:075404, Aug 2016.

[33] Avishek Kumar, Mark Wilson, and M F Thorpe. Amorphous graphene: a realization of Zachariasen's glass. Journal of Physics: Condensed Matter, 24(48):485003, 2012.

[34] Mehrshad Mehboudi, Alex M. Dorio, Wenjuan Zhu, Arend van der Zande, Hugh O. H. Churchill, Alejandro A. Pacheco-Sanjuan, Edmund O. Harriss, Pradeep Kumar, and Salvador Barraza-Lopez. Two-dimensional disorder in black phosphorus and monochalcogenide monolayers. Nano Letters, 16(3):1704–1712, 2016.

[35] Gerardo G. Naumis. Low-Frequency Vibrational Modes Anomalies and Rigidity: A Key to Understanding the Glass and the Electronic Properties of Flexible Materials from a Topological Perspective. Frontiers in Materials, 2:44, 2015.

[36] G. Montambaux, F. Piéchon, J.-N. Fuchs, and M. O. Goerbig. Merging of Dirac points in a two-dimensional crystal. Phys. Rev. B, 80:153412, Oct 2009.

[37] G. Montambaux, F. Piéchon, J.-N. Fuchs, and M. O. Goerbig. A universal Hamiltonian for motion and merging of Dirac points in a two-dimensional crystal. The European Physical Journal B, 72(4):509–520, 2009.

[38] R. de Gail, J.-N. Fuchs, M.O. Goerbig, F. Piéchon, and G. Montambaux. Manipulation of Dirac points in graphene-like crystals. Physica B: Condensed Matter, 407(11):1948–1952, 2012.

[39] Matthieu Bellec, Ulrich Kuhl, Gilles Montambaux, and Fabrice Mortessagne. Topological Transition of Dirac Points in a Microwave Experiment. Phys. Rev. Lett., 110:033902, Jan 2013.

[40] Pedro Roman-Taboada and Gerardo G. Naumis. Spectral butterfly, mixed Dirac-Schrödinger fermion behavior, and topological states in armchair uniaxial strained graphene. Phys. Rev. B, 90:195435, Nov 2014.

[41] A. H. Castro Neto, F. Guinea, N. M. R. Peres, K. S. Novoselov, and A. K. Geim. The electronic properties of graphene. Rev. Mod. Phys., 81:109–162, 2009.

[42] Gerardo G. Naumis, Rafael A. Barrio, and Chumin Wang. Effects of frustration and localization of states in the Penrose lattice. Phys. Rev. B, 50:9834–9842, Oct 1994.

[43] Gerardo G. Naumis, Chumin Wang, and Rafael A. Barrio. Frustration effects on the electronic density of states of a random binary alloy. Phys. Rev. B, 65:134203, Mar 2002.

[44] Gerardo G. Naumis. Internal mobility edge in doped graphene: Frustration in a renormalized lattice. Phys. Rev. B, 76:153403, Oct 2007.

[45] J E Barrios-Vargas and Gerardo G Naumis. Doped graphene: the interplay between localization and frustration due to the underlying triangular symmetry. Journal of Physics: Condensed Matter, 23(37):375501, 2011.

[46] J.E. Barrios-Vargas and Gerardo G. Naumis. Pseudo-gap opening and Dirac point confined states in doped graphene. Solid State Communications, 162:23–27, 2013.

[47] N.W. Ashcroft and N.D. Mermin. Solid State Physics. Saunders College Publishing, Fort Worth, 1976.

[48] Jannik C. Meyer, A. K. Geim, M. I. Katsnelson, K. S. Novoselov, T. J. Booth, and S. Roth. The structure of suspended graphene sheets. Nature, 446(7131):6063, mar 2007. 10.1038/nature05545.

[49] L.E. Malvern. Introduction to the mechanics of a continuous medium. Prentice Hall, Englefford, New Jersey, USA, 1969.

[50] D. Lai W. M., Rubin and E. Krempl. Introduction to continuum mechanics. Butterworth-Heinemann, Oxford, U.K., 2010.

[51] L. Landau and E. Lifshitz. Theory of Elasticity. Pergamon Press, Oxford, U.K., 1976.

[52] Alexander L. Kitt, Vitor M. Pereira, Anna K. Swan, and Bennett B. Goldberg. Erratum: Lattice-corrected strain-induced vector potentials in graphene [Phys. Rev. B **85** , 115432 (2012)]. Phys. Rev. B, 87:159909, Apr 2013.

[53] Daniel Midtvedt, Caio H Lewenkopf, and Alexander Croy. Strain–displacement relations for strain engineering in single-layer 2d materials. 2D Materials, 3(1):011005, 2016.

[54] Wilfrido A. Gomez-Arias and Gerardo G. Naumis. Analytical calculation of electron group velocity surfaces in uniform strained graphene. International Journal of Modern Physics B, 30(03):1550263, 2016.

[55] C. Janot. Quasicrystals: A Primer. Monographs on the Physics and Chemistry of Materials. Oxford University Press, USA, 2 edition, 1995.

[56] Artaud A., Magaud L., Le Quang T., Guisset V.,

David P., Chapelier C., and Coraux J. Universal classification of twisted, strained and sheared graphene moiré superlattices. Scientific Reports, 6:25670, may 2016.

[57] GG Naumis and JL Aragon. The influence of phason disorder on the electronic spectrum and eigenstates of Fibonacci lattices. PHYSICS LETTERS A, 244(1-3):133–138, JUL 13 1998.

[58] GG Naumis, CM Wang, MF Thorpe, and RA Barrio. Coherency of phason dynamics in Fibonacci chains. PHYSICAL REVIEW B, 59(22):14302–14312, JUN 1 1999.

[59] GG Naumis. Phason hierarchy and electronic stability of quasicrystals. PHYSICAL REVIEW B, 71(14), APR 2005.

[60] GG Naumis and JL Aragon. Analytic expressions for the vertex coordinates of quasiperiodic lattices. ZEITSCHRIFT FUR KRISTALLOGRAPHIE, 218(6):397–402, 2003.

[61] T Janssen and O Radulescu. Theory of phasons in aperiodic crystals. FERROELECTRICS, 305:179–184, 2004. Aperiodic 2003 Conference, Belo Horizonte, BRAZIL, SEP 08-13, 2003.

[62] Enrique Maciá. The role of aperiodic order in science and technology. Reports on Progress in Physics, 69(2):397, 2006.

[63] Alpha T N'Diaye, Johann Coraux, Tim N Plasa, Carsten Busse, and Thomas Michely. Structure of epitaxial graphene on Ir(111). New Journal of Physics, 10(4):043033, 2008.

[64] Fengmei Wang, Yuanchang Li, Tofik Ahmed Shifa, Kaili Liu, Feng Wang, Zhenxing Wang, Peng Xu, Qisheng Wang, and Jun He. Selenium-Enriched Nickel Selenide Nanosheets as a Robust Electrocatalyst for Hydrogen Generation. Angewandte Chemie, 128(24):7033–7038, 2016.

[65] T. C. Lubensky, Sriram Ramaswamy, and John Toner. Hydrodynamics of icosahedral quasicrystals. Phys. Rev. B, 32:7444–7452, Dec 1985.

[66] Colin Daniels, Andrew Horning, Anthony Phillips, Daniel V P Massote, Liangbo Liang, Zachary Bullard, Bobby G Sumpter, and Vincent Meunier. Elastic, plastic, and fracture mechanisms in graphene materials. Journal of Physics: Condensed Matter, 27(37):373002, 2015.

[67] Kai Liu and Junqiao Wu. Mechanical properties of two-dimensional materials and heterostructures. Journal of Materials Research, 31(7):832–844, 2015.

[68] Deji Akinwande et al. A review on mechanics and mechanical properties of 2d materials - graphene and beyond. arXiv:1611.01555, 2016.

[69] J. Scott Bunch, Scott S. Verbridge, Jonathan S. Alden, Arend M. van der Zande, Jeevak M. Parpia, Harold G. Craighead, and Paul L. McEuen. Impermeable Atomic Membranes from Graphene Sheets. Nano Letters, 8(8):2458–2462, 2008.

[70] Wenzhong Bao, Feng Miao, Zhen Chen, Hang Zhang, Wanyoung Jang, Chris Dames, and Chun Ning Lau. Controlled ripple texturing of suspended graphene and ultrathin graphite membranes. Nat Nano, 4:562–566, Sept 2009.

[71] Kwanpyo Kim, Zonghoon Lee, Brad D. Malone, Kevin T. Chan, Benjamín Alemán, William Regan, Will Gannett, M. F. Crommie, Marvin L. Cohen, and A. Zettl. Multiply folded graphene. Phys. Rev. B, 83:245433, Jun 2011.

[72] J. Scott Bunch, Arend M. van der Zande, Scott S. Verbridge, Ian W. Frank, David M. Tanenbaum, Jeevak M. Parpia, Harold G. Craighead, and Paul L. McEuen. Electromechanical Resonators from Graphene Sheets. Science, 315(5811):490–493, 2007.

[73] Quan Wang and Behrouz Arash. A review on applications of carbon nanotubes and graphenes as nano-resonator sensors. Computational Materials Science, 82:350–360, 2014.

[74] John P. Mathew, Raj N. Patel, Abhinandan Borah, R. Vijay, and Mandar M. Deshmukh. Dynamical strong coupling and parametric amplification of mechanical modes of graphene drums. Nat Nano, 11:747–751, 2016.

[75] Sang Jin Kim, Kyoungjun Choi, Bora Lee, Yuna Kim, and Byung Hee Hong. Materials for Flexible, Stretchable Electronics: Graphene and 2D Materials. Annual Review of Materials Research, 45(1):63–84, 2015.

[76] Houk Jang, Yong Ju Park, Xiang Chen, Tanmoy Das, Min-Seok Kim, and Jong-Hyun Ahn. Graphene-Based Flexible and Stretchable Electronics. Advanced Materials, 28(22):4184–4202, 2016.

[77] C D Reddy, S Rajendran, and K M Liew. Equilibrium configuration and continuum elastic properties of finite sized graphene. Nanotechnology, 17(3):864, 2006.

[78] F Scarpa, S Adhikari, A J Gil, and C Remillat. The bending of single layer graphene sheets: the lattice versus continuum approach. Nanotechnology, 21(12):125702, 2010.

[79] Xiaoding Wei, Benjamin Fragneaud, Chris A. Marianetti, and Jeffrey W. Kysar. Nonlinear elastic behavior of graphene: *Ab initio* calculations to continuum description. Phys. Rev. B, 80:205407, Nov 2009.

[80] Luciano Colombo and Stefano Giordano. Nonlinear elasticity in nanostructured materials. Reports on Progress in Physics, 74(11):116501, 2011.

[81] Niklas Lindahl, Daniel Midtvedt, Johannes Svensson, Oleg A. Nerushev, Niclas Lindvall, Andreas Isacsson, and Eleanor E. B. Campbell. Determination of the Bending Rigidity of Graphene via Electrostatic Actuation of Buckled Membranes. Nano Letters, 12(7):3526–3531, 2012.

[82] L. D. Landau and E. M. Lifshitz. Course of Theoretical Physics, Theory of Elasticity, volume 7. Pergamon Press Oxford, 3rd edition, 1986.

[83] Steven Weinberg T Piran David Nelson. Statistical mechanics of membranes and surfaces. World Scientific Pub, 2nd edition, 2004.

[84] Matthew R. Begley and Thomas J. Mackin. Spherical indentation of freestanding circular thin films in the membrane regime. Journal of the Mechanics and Physics of Solids, 52(9):2005–2023, 2004.

[85] U. Komaragiri, M. R. Begley, and J. G. Simmonds. The Mechanical Response of Freestanding Circular Elastic Films Under Point and Pressure Loads. Journal of Applied Mechanics, 72(2):203–212, 2004.

[86] Emiliano Cadelano, Pier Luca Palla, Stefano Giordano, and Luciano Colombo. Nonlinear Elasticity of Monolayer Graphene. Phys. Rev. Lett., 102:235502, Jun 2009.

[87] Mingyuan Huang, Tod A. Pascal, Hyungjun Kim, William A. Goddard, and Julia R. Greer. Electronic-Mechanical Coupling in Graphene from in situ Nanoindentation Experiments and Multiscale Atomistic Simulations. Nano Letters, 11(3):1241–1246, 2011.

[88] Gwan-Hyoung Lee, Ryan C. Cooper, Sung Joo An, Sunwoo Lee, Arend van der Zande, Nicholas Petrone, Alexandra G. Hammerberg, Changgu Lee, Bryan Crawford, Warren Oliver, Jeffrey W. Kysar, and James Hone. High-Strength Chemical-Vapor–Deposited Graphene and Grain Boundaries. Science, 340(6136):1073–1076, 2013.

[89] Guillermo Lopez-Polin, Cristina Gomez-Navarro, Vincenzo Parente, Francisco Guinea, Mikhail I. Katsnelson, Francesc Perez-Murano, and Julio Gomez-Herrero. Increasing the elastic modulus of graphene by controlled

defect creation. Nat Phys, 11(1):26–31, 2011.

[90] Erik G. Herbert, Warren C. Oliver, Maarten P. de Boer, and George M. Pharr. Measuring the elastic modulus and residual stress of freestanding thin films using nanoindentation techniques. Journal of Materials Research, 24(9):2974–2985, 2011.

[91] C-L Wong, M Annamalai, Z-Q Wang, and M Palaniapan. Characterization of nanomechanical graphene drum structures. Journal of Micromechanics and Microengineering, 20(11):115029, 2010.

[92] Antonio Politano and Gennaro Chiarello. Probing the Young's modulus and Poisson's ratio in graphene/metal interfaces and graphite: a comparative study. Nano Research, 8(6):1847–1856, 2015.

[93] K. V. Zakharchenko, M. I. Katsnelson, and A. Fasolino. Finite Temperature Lattice Properties of Graphene beyond the Quasiharmonic Approximation. Phys. Rev. Lett., 102:046808, Jan 2009.

[94] Fang Liu, Pingbing Ming, and Ju Li. *Ab initio* calculation of ideal strength and phonon instability of graphene under tension. Phys. Rev. B, 76:064120, Aug 2007.

[95] D.-B. Zhang, E. Akatyeva, and T. Dumitrică. Bending Ultrathin Graphene at the Margins of Continuum Mechanics. Phys. Rev. Lett., 106:255503, Jun 2011.

[96] Gang Zhang and Yong-Wei Zhang. Strain effects on thermoelectric properties of two-dimensional materials. Mechanics of Materials, 91, Part 2:382 – 398, 2015. Mechanics of energy conversion and storage.

[97] Ke-Ke Bai, Yu Zhou, Hong Zheng, Lan Meng, Hailin Peng, Zhongfan Liu, Jia-Cai Nie, and Lin He. Creating One-Dimensional Nanoscale Periodic Ripples in a Continuous Mosaic Graphene Monolayer. Phys. Rev. Lett., 113:086102, Aug 2014.

[98] Hichem Hattab, Alpha T. NDiaye, Dirk Wall, Claudius Klein, Giriraj Jnawali, Johann Coraux, Carsten Busse, Raoul van Gastel, Bene Poelsema, Thomas Michely, Frank-J. Meyer zu Heringdorf, and Michael Horn-von Hoegen. Interplay of wrinkles, strain, and lattice parameter in graphene on iridium. Nano Letters, 12(2):678–682, 2012. PMID: 22175792.

[99] Fabien Jean, Tao Zhou, Nils Blanc, Roberto Felici, Johann Coraux, and Gilles Renaud. Topography of the graphene/Ir(111) moiré studied by surface x-ray diffraction. Phys. Rev. B, 91:245424, Jun 2015.

[100] Vitor M. Pereira and A. H. Castro Neto. Strain engineering of graphene's electronic structure. Phys. Rev. Lett., 103:046801, Jul 2009.

[101] Toen Castle, Yigil Cho, Xingting Gong, Euiyeon Jung, Daniel M. Sussman, Shu Yang, and Randall D. Kamien. Making the cut: Lattice *Kirigami* rules. Phys. Rev. Lett., 113:245502, Dec 2014.

[102] Melina K. Blees, Arthur W. Barnard, Peter A. Rose, Samantha P. Roberts, Kathryn L. McGill, Pinshane Y. Huang, Alexander R. Ruyack, Joshua W. Kevek, Bryce Kobrin, David A. Muller, David A. Muller, and Paul L. McEuen. Graphene kirigami. Nature, 524(7564):204–207, 2015.

[103] Bastien F. Grosso and E. J. Mele. Bending rules in graphene kirigami. Phys. Rev. Lett., 115:195501, Nov 2015.

[104] Toen Castle, Daniel M. Sussman, Michael Tanis, and Randall D. Kamien. Additive lattice kirigami. Science Advances, 2(9), 2016.

[105] J.C. Meyer, A.K. Geim, M.I. Katsnelson, K.S. Novoselov, D. Obergfell, S. Roth, C. Girit, and A. Zettl. On the roughness of single- and bi-layer graphene membranes. Solid State Communications, 143(1–2):101–109, 2007. Exploring graphene Recent research advances.

[106] Elena Stolyarova, Kwang Taeg Rim, Sunmin Ryu, Janina Maultzsch, Philip Kim, Louis E. Brus, Tony F. Heinz, Mark S. Hybertsen, and George W. Flynn. High-resolution scanning tunneling microscopy imaging of mesoscopic graphene sheets on an insulating surface. Proceedings of the National Academy of Sciences, 104(22):9209–9212, 2007.

[107] N. A. Vinogradov, A. A. Zakharov, V. Kocevski, J. Rusz, K. A. Simonov, O. Eriksson, A. Mikkelsen, E. Lundgren, A. S. Vinogradov, N. Mårtensson, and A. B. Preobrajenski. Formation and Structure of Graphene Waves on Fe(110). Phys. Rev. Lett., 109:026101, Jul 2012.

[108] J. V. Sloan, A. A. Pacheco Sanjuan, Zhengfei Wang, C. Horvath, and S. Barraza-Lopez. Strain gauge fields for rippled graphene membranes under central mechanical load: An approach beyond first-order continuum elasticity. Phys. Rev. B, 87:155436, 2013.

[109] S. Barraza-Lopez, A. A. Pacheco Sanjuan, Zhengfei Wang, and Vanević. Strain-engineering of graphene's electronic structure beyond continuum elasticity. Solid State Communications, 166:70–75, 2013.

[110] U. Monteverde, J. Pal, M.A. Migliorato, M. Missous, U. Bangert, R. Zan, R. Kashtiban, and D. Powell. Under pressure: Control of strain, phonons and bandgap opening in rippled graphene. Carbon, 91:266–274, 2015.

[111] M. L. Ackerman, P. Kumar, M. Neek-Amal, P. M. Thibado, F. M. Peeters, and Surendra Singh. Anomalous Dynamical Behavior of Freestanding Graphene Membranes. Phys. Rev. Lett., 117:126801, Sep 2016.

[112] K. I. Bolotin, K. J. Sikes, J. Hone, H. L. Stormer, and P. Kim. Temperature-Dependent Transport in Suspended Graphene. Phys. Rev. Lett., 101:096802, Aug 2008.

[113] Eduardo V. Castro, H. Ochoa, M. I. Katsnelson, R. V. Gorbachev, D. C. Elias, K. S. Novoselov, A. K. Geim, and F. Guinea. Limits on Charge Carrier Mobility in Suspended Graphene due to Flexural Phonons. Phys. Rev. Lett., 105:266601, Dec 2010.

[114] Alexander S. Mayorov, Roman V. Gorbachev, Sergey V. Morozov, Liam Britnell, Rashid Jalil, Leonid A. Ponomarenko, Peter Blake, Kostya S. Novoselov, Kenji Watanabe, Takashi Taniguchi, and A. K. Geim. Micrometer-Scale Ballistic Transport in Encapsulated Graphene at Room Temperature. Nano Letters, 11(6):2396–2399, 2011. PMID: 21574627.

[115] S. Das Sarma, Shaffique Adam, E. H. Hwang, and Enrico Rossi. Electronic transport in two-dimensional graphene. Rev. Mod. Phys., 83:407–470, May 2011.

[116] Alessandro Cresti, Norbert Nemec, Blanca Biel, Gabriel Niebler, François Triozon, Gianaurelio Cuniberti, and Stephan Roche. Charge transport in disordered graphene-based low dimensional materials. Nano Research, 1(5):361–394, 2008.

[117] R. Saito, G. Dresselhaus, and M. S. Dresselhaus. Physical Properties of Carbon Nanotubes. World Scientific, Singapore, 1998.

[118] M. Oliva-Leyva and Gerardo G. Naumis. Understanding electron behavior in strained graphene as a reciprocal space distortion. Phys. Rev. B, 88:085430, Aug 2013.

[119] G.E. Volovik and M.A. Zubkov. Emergent geometry experienced by fermions in graphene in the presence of dislocations. Annals of Physics, 356:255–268, 2015.

[120] M. Oliva-Leyva and Gerardo G. Naumis. Generalizing the fermi velocity of strained graphene from uniform to nonuniform strain. Physics Letters A, 379(40–41):2645–2651, 2015.

[121] P. Xu, Yurong Yang, S. D. Barber, M. L. Ackerman, J. K. Schoelz, D. Qi, Igor A. Kornev, Lifeng Dong, L. Bellaiche, Salvador Barraza-Lopez, and P. M. Thibado. Atomic control of strain in freestanding

graphene. Phys. Rev. B, 85:121406, Mar 2012.

[122] Ferdinand Evers and Alexander D. Mirlin. Anderson transitions. Rev. Mod. Phys., 80:1355–1417, Oct 2008.

[123] Yasumasa Hasegawa, Rikio Konno, Hiroki Nakano, and Mahito Kohmoto. Zero modes of tight-binding electrons on the honeycomb lattice. Phys. Rev. B, 74:033413, Jul 2006.

[124] Gerardo G. Naumis and Pedro Roman-Taboada. Mapping of strained graphene into one-dimensional Hamiltonians: Quasicrystals and modulated crystals. Phys. Rev. B, 89:241404, Jun 2014.

[125] Pedro Roman-Taboada and Gerardo G. Naumis. Spectral butterfly and electronic localization in rippled-graphene nanoribbons: Mapping onto effective one-dimensional chains. Phys. Rev. B, 92:035406, Jul 2015.

[126] Fernando de Juan, Mauricio Sturla, and Maria A. H. Vozmediano. Space Dependent Fermi Velocity in Strained Graphene. Phys. Rev. Lett., 108:227205, May 2012.

[127] G.E. Volovik and M.A. Zubkov. Emergent Horava gravity in graphene. Annals of Physics, 340(1):352–368, 2014.

[128] F. Guinea, M. I. Katsnelson, and A. K. Geim. Energy gaps and a zero-field quantum Hall effect in graphene by strain engineering. Nat. Phys., 6:30–33, 2010.

[129] F. Guinea, A. K. Geim, M. I. Katsnelson, and K. S. Novoselov. Generating quantizing pseudomagnetic fields by bending graphene ribbons. Phys. Rev. B, 81:035408, Jan 2010.

[130] Vitor M. Pereira, R. M. Ribeiro, N. M. R. Peres, and A. H. Castro Neto. Optical properties of strained graphene. EPL (Europhysics Letters), 92(6):67001, 2010.

[131] M. Oliva-Leyva and Gerardo G. Naumis. Tunable dichroism and optical absorption of graphene by strain engineering. 2D Materials, 2(2):025001, 2015.

[132] S. Reich, J. Maultzsch, C. Thomsen, and P. Ordejón. Tight-binding description of graphene. Phys. Rev. B, 66:035412, Jul 2002.

[133] Luis E.F. Foa-Torres, Stephan Roche, and Jean-Christophe Charlier. Introduction to Graphene-Based Nanomaterials. Cambridge University Press, 1st edition, 2014.

[134] J E Barrios-Vargas and Gerardo G Naumis. Critical wavefunctions in disordered graphene. Journal of Physics: Condensed Matter, 24(25):255305, 2012.

[135] Yang Li, Xiaowei Jiang, Zhongfan Liu, and Zhirong Liu. Strain effects in graphene and graphene nanoribbons: The underlying mechanism. Nano Research, 3(8):545–556, 2010.

[136] M.I Katsnelson and A.K Geim. Electron scattering on microscopic corrugations in graphene. Philosophical Transactions of the Royal Society of London A: Mathematical, Physical and Engineering Sciences, 366(1863):195–204, 2008.

[137] Y Hatsugai. Topological aspect of graphene physics. Journal of Physics: Conference Series, 334(1):012004, 2011.

[138] Gerardo G. Naumis. Topological map of the Hofstadter butterfly: Fine structure of Chern numbers and Van Hove singularities. Physics Letters A, 380(20):1772–1780, 2016.

[139] D. S. L. Abergel, V. Apalkov, J. Berashevich, K. Ziegler, and Tapash Chakraborty. Properties of graphene: a theoretical perspective. ADVANCES IN PHYSICS, 59(4):261–482, 2010.

[140] Aaron Bostwick, Jessica L. McChesney, Konstantin V. Emtsev, Thomas Seyller, Karsten Horn, Stephen D. Kevan, and Eli Rotenberg. Quasiparticle Transformation during a Metal-Insulator Transition in Graphene. Phys. Rev. Lett., 103:056404, Jul 2009.

[141] J.E. Barrios-Vargas and Gerardo G. Naumis. Electrical conductivity and resonant states of doped graphene considering next-nearest neighbor interaction. Philosophical Magazine, 91(29):3844–3857, 2011.

[142] Rocco Martinazzo, Simone Casolo, and Gian Franco Tantardini. The effect of atomic-scale defects and dopants on graphene electronic structure. In Dr. Sergey Mikhailov, editor, Physics and Applications of Graphene - Theory, chapter 3. InTech, 2010.

[143] Scott Kirkpatrick and Thomas P. Eggarter. Localized states of a binary alloy. Phys. Rev. B, 6:3598–3609, Nov 1972.

[144] Mahito Kohmoto and Bill Sutherland. Electronic states on a penrose lattice. Phys. Rev. Lett., 56:2740–2743, Jun 1986.

[145] Denis Bernard and André LeClair. A classification of 2D random Dirac fermions. Journal of Physics A: Mathematical and General, 35(11):2555, 2002.

[146] F. V. Tikhonenko, A. A. Kozikov, A. K. Savchenko, and R. V. Gorbachev. Transition between Electron Localization and Antilocalization in Graphene. Phys. Rev. Lett., 103:226801, Nov 2009.

[147] M.J Katsnelson. Graphene: Carbon in two dimensions. Cambridge University Press, 1st edition, 2012.

[148] Fernando de Juan, Juan L. Mañes, and Maria A. H. Vozmediano. Gauge fields from strain in graphene. Phys. Rev. B, 87:165131, Apr 2013.

[149] J.C. Phillips and M.F. Thorpe. Constraint theory, vector percolation and glass formation. Solid State Communications, 53(8):699702, 1985.

[150] Hugo M. Flores-Ruiz, Gerardo G. Naumis, and J. C. Phillips. Heating through the glass transition: A rigidity approach to the boson peak. Phys. Rev. B, 82:214201, Dec 2010.

[151] J.C. Phillips. Topology of covalent non-crystalline solids I: Short-range order in chalcogenide alloys. Journal of Non-Crystalline Solids, 34(2):153181, 1979.

[152] H. Suzuura and T. Ando. Phonons and electron-phonon scattering in carbon nanotubes. Phys. Rev. B, 65:235412, 2002.

[153] Eun-Ah Kim and A. H. Castro Neto. Graphene as an electronic membrane. EPL (Europhysics Letters), 84(5):57007, 2008.

[154] R. M. Ribeiro, Vitor M. Pereira, N. M. R. Peres, P. R. Briddon, and A. H. Castro Neto. Strained graphene: tight-binding and density functional calculations. New J. Phys., 11(11):115002, 2009.

[155] T. M. G. Mohiuddin, A. Lombardo, R. R. Nair, A. Bonetti, G. Savini, R. Jalil, N. Bonini, D. M. Basko, C. Galiotis, N. Marzari, K. S. Novoselov, A. K. Geim, and A. C. Ferrari. Uniaxial strain in graphene by Raman spectroscopy: G peak splitting, Grüneisen parameters, and sample orientation. Phys. Rev. B, 79:205433, May 2009.

[156] Fei Ding, Hengxing Ji, Yonghai Chen, Andreas Herklotz, Kathrin Dörr, Yongfeng Mei, Armando Rastelli, and Oliver G. Schmidt. Stretchable Graphene: A Close Look at Fundamental Parameters through Biaxial Straining. Nano Letters, 10(9):3453–3458, 2010. PMID: 20695450.

[157] Y. C. Cheng, Z. Y. Zhu, G. S. Huang, and U. Schwingenschlögl. Grüneisen parameter of the G mode of strained monolayer graphene. Phys. Rev. B, 83:115449, Mar 2011.

[158] M. Oliva-Leyva and Gerardo G. Naumis. Effective dirac hamiltonian for anisotropic honeycomb lattices: Optical properties. Phys. Rev. B, 93:035439, Jan 2016.

[159] I. I. Naumov and A. M. Bratkovsky. Gap opening in graphene by simple periodic inhomogeneous strain. Phys. Rev. B, 84:245444, Dec 2011.

[160] Nicolas Kerszberg and Phanish Suryanarayana. Ab initio strain engineering of graphene: opening bandgaps up to 1 eV. RSC Adv., 5:43810–43814, 2015.

[161] M.A. Zubkov. Emergent gravity and chiral anomaly in Dirac semimetals in the presence of dislocations. Annals of Physics, 360:655–678, 2015.

[162] M. O. Goerbig, J.-N. Fuchs, G. Montambaux, and F. Piéchon. Tilted anisotropic Dirac cones in quinoid-type graphene and α-(BEDT-TTF)$_2$I$_3$. Phys. Rev. B, 78:045415, Jul 2008.

[163] Seon-Myeong Choi, Seung-Hoon Jhi, and Young-Woo Son. Effects of strain on electronic properties of graphene. Phys. Rev. B, 81:081407, Feb 2010.

[164] Zhen Hua Ni, Ting Yu, Yun Hao Lu, Ying Ying Wang, Yuan Ping Feng, and Ze Xiang Shen. Uniaxial Strain on Graphene: Raman Spectroscopy Study and Band-Gap Opening. ACS Nano, 2(11):2301–2305, 2008. PMID: 19206396.

[165] Ni Zhen Hua, Yu Ting, Lu Yun Hao, Wang Ying Ying, Feng Yuan Ping, and Shen Ze Xiang. Uniaxial Strain on Graphene: Raman Spectroscopy Study and Band-Gap Opening. ACS Nano, 3(2):483–483, 2009. doi: 10.1021/nn8008323.

[166] Tsuneya Ando, Yisong Zheng, and Hidekatsu Suzuura. Dynamical Conductivity and Zero-Mode Anomaly in Honeycomb Lattices. Journal of the Physical Society of Japan, 71(5):1318–1324, 2002.

[167] Eduardo Fradkin. Field Theories of Condensed Matter Physics. Cambridge University Press, 2 edition, 2013.

[168] Jing Wang, Guiping Zhang, Fei Ye, and Xiaoqun Wang. Mechanical manipulations on electronic transport of graphene nanoribbons. Journal of Physics: Condensed Matter, 27(22):225305, 2015.

[169] Daniel Huertas-Hernando, F. Guinea, and Arne Brataas. Spin-orbit coupling in curved graphene, fullerenes, nanotubes, and nanotube caps. Phys. Rev. B, 74:155426, Oct 2006.

[170] Juan L. Mañes, Fernando de Juan, Mauricio Sturla, and María A. H. Vozmediano. Generalized effective hamiltonian for graphene under nonuniform strain. Phys. Rev. B, 88:155405, Oct 2013.

[171] R. Carrillo-Bastos, C. León, D. Faria, A. Latgé, E. Y. Andrei, and N. Sandler. Strained fold-assisted transport in graphene systems. Phys. Rev. B, 94:125422, Sep 2016.

[172] DeanC. R., YoungA. F., MericI., LeeC., WangL., SorgenfreiS., WatanabeK., TaniguchiT., KimP., ShepardK. L., and HoneJ. Boron nitride substrates for high-quality graphene electronics. Nat Nano, 5(10):722–726, oct 2010. 10.1038/nnano.2010.172.

[173] M. Kindermann, Bruno Uchoa, and D. L. Miller. Zero-energy modes and gate-tunable gap in graphene on hexagonal boron nitride. Phys. Rev. B, 86:115415, Sep 2012.

[174] F. Amet, J. R. Williams, A. G. F. Garcia, M. Yankowitz, K. Watanabe, T. Taniguchi, and D. Goldhaber-Gordon. Tunneling spectroscopy of graphene-boron-nitride heterostructures. Phys. Rev. B, 85:073405, Feb 2012.

[175] J. Hass, R. Feng, J. E. Millán-Otoya, X. Li, M. Sprinkle, P. N. First, W. A. de Heer, E. H. Conrad, and C. Berger. Structural properties of the multilayer graphene/4H-SiC(000$\bar{1}$) system as determined by surface x-ray diffraction. Phys. Rev. B, 75:214109, Jun 2007.

[176] Indubala I. Satija and Gerardo G. Naumis. Chern and Majorana modes of quasiperiodic systems. Phys. Rev. B, 88:054204, Aug 2013.

[177] Gerardo G. Naumis. Use of the trace map for evaluating localization properties. Phys. Rev. B, 59:11315–11321, May 1999.

[178] Norbert Nemec and Gianaurelio Cuniberti. Hofstadter butterflies of carbon nanotubes: Pseudofractality of the magnetoelectronic spectrum. Phys. Rev. B, 74:165411, Oct 2006.

[179] Ralph Skomski, P. A. Dowben, M. Sky Driver, and Jeffry A. Kelber. Sublattice-induced symmetry breaking and band-gap formation in graphene. Mater. Horiz., 1:563–571, 2014.

[180] Jung Jeil, DaSilva Ashley M., MacDonald Allan H., and Adam Shaffique. Origin of band gaps in graphene on hexagonal boron nitride. Nat Commun, 6, feb 2015.

[181] Wang Eryin, Lu Xiaobo, Ding Shijie, Yao Wei, Yan Mingzhe, Wan Guoliang, Deng Ke, Wang Shuopei, Chen Guorui, Ma Liguo, Jung Jeil, Fedorov Alexei V., Zhang Yuanbo, Zhang Guangyu, and Zhou Shuyun. Gaps induced by inversion symmetry breaking and second-generation Dirac cones in graphene/hexagonal boron nitride. Nat Phys, advance online publication, aug 2016.

[182] Gutierrez Christopher, Kim Cheol-Joo, Brown Lola, Schiros Theanne, Nordlund Dennis, Lochocki Edward B., Shen Kyle M., Park Jiwoong, and Pasupathy Abhay N. Imaging chiral symmetry breaking from Kekule bond order in graphene. Nat Phys, 12(10):950–958, oct 2016.

[183] Xue Jiamin, Sanchez-Yamagishi Javier, Bulmash Danny, Jacquod Philippe, Deshpande Aparna, Watanabe K., Taniguchi T., Jarillo-Herrero Pablo, and LeRoy Brian J. Scanning tunnelling microscopy and spectroscopy of ultra-flat graphene on hexagonal boron nitride. Nat Mater, 10(4):282–285, apr 2011. 10.1038/nmat2968.

[184] Summerfield Alex, Davies Andrew, Cheng Tin S., Korolkov Vladimir V., Cho YongJin, Mellor Christopher J., Foxon C. Thomas, Khlobystov Andrei N., Watanabe Kenji, Taniguchi Takashi, Eaves Laurence, Novikov Sergei V., and Beton Peter H. Strain-Engineered Graphene Grown on Hexagonal Boron Nitride by Molecular Beam Epitaxy. Scientific Reports, 6:22440, mar 2016.

[185] Pablo San-Jose, A. Gutiérrez-Rubio, Mauricio Sturla, and Francisco Guinea. Electronic structure of spontaneously strained graphene on hexagonal boron nitride. Phys. Rev. B, 90:115152, Sep 2014.

[186] Z. F. Wang, Feng Liu, and M. Y. Chou. Fractal landau-level spectra in twisted bilayer graphene. Nano Letters, 12(7):3833–3838, 2012. PMID: 22716657.

[187] Zhou S. Y., Gweon G.-H., Fedorov A. V., First P. N., de Heer W. A., Lee D.-H., Guinea F., Castro Neto A. H., and Lanzara A. Substrate-induced bandgap opening in epitaxial graphene. Nat Mater, 6(10):770–775, oct 2007. 10.1038/nmat2003.

[188] Zhou S.Y., Siegel D.A., Fedorov A.V., Gabaly F.El, Schmid A.K., Neto A.H. Castro, Lee D.-H., and Lanzara A. Origin of the energy bandgap in epitaxial graphene. Nat Mater, 7(4):259–260, apr 2008. 10.1038/nmat2154b.

[189] Bostwick Aaron, Ohta Taisuke, Seyller Thomas, Horn Karsten, and Rotenberg Eli. Quasiparticle dynamics in graphene. Nat Phys, 3(1):36–40, jan 2007. 10.1038/nphys477.

[190] Lingmei Kong, Cameron Bjelkevig, Sneha Gaddam, Mi Zhou, Young Hee Lee, Gang Hee Han, Hae Kyung Jeong, Ning Wu, Zhengzheng Zhang, Jie Xiao, P. A. Dowben, and Jeffry A. Kelber. Graphene/Substrate Charge Transfer Characterized by Inverse Photoelectron Spectroscopy. The Journal of Physical Chemistry C, 114(49):21618–21624, 2010.

[191] Sneha Gaddam, Cameron Bjelkevig, Siping Ge, Keisuke Fukutani, Peter A Dowben, and Jeffry A Kelber. Direct graphene growth on MgO: origin of the band gap.

Journal of Physics: Condensed Matter, 23(7):072204, 2011.

[192] H. García-Cervantes, L. M. Gaggero-Sager, O. Sotolongo-Costa, G. G. Naumis, and I. Rodríguez-Vargas. Angle-dependent bandgap engineering in gated graphene superlattices. AIP Advances, 6(3), 2016.

[193] Farhad Sattari. Spin transport in graphene superlattice under strain. Journal of Magnetism and Magnetic Materials, 414:19–24, 2016.

[194] Xiao-Liang Qi and Shou-Cheng Zhang. Topological insulators and superconductors. Rev. Mod. Phys., 83:1057–1110, Oct 2011.

[195] Shuze Zhu, Joseph A. Stroscio, and Teng Li. Programmable Extreme Pseudomagnetic Fields in Graphene by a Uniaxial Stretch. Phys. Rev. Lett., 115:245501, Dec 2015.

[196] Gomes Kenjiro K., Mar Warren, Ko Wonhee, Guinea Francisco, and Manoharan Hari C. Designer Dirac fermions and topological phases in molecular graphene. Nature, 483(7389):306–310, mar 2012. 10.1038/nature10941.

[197] Polini Marco, Guinea Francisco, Lewenstein Maciej, Manoharan Hari C., and Pellegrini Vittorio. Artificial honeycomb lattices for electrons, atoms and photons. Nat Nano, 8(9):625633, sep 2013.

[198] Liu Y., Li Y. Y., Rajput S., Gilks D., Lari L., Galindo P. L., Weinert M., Lazarov V. K., and Li L. Tuning Dirac states by strain in the topological insulator Bi2Se3. Nat Phys, 10(4):294–299, apr 2014.

[199] Marcos R. Guassi, Ginetom S. Diniz, Nancy Sandler, and Fanyao Qu. Zero-field and time-reserval-symmetry-broken topological phase transitions in graphene. Phys. Rev. B, 92:075426, Aug 2015.

[200] W. P. Su, J. R. Schrieffer, and A. J. Heeger. Solitons in Polyacetylene. Phys. Rev. Lett., 42:1698–1701, Jun 1979.

[201] Sergey S. Pershoguba and Victor M. Yakovenko. Shockley model description of surface states in topological insulators. Phys. Rev. B, 86:075304, Aug 2012.

[202] Sriram Ganeshan, Kai Sun, and S. Das Sarma. Topological zero-energy modes in gapless commensurate aubry-andré-harper models. Phys. Rev. Lett., 110:180403, May 2013.

[203] T. T. Heikkilä, N. B. Kopnin, and G. E. Volovik. Flat bands in topological media. JETP Letters, 94(3):233–239, 2011.

[204] G. E. Volovik. Flat band in topological matter. Journal of Superconductivity and Novel Magnetism, 26(9):2887–2890, 2013.

[205] Thomas Iadecola, David Campbell, Claudio Chamon, Chang-Yu Hou, Roman Jackiw, So-Young Pi, and Silvia Viola Kusminskiy. Materials Design from Nonequilibrium Steady States: Driven Graphene as a Tunable Semiconductor with Topological Properties. Phys. Rev. Lett., 110:176603, Apr 2013.

[206] Pierre Delplace, Álvaro Gómez-León, and Gloria Platero. Merging of dirac points and floquet topological transitions in ac-driven graphene. Phys. Rev. B, 88:245422, Dec 2013.

[207] P. San-Jose, J. L. Lado, R. Aguado, F. Guinea, and J. Fernández-Rossier. Majorana zero modes in graphene. Phys. Rev. X, 5:041042, Dec 2015.

[208] P. Roman-Taboada and G. G. Naumis. Topological flat bands in time-periodically driven uniaxial strained graphene nanoribbons. arXiv:1608.08563, 2016.

[209] P. R. Wallace. The band theory of graphite. Phys. Rev., 71:622–634, May 1947.

[210] J. C. Slonczewski and P. R. Weiss. Band structure of graphite. Phys. Rev., 109:272–279, Jan 1958.

[211] Gordon W. Semenoff. Condensed-matter simulation of a three-dimensional anomaly. Phys. Rev. Lett., 53:2449–2452, Dec 1984.

[212] J. D. Bjorken and S. D. Drell. Relativistic Quantum Mechanics. McGraw-Hill, New York, 1964.

[213] M. I. Katsnelson and K. S. Novoselov. Graphene: New bridge between condensed matter physics and quantum electrodynamics. Solid State Communications, 143(1–2):3–13, 2007.

[214] Daniel R. Cooper, Benjamin D'Anjou, Nageswara Ghattamaneni, Benjamin Harack, Michae Hilke, Alexandre Horth, Norberto Majlis, Mathieu Massicotte, Leron Vandsburger, and Victorl Yu. Experimental review of graphene. ISRN Condensed Matter Physics, 2012:501686, 2012.

[215] Y. Betancur-Ocampo, M.E. Cifuentes-Quintal, G. Cordourier-Maruri, and R. de Coss. Landau levels in uniaxially strained graphene: A geometrical approach. Annals of Physics, 359:243 – 251, 2015.

[216] M. Ramezani Masir, D. Moldovan, and F.M. Peeters. Pseudo magnetic field in strained graphene: Revisited. Solid State Communications, 175–176(0):76–82, 2013.

[217] N. Ray, F. Rost, D. Weckbecker, M. Vogl, S. Sharma, R. Gupta, O. Pankratov, and S. Shallcross. Going beyond k.p theory: a general method for obtaining effective Hamiltonians in both high and low symmetry situations. arXiv:1607.00920, 2016.

[218] M. Oliva-Leyva and Gerardo G. Naumis. Anisotropic AC conductivity of strained graphene. Journal of Physics: Condensed Matter, 26(12):125302, 2014.

[219] M. Oliva-Leyva and Gerardo G. Naumis. Corrigendum: Anisotropic AC conductivity of strained graphene (2014 J. Phys.: Condens. Matter 26 125302). Journal of Physics: Condensed Matter, 26(27):279501, 2014.

[220] Won-Jun Jang, Howon Kim, Yong-Ro Shin, Min Wang, Sung Kyu Jang, Minwoo Kim, Sungjoo Lee, Sang-Woo Kim, Young Jae Song, and Se-Jong Kahng. Observation of spatially-varying Fermi velocity in strained-graphene directly grown on hexagonal boron nitride. Carbon, 74:139–145, 2014.

[221] M. O. Goerbig. Electronic properties of graphene in a strong magnetic field. Rev. Mod. Phys., 83:1193–1243, Nov 2011.

[222] Zakhar V. Khaidukov and Mikhail A. Zubkov. Landau levels in graphene in the presence of emergent gravity. The European Physical Journal B, 89(10):213, 2016.

[223] Yong Zhang. Motion of electrons in semiconductors under inhomogeneous strain with application to laterally confined quantum wells. Phys. Rev. B, 49:14352–14366, May 1994.

[224] T L Linnik. Effective Hamiltonian of strained graphene. Journal of Physics: Condensed Matter, 24(20):205302, 2012.

[225] Hua Tong Yang. Strain induced shift of Dirac points and the pseudo-magnetic field in graphene. Journal of Physics: Condensed Matter, 23(50):505502, 2011.

[226] Alexander L. Kitt, Vitor M. Pereira, Anna K. Swan, and Bennett B. Goldberg. Lattice-corrected strain-induced vector potentials in graphene. Phys. Rev. B, 85:115432, Mar 2012.

[227] Ken-ichi Sasaki and Riichiro Saito. Pseudospin and deformation-induced gauge field in graphene. Progress of Theoretical Physics Supplement, 176:253–278, 2008.

[228] D. C. Cabra, N. E. Grandi, G. A. Silva, and M. B. Sturla. Low-energy electron-phonon effective action from symmetry analysis. Phys. Rev. B, 88:045126, Jul 2013.

[229] Alfredo Iorio and Pablo Pais. Revisiting the gauge fields of strained graphene. Phys. Rev. D, 92:125005, Dec 2015.

[230] Enrique Arias, Alexis R. Hernández, and Caio Lewenkopf. Gauge fields in graphene with nonuniform elastic deformations: A quantum field theory approach. Phys.

Rev. B, 92:245110, Dec 2015.

[231] Alberto Cortijo and M.A. Zubkov. Emergent gravity in the cubic tight-binding model of Weyl semimetal in the presence of elastic deformations. Annals of Physics, 366:45–56, 2016.

[232] C. D. Froggatt and H. B. Nielsen. Origin of Symmetry. World Scientific, Singapore, 1991.

[233] G. E. Volovik. The Universe in a Helium Droplet. Clarendon Press, Oxford, 2003.

[234] Petr Hořava. Stability of Fermi Surfaces and K Theory. Phys. Rev. Lett., 95:016405, Jun 2005.

[235] Diana A. Gradinar, Marcin Mucha-Kruczyński, Henning Schomerus, and Vladimir I. Fal'ko. Transport signatures of pseudomagnetic landau levels in strained graphene ribbons. Phys. Rev. Lett., 110:266801, Jun 2013.

[236] Dario A. Bahamon, Zenan Qi, Harold S. Park, Vitor M. Pereira, and David K. Campbell. Conductance signatures of electron confinement induced by strained nanobubbles in graphene. Nanoscale, 7:15300–15309, 2015.

[237] Thomas Stegmann and Nikodem Szpak. Current flow paths in deformed graphene: from quantum transport to classical trajectories in curved space. New Journal of Physics, 18(5):053016, 2016.

[238] Jörn W. F. Venderbos and Liang Fu. Interacting dirac fermions under a spatially alternating pseudomagnetic field: Realization of spontaneous quantum hall effect. Phys. Rev. B, 93:195126, May 2016.

[239] V. J. Kauppila, F. Aikebaier, and T. T. Heikkilä. Flat-band superconductivity in strained dirac materials. Phys. Rev. B, 93:214505, Jun 2016.

[240] Mikkel Settnes, Stephen R. Power, and Antti-Pekka Jauho. Pseudomagnetic fields and triaxial strain in graphene. Phys. Rev. B, 93:035456, Jan 2016.

[241] N.-C. Yeh, C.-C. Hsu, M. L. Teague, J.-Q. Wang, D. A. Boyd, and C.-C. Chen. Nanoscale strain engineering of graphene and graphene-based devices. Acta Mechanica Sinica, 32(3):497–509, 2016.

[242] Mikkel Settnes, Nicolas Leconte, Jose E Barrios-Vargas, Antti-Pekka Jauho, and Stephan Roche. Quantum transport in graphene in presence of strain-induced pseudo-landau levels. 2D Materials, 3(3):034005, 2016.

[243] David L. Miller, Kevin D. Kubista, Gregory M. Rutter, Ming Ruan, Walt A. de Heer, Phillip N. First, and Joseph A. Stroscio. Observing the quantization of zero mass carriers in graphene. Science, 324(5929):924–927, 2009.

[244] N.-C. Yeh, M.-L. Teague, S. Yeom, B.L. Standley, R.T.-P. Wu, D.A. Boyd, and M.W. Bockrath. Strain-induced pseudo-magnetic fields and charging effects on cvd-grown graphene. Surface Science, 605(1718):1649 – 1656, 2011. Graphene Surfaces and Interfaces.

[245] Jiong Lu, A.H. Castro Neto, and Kian Ping Loh. Transforming moiré blisters into geometric graphene nano-bubbles. Nat Commun, 3:823, May 2012.

[246] Donghui Guo et al. Observation of landau levels in potassium-intercalated graphite under a zero magnetic field. Nat Commun, 3:1068, Sept 2012.

[247] Nikolai N. Klimov, Suyong Jung, Shuze Zhu, Teng Li, C. Alan Wright, Santiago D. Solares, David B. Newell, Nikolai B. Zhitenev, and Joseph A. Stroscio. Electromechanical properties of graphene drumheads. Science, 336(6088):1557–1561, 2012.

[248] Lan Meng, Wen-Yu He, Hong Zheng, Mengxi Liu, Hui Yan, Wei Yan, Zhao-Dong Chu, Keke Bai, Rui-Fen Dou, Yanfeng Zhang, Zhongfan Liu, Jia-Cai Nie, and Lin He. Strain-induced one-dimensional landau level quantization in corrugated graphene. Phys. Rev. B, 87:205405, May 2013.

[249] Si-Yu Li, Ke-Ke Bai, Long-Jing Yin, Jia-Bin Qiao, Wen-Xiao Wang, and Lin He. Observation of unconventional splitting of landau levels in strained graphene. Phys. Rev. B, 92:245302, Dec 2015.

[250] Wei Yan, Si-Yu Li, Long-Jing Yin, Jia-Bin Qiao, Jia-Cai Nie, and Lin He. Spatially resolving unconventional interface landau quantization in a graphene monolayer-bilayer planar junction. Phys. Rev. B, 93:195408, May 2016.

[251] Alexander Georgi et al. Tunable pseudo-zeeman effect in graphene. arXiv:1611.06123, 2016.

[252] Mikael C. Rechtsman, Julia M. Zeuner, Andreas Tunnermann, Stefan Nolte, Mordechai Segev, and Alexander Szameit. Strain-induced pseudomagnetic field and photonic landau levels in dielectric structures. Nat Photon, 7(2):153158, feb 2013. 10.1038/nphoton.2012.302.

[253] Binbin Tian, Manuel Endres, and David Pekker. Landau levels in strained optical lattices. Phys. Rev. Lett., 115:236803, Dec 2015.

[254] Eros Mariani, Alexander J. Pearce, and Felix von Oppen. Fictitious gauge fields in bilayer graphene. Phys. Rev. B, 86:165448, Oct 2012.

[255] Wei Yan, Wen-Yu He, Zhao-Dong Chu, Mengxi Liu, Lan Meng, Rui-Fen Dou, Yanfeng Zhang, Zhongfan Liu, Jia-Cai Nie, and Lin He. Strain and curvature induced evolution of electronic band structures in twisted graphene bilayer. Nature Communications, 4:2159, jul 2013.

[256] Wen-Yu He, Ying Su, Mudan Yang, and Lin He. Creating in-plane pseudomagnetic fields in excess of 1000 T by misoriented stacking in a graphene bilayer. Phys. Rev. B, 89:125418, Mar 2014.

[257] A. D. Zabolotskiy and Yu. E. Lozovik. Strain-induced pseudomagnetic field in the dirac semimetal borophene. Phys. Rev. B, 94:165403, Oct 2016.

[258] Evelyn Tang and Liang Fu. Strain-induced partially flat band, helical snake states and interface superconductivity in topological crystalline insulators. Nat Phys, 10:964, Dec 2014.

[259] Alexander J. Pearce, Eros Mariani, and Guido Burkard. Tight-binding approach to strain and curvature in monolayer transition-metal dichalcogenides. Phys. Rev. B, 94:155416, Oct 2016.

[260] Hector Ochoa, Ricardo Zarzuela, and Yaroslav Tserkovnyak. Emergent gauge fields from curvature in single layers of transition metal dichalcogenides. arXiv:1605.07326, 2016.

[261] Alberto Cortijo, Yago Ferreirós, Karl Landsteiner, and María A. H. Vozmediano. Elastic gauge fields in weyl semimetals. Phys. Rev. Lett., 115:177202, Oct 2015.

[262] D. I. Pikulin, Anffany Chen, and M. Franz. Chiral anomaly from strain-induced gauge fields in dirac and weyl semimetals. Phys. Rev. X, 6:041021, Oct 2016.

[263] Adolfo G. Grushin, Jorn W. F. Venderbos, Ashvin Vishwanath, and Roni Ilan. Inhomogeneous weyl and dirac semimetals: Transport in axial magnetic fields and fermi arc surface states from pseudo landau levels. arXiv:1607.04268, 2016.

[264] N M R Peres. Scattering in one-dimensional heterostructures described by the dirac equation. Journal of Physics: Condensed Matter, 21(9):095501, 2009.

[265] Victor Atanasov and Avadh Saxena. Tuning the electronic properties of corrugated graphene: Confinement, curvature, and band-gap opening. Phys. Rev. B, 81:205409, May 2010.

[266] Fernando de Juan, Alberto Cortijo, and María A. H. Vozmediano. Charge inhomogeneities due to smooth ripples in graphene sheets. Phys. Rev. B, 76:165409, Oct 2007.

[267] Arnaud Raoux, Marco Polini, Reza Asgari, A. R. Hamil-

ton, Rosario Fazio, and A. H. MacDonald. Velocity-modulation control of electron-wave propagation in graphene. Phys. Rev. B, 81:073407, Feb 2010.

[268] P. V. Ratnikov and A. P. Silin. Novel type of superlattices based on gapless graphene with the alternating fermi velocity. JETP Letters, 100(5):311–318, 2014.

[269] Jonas R.F. Lima and F. Moraes. Indirect band gap in graphene from modulation of the fermi velocity. Solid State Communications, 201:82 – 87, 2015.

[270] Jonas R. F. Lima, Luiz Felipe C. Pereira, and C. G. Bezerra. Controlling resonant tunneling in graphene via fermi velocity engineering. Journal of Applied Physics, 119(24), 2016.

[271] Felix von Oppen, Francisco Guinea, and Eros Mariani. Synthetic electric fields and phonon damping in carbon nanotubes and graphene. Phys. Rev. B, 80:075420, Aug 2009.

[272] Mircea Trif, Pramey Upadhyaya, and Yaroslav Tserkovnyak. Theory of electromechanical coupling in dynamical graphene. Phys. Rev. B, 88:245423, Dec 2013.

[273] Abolhassan Vaezi, Nima Abedpour, Reza Asgari, Alberto Cortijo, and María A. H. Vozmediano. Topological electric current from time-dependent elastic deformations in graphene. Phys. Rev. B, 88:125406, Sep 2013.

[274] Kai Zhang, Erhu Zhang, Huawei Chen, and Shengli Zhang. Odd-parity currents induced by dynamic deformations in graphene-like systems. Journal of Physics: Condensed Matter, 28(45):455301, 2016.

[275] Ken-ichi Sasaki, Hideki Gotoh, and Yasuhiro Tokura. Valley-antisymmetric potential in graphene under dynamical deformation. Phys. Rev. B, 90:205402, Nov 2014.

[276] M Oliva-Leyva and Gerardo G Naumis. Sound waves induce volkov-like states, band structure and collimation effect in graphene. Journal of Physics: Condensed Matter, 28(2):025301, 2016.

[277] Feng Zhai, Xiaofang Zhao, Kai Chang, and H. Q. Xu. Magnetic barrier on strained graphene: A possible valley filter. Phys. Rev. B, 82:115442, Sep 2010.

[278] D. M. Wolkow. Über eine klasse von lösungen der diracschen gleichung. Zeitschrift für Physik, 94(3):250–260, 1935.

[279] F. J. López-Rodríguez and G. G. Naumis. Analytic solution for electrons and holes in graphene under electromagnetic waves: Gap appearance and nonlinear effects. Phys. Rev. B, 78:201406, Nov 2008.

[280] Cheol-Hwan Park, Young-Woo Son, Li Yang, Marvin L. Cohen, and Steven G. Louie. Electron beam supercollimation in graphene superlattices. Nano Letters, 8(9):2920–2924, 2008.

[281] Zhengfei Wang and Feng Liu. Manipulation of electron beam propagation by hetero-dimensional graphene junctions. ACS Nano, 4(4):2459–2465, 2010.

[282] Gonzalo Usaj, P. M. Perez-Piskunow, L. E. F. Foa Torres, and C. A. Balseiro. Irradiated graphene as a tunable Floquet topological insulator. Phys. Rev. B, 90:115423, Sep 2014.

[283] Alexander I. Bobenko, Peter Schr´oder, John M. Sullivan, and G. M. Ziegler, editors. Discrete Differential Geometry, volume 38 of Oberwolfach Seminars. Birkhuser, Basel, 1 edition, 2008.

[284] A. A. Pacheco Sanjuan, Zhengfei Wang, H. P. Imani, M. Vanević, and S. Barraza-Lopez. Graphene's morphology and electronic properties from discrete differential geometry. Phys. Rev. B, 89:121403, 2014.

[285] F. Guinea. Strain engineering in graphene. Solid State Communications, 152(15):1437 – 1441, 2012. Exploring Graphene, Recent Research Advances.

[286] J. Zhou and R. Huang. Internal lattice relaxation of single-layer graphene under in-plane deformation. J. Mech. Phys. Solids, 56:1609–1623, 2007.

[287] G. J. Verbiest, C. Stampfer, S. E. Huber, M. Andersen, and K. Reuter. Interplay between nanometer-scale strain variations and externally applied strain in graphene. Phys. Rev. B, 93:195438, May 2016.

[288] Alejandro A. Pacheco Sanjuan, Mehrshad Mehboudi, Edmund O. Harriss, Humberto Terrones, and Salvador Barraza-Lopez. Quantitative chemistry and the discrete geometry of conformal atom-thin crystals. ACS Nano, 8(2):1136–1146, 2014. PMID: 24400916.

[289] Zhiqiang Xu and Guoliang Xu. Discrete schemes for gaussian curvature and their convergence. Computers and Mathematics with Applications, 57(7):1187 – 1195, 2009.

[290] P. Hohenberg and W. Kohn. Inhomogeneous electron gas. Phys. Rev., 136:B864–B871, Nov 1964.

[291] Mel Levy. Universal variational functionals of electron densities, first-order density matrices, and natural spin-orbitals and solution of the v-representability problem. Proceedings of the National Academy of Sciences, 76(12):6062–6065, 1979.

[292] L. Hedin and B. I. Lundqvist. Explicit local exchange-correlation potentials. Journal of Physics C: Solid State Physics, 4(14):2064, 1971.

[293] D. M. Ceperley and B. J. Alder. Ground state of the electron gas by a stochastic method. Phys. Rev. Lett., 45:566–569, Aug 1980.

[294] John P. Perdew and Yue Wang. Accurate and simple analytic representation of the electron-gas correlation energy. Phys. Rev. B, 45:13244–13249, Jun 1992.

[295] A. D. Becke. A multicenter numerical integration scheme for polyatomic molecules. The Journal of Chemical Physics, 88(4):2547–2553, 1988.

[296] Chengteh Lee, Weitao Yang, and Robert G. Parr. Development of the colle-salvetti correlation-energy formula into a functional of the electron density. Phys. Rev. B, 37:785–789, Jan 1988.

[297] On line Castep Theory Manual, Materials Studio 2016, Biovia Dassault Systèmes.

[298] Xavier Gonze, Douglas C. Allan, and Michael P. Teter. Dielectric tensor, effective charges, and phonons in α-quartz by variational density-functional perturbation theory. Phys. Rev. Lett., 68:3603–3606, Jun 1992.

[299] Stefano Baroni, Stefano de Gironcoli, Andrea Dal Corso, and Paolo Giannozzi. Phonons and related crystal properties from density-functional perturbation theory. Rev. Mod. Phys., 73:515–562, Jul 2001.

[300] Xavier Gonze. First-principles responses of solids to atomic displacements and homogeneous electric fields: Implementation of a conjugate-gradient algorithm. Phys. Rev. B, 55:10337–10354, Apr 1997.

[301] Jean-Christophe Charlier, Xavier Blase, and Stephan Roche. Electronic and transport properties of nanotubes. Rev. Mod. Phys., 79:677–732, May 2007.

[302] M. I. Heggie, M. Terrones, B. R. Eggen, G. Jungnickel, R. Jones, C. D. Latham, P. R. Briddon, and H. Terrones. Quantitative density-functional study of nested fullerenes. Phys. Rev. B, 57:13339–13342, Jun 1998.

[303] Thomas Lenosky, Xavier Gonze, Michael Teter, and Vert Elser. Energetics of negatively curved graphitic carbon. Nature, 355(6358):333335, jan 1992. 10.1038/355333a0.

[304] Aurélien Lherbier, Humberto Terrones, and Jean-Christophe Charlier. Three-dimensional massless dirac fermions in carbon schwarzites. Phys. Rev. B, 90:125434, Sep 2014.

[305] Gui Gui, Jin Li, and Jianxin Zhong. Band structure engineering of graphene by strain: First-principles calculations. Phys. Rev. B, 78:075435, Aug 2008.

[306] R. R. Nair et al. Fine Structure Constant Defines Visual Transparency of Graphene. Science, 320(5881):1308, 2008.

[307] Kin Fai Mak et al. Measurement of the Optical Conductivity of Graphene. Phys. Rev. Lett., 101:196405, Nov 2008.

[308] V. P. Gusynin, S. G. Sharapov, and J. P. Carbotte. AC conductivity of graphene: from tight-binding model to 2 + 1-dimensional quantum electrodynamics. International Journal of Modern Physics B, 21(27):4611–4658, 2007.

[309] S. A. Mikhailov and K. Ziegler. New Electromagnetic Mode in Graphene. Phys. Rev. Lett., 99:016803, Jul 2007.

[310] T. Stauber, D. Noriega-Pérez, and J. Schliemann. Universal absorption of two-dimensional systems. Phys. Rev. B, 91:115407, Mar 2015.

[311] G. L. Klimchitskaya and V. M. Mostepanenko. Conductivity of pure graphene: Theoretical approach using the polarization tensor. Phys. Rev. B, 93:245419, Jun 2016.

[312] F. M. D. Pellegrino, G. G. N. Angilella, and R. Pucci. Strain effect on the optical conductivity of graphene. Phys. Rev. B, 81:035411, 2010.

[313] F. M. D. Pellegrino, G. G. N. Angilella, and R. Pucci. Linear response correlation functions in strained graphene. Phys. Rev. B, 84:195407, Nov 2011.

[314] Saúl Hernández-Ortiz, David Valenzuela, Alfredo Raya, and Saúl Sánchez-Madrigal. Light absorption in distorted graphene. International Journal of Modern Physics B, 30(14):1650084, 2016.

[315] Shaloo Rakheja and Parijat Sengupta. The tuning of light-matter coupling and dichroism in graphene for enhanced absorption: Implications for graphene-based optical absorption devices. Journal of Physics D: Applied Physics, 49(11):115106, 2016.

[316] Huy-Viet Nguyen and V. Hung Nguyen. Comment on "Orientation dependence of the optical spectra in graphene at high frequencies". Phys. Rev. B, 94:117401, Sep 2016.

[317] Jin-Hui Chen, Wei Luo, Zhao-Xian Chen, Shao-Cheng Yan, Fei Xu, and Yan-Qing Lu. Mechanical Modulation of a Hybrid Graphene–Microfiber Structure. Advanced Optical Materials, 4(6):853–857, 2016.

[318] Guang-Xin Ni, Hong-Zhi Yang, Wei Ji, Seung-Jae Baeck, Chee-Tat Toh, Jong-Hyun Ahn, Vitor M. Pereira, and Barbaros Ozyilmaz. Tuning Optical Conductivity of Large-Scale CVD Graphene by Strain Engineering. Advanced Materials, 26(7):1081–1086, 2014.

[319] DS Bethune, G Meijer, WC Tang, HJ Rosen, WG Golden, H Seki, CA Brown, and MS Devries. Vibrational Raman and Infrared-Spectra of Chromatographically separated C_{60} and C_{70} Fullerene Clusters. Chemical Physics Letters, 179(1-2):181–186, APR 12 1991.

[320] MS Dresselhaus, G Dresselhaus, R Saito, and A Jorio. Raman spectroscopy of carbon nanotubes. Physics Reports- Review Section of Physics Letters, 409(2):47–99, MAR 2005.

[321] A. C. Ferrari, J. C. Meyer, V. Scardaci, C. Casiraghi, M. Lazzeri, F. Mauri, S. Piscanec, D. Jiang, K. S. Novoselov, S. Roth, and A. K. Geim. Raman spectrum of graphene and graphene layers. Physical Review Letters, 97(18), NOV 3 2006.

[322] Andrea C. Ferrari. Raman spectroscopy of graphene and graphite: Disorder, electron-phonon coupling, doping and nonadiabatic effects. Solid State Communications, 143(1-2):47–57, JUL 2007.

[323] Andrea C. Ferrari and Denis M. Basko. Raman spectroscopy as a versatile tool for studying the properties of graphene. Nature nanotechnology, 8(4):235–246, APR 2013.

[324] Eric J. Heller, Yuan Yang, Lucas Kocia, Wei Chen, Shiang Fang, Mario Borunda, and Efthimios Kaxiras. Theory of graphene raman scattering. ACS Nano, 10(2):2803–2818, 2016. PMID: 26799915.

[325] Ruitao Lv, Qing Li, Andres R. Botello-Mendez, Takuya Hayashi, Bei Wang, Ayse Berkdemir, Qingzhen Hao, Ana Laura Elias, Rodolfo Cruz-Silva, Humberto R. Gutierrez, Yoong Ahm Kim, Hiroyuki Muramatsu, Jun Zhu, Morinobu Endo, Humberto Terrones, Jean-Christophe Charlier, Minghu Pan, and Mauricio Terrones. Nitrogen-doped graphene: beyond single substitution and enhanced molecular sensing. Scientific Reports, 2, AUG 17 2012.

[326] Mingyuan Huang, Hugen Yan, Changyao Chen, Daohua Song, Tony F. Heinz, and James Hone. Phonon softening and crystallographic orientation of strained graphene studied by raman spectroscopy. Proceedings of the National Academy of Sciences, 106(18):7304–7308, 2009.

[327] Mingyuan Huang, Hugen Yan, Tony F. Heinz, and James Hone. Probing Strain-Induced Electronic Structure Change in Graphene by Raman Spectroscopy. Nano Letters, 10(10):4074–4079, OCT 2010.

[328] Androulidakis Charalampos, Koukaras Emmanuel N., Parthenios John, Kalosakas George, Papagelis Konstantinos, and Galiotis Costas. Graphene flakes under controlled biaxial deformation. Scientific Reports, 5:18219, dec 2015.

[329] Ruitao Lv, Humberto Terrones, Ana Laura Elias, Nestor Perea-Lopez, Humberto R. Gutierrez, Eduardo Cruz-Silva, Lakshmy Pulickal Rajukumar, Mildred S. Dresselhaus, and Mauricio Terrones. Two-dimensional transition metal dichalcogenides: Clusters, ribbons, sheets and more. Nano Today, 10(5):559–592, OCT 2015.

[330] H. Terrones, E. Del Corro, S. Feng, J. M. Poumirol, D. Rhodes, D. Smirnov, N. R. Pradhan, Z. Lin, M. A. T. Nguyen, A. L. Elias, T. E. Mallouk, L. Balicas, M. A. Pimenta, and M. Terrones. New First Order Raman-active Modes in Few Layered Transition Metal Dichalcogenides. Scientific Reports, 4, FEB 27 2014.

[331] Liangbo Liang and Vincent Meunier. First-principles Raman spectra of MoS2, WS2 and their heterostructures. Nanoscale, 6(10):5394–5401, 2014.

[332] Shuang Zhang, Jiong Yang, Renjing Xu, Fan Wang, Weifeng Li, Muhammad Ghufran, Yong-Wei Zhang, Zongfu Yu, Gang Zhang, Qinghua Qin, and Yuerui Lu. Extraordinary Photoluminescence and Strong Temperature/Angle-Dependent Raman Responses in Few-Layer Phosphorene. Acs Nano, 8(9):9590–9596, SEP 2014.

[333] Xi Ling, Liangbo Liang, Shengxi Huang, Alexander A. Puretzky, David B. Geohegan, Bobby G. Sumpter, Jing Kong, Vincent Meunier, and Mildred S. Dresselhaus. Low-Frequency Interlayer Breathing Modes in Few-Layer Black Phosphorus. Nano Letters, 15(6):4080–4088, JUN 2015.

[334] Cheol-Joo Kim, A. Sánchez-Castillo, Zack Ziegler, Yui Ogawa, Cecilia Noguez, and Jiwoong Park. Chiral atomically thin films. Nat Nano, 11(6):520524, jun 2016.

[335] Taemin Lee, Sa Hoon Min, Minsu Gu, Yun Kyung Jung, Wonoh Lee, Jea Uk Lee, Dong Gi Seong, and Byeong-Su Kim. Layer-by-Layer Assembly for Graphene-Based Multilayer Nanocomposites: Synthesis and Applications. Chemistry of Materials, 27(11):3785–3796, 2015.

[336] Sylvain Latil, Vincent Meunier, and Luc Henrard. Massless fermions in multilayer graphitic systems

with misoriented layers: *Ab initio* calculations and experimental fingerprints. Phys. Rev. B, 76:201402, Nov 2007.

[337] Freitag Marcus. Graphene: Trilayers unravelled. Nat Phys, 7(8):596–597, aug 2011. 10.1038/nphys2032.

[338] Edward McCann and Mikito Koshino. The electronic properties of bilayer graphene. Reports on Progress in Physics, 76(5):056503, 2013.

[339] A. B. Kuzmenko, I. Crassee, D. van der Marel, P. Blake, and K. S. Novoselov. Determination of the gate-tunable band gap and tight-binding parameters in bilayer graphene using infrared spectroscopy. Phys. Rev. B, 80:165406, Oct 2009.

[340] Bao W., Jing L., Velasco J. , Lee Y., Liu G., Tran D., Standley B., Aykol M., Cronin S. B., Smirnov D., Koshino M., McCann E., Bockrath M., and Lau C. N. Stacking-dependent band gap and quantum transport in trilayer graphene. Nat Phys, 7(12):948–952, dec 2011. 10.1038/nphys2103.

[341] VelascoJ. , JingL., BaoW., LeeY., KratzP., AjiV., BockrathM., LauC. N., VarmaC., StillwellR., SmirnovD., Zhang Fan, JungJ., and MacDonaldA. H. Transport spectroscopy of symmetry-broken insulating states in bilayer graphene. Nat Nano, 7(3):156–160, mar 2012. 10.1038/nnano.2011.251.

[342] Velasco Jr J., Lee Y., Zhang F., Myhro K., Tran D., Deo M., Smirnov D., MacDonald A. H., and Lau C. N. Competing ordered states with filling factor two in bilayer graphene. Nature Communications, 5:4550, jul 2014.

[343] B. R. K. Nanda and S. Satpathy. Strain and electric field modulation of the electronic structure of bilayer graphene. Phys. Rev. B, 80:165430, Oct 2009.

[344] B. Verberck, B. Partoens, F. M. Peeters, and B. Trauzettel. Strain-induced band gaps in bilayer graphene. Phys. Rev. B, 85:125403, Mar 2012.

[345] Dean Moldovan and Francois M. Peeters. Strain engineering of the electronic properties of bilayer graphene quantum dots. physica status solidi (RRL) – Rapid Research Letters, 10(1):39–45, 2016.

[346] Eva Y Andrei, Guohong Li, and Xu Du. Electronic properties of graphene: a perspective from scanning tunneling microscopy and magnetotransport. Reports on Progress in Physics, 75(5):056501, 2012.

[347] Mehrshad Mehboudi, Benjamin M. Fregoso, Yurong Yang, Wenjuan Zhu, Arend van der Zande, Jaime Ferrer, L. Bellaiche, Pradeep Kumar, and Salvador Barraza-Lopez. Structural phase transition and material properties of few-layer monochalcogenides. arXiv:1603.03748 (accepted at PRL on 11/14/2016), 2016.

[348] S. Cahangirov, M. Topsakal, E. Aktürk, H. Şahin, and S. Ciraci. Two- and one-dimensional honeycomb structures of silicon and germanium. Phys. Rev. Lett., 102:236804, Jun 2009.

[349] Li Tao, Eugenio Cinquanta, Daniele Chiappe, Carlo Grazianetti, Marco Fanciulli, Madan Dubey, Alessandro Moll, and Deji Akinwande. Silicene field-effect transistors operating at room temperature. Nat. Nano, 10:227–231, Feb 2014.

[350] Suman Chowdhury and Debnarayan Jana. A theoretical review on electronic, magnetic and optical properties of silicene. Reports on Progress in Physics, 79(12):126501, 2016.

[351] Abdelkader Kara, Hanna Enriquez, Ari P. Seitsonen, L.C. Lew Yan Voon, Sébastien Vizzini, Bernard Aufray, and Hamid Oughaddou. A review on silicene — New candidate for electronics. Surface Science Reports, 67(1):1–18, 2012.

[352] Gian G. Guzmán-Verri and L. C. Lew Yan Voon. Electronic structure of silicon-based nanostructures. Phys. Rev. B, 76:075131, Aug 2007.

[353] T. P. Kaloni, Y. C. Cheng, and U. Schwingenschlögl. Hole doped Dirac states in silicene by biaxial tensile strain. Journal of Applied Physics, 113(10), 2013.

[354] Jia-An Yan, Mack A. Dela Cruz, Salvador Barraza-Lopez, and Li Yang. Strain-tunable topological quantum phase transition in buckled honeycomb lattices. Applied Physics Letters, 106(18), 2015.

[355] C. L. Kane and E. J. Mele. Quantum spin hall effect in graphene. Phys. Rev. Lett., 95:226801, Nov 2005.

[356] Motohiko Ezawa. A topological insulator and helical zero mode in silicene under an inhomogeneous electric field. New Journal of Physics, 14(3):033003, 2012.

[357] Motohiko Ezawa. Valley-polarized metals and quantum anomalous hall effect in silicene. Phys. Rev. Lett., 109:055502, Aug 2012.

[358] Jia-An Yan, Shang-Peng Gao, Ryan Stein, and Gregory Coard. Tuning the electronic structure of silicene and germanene by biaxial strain and electric field. Phys. Rev. B, 91:245403, Jun 2015.

[359] M. R. Chavez-Castillo, M. A. Rodriguez-Meza, and L. Meza-Montes. Size, vacancy and temperature effects on Young's modulus of silicene nanoribbons. RSC Adv., 5:96052–96061, 2015.

[360] Pablo Rivero, Jia-An Yan, Víctor M. García-Suárez, Jaime Ferrer, and Salvador Barraza-Lopez. Stability and properties of high-buckled two-dimensional tin and lead. Phys. Rev. B, 90:241408, Dec 2014.

[361] Yandong Ma, Ying Dai, Meng Guo, Chengwang Niu, and Baibiao Huang. Intriguing behavior of halogenated two-dimensional tin. The Journal of Physical Chemistry C, 116(23):12977–12981, 2012.

[362] Yong Xu, Binghai Yan, Hai-Jun Zhang, Jing Wang, Gang Xu, Peizhe Tang, Wenhui Duan, and Shou-Cheng Zhang. Large-gap quantum spin hall insulators in tin films. Phys. Rev. Lett., 111:136804, Sep 2013.

[363] Lídia C. Gomes and A. Carvalho. Phosphorene analogues: Isoelectronic two-dimensional group-iv monochalcogenides with orthorhombic structure. Phys. Rev. B, 92:085406, Aug 2015.

[364] David Wales. Energy Landscapes: Applications to Clusters, Biomolecules and Glasses. Cambridge U. Press, UK, 2001.

[365] A. S. Rodin, A. Carvalho, and A. H. Castro Neto. Strain-induced gap modification in black phosphorus. Phys. Rev. Lett., 112:176801, May 2014.

[366] Ruixiang Fei and Li Yang. Strain-engineering the anisotropic electrical conductance of few-layer black phosphorus. Nano Letters, 14(5):2884–2889, 2014.

[367] A. N. Rudenko and M. I. Katsnelson. Quasiparticle band structure and tight-binding model for single- and bilayer black phosphorus. Phys. Rev. B, 89:201408, May 2014.

[368] Deniz Çakır, Hasan Sahin, and François M. Peeters. Tuning of the electronic and optical properties of single-layer black phosphorus by strain. Phys. Rev. B, 90:205421, Nov 2014.

[369] Han Liu, Adam T. Neal, Zhen Zhu, Zhe Luo, Xianfan Xu, David Tomnek, and Peide D. Ye. Phosphorene: An unexplored 2d semiconductor with a high hole mobility. ACS Nano, 8(4):4033–4041, 2014.

[370] Hugh O. H. Churchill and Pablo Jarillo-Herrero. Two-dimensional crystals: Phosphorus joins the family. Nat. Nano, 9:330–331, 2014.

[371] Xi Ling, Han Wang, Shengxi Huang, Fengnian Xia, and Mildred S. Dresselhaus. The renaissance of black phosphorus. Proceedings of the National Academy of Sciences, 112(15):4523–4530, 2015.

[372] Zhen Zhu and David Tománek. Semiconducting layered blue phosphorus: A computational study. Phys. Rev.

Lett., 112:176802, May 2014.

[373] Jie Guan, Zhen Zhu, and David Tománek. Phase coexistence and metal-insulator transition in few-layer phosphorene: A computational study. Phys. Rev. Lett., 113:046804, Jul 2014.

[374] Jie Guan, Zhen Zhu, and David Tománek. Tiling phosphorene. ACS Nano, 8(12):12763–12768, 2014. PMID: 25418761.

[375] Menghao Wu, Huahua Fu, Ling Zhou, Kailun Yao, and Xiao Cheng Zeng. Nine new phosphorene polymorphs with non-honeycomb structures: A much extended family. Nano Letters, 15(5):3557–3562, 2015. PMID: 25844524.

[376] Li Likai, Yu Yijun, Ye Guo Jun, Ge Qingqin, Ou Xuedong, Wu Hua, Feng Donglai, Chen Xian Hui, and Zhang Yuanbo. Black phosphorus field-effect transistors. Nat Nano, 9(5):372377, may 2014.

[377] Marcel Demarteau Saptarshi Das and Andreas Roelofs. Ambipolar phosphorene field effect transistor. ACS Nano, 8(11):11730–11738, 2014.

[378] Changfeng Chen Liangzhi Kou and Sean C. Smith. Phosphorene: Fabrication, properties, and applications. The Journal of Physical Chemistry Letters, 6(14):2794–2805, 2015.

[379] Jin-Wu Jiang and Harold S Park. Mechanical properties of single-layer black phosphorus. Journal of Physics D: Applied Physics, 47(38):385304, 2014.

[380] Yanfeng Ge, Wenhui Wan, Fan Yang, and Yugui Yao. The strain effect on superconductivity in phosphorene: a first-principles prediction. New Journal of Physics, 17(3):035008, 2015.

[381] E. Taghizadeh Sisakht, F. Fazileh, M. H. Zare, M. Zarenia, and F. M. Peeters. Strain-induced topological phase transition in phosphorene and in phosphorene nanoribbons. Phys. Rev. B, 94:085417, Aug 2016.

[382] Mehboudi Mehrshad, Utt Kainen, Terrones Humberto, Harriss Edmund O, Pacheco SanJuan Alejandro A, and Barraza-Lopez Salvador. Strain and the optoelectronic properties of nonplanar phosphorene monolayers. Proceedings of the National Academy of Sciences of the United States of America, 112(19):5888–5892, apr 2015.

[383] Yuanyue Liu, Fangbo Xu, Ziang Zhang, Evgeni S. Penev, and Boris I. Yakobson. Two-dimensional monoelemental semiconductor with electronically inactive defects: The case of phosphorus. Nano Letters, 14(12):6782–6786, 2014. PMID: 25162380.

[384] Robert C. Haddon. Chemistry of the fullerenes: The manifestation of strain in a class of continuous aromatic molecules. Science, 261:1545–1550, 1993.

[385] Kainen L. Utt, Pablo Rivero, Mehrshad Mehboudi, Edmund O. Harriss, Mario F. Borunda, Alejandro A. Pacheco SanJuan, and Salvador Barraza-Lopez. Intrinsic defects, fluctuations of the local shape, and the photo-oxidation of black phosphorus. ACS Central Science, 1(6):320–327, 2015. PMID: 27162987.

[386] Joshua D. Wood, Spencer A. Wells, Deep Jariwala, Kan-Sheng Chen, EunKyung Cho, Vinod K. Sangwan, Xiaolong Liu, Lincoln J. Lauhon, Tobin J. Marks, and Mark C. Hersam. Effective passivation of exfoliated black phosphorus transistors against ambient degradation. Nano Letters, 14(12):6964–6970, 2014. PMID: 25380142.

[387] Alexandre Favron, Etienne Gaufrès, Frederic Fossard, Anne-Laurence Phaneuf-L'Heureux, Nathalie Y-W. Tang, Pierre L. Levesque, Annick Loiseau, Richard Leonelli, Sebastien Francoeur, and Richard Martel. Photooxidation and quantum confinement effects in exfoliated black phosphorus. Nat. Mater., 14:826–832, 2015.

[388] Jorge Quereda, Pablo San-Jose, Vincenzo Parente, Luis Vaquero-Garzon, Aday J. Molina-Mendoza, Nicolás Agrat, Gabino Rubio-Bollinger, Francisco Guinea, Rafael Roldán, and Andres Castellanos-Gomez. Strong Modulation of Optical Properties in Black Phosphorus through Strain-Engineered Rippling. Nano Letters, 16(5):2931–2937, 2016. PMID: 27042865.

[389] Eric M. Vogel and Joshua A. Robinson. Two-dimensional layered transition-metal dichalcogenides for versatile properties and applications. MRS Bulletin, 40:558–563, 7 2015.

[390] Agnieszka Kuc, Thomas Heine, and Andras Kis. Electronic properties of transition-metal dichalcogenides. MRS Bulletin, 40:577–584, 7 2015.

[391] RadisavljevicB., RadenovicA., BrivioJ., GiacomettiV., and KisA. Single-layer MoS2 transistors. Nat Nano, 6(3):147–150, mar 2011. 10.1038/nnano.2010.279.

[392] Linyou Cao. Two-dimensional transition-metal dichalcogenide materials: Toward an age of atomic-scale photonics. MRS Bulletin, 40:592–599, 7 2015.

[393] J. A. Reyes-Retana, G. G. Naumis, and Felipe Cervantes-Sodi. Centered Honeycomb NiSe2 Nanoribbons: Structure and Electronic Properties. The Journal of Physical Chemistry C, 118(6):3295–3304, 2014.

[394] Xiao Zhang, Mengmeng Zhen, Jinwu Bai, Shaowei Jin, and Lu Liu. Efficient NiSe-Ni3Se2/Graphene Electrocatalyst in Dye-Sensitized Solar Cells: The Role of Hollow Hybrid Nanostructure. ACS Applied Materials & Interfaces, 8(27):17187–17193, 2016. PMID: 27314283.

[395] M. Ghorbani-Asl, S. Borini, A. Kuc, and T. Heine. Strain-dependent modulation of conductivity in single-layer transition-metal dichalcogenides. Phys. Rev. B, 87:235434, Jun 2013.

[396] Keliang He, Charles Poole, Kin Fai Mak, and Jie Shan. Experimental Demonstration of Continuous Electronic Structure Tuning via Strain in Atomically Thin MoS2. Nano Letters, 13(6):2931–2936, 2013. PMID: 23675872.

[397] David Lloyd, Xinghui Liu, Jason W. Christopher, Lauren Cantley, Anubhav Wadehra, Brian L. Kim, Bennett B. Goldberg, Anna K. Swan, and J. Scott Bunch. Band Gap Engineering with Ultralarge Biaxial Strains in Suspended Monolayer MoS2. Nano Letters, 0(0):null, 2016. PMID: 27509768.

[398] Tingting Shen, Ashish V. Penumatcha, and Joerg Appenzeller. Strain Engineering for Transition Metal Dichalcogenides Based Field Effect Transistors. ACS Nano, 10(4):4712–4718, 2016. PMID: 27043387.

[399] Yoichi Ando and Liang Fu. Topological crystalline insulators and topological superconductors: From concepts to materials. Annual Review of Condensed Matter Physics, 6(1):361–381, 2015.

[400] I. Lefebvre, M. A. Szymanski, J. Olivier-Fourcade, and J. C. Jumas. Electronic structure of tin monochalcogenides from sno to snte. Phys. Rev. B, 58:1896–1906, Jul 1998.

[401] T. Chattopadhyay, J. Pannetier, and H.G. Von Schnering. Neutron diffraction study of the structural phase transition in sns and snse. J. Phys. Chem. Solids, 47(9):879–885, 1986.

[402] Li-Dong Zhao, Shih-Han Lo, Yongsheng Zhang, Hui Sun, Gangjian Tan, Ctirad Uher, C. Wolverton, Vinayak P. Dravid, and Mercouri G. Kanatzidis. Ultralow thermal conductivity and high thermoelectric figure of merit in snse crystals. Nature, 508:373–377, 2014.

[403] C. W. Li, J. Hong, A. F. May, D. Bansal, S. Chi, T. Hong, G. Ehlers, and O. Delaire. Orbitally driven giant phonon anharmonicity in snse. Nat. Phys., 11:1063–1069, 2015.

[404] Georgios A. Tritsaris, Brad D. Malone, and Efthimios

Kaxiras. Optoelectronic properties of single-layer, double-layer, and bulk tin sulfide: A theoretical study. Journal of Applied Physics, 113(23), 2013.

[405] Arunima K. Singh and Richard G. Hennig. Computational prediction of two-dimensional group-iv monochalcogenides. Applied Physics Letters, 105(4), 2014.

[406] Houlong L. Zhuang and Richard G. Hennig. Computational discovery, characterization, and design of single-layer materials. JOM, 66(3):366–374, 2014.

[407] A. S. Rodin, Lidia C. Gomes, A. Carvalho, and A. H. Castro Neto. Valley physics in tin (ii) sulfide. Phys. Rev. B, 93:045431, Jan 2016.

[408] Zhen Zhu, Jie Guan, Dan Liu, and David Tomnek. Designing isoelectronic counterparts to layered group v semiconductors. ACS Nano, 9(8):8284–8290, 2015. PMID: 26190265.

[409] Di Xiao, Gui-Bin Liu, Wanxiang Feng, Xiaodong Xu, and Wang Yao. Coupled spin and valley physics in monolayers of mos_2 and other group-vi dichalcogenides. Phys. Rev. Lett., 108:196802, May 2012.

[410] Xiaoming Mao, Anton Souslov, Carlos I. Mendoza, and T. C. Lubensky. Mechanical instability at finite temperature. Nat. Comm., 6:5968, 2015.

[411] Hua Wang and Xiaofeng Qian. Two-dimensional multiferroics: ferroelasticity, ferroelectricity, domain wall, and potential mechano-opto-electronic applications. arXiv:1606.04522, 2016.

[412] Menghao Wu and Xiao Cheng Zeng. Intrinsic ferroelasticity and/or multiferroicity in two-dimensional phosphorene and phosphorene analogues. Nano Letters, 16(5):3236–3241, 2016. PMID: 27096689.

[413] Pablo Rivero, Vctor Manuel Garca-Surez, David Pereiguez, Kainen Utt, Yurong Yang, Laurent Bellaiche, Kyungwha Park, Jaime Ferrer, and Salvador Barraza-Lopez. Systematic pseudopotentials from reference eigenvalue sets for {DFT} calculations. Computational Materials Science, 98:372 – 389, 2015.

[414] Ruixiang Fei, Wei Kang, and Li Yang. Ferroelectricity and phase transitions in monolayer group-iv monochalcogenides. Phys. Rev. Lett., 117:097601, Aug 2016.